The evolution of a sensor integrated laser welding head.

Sensor Development and Integration for Robotized Laser Welding

Dimitrios Iakovou

Sensor Development and Integration for Robotized Laser Welding

D. Iakovou

Invitation

On Thursday 5th February at 16:45 I will defend my dissertation, titled:

Sensor Development and Integration for Robotized Laser Welding

The defense takes place in "zaal 2" of the building "de Spiegel" at Twente University. Prior to the defense, at 16:30, I will give a small presentation about my work.

I would be happy to see you and your partner at the defense and the reception that will follow immediately afterwards.

Dimitrios Iakovou
Pasteurstraat 200
2522RR Den Haag
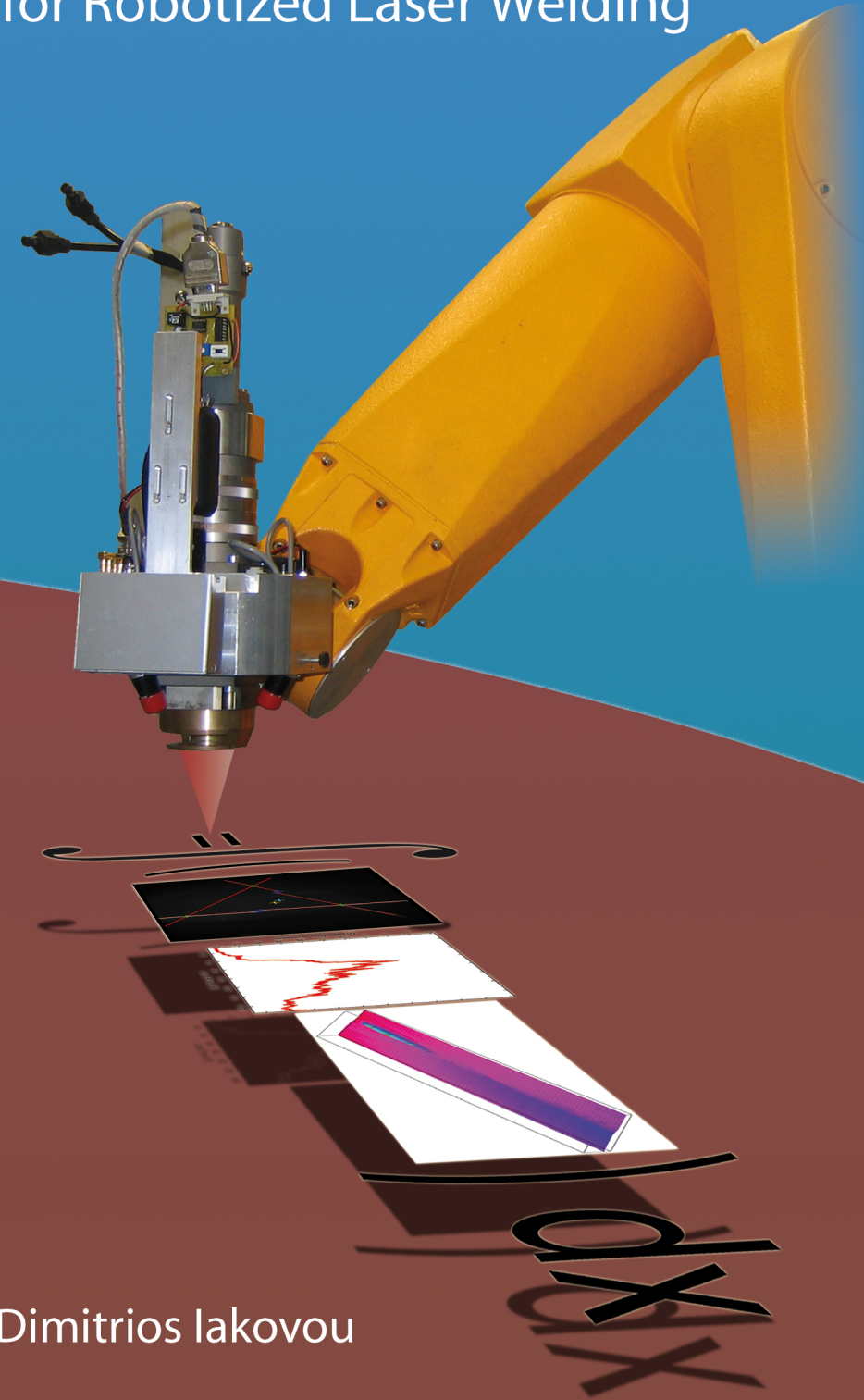06-28747312
d.iakovou@gmail.com

Paranymphs:

Jeffrey Thé
jeffreythe@gmail.com
06-12118123

Marco Olthof
marco.olthof@gmail.com
06-16078822

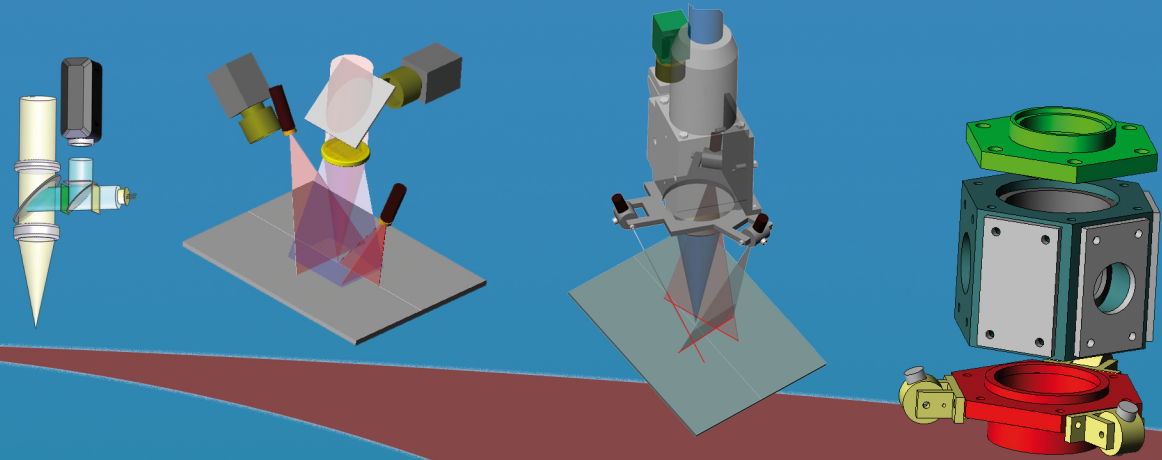# Sensor Development and Integration for Robotized Laser Welding

Dimitrios Iakovou

SENSOR DEVELOPMENT AND INTEGRATION FOR ROBOTIZED LASER WELDING

DISSERTATION

to obtain
the degree of doctor at the University of Twente,
on the authority of the rector magnificus,
prof.dr. H. Brinksma,
on account of the decision of the graduation committee,
to be publicly defended
on Thursday, 5 February 2009 at 16:45

by

Dimitrios Iakovou
born on 5 November 1975
in Thessaloniki, Greece

This dissertation is approved by
prof.dr.ir. J. Meijer, promotor
prof.dr.ir. J.B. Jonker, promotor
dr.ir. R.G.K.M. Aarts, assistant-promotor

Summary

Laser welding requires fast and accurate positioning of the laser beam over the seam trajectory. The task of accurate positioning the laser tools is performed by robotic systems. It is therefore necessary to be able to teach the robot the path that it has to follow. Seam teaching is implemented in several ways: Offline Programming, Manual Point-to-point, Sensor Guided. The first two are time consuming processes with the second requiring constant human interaction, whereas the last one is a fast and automated process.

The most commonly used seam detection sensors are based on optical triangulation with a single structured light line. The use of these sensors with the laser tool imposes restrictions on the laser tool orientation in relation to the seam trajectory, as the measurement always has to be ahead of the tool and not parallel to the seam. The shape of the seam trajectory in combination with the required speed, can in turn force the robot into positioning errors due to robot dynamics. Furthermore, closed looped seam trajectories such as circles or rectangles are not possible to be taught.

Solution to these problems is given by the seam detection sensor of the integrated laser welding head. The designed perimetric sensor allows the detection and following of seam trajectories without restriction on the relative position of the welding head. This enables it to reduce the positioning errors due robot dynamics and follow complete looped seam trajectories.

The developed integrated laser welding head carries two additional sensing functionalities: seam inspection and process monitor. The seam inspection sensor provides a quality estimation of the surface of the weld according to ISO 13919, as well as measurements about several weld defects (misalignment, undercut, convexity, etc). Furthermore, a 3D representation of the inspected weld is also provided with indicators of the defect positions. The developed process monitor sensor allows the detection of the formation of a keyhole in full penetration welding. The output of

the process monitor sensor can be used for controlling the laser power of the welding process.

The integration of the sensors in one integrated laser welding head requires the combination of common sensor resources. The optical paths of the sensor's are fused to produce a compact design. All developed electronic boards are integrated into the welding head housing.

For the integrated laser welding head to be easily used by robots, several calibrations are required. For this reason, the necessary sensor and laser tool calibrations routines are automated and included in the sensor software application. The calibration process makes use of the robot as a measuring tool.

Furthermore a user friendly software application is developed to give overview and access to the welding head's running processes and measurements, as well as the sensor configuration parameters. Within this software also the required calibrations are performed. Finally, the software makes use of several communication protocols for its communication with the several parts of the welding head, but also for the communication of the welding head with the robot and the transmission of its measurement data to rest of the world.

Samenvatting

Laserlassen vergt een snelle en nauwkeurige positionering van de laser-straal over de naad. Deze taak van wordt uitgevoerd door robots. Het is daarbij nodig om de robot nauwkeurig het pad te leren dat hij moet volgen. Dit "naadonderwijs" wordt op verschillende manieren gemplementeerd: offline programmering, handmatig point-to-point of sensor gestuurd. De eerste twee zijn tijdrovende processen en vereisen een continue menselijke interactie, terwijl het laatste een snel en geautomatiseerd proces is.

De meest toegepaste naaddetectie sensoren zijn gebaseerd op optische triangulatie met n enkele gestructureerde lichtlijn. Het gebruik van deze sensoren gekoppeld aan de lasertool legt beperkingen op aan de orintatie. Zo moet de meting vooraf gaan aan het lasproces en mag de lichtlijn niet parallel zijn met de naad. De vorm van het lasnaadtraject in combinatie met de vereiste snelheid, zal daarom aanleiding geven tot positioneringfouten ten gevolge van de robotdynamiek. Bovendien kunnen gesloten lasnaadtrajecten zoals cirkels of rechthoeken niet worden ingeleerd.

De oplossing voor deze problemen is een naad-detectie-sensor gentegreerd in de laserlaskop. De ontworpen perimetric-sensor maakt het detecteren en het volgen van naadtrajecten zonder beperkingen aan de positie van de laskop mogelijk. Hierdoor worden positioneringfouten ten gevolge van de robotdynamiek gereduceerd en kan het volledige lasnaadtraject zonder beperkingen gevolgd worden.

De ontwikkelde gentegreerde laserlaskop heeft nog twee extra sensor functies: naadinspectie en proces monitoring. De naadinspectie sensor geeft een kwalitatieve schatting van de oppervlakte van de las volgens de norm ISO 13919, alsook meetresultaten van diverse mogelijke lasgebreken (uitlijnfout, ondersnijding, convexiteit, etc). Bovendien wordt een 3D-afbeelding gemaakt van de genspecteerde las met indicaties van de defecte posities. De ontwikkelde sensor voor proces monitoring maakt

detectie van volledig doorlasssen mogelijk. De output van de procesmonitor sensor kan worden gebruikt voor het regelen van het laservermogen of van het lasproces.

De integratie van de sensoren in een gentegreerde laserlaskop vereist de combinatie van gemeenschappelijke sensor hulpmiddelen. De optische paden van de sensoren zijn in n compact design gentegreerd. Zo is ook alle ontwikkelde elektronica is gentegreerd in de laskop behuizing.

Alvorens de gentegreerde laserlaskop te kunnen gebruiken, zijn meerdere kalibraties nodig. Alle noodzakelijke sensor en lasertool kalibratieroutines zijn volledig geautomatiseerd en in de grafische gebruikers interface van de sensor opgenomen. De kalibratieroutine gebruikt de robot zelf als een meetinstrument.

Verder is er gebruiksvriendelijke software ontwikkeld om het overzicht en directe toegang tot de laskoppen tijdens lopende processen mogelijk te maken. Daarbij zijn alle sensorconfiguratie parameters on-line toegankelijk. Ook de benodigde kalibraties worden softwarematig uitgevoerd. De software gebruikt meerdere communicatieprotocollen voor de communicatie met de verschillende units van de laskop, maar ook voor de communicatie van de laskop met de robot en voor communicatie naar externe computers voor bijvoorbeeld het versturen van meetrapporten naar een productie bewakingssysteem.

Acknowledgements

Everything that has a start is destined to have an end. Neither the start nor the end is as important as the period in between. Within this period, which for my case lasted for about five years, I had the chance to explore and learn about new engineering fields, and "play" with very expensive high-tech "toys". Next to my work, I had a chance to get involved in the development of a Cybernetic Laboratory (CyberLab), and investigate the possibility to start my own company. Of course traveling for conferences and meetings was also part of my responsibilities (Munich, Miami, Orlando, Göteborg, Aachen, Budapest, Paris), as was providing the cookies for the afternoon coffee break.

I want to thank my supervisors Johan and Ronald. Their positive attitude, constructive criticism and ability to provide valuable suggestions kept me motivated and on track. Together with Ben, they also helped in the editing of a coherent dissertation. My thanks also extend to Leo and Martina. Without the creative mind of Leo, the mechanical designs of the two welding head prototypes might not have been so elegant and functional, and some of the experiments might not be possible to implement. Martina kept me out of administrative and organizational trouble, always with a smile. Of course I must not forget my room mate at work, Toon (a.k.a. "Con I Dita Rapida" or "Tony Quick-Fingers"), and be thankful that he did not try to improve his stress-ball throwing skills.

In any way, none of this would have happened if the people who have thought of this research topic had not worked towards its realization, or if the STW foundation did not approve its funding. A "huge" thanks to them as well as to all the rest of the Mechanical Automation group members: Benno, Bert, Bertus, Dannis, Dirk, Frank, Frits, Gert, Gert-Willem, Jilles, Jeroen OB, Jeroen vT, Johannes, Jonathan, Max, Menno, Pathiraj, Rob, Tjeerd, Tyrone, Wouter, who made the endless hours of programming (debugging), soldering, business developing, testing, feel like minutes. I

also had the fortune to supervise two MSc. projects related to my work. I would therefore like to thank Jorg, and Niels for enduring the hell I put them through and for contributing to my work.

Further I would like to acknowledge the people that sweated and fought beside me in the battlefield of the volleyball court. Most of them were, some of them still are, members of Harambee volleyball club. With Harambee I had a lot of fun (parties, tournaments, coaching/training), had several memorable moments (championships, cup-games) but most importantly I made new friends.

I am also thankful of the people that helped me to get here. This includes members of past departments, research groups and supervisors, who through their guidance and support have assisted me to get where I am.

Last but not least are my friends and family. I want to thank my friends here and abroad for not letting me feel alone, and my friends back in Greece for making me feel as if I never went away every time we meet and not letting me lose my Greek spirit. As for my family, well, they have supported me all my life, so there is no "Thank You!" big enough for that. This goes especially to both my brothers and mother, but also to my father. He might not be among us anymore, but the biggest part of who I am, I owe to him.

Dimitrios Iakovou
Enschede, February 2009

Nomenclature

Latin Symbols

Symbol	Unit	Description
$\tilde{}$		Tilde as in $\tilde{\mathbf{v}}$ is used to denote an augmented vector $[\mathbf{v}^T 1]^T$
$\check{}$		Denotes a distorted camera coordinate, with subscripts r and t to indicate radial and/or tangential distortion
c	[pxl]	Principal point on image where optical axis crosses the image plane $[u_0, v_0]$
c_p	[pxl/mm]	Pixel-to-mm scaling factor
CoG_{sd}	[pxl]	Position of pixel center of gravity along the scanning direction sd
d_{3D}	[mm/frame]	Distance between two seam inspection measurement samples
$d_{L,x}$	[mm]	Correction of the x parameter of ${}^L_F\text{T}$, where F stands for robot Flange and L for the Laser tool.
$d_{L,y}$	[mm]	Correction of the y parameter of ${}^L_F\text{T}$
$d_{L,z}$	[mm]	Correction of the z parameter of ${}^L_F\text{T}$
d_R	[mm]	Distance between imaging lens and reference plane
$d_{S,x}$	[mm]	Correction of the x parameter of ${}^S_L\text{T}$, where L stands for Laser tool and S for the Sensor tool.
$d_{S,y}$	[mm]	Correction of the y parameter of ${}^S_L\text{T}$

Symbol	Unit	Description
dx_S	[mm]	Displacement of TCP$_S$ along the x_S in triangular sensor seam teaching
dy_S	[mm]	Displacement of TCP$_S$ along the y_S in triangular sensor seam teaching
D_X,D_Y,D_Z D		Determinants for plane definition of $D_X x + D_Y y + D_Z z - D = 0$. If subscript includes Ref, then it refers to the sensor reference plane
E_L		Left weld edge point
E_R		Right weld edge point
f	[mm]	Focal length of optical system
f_c	[mm]	Focal length of optical system for camera to image
f_I	[mm]	Focal length of camera lens
f_L	[mm]	Focal length of laser focus lens
f_S	[frames/s]	Measuring speed of the sensor
f_T	[mm]	Optical triangulation focal distance of imaging lens
G		Process monitor signal amplification gain
h_{CoG}	[pxl, mm]	Center of gravity of single height profile
h_C	[mm]	Convexity weld defect value
h_I	[mm]	Image field of view height
h_M	[mm]	Misalignment weld defect value
h_O	[mm]	Object field of view height
h_S	[mm]	Sagging weld defect value
h_U	[mm]	Undercut weld defect value
h_W	[mm]	Weld Width
I	[mm]	The image of an object from a lens system
k_1, k_2		Radial distortion parameters
k_u		Camera pixel size in u direction
k_v		Camera pixel size in v direction
m	[pxl]	Position of projection of point M_c on image plane
M		Real world coordinates point
M$_c$		Camera coordinates point

Symbol	Unit	Description
max_{sd}		Maximum pixel value along scanning direction sd
min_{sd}		Minimum pixel value along scanning direction sd
$\mathbf{n}$		Normal vector of a plane
$\mathbf{n}_{Ref}$		Normal vector of a reference plane
O	[mm]	Object placed in front of a lens system
$p_{u,v}$		Pixel value at coordinates u,v
$\hat{p}_{u,v}$		Intensity of normalized pixel at image coordinates u, v
$\check{p}_{u,v}$		Intensity of thresholded pixel at image coordinates u, v
P_A		Seam point A
P_B		Seam point B
Q		Quaternion
q_0, q_1, q_2, q_3		Quaternion components
R		Rotation Matrix
S_{out}	[V]	Process monitor output signal
T		Threshold value
$^{B}_{A}T$		Transformation of coordinate frame A to B
TCP_L		Laser Tool Center Point
TCP_S		Sensor Tool Center Point
$\bar{u}_R$	[mm/s]	Robot velocity
u,v	[pxl]	Camera image coordinates (Columns, Rows)
V		Magnification factor
$\mathbf{v}_R$		Rotation axis for the dihedral angle
$v_{R_x}, v_{R_y}, v_{R_z}$		Dihedral angle rotation axis components
w_I	[mm]	Image field of view width
w_O	[mm]	Object field of view width
x, y, z	[mm]	Axes of a coordinate frame or values along those axes. The coordinate frame or value that they represent is indicated by their subscript
x_p, y_p	[mm]	Coordinates of a point on the photodetector surface
z_{CoG}	[mm]	The height of the detected center of gravity line

Greek Symbols

Symbol	Unit	Description
α, β		Line parameters of type $y = \alpha x + \beta$
$\alpha_{\ell_1}, \beta_{\ell_1}$		Line parameters of ℓ_1 linear part of height profile
$\alpha_{\ell_2}, \beta_{\ell_2}$		Line parameters of ℓ_2 linear part of height profile
α_S, β_S		Line parameters structured light line image
α_T		Relative orientation of a seam inspection height profile
γ		Forgetting factor
θ	[rad, deg]	Dihedral angle
θ_c	[rad, deg]	Angle between u and v axes of the image in camera calibration
θ_ℓ	[rad, deg]	Angle of a line ℓ in a Radon map
ϖ	[rad, deg]	Optical Triangulation angle between the TCP_S y and the reference line from z view
ρ_ℓ	[pxl]	The distance of a line ℓ in a Radon map
$\sigma_{p,sd}$		Standard deviation of pixels along the scanning direction sd
σ_{var}		Standard deviation of height profile around h_{CoG}
τ_1, τ_2		Tangential distortion parameter
ϕ	[rad, deg]	Structured light diode projection angle
φ, ψ, ω	[rad, deg]	Rotation around the axes of a coordinate frame. The coordinate frame or value that they represent is indicated by their subscript

Subscripts of $x,y,z,\varphi,\psi,\omega$

Symbol	Description
c	Calibration camera position in world coordinates
F	Values along the robot flange coordinate system axes

Symbol	Description
FL	Translations and orientations of the origin of the flange coordinate system origin to coincide with the one of the laser tool
L	Values along the laser tool TCP_L coordinate system axes
mm, s	Passive reconstruction coordinate frame axes
mm, w	Active reconstruction coordinate frame axes
Pd	Axes of the process monitor sensor photodiode coordinate system
S	Values along the sensor tool TCP_S coordinate system axes
SN	Estimated seam point during triangular sensor seam tracking

Acronyms and Abbreviations

CAD	**C**omputer **A**ided **D**esign
CCD	**C**harged **C**oupled **D**evice
CMOS	**C**omplementary **M**etal **O**xide **S**emiconductors
DoF	**D**egrees **o**f **F**reedom
DSP	**D**igital **S**ignal **P**rocessor
EMATs	**E**lectro-**M**agnetic **A**coustic **T**ransducer
FoV	**F**ield **o**f **V**iew
FPGA	**F**ield **P**rogrammable **G**ate **A**rray
GUI	**G**raphic **U**ser **I**nterface
IC	**I**ntegrated **C**ircuit
IR	**I**nfra-**R**ed
LUT	**L**ook-**U**p **T**able
Nd:YAG	**N**eodymium-**d**oped **Y**ttrium **A**luminium **G**arnet
RMS	**R**oot **M**ean **S**quare
ROI	**R**egion **O**f **I**nterest
RS232	**R**ecommended **S**tandard 232 (Serial Communication)
TTL	**T**ransistor**T**ransistor **L**ogic

xvi

Contents

Contents   **xix**

Chapter 1

Introduction to Robotic Laser Welding

Technology advancement requires continuous improvement of the tools and processes that are used in industry. In every branch there are breakthroughs that reveal new ways to handle and solve problems. Such improvements also occur in the field of laser welding.

Merriam−Webster defines welding as *the uniting of metallic parts by heating and allowing the metals to flow together or by hammering or compressing with or without previous heating*. These days the term welding is used to define the joining of any type of materials by local melting. The distinction between the types of welding is performed according the manner in which the heat is applied on the work piece. The most widely known and used types of welding are Electric Arc Welding, Gas Flame Welding, Gas Metal Arc Welding (GMAW), Resistance Welding, Energy Beam Welding and Solid State Welding.

In the early years, welding involved the use of the welding tools by a specialized worker. The quality of the weld was mainly dependent on the experience and skills of that individual. Eventually, some of the later developed welding techniques prohibited the physical handling of the tool by the user due to the hazardous nature of the process. This lead to the development of machinery that enabled operators to handle the welding tools without being directly exposed to the welding process emissions.

The ability to handle the welding tools from distance was the main step towards the automatization of the welding processes. The welding tools were mounted on mechanical manipulators (gantry robots, robotic

arms,etc) and could perform the basic welding operations without human interaction. Even though these machines could perform only simple welding jobs, they had better repeatability than the human counterparts. By automating as many welding functionalities as possible the machines could perform more complex welding jobs.

In this thesis the description for the development of such a multifunctional welding tool will be given. The tool is designed for laser welding processes, and is handled by industrial robots.

1.1 Laser Welding

Laser welding belongs under the Energy Beam welding category. In laser welding, optics are used to focus a laser beam into a high power density spot. When this focused beam is applied on the surface of a material it increases the local temperature of the surface. When sufficient heat is absorbed by the material, local melting occurs jointing two pieces together. This process is called laser welding.

For even higher laser intensity the molten material begins to evaporate. The pressure built by this vapor forces the molten material aside. This way a cavity is formed filled with vapor, which is known as the keyhole. Depending on the existence and depth of a keyhole the laser welding process can be divided into three types: conduction, partial penetration, full penetration (Fig.1.1).
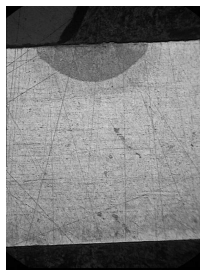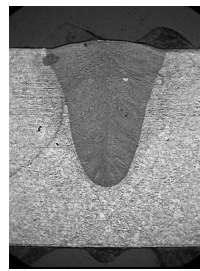
(a) Conduction (b) Keyhole Partial Penetration (c) Keyhole Full Penetration
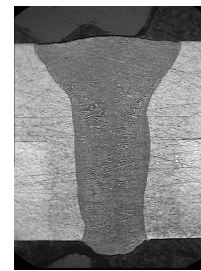
Figure 1.1: Images of the different types of laser welding of material with 2mm thickness. The darker part of the material is the area that has been molten by the laser beam.

In the conduction type there is no keyhole formation. The heat is absorbed on the surface of the material and transported by conduction to the depth. In the partial penetration type there is a keyhole but the penetration depth of the keyhole into the material is less than the material's thickness. In the full penetration type, the keyhole penetrates through the full thickness of the material. The keyhole formation and its penetration depth depend on the laser beam intensity and the speed at which the welding process is being performed. Keyhole welding is advantageous for the welding of thick materials as it has a high weld depth/weld width ratio.

To perform laser welding, tools equipped with optical components for the focusing of the laser beam are required. In Fig.1.2, such a laser tool is presented. Laser welding tools focus the laser beam into a focal point which is called Laser Tool Center Point (TCP_L). This point has to be accurately positioned on the seam. A typical laser beam focus profile shows that the the beam converges to a focal point and diverges again after it (Fig.1.2). Therefore, there is only a small part along the laser beam axis where the beam is concentrated enough to be used for welding applications. This area is called the depth of focus and its size depends on the specifications of the optical components that are used (fiber, mirrors, lenses, etc). Laser welding can be implemented at velocities as high as 250 mm/s, and the required position accuracy of the focused spot on the seam is in the order of 0.1 mm.
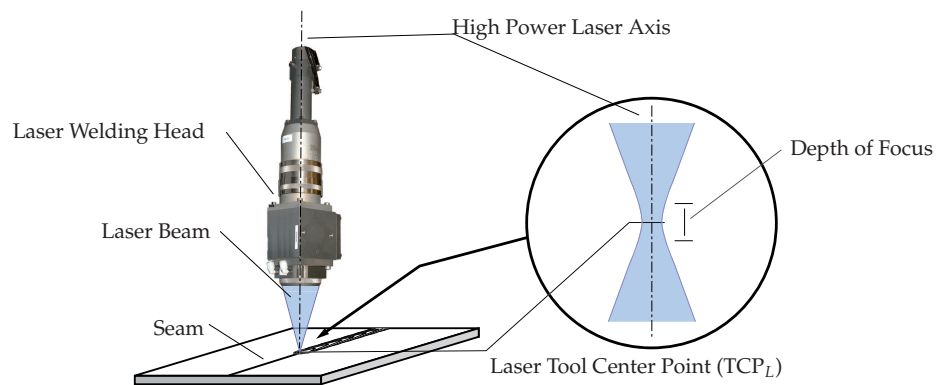

Figure 1.2: Representation of a laser welding head (standard Trumpf laser head) over a seam and a typical beam focus profile.

1.2 Industrial Robots

Industrial robots are mechanisms that replicate human motions. They are defined in ISO 8373:1994 as *automatically controlled, reprogrammable, multi-purpose manipulators programmable in three or more axes.* They are used for a variety of applications (welding, positioning, cutting, placing, etc), depending on their degrees of freedom and speed.

The degrees of freedom (DoF) of a robot are the number of independent displacements that the robot can perform. The more DoF of a mechanism, the greater the number of ways by which the mechanism can reach a point is space.

For simple welding applications in two-dimensions, like the welding of flat planes, Gantry robots with 3 DoF suffice for the task. When additional welding requirements arise (eg. welding orientation) then extra DoFs are necessary. For welding of three-dimensional geometries 6 DoF robots (Fig.1.3) are often used. These types of robots allow the welding tool to reach a certain point in their working area from various directions.
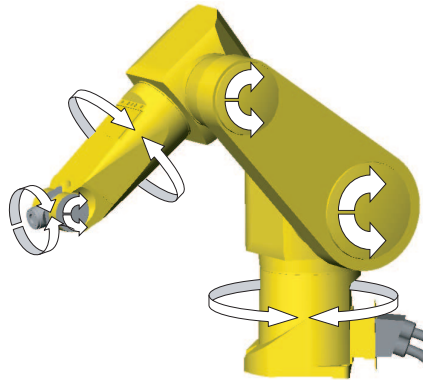
Figure 1.3: Drawing of a 6DoF Stäubli RX130 industrial robot. Each set of arrows is one degree of freedom

.

This ability can be used for laser welding if a welding head is attached to the end effector of the robot. Fiber coupled lasers (Nd:YAG, diode, fiber) can be easily used for laser welding on any robot, since the transportation of the laser bundle can be implemented with a use of an optical fiber connected directly on the tool. CO_2 lasers on the other hand, require mirror assemblies in order to transfer the laser bundle to the laser tool. Such mir-

ror assemblies are very sensitive on their correct alignment and introduce limitations to the movements of 6 DoF robots.

Before a robot can be used for laser welding, it has to know the path that it must follow. This path can be either taught to the robot manually or autonomously with the help of sensors, or defined with the use of CAD software. As it is outlined in §1.1 laser welding requires a positioning accuracy in the order of 0.1 mm at a velocity of e.g. 250 mm/sec. Although these velocities can be obtained by industrial robots, their positioning accuracy is insufficient for most of the laser welding processes. Furthermore, the use of CAD data does not guarantee that the laser tool will be positioned exactly on the seam location. The problem of positioning inaccuracy, can be overcome by using additional sensory systems that correct the position of the robot and the welding tool in real time.

1.3 Sensor Requirements for Robotic Laser Welding

As it is mentioned in §1.2 sensors are required to measure and correct the positioning inaccuracy of the industrial robots. This sensor must be able to measure the position of the seam in relation to the tool and notify the robot about it. This process will be refereed to as **Seam Detection**, and it can be used for **Seam Teaching** and **Seam Tracking**. With seam teaching the position of an unknown or known seam is measured and stored for further processing. During **Seam Tracking** the current measured position is compared to a predefined seam path and any deviations from that path are corrected in real-time.

Even though seam detection is very important for the implementation of laser welding, there are another two main functions that are of similar importance. These additional processes are welding **Process Control** and **Weld Inspection**.

Process control monitors the laser welding process and controls the power output of the laser beam. Most process control sensors are monitoring the radiation emissions around the laser tool center point during welding, detecting selected radiation wavelengths in order to provide useful data about the status of the welding. This data is used by the process controller to set the required laser power output in order to perform a selected laser welding type (conduction, keyhole partial penetration, keyhole full penetration).

Weld inspection is the process that provides a measure of the quality of

the resulted weld. This sensor must be able to detect the existence of probable defects along the welded seam, measure their size and estimate the overall quality of the welded part. Seam inspection is performed behind the laser welding process area where the material has been re-solidified.

1.4 State of the Art

There is a variety of sensors available that can perform the required measurements that are described in §1.3. The majority of these sensors are individual systems that can perform one type of measurements at a time and are mounted externally on the required welding head. When more sensing functionalities are necessary, additional sensors have to be connected on the same tool. Depending on the type and number of sensors that are used, the resulting construction becomes bulky. The bigger the resulting system, the more difficult its manipulation with industrial robots becomes, especially when the accessability of seams in three dimensional products is considered. Furthermore, since the several sensors are not integrated with each other, separate control hardware will be required, adding to the volume that is needed for the use of such tool. These problems have initiated the development of sensor integrated or modular tools. A representative list of individual sensor systems is given in Table 1.1.

For seam detection most of the sensors apply optical triangulation with the use of structured laser light and imaging sensors. The variations within this type of sensors depend mainly on the shape of the projection of the structured light used (concentric circles and crosshair (Jäckel et al. (2003)), single structured laser lines (Lindskog (2002), Vodanovic (1996), Luo and Chen (2004)), multi-lines (Bosner and Parker (1999)). Additional to the optical triangulation sensors there are other types of sensors that can also be used like the proximity and tactile ones. Their response and applicability is not as good as the triangulation ones and therefore they are not widely used in robotized welding.

The welding process control is usually implemented by measuring changes of the weld pool and the emissions of the welding process. For this purpose mainly optical sensors are used which can be photodiodes (Sanders et al. (1997), Postma (2003)), or CCD/CMOS cameras (Beersiek (2001)), or both in combination. Optical filters play a critical role in these sensors as they distinguish between the spectral areas that are monitored.

Weld inspection sensors also mainly operate with the same optical tri-

Table 1.1: Representative Overview of Commercial Sensors

Developer	LW	SD	PC	WI	Description
Bosner and Parker (1999)	−	√	−	−	Optical triangulation system with number of parallel structured light lines are used for the detection of the joints in saddle type joints. Changes in the curvatures across the structured light lines reveal the seam points.
Jurca (2001)	−	−	√	−	Three different photodiode based sensors that measure the plume radiation (400 nm to 600 nm Jurca P), the Nd:YAG laser radiation (1064 nm Jurca R), the thermal surface radiation (1100 nm to 1800 nm Jurca T).
Jäckel et al. (2003)	−	√	−	−	Optical triangulation system with two concentric structured light circles and two structured light lines forming a cross.
INESS (2003)	√	√	√	√	An integrated laser welding head with one structured light line on either side of the laser focus point. Uses a coaxial camera for seam detection and weld inspection and process control.
Innotec (2004)	−	√	−	−	Tactile touch sensitive pin is used to follow the seam
Falldorf (2004)	−	√	−	√	A 2W Low power single laser structured light line optical triangulation system.
HIGHYAG (2005)	−	√	−	−	Tactile finger-shaped seam following sensor what uses touch to follow the seam.

LW = Laser Welding Tool, **SD**= Seam Detection, **PC** = Process Control, **WI**= Weld Inspection

Continuation of Table 1.1.

Developer	LW	SD	PC	WI	Description
MetaVision (2005)	–	√	–	–	A variety of sensors (Multi-line parallel lines or single line structured light) all using optical triangulation.
OST (2005)	–	√	–	√	Optical triangulation system with a rotating spot that forms a circle.
Precitec (2005)	√	–	√	–	Welding head equipped with a Jurca process control sensor.
ServoRobot (2005)	√	√	–	√	Single line structured light optical triangulation sensor. Two of these sensors are combined with a welding head to get a integrated system.
Soudronic (2005)	–	√	–	–	The sensor is equipped with two parallel structured light lines and a uniform flash light. Optical triangulation and texture analysis are used to implement the functionalities.
Vitronic (2005)	–	–	–	√	An optical triangulation based sensor for seam inspection.
Plasmo® (2006)	–	–	√	√	Two separate sensors systems. The process control sensor measures the reflected meld pool radiation. The weld inspection sensor uses optical triangulation.
Rimrock (2006)	–	√	–	–	Tactile seam detection sensor what uses an electrically charged wire to detect the seam
Fraunhofer ILT	√	+	+	+	Modular welding head. Additional parts can be stacked along the high power laser path or beside it to add functionality. The seam detection system consists of a structured light circle projected coaxially to the high power laser beam.

Where '+' indicates that complete sensor systems can be interfaced to the tool

angulation method as the seam detection sensors. The structured light is projected on the welded seam and the deformations of the line are used to determine the surface quality of the welding. Additionally uniform light is also used for the detection of pores and texture (Halscha et al. (2003)). Older seam inspection research use electromagnetic acoustic transducers (Camplin (2001)), or IR and acoustic sensors (Bates and Kelkar (2002)), or laser-based ultrasound (Klein et al. (2002)). The later detects of pores in the weld. This ultrasonic method can be also classified as a process control method as it can be performed during the welding process.

Integrated sensory systems have also been developed. Representative examples of such systems is the DigiLas welding head of ServoRobot (Noruk and Boillot (2006)) and the INESS welding head from INESS (2003). The DigiLas welding head is a laser welding head with two triangulation sensors integrated on its mechanical housing. One triangulation sensor scans the area in front of the heads TCP_L to detect the seam, whereas the second sensor performs weld inspection behind the TCP_L. Similar principle is used by the INESS system. Here two structured lines are projected one before and the other after the TCP_L of the head, but the processing of the triangulation data is being implemented for both projected lines by a coaxial camera. The captured image of the coaxial camera is split in three parts. The first and third parts, are used for the requirements of the triangulation sensors (seam detection, weld inspection) whereas the second (middle) part of the image is used for process monitoring.

1.5 Objectives of this Work

The addition of sensors to a tool increases the functionality of a tool but it also introduces some restrictions. These restrictions are mainly related to the working requirements of the sensor like its mounting conditions and the requirements for the sensor to operate properly. Furthermore, additional sensors tend to increase the size of the tool. The use of industrial robots also imposes some additional challenges to the task as robot dynamics also affect the outcome of the welding. These challenges are going to be addressed in the following paragraphs.

Tool size

Most measuring sensors are supplied as closed box-systems that has to be installed externally on the welding head. If a tool requires several sensing capabilities, then a number of different sensors have to be attached to it. Since each sensor is an autonomous closed system and no integration between the sensors' components is possible, such multi-sensing tools are usually bulky (Fig.1.4). Such systems require more powerful robots to manipulate them, and their size introduces restrictions on the seam geometries for which the tool can be used.
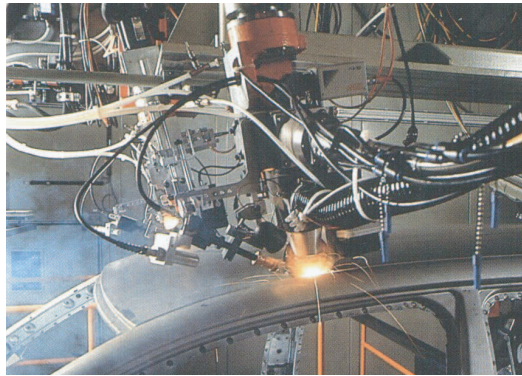

Figure 1.4: Laser welding of a VW Passat in Emden (2001), courtesy of VW.

Joint configurations

The joint configuration defines the positioning of two separate parts of material in order to form a seam. Some sample joint configurations are depicted in Fig.1.5 whereas a more extensive listing of the various configurations and their tolerances is given in Appendix D.1. Depending on the properties of each configuration a specific seam detection approach has to be implemented. Therefore it is important that a variety of joint configurations can be detected and inspected by the developed sensory system.

Detection of sharp corners paths

Many seam detection sensors use a structured light source that projects one or more laser lines on the work piece. For the correct operation of the sensors, these lines have to cross the seam path and maintain a close to
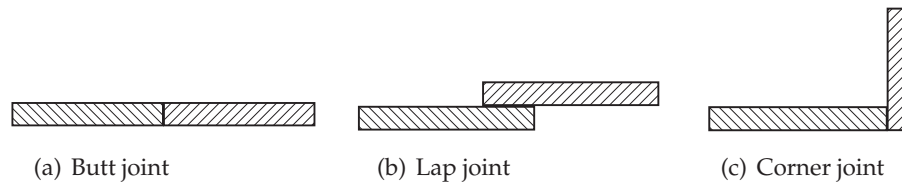
(a) Butt joint   (b) Lap joint   (c) Corner joint

Figure 1.5: Samples of joint configurations.

perpendicular orientation towards the seam path. When a seam position is measured then the tool moves over a predefined step along the seam path before the next measurement is made. The direction of this step is along the interpolated line of the two last measured points. When this path is a smooth curve (Fig.1.6(a)) or a line (initial part of the seam at Fig.1.6(b)), then the sensor can follow it without difficulty. However, when a sharp corner appears along this linear path (last part of the seam at Fig.1.6(b)), then the sensor fails to detect it. When seam teaching is performed, the corner detection failure can be overcome with additional algorithms that assist the sensor to find the seam again. But in the case of seam tracking such a failure to detect a corner will have a great effect to the result of the process.
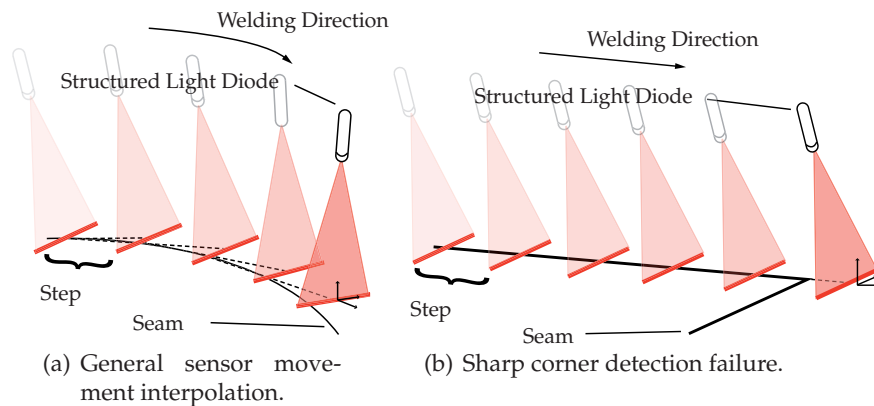

(a) General sensor move-
    ment interpolation.

(b) Sharp corner detection failure.

Figure 1.6: Single line sensors are incapable of detecting the existence of sharp corners along the seam.

Robot dynamics and kinematics

As it is mentioned before, the majority of the sensory systems are orientation dependent. Typically, the line projected on a surface in Fig.1.6 should not become parallel to the weld seam. Assuming the existence of the sharp corner in Fig.1.6(b) is known from e.g. CAD data and the single line triangulation sensor is mounted on the end effector of the robot, then in order to both keep on track with the seam and maintain the required orientation the robot will be forced to perform several fast movements over the corner (see e.g. Fig.1.7). In such cases robot dynamics introduce additional positioning errors that influence the accuracy of the welding process.
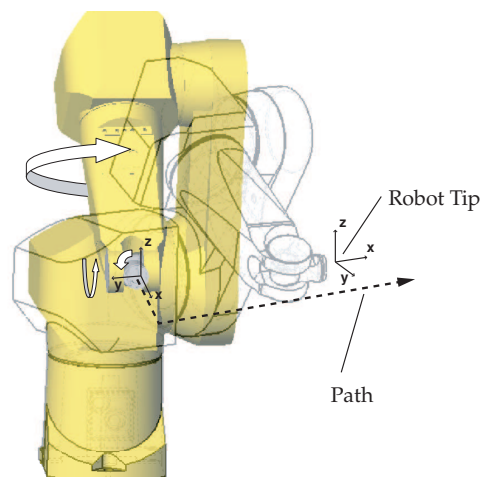
Figure 1.7: Required robot movements (arrows) to keep the tip with the same orientation towards the seam over a sharp corner

Waiboer (2007) made a comparison of analyzed positioning errors of an industrial robot's tip movements. In this study a laser welding head was mounted at a Stäubli RX90 industrial robot to investigate the influence of the robot's movement to the positioning of the laser head's tool tip. Two cases were studied, where the welding head has to follow a rounded corner shaped seam trajectory with a velocity of 100 mm/s. In the first case the welding head's tool tip has to maintain an orientation tangential to the seam, whereas in the second case there is no such restriction. The radius of the rounded corner in the first case was 100 mm, and the required movement results to positioning errors of approximately 0.2 mm. In the second case a smaller rounded corner of 50 mm radius was used, nevertheless the

positioning errors are reduced to approximately 0.1 mm. It is therefore desirable to allow, if possible, the robot movements to be performed without orientation restrictions.

Sensor speed

For seam teaching, the required time for the seam detection is usually not so important, as the joint path can first be taught and then replayed. For real-time seam tracking however, the measurements take place at high velocities and the data has to be available in time to correct path errors. That makes the speed of the detection process an important parameter for the robotic implementation of the laser welding processes.

When a seam detection sensor with a frequency of 50 Hz, is used for welding at 250 mm/s, this would result to one measurement in every 5 mm. For some seam geometries, like linear paths, a measurement every 5 mm might suffice but for complex three-dimensional seam geometries faster sensors are required.

Summary of the objectives

This research is focused on the development of a sensor integrated laser welding head for robotized laser welding. Three sensing functionalities must be integrated in the laser welding head (Seam Detection,Process Control and Weld Inspection). According to the challenges that robotized welding imposes, the following set of objectives has been set. The developed system:

- Has integrated sensors into it for seam detection, process control and weld inspection.

- Is compact in size and weight and therefore can be handled by industrial robots.

- Does not introduce restrictions to the handling manipulator.

- Performs operations in real-time.

1.6 Thesis Overview

The design and implementation of a sensor integrated laser welding tool will be presented in the following chapters.

Chapter 2 presents and overview of the available principles for the implementation of the required sensory functionalities. Furthermore, a selection of the more suitable systems will be made and a more thorough explanation of their methodology is given.

In chapter 3 an overview of the design of the integrated laser welding head is presented. Within this chapter a description of the design decisions concerning the selected components and strategies is given. Additionally, the integration of the sensor in the mechanical design is presented together with the interfacing of the sensors by means of hardware and software.

A description of the sensor and laser tool calibrations is given in chapter 4 while a detailed explanation of the functionality of the sensors and their experimental results are presented in chapters 5, 6 and 7.

Finally, the conclusions of this research are presented in chapter 8.

Chapter 2

Processes and Sensing Principles

The integrated laser welding head has to perform three functions: seam detection, process control, and weld inspection. There are several methods from different domains (optical, mechanical, electrical, etc) that can be applied for the implementation of these functions. Depending on the environment in which these measuring techniques will be applied, some of the solutions are more suitable than others. The choice of the optimal one also depends on its volume, the required functionalities and type of data that it can deliver.

In this chapter, an overview of the methodologies that can be used will be given. The ones that are selected as more suitable, are then explained in detail.

2.1   Methodology Overview

An analysis of the purpose of the integrated laser welding head measuring functions provides a quick overview of the type of techniques that should be considered as candidates. For instance seam detection immediately points towards position measuring techniques, as the position of the seam and the workpiece towards the tool is of importance. Position measuring techniques can also be applied for weld inspection in order to reconstruct the surface of the weld. Furthermore, texture analysis techniques can be used for weld inspection. Finally, the requirements of process control points towards techniques that can measure the effect of the

laser beam to the material during the welding process. Such techniques must process signals that result from the laser process (in the TCP_L) itself or the area around it. Such signals can be emissions from the laser process or even changes of the physical properties of the welded material.

For the selection of the most suitable method, it is important that first the sensing requirements for each of the functionalities (Seam Detection, Process Control, Weld Inspection) are established. In laser welding, it is important for the focused beam to be accurately positioned on the seam. Depending on the joint configuration and the seam geometry, it might also be necessary for the focused beam to be positioned under a given angle in relation to the workpiece. There are therefore two important points for the seam detection functionality. The first is that it must be able to measure the position of the seam in three dimensional space in order to keep the focused beam on the seam. The second point is that the orientation of the workpiece towards the laser tool can also be detected.

During the welding process, depending on the requirements of the welded product, it is important to detect the formation of pores in the weld, or the keyhole formation and the penetration depth, or even the presence of spatter and other surface characteristics around the meltpool. These are the type of measurements that are required from a process control sensor. Several of these characteristics are not easily measurable during welding, therefore an applicable method must be selected.

Finally, for the weld inspection sensor, a quality estimate of the welded surface's profile is required. Several characteristics (pores, spatter, undercuts, cracks, groves, etc) are involved to the formation of a surface profile. The purpose of the sensor is to measure those characteristics. The result of the quality estimate depends on the norm that is used to categorize this measurement data.

Optical Triangulation

Optical triangulation is a widely used technique for measuring seam positions. The basic components of this method are a position sensitive photo-detecting device and a structured light source, an illumination source that can project light patterns. In the most simple case, a narrow light line is used as a light source illuminating a small spot. In Fig.2.1 such a spot-shaped structured light source is shown and its position relative to the position sensitive photo-detector. The optical axes of the photo-detector and the structured light source are placed under an angle ϕ. The diffused

reflection of the structured light spot is imaged onto the photo-detector through a lens. Any height variation of the position of the plane from which the spot is being reflected results to variations of the position of the spot image on the photo-detector. By measuring the position of the spot image on the photo-detector we can easily calculate the height of the plane along the axis of the photo-detector.
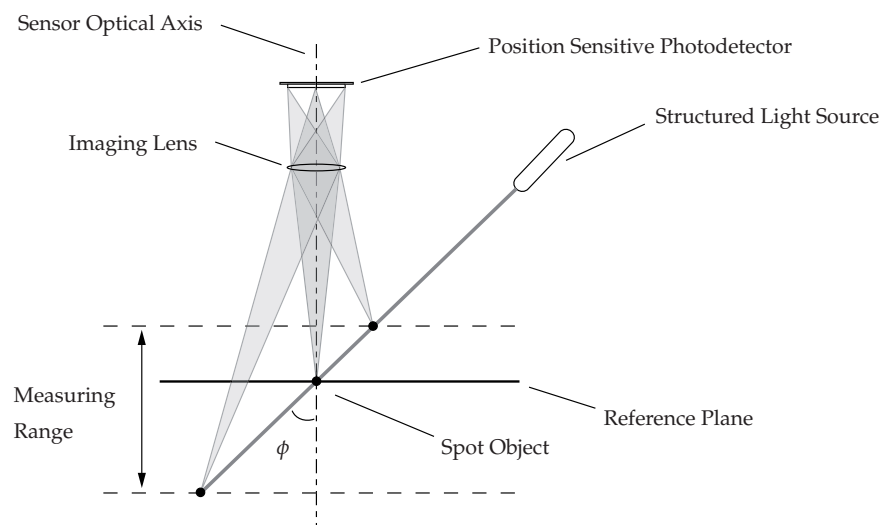

Figure 2.1: Single spot triangulation setup for position measurement.

If a line is projected instead of a spot, then the height of each point on the projected line can be measured, resulting to a height profile along the projected line. Any existing height differences on the surface where the line is projected will appear on the height profile. These differences can occur from the type of joint configuration (overlap, corner, etc) or from the outcome of the welding process (spatter, undercuts, holes, etc). It is therefore possible to use optical triangulation for both seam detection and surface weld inspection.

Alterations of the triangulation method apply different structured light shapes (line, cross, circle, etc.), and a tilted angle of the photo-detector (Scheimpflug principle, see e.g. Merklinger (1992)). Depending on the projected shape of the structured light additional information about the orientation of the surface or the position of elements on the surface can be measured. The measuring range of the method depends on the size of the photo-detector and the imaging lens that is used.

Tactile Sensing

Tactile sensing uses physical contact with the workpiece to identify a position. The most simple type of tactile sensors are the touch sensors and can be described as buttons which produce a signal when they touch the workpiece. More complex tactile sensors make use of materials that change their electrical resistive properties when force is applied on their surface. For welding applications two additional types of tactile sensing method are also used. The first one makes use of an electrode (Fig.2.2(a)). When this touches the metallic workpiece, then it creates a closed circuit and a signal is produced. The second method measures the displacement of the tip during contact to sense when a probe has touched the workpiece and the direction of the touch (Fig.2.2(b)).
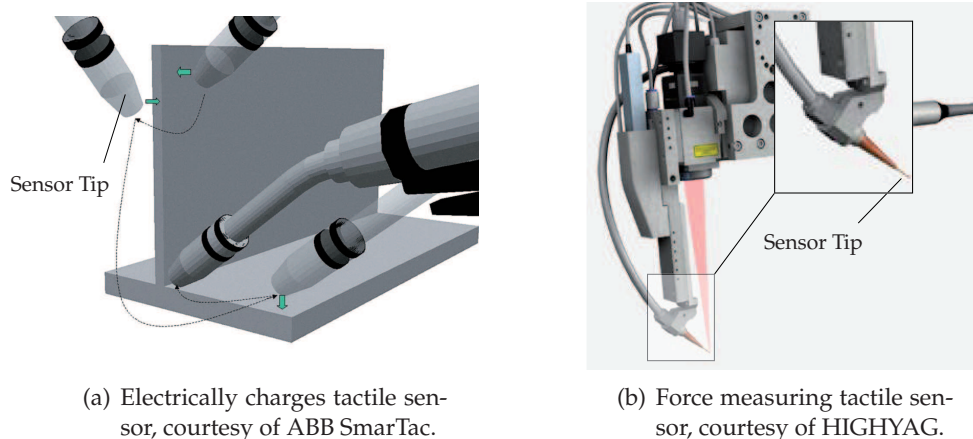

Sensor Tip

Sensor Tip

(a) Electrically charges tactile sensor, courtesy of ABB SmarTac.

(b) Force measuring tactile sensor, courtesy of HIGHYAG.

Figure 2.2: Tactile sensors already in use for robotic welding.

Additional to elctrodes and probes several other devices (pins, rollers, balls, etc) can be used as the tips of tactile sensors. Depending on the number and the position of the tactile sensors, three dimensional positions of a workpiece can be measured. In general, tactile sensors can be used to identify position and orientation but also to measure forces as mentioned in Jones (1987).

In robotic welding, tactile sensing are sometimes used for seam detection, but it is mostly used for seam tracking of an roughly known seam trajectory geometry. The application range is limited to groves, overlap and

corner configurations with large dimensions and approximately straight paths (Dilthey (2005) chapter 16).

Inductive Sensing

Inductive sensing is a non-contact sensing that uses the fluctuations of a coil generated magnetic field. When alternating current flows though a coil, a magnetic field is formed (Fig.2.3). When the coil approaches the workpiece surface, its magnetic field induces the creation of eddy currents on it. These currents also produce an electromagnetic field on the workpiece which interacts with the coil's field. This causes fluctuation on the amplitude of the coil's current. By measuring the changes of the current amplitude, the distance of the coil towards the workpiece can be derived.
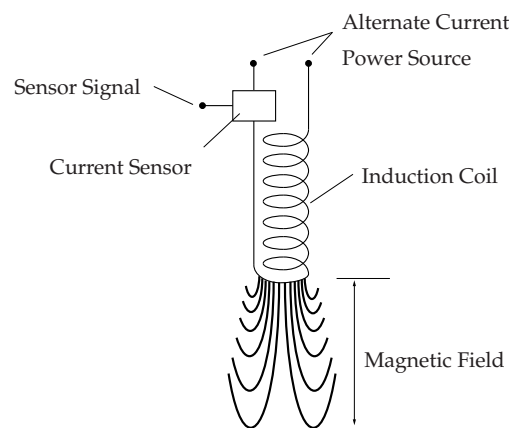

Figure 2.3: Induction method for seam detection and following.

To detect a seam multi-coil inductive sensors are necessary. These sensors require a magnetic field generator and two or more detector coils. When there is nothing within the generator's magnetic field, then its influence on the detector coils will produce output currents of equal amplitude. The same will occur, when a flat workpiece is placed perpendicular to the sensors's direction, or the seam is position exactly between the two detector coils. The presence of a seam at one of the detectors will result to asymmetries between the magnetic fields on each of the detectors coils, which will lead to different amplitudes of output currents. The comparison of the currents amplitudes provides information about the position of the seam.

Inductive sensors are used for seam detection and for weld inspection, the latter only for the recognition of grooves or holes (Jones (1987) and Dilthey (2005) chapter 16).
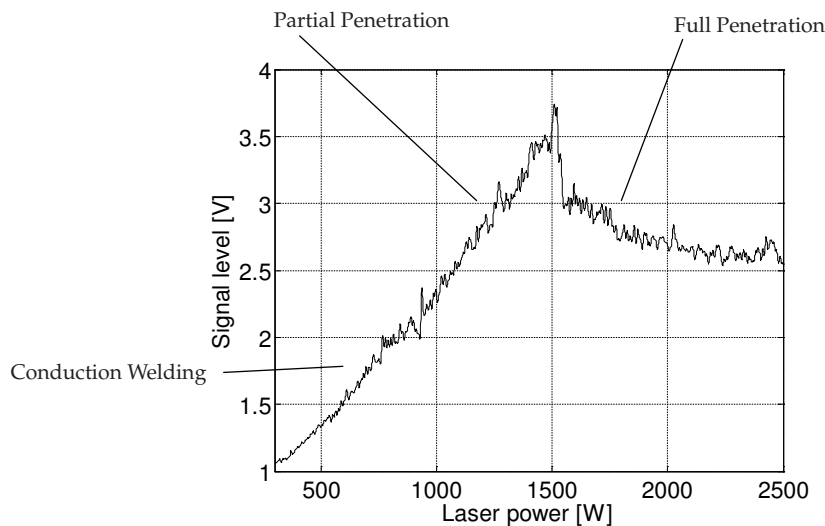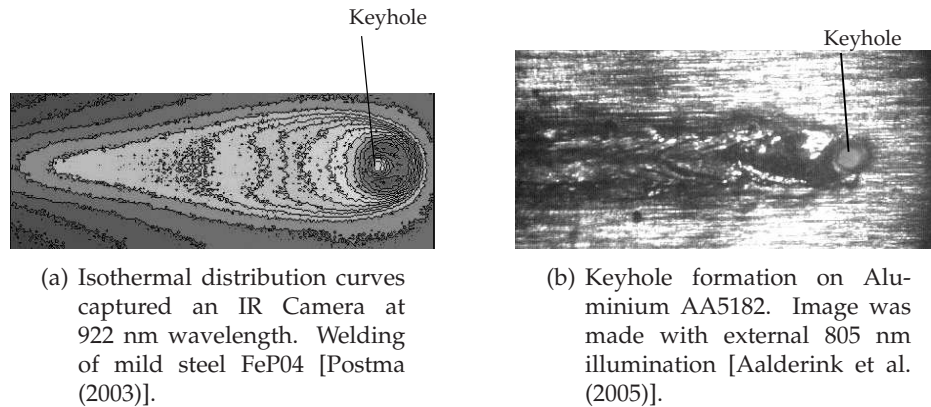
Optical Melt Pool Monitoring

For melt pool monitoring, photodiodes or imaging sensors are used to measure the light that is back reflected from the weld pool during welding. The light can be either from the welding process itself of an external illumination source. Depending on the workpiece material and the property of the melt pool that is to be observed, different wavelengths are applied. The most important properties of the melt pool are the existence and size of the keyhole, and the thermal profile around the welding spot.

For the thermal distribution, an easy method is to use a camera to monitor a small band of the infra-red (922 ± 10 nm) emissions of the melt pool (Postma (2003) and Lhospitalier et al. (1999)). By applying dynamic thresholding on different levels of grayscale on the captured image, the result is an isothermal curve image like Fig.2.4(a). From the isothermal curves also the keyhole formation can be detected. A lower temperature area in the middle of the melt pool indicates the existence of a through hole. This sensing method is particular useful for laser welding of steel where melt pool temperatures are high enough to give sufficient radiation at the observed wavelength.

For laser welding of aluminium, this approach is less successful as the melt pool emits less radiation. In this case, the detection of the keyhole can be implemented with external illumination of 805 nm (Aalderink et al. (2005)) and a camera that is set to detect only that wavelength (e.g. with the use of 805 nm band pass optical filter). With such a setup image like the one of Fig.2.4(b)are obtained. As shown by this figure, the keyhole is clearly visible and its size can be measured.

When a detailed measurement of the radiation emissions at the surface of the workpiece is not needed, a single photo-detector can be applied to measure the radiation of the light emissions from the melt pool in a selected wavelength range. The changes in the light intensity is used to indentify the type of the welding that is being performed. These signals are similar to the one of Fig.2.4(c), where the drop of signal after the peek shows that a keyhole is formed. The melt pool monitoring methods are used mainly for laser welding process control.

(a) Isothermal distribution curves captured an IR Camera at 922 nm wavelength. Welding of mild steel FeP04 [Postma (2003)].

(b) Keyhole formation on Aluminium AA5182. Image was made with external 805 nm illumination [Aalderink et al. (2005)].

(c) Sensor signal of emissions of the plume at 400-600 nm [Postma (2003)], depending on the applied laser power.

Figure 2.4: Melt pool reflections measuring technique.

Acoustic Sensing

Acoustic sensing uses the sound emissions generated by the welding process. The basis of this method is that several frequency components of the sounds that are produced during the welding process can be related to physical interactions in the weld area. Statistical analysis of these fre-

quencies is used for process monitoring and diagnostics (Gu and Duley (1996)).

A variation of the acoustic method is the Electromagnetic Acoustic Transducers (EMATs) as described in Camplin (2001). This is also a non-contact method and makes use of electromagnetic acoustic transducers. It can be used only with conductive workpieces in which a magnetic field is formed. A coil is then used to transmit a high frequency (RF) pulse above the workpiece. The interaction of the pulse with the magnetic field introduces a force on the workpiece which results to an acoustic pulse of the same frequency (usually ultrasonic). By sensing the generated acoustic pulse, an ultrasonic scan of the workpiece is obtained. For the measurements to be reliable, the transducer has to be placed approximately 1 mm from the workpiece's surface. This method can be used for post weld quality inspection.

Uniform Illumination

Uniform illumination can be produced by one or more diffuse illumination sources, that lightens the work piece on a wide area around the seam. This technique can not be used for three dimensional position measurements but it can be very useful for weld inspection.

When uniform light hits the welded seam shadows will emerge out of the irregularities of the weld. Image processing can then be used to perform texture analysis on the surface of the weld (Fig.2.5(a)). For seam detection, uniform light can be used to reveal the lateral position of the seam (Fig.2.5(b)). In combination with a triangulation sensor it can be used for the detection of the three dimensional position of butt-joint seam configurations.

2.2   Sensor Implementation

The choice of the sensor to be implemented in the laser welding head depends on its compactness, the number of functionalities, and its compatibility with the other sensory systems and the laser welding process.

For seam detection, the use of tactile sensors will be problematic. These sensors require continuous contact with the work piece which is not always possible when the sensor is used for seam tracking of complex seam geometries. Furthermore it limits the seam types that can be detected.

(a) Uniform light for weld inspection. The texture of the weld can now be used for further analysis.

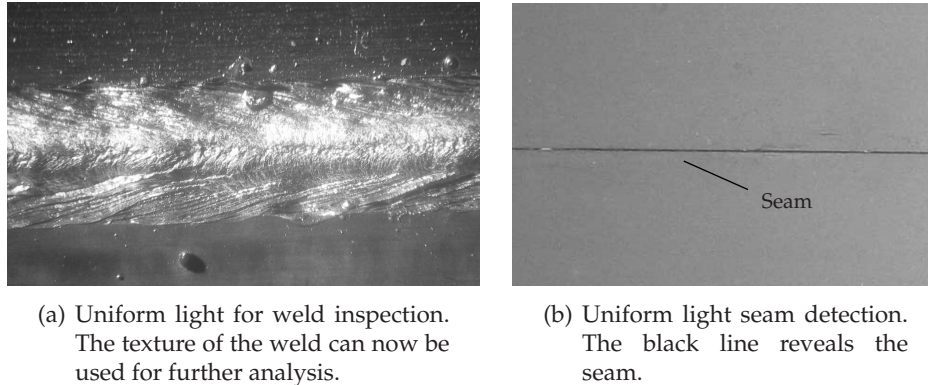(b) Uniform light seam detection. The black line reveals the seam.

Figure 2.5: Uniform light can be used for texture analysis in weld inspection and can provide the lateral seam position in butt joint configurations.

Similar conclusions hold for the induction sensors, which also need to be in quite close range from the workpiece. For this reason, optical sensors will be used. Since uniform light can reveal the position of the seam in an image but not its distance to the welding head, optical triangulation is chosen for seam detection.

For reasons of compactness optical triangulation is also used for weld inspection. For the cases were optical triangulation can not detect the seam (eg. Butt joint configurations), uniform light can be integrated to the system externally. The mechanical configuration or the components of the system do not need any changes, and only the controlling software must be adapted to process the new type of imaging data.

Optical sensors will be used for the process monitoring as well. Therefore, the emissions from and around the melt pool will be used to control the laser welding process.

2.2.1 Optical Triangulation

The basic principle of optical triangulation was presented in §2.1. There are many variations of the optical triangulation principle and most of them are related to the projected structured light shape. Different shapes can provide additional information but also require additional processing of the measurement data. The most used structured light shapes are either a spot, a line, or a geometrical shape like crosses, circles, rectangles, etc.

In order to perform a measurement, a coordinate system must be established. The position and orientations of the sensor's coordinate system can vary depending on the measuring capabilities of the sensor. In its most simple form the z axis of the sensor coordinate systems is parallel or coincides with the sensor's imaging lens optical axis, as in Fig.2.6. The plane that is formed by the x and y axes of the sensor coordinate system form the sensor's reference plane. The relation of the sensor's coordinate system to that of the manipulating machine is derived by a number of calibrations which are discussed in Chapter 4.

All measurements in the following paragraphs are presented in the sensor's coordinate system.

Single Spot

Single spot systems measure vertical distance along the sensor's optical axis. For the setup of Fig.2.6, the sensor's z axis coincides with imaging lens optical axis. The origin of the coordinate systems is taken on the point where the imaging lens axis crosses the structured light axis (point B). The reference plane is perpendicular to the imaging lens optical axis at point B.

As it is seen in Fig.2.6, equal displacements of the spot's image on the photo-detector (A'B' and B'C') do not correspond to equal displacements of the actual spot in the real world (AB and BC). To conduct accurate measurements, a relation (Eq.2.1) between the z displacement of the sensor in the real world and the corresponding x_p displacement on the photo-detector is used. The derivation of this formula is presented in Appendix B.1.

$$z = \frac{d_R \cdot x_p}{f_T \tan \phi + x_p} \ , \tag{2.1}$$

where d_R is the reference distance from the imaging lens to the reference plane along the optical axis of the lens, f_T is the focal length of the imaging optics, and ϕ is the fixed angle between the photo-detector and the photodiode axes.

With this setup, a single spot can only measure the z position of a single point. If the measurement of the orientation of the plane is required then an additional number of measurements must be performed on different positions over the surface. Such single spot scanning methods can
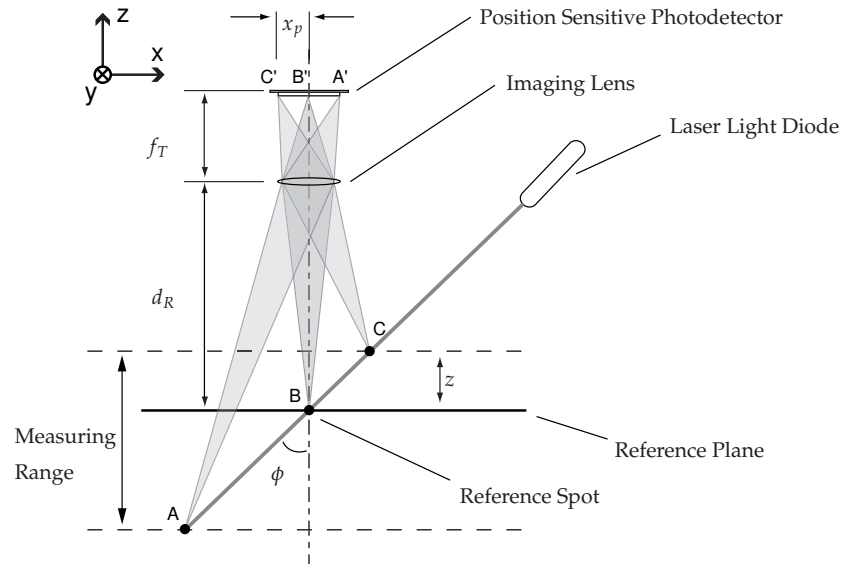
Figure 2.6: Single spot triangulation setup for position measurement. The origin of the coordinate system exists on point B and is moved to the left top corner to improve readability.

be applied for seam detection and seam inspection as in both cases, height information is used to reveal the position the seam or the quality of a weld.

Single Line

When a structured light line is projected, the measuring capabilities of the system increase. As a detector, in such triangulation systems, imaging array chips are used. The line can be perceived as an infinite number of single spots arranged closely next to each other. Like the scanning single spot triangulation systems that were mentioned in the previous paragraph, the single line setup delivers a height profile along the projected structured light line. In Fig.2.7 such a structured light laser line is projected on an overlap joint. Due to the change of height between the two surfaces that form the overlap joint, there is a breaking of the line which is captured by the imaging chip. By measuring the image positions of the line parts the position of the seam towards the photo-detector can be calculated. Furthermore the breaking of the line can be used to reveal the position of the seam in this case.
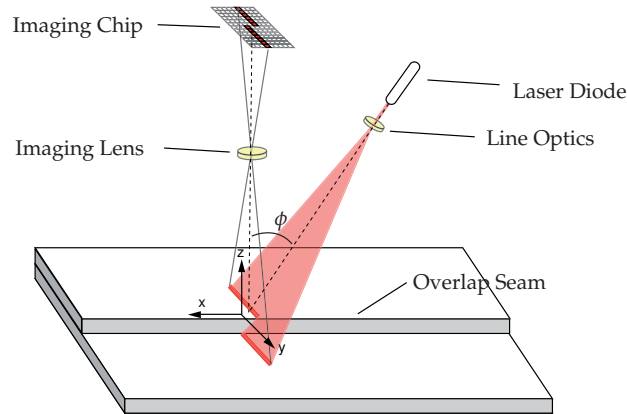
Figure 2.7: Triangulation setup with a line

The projected line allows the position measurement of every point of the workpiece along the projected line according Eq. 2.1. The only orientation measurement that it can perform are the rotations of the workpiece that have a component around the x axis of the principal axes system as shown in Fig.2.7. As it can be seen in Fig.2.8(d), the rotation around the x axis is the only one that introduces changes on the orientation of the projected line image on the imaging chip. All the other rotations or translations do not influence the orientation of the line image, as is shown by Fig.2.8.

For the line shape, the y component of the sensors coordinate systems exists on the reference line as shown in Fig.2.9. Since rotations around x component of the axes can be measured, the reference line can also hold a rotation around the x axis, which would result to an angle ϕ between the sensor's z axis and the imaging lens optical axis.

To measure the angle of rotation around the x axis of the sensor coordinate system, the angle φ of Fig.2.9 must be calculated. For the example of Fig.2.9 the reference line does not have any rotational component around the x sensor axis. In the top sensor view (along z coordinate) it is shown that ϖ is the angle that is formed between the projected line and the y axis of the sensor. The angle φ is determined by the projected line and y axis of the sensor when viewed from the direction of the sensor's x coordinate.

From the above it is derived that:

$$\tan(\varpi) = \frac{x}{y}, \quad \tan(\varphi) = \frac{z}{y}, \tag{2.2}$$

(a) Translation along the x axis.

(b) Translation along the y axis.

(c) Translation along the z axis.

(d) Rotation around the x axis.

(e) Rotation around the y axis.

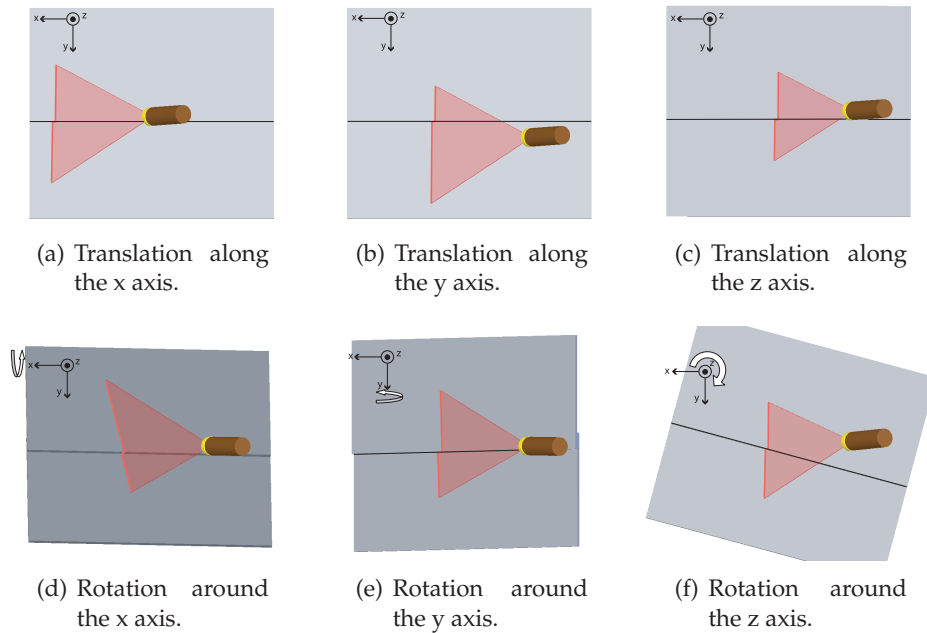(f) Rotation around the z axis.

Figure 2.8: Change of the projected laser line shape image in relation to the translations and rotations of the underlaying surface.
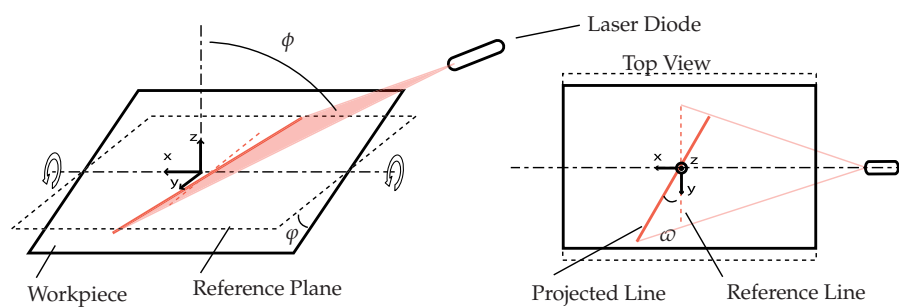

Figure 2.9: A setup with a single structured light line where the workpiece has rotated around the x axis (left) and the sensor view (right).

where x, y and z are the coordinate values of any point of the projected structured light line in three dimensional space.

From Eq.2.2 and Eq.2.1 follows:

$$\varphi = \arctan\left(\frac{z}{y}\right) = \arctan\left(\frac{d_R \tan(\omega)}{f_T \tan(\phi) + x}\right). \qquad (2.3)$$

Additional to the detection of φ, the position of a seam or its surface quality after welding can also be detected with the use of a single line. Depending on the joint configuration, the seam can cause deformations or discontinuities to appear along the structured line image. For example height differences of an overlap joint seam introduces discontinuities on the line (Fig.2.10(a)). This information can be used for seam detection as the discontinuity reveals the position of the seam. Similar deformations and discontinuities can occur from the projection of the structured line on the welded seam (Fig.2.10(b)). The type and size of deformation or discontinuity allows the detection of existing features on the workpiece (holes, bends, bumps, etc).
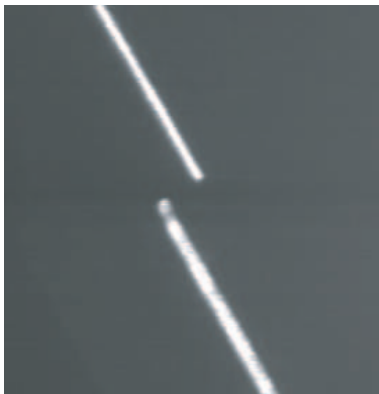
(a) Discontinuities of the structured line reveal the position of the seam.
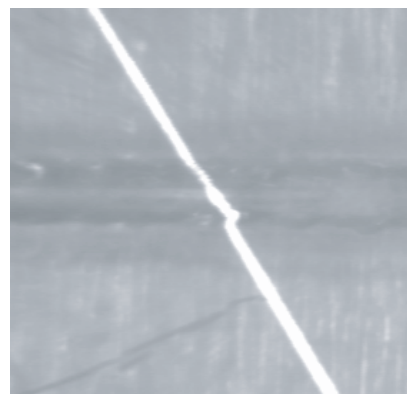
(b) Deformations of the structured line reveal the texture of the weld.

Figure 2.10: Use of single laser line structured light images for seam detection and weld inspection.
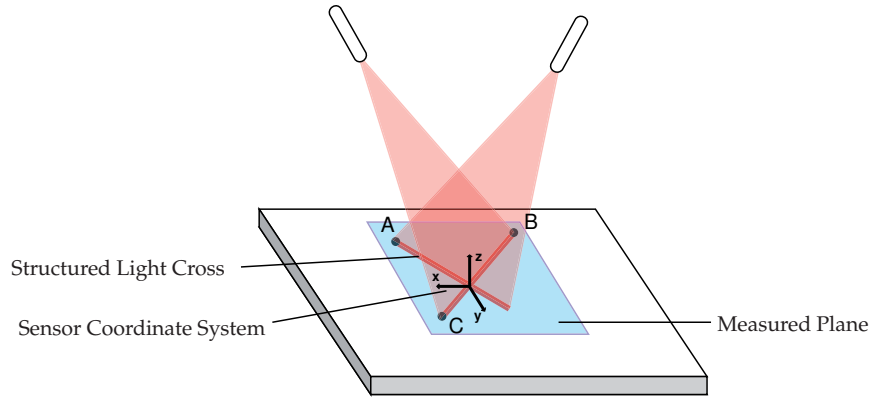
Figure 2.11: Projection of 2D cross shape on a surface and detection of surface plane with the use of three points A, B and C.

2D Structured Light Shapes

Two dimensional structured light shapes define a plane by their projection. These shapes can vary from crosses to triangles, rectangles, circles, etc. When such a shape is projected, the full surface position and orientation of the workpiece at the area where the structured shape is projected can be obtained in relation to the sensor's coordinate system.

Since all positions and orientations are measurable with a 2D shape, the sensor's coordinate system can also be selected with any orientation and position. The detection of the position and orientation of a measured surface with the 2D shape, requires two steps. The first is the identification of the measured plane, and the second is the correlation of the measure plane with the reference plane of the sensor's coordinate system (x and y axes plane).

In Fig.2.11 a structured light cross is projected on a workpiece. The workpiece plane (measured plane) can be defined with three points A, B and C along the structured light cross, as long as not all of these points do belong on the same line. The three dimensional coordinates, in the sensor coordinate system, of each of these points are calculated in the same way as for the spot and line cases. Three points A, B and C define a plane in 3D space by:

$$D_X x + D_Y y + D_Z z - D = 0, \qquad (2.4)$$

where the determinants are defined as,

$$
D_X = \begin{vmatrix} 1 & y_A & z_A \\ 1 & y_B & z_B \\ 1 & y_C & z_C \end{vmatrix}, \quad
D_Y = \begin{vmatrix} x_A & 1 & z_A \\ x_B & 1 & z_B \\ x_C & 1 & z_C \end{vmatrix},
$$

$$
D_Z = \begin{vmatrix} x_A & y_A & 1 \\ x_B & y_B & 1 \\ x_C & y_C & 1 \end{vmatrix}, \quad
D = \begin{vmatrix} x_A & y_A & z_A \\ x_B & y_B & z_B \\ x_C & y_C & z_C \end{vmatrix}. \tag{2.5}
$$

The normal vector of the measured plane is:

$$
\mathbf{n} = \begin{bmatrix} D_X \\ D_Y \\ D_Z \end{bmatrix}. \tag{2.6}
$$

Once the measured plane is defined it is possible to identify its orientation and position towards the sensor reference plane. For the calculation of the orientations the dihedral angle θ is used. The dihedral angle is the angle that is formed between the normal vectors of the measured and reference frames as shown in Fig.2.12.

Applying Eq. 2.4 for the reference plane yields:

$$
D_{X,Ref}x + D_{Y,Ref}y + D_{Z,Ref}z - D_{Ref} = 0 \tag{2.7}
$$

Then the dihedral angle θ can be calculated with the use of the plane normal vectors according to

$$
\theta = \arccos\left(\frac{\mathbf{n}_{Ref} \cdot \mathbf{n}}{|\mathbf{n}_{Ref}||\mathbf{n}|} \right), \tag{2.8}
$$

where $\mathbf{n}_{Ref}$ is the normal vector of the reference plane and $\mathbf{n}$ is the normal vector of the measured one.

The orientational axis of rotation $\mathbf{v}_R$ for the dihedral angle is given by the cross product of the plane normal vectors, and it is described by

$$
\mathbf{v}_R = \mathbf{n}_{Ref} \times \mathbf{n} = \begin{bmatrix} D_Z D_{Y,Ref} - D_Y D_{Z,Ref} \\ D_X D_{Z,Ref} - D_Z D_{X,Ref} \\ D_Y D_{X,Ref} - D_X D_{Y,Ref} \end{bmatrix} = \begin{bmatrix} v_{R_x} \\ v_{R_y} \\ v_{R_z} \end{bmatrix} \tag{2.9}
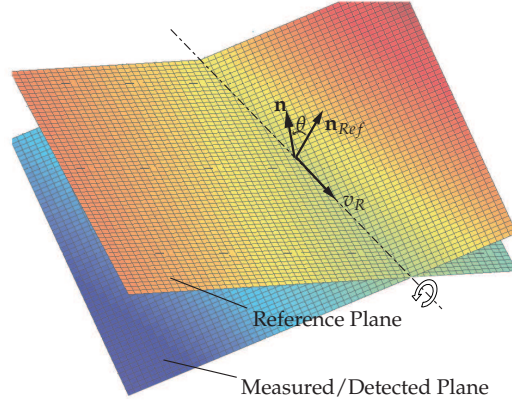$$

Figure 2.12: Two planes forming a dihedral angle. The normal vectors of the planes and the rotation axis are presented.

Since the reference plane and the measured plane are defined in relation to the sensor's coordinate system, the same is true for the rotation axis of the dihedral angle. To use this information for the manipulation of a robot, it is desired to convert the rotation around the axis $\mathbf{v}_R$ into rotations around the axes of the sensor coordinate system. With the use of quaternions it is possible to describe the dihedral angle θ to rotations around the axis of the sensor coordinate system in which $\mathbf{v}_R$ is defined (Appendix B.2). A quaternion Q is defined from the axis of rotation $\mathbf{v}_R$ and the angle θ according to

$$Q = \begin{bmatrix} q_0 \\ q_1 \\ q_2 \\ q_3 \end{bmatrix} = \begin{bmatrix} \cos\left(\frac{\theta}{2}\right) \\ \frac{v_{R_x}}{|\mathbf{v}_R|}\sin\left(\frac{\theta}{2}\right) \\ \frac{v_{R_y}}{|\mathbf{v}_R|}\sin\left(\frac{\theta}{2}\right) \\ \frac{v_{R_z}}{|\mathbf{v}_R|}\sin\left(\frac{\theta}{2}\right) \end{bmatrix} \tag{2.10}$$

Alternatively, the rotation can be described with the rotation matrix R that can be expressed in quaternion elements by:

$$R = \begin{bmatrix} r_{xx} & r_{yx} & r_{zx} \\ r_{xy} & r_{yy} & r_{zy} \\ r_{xz} & r_{yz} & r_{zz} \end{bmatrix} = \begin{bmatrix} 2(q_0^2 + q_1^2) - 1 & 2(q_1 q_2 - q_0 q_3) & 2(q_1 q_3 + q_0 q_2) \\ 2(q_1 q_2 + q_0 q_3) & 2(q_0^2 + q_2^2) - 1 & 2(q_2 q_3 - q_0 q_1) \\ 2(q_1 q_3 - q_0 q_2) & 2(q_2 q_3 + q_0 q_1) & 2(q_0^2 + q_3^2) - 1 \end{bmatrix} \tag{2.11}$$

Once the rotation matrix has been defined, the rotation angles around each of the sensor's coordinate system can be calculated by

$$\varphi = \arctan 2(r_{yz}, -r_{zz}) \tag{2.12}$$
$$\psi = \arctan 2(r_{xz}, r_{zz}\cos(\varphi) - r_{yz}\sin(\varphi)) \tag{2.13}$$
$$\omega = \arctan 2(r_{yx}\cos(\varphi) + r_{zx}\sin(\varphi), r_{yy}\cos(\varphi) + r_{zy}\sin(\varphi)) \tag{2.14}$$

where φ is the rotation around x axis, ψ is the rotation around y axis and ω is the rotation around the z axis of the sensor's coordinate system with respect to its current orientation.

Even though the structured light cross shape provides all required position and orientation information of the workpiece towards the sensor's coordinate system, it can be easily concluded that such a system would also fail to detect certain seam geometries with sharp corners. An alternative solution would be to use perimetric structured light shapes like circles, triangles, rectangles, etc. With the use of such shapes any type of seam trajectory can be detected and the relative positions and orientations can be derived from a single measurement (Fig.2.13(a)). Furthermore, by placing the laser focus in the center of the perimetric shape, it is possible to use one part of the shape for seam detection and another part for weld inspection (Fig.2.13(c)). The most important benefit of such a system is that it helps to simplify the robots movements. Since any part of the perimetric shape can be used for seam detection and weld inspection, there is no more need for the sensor to keep a certain orientation towards the seam's trajectory (Fig.2.13(b)). Therefore the robots do not have to undergo all the extensive rotations over sharp corners (§1.5).

System Resolution Issues

The triangulation sensor is used to provide measurements regarding the lateral displacement of the structured light on the workpiece as well as the distance to the workpiece. The sensitivity of measurements that are obtained by triangulation depend on the angle ϕ between the structured light source and the sensor's optical axis and the pixel density of the sensor.

See the triangulation setup of Fig.2.14 where the only change is the projection angle ϕ of the laser diode. It is shown that for smaller ϕ less area of the imaging sensor is illuminated (for the same measuring range),
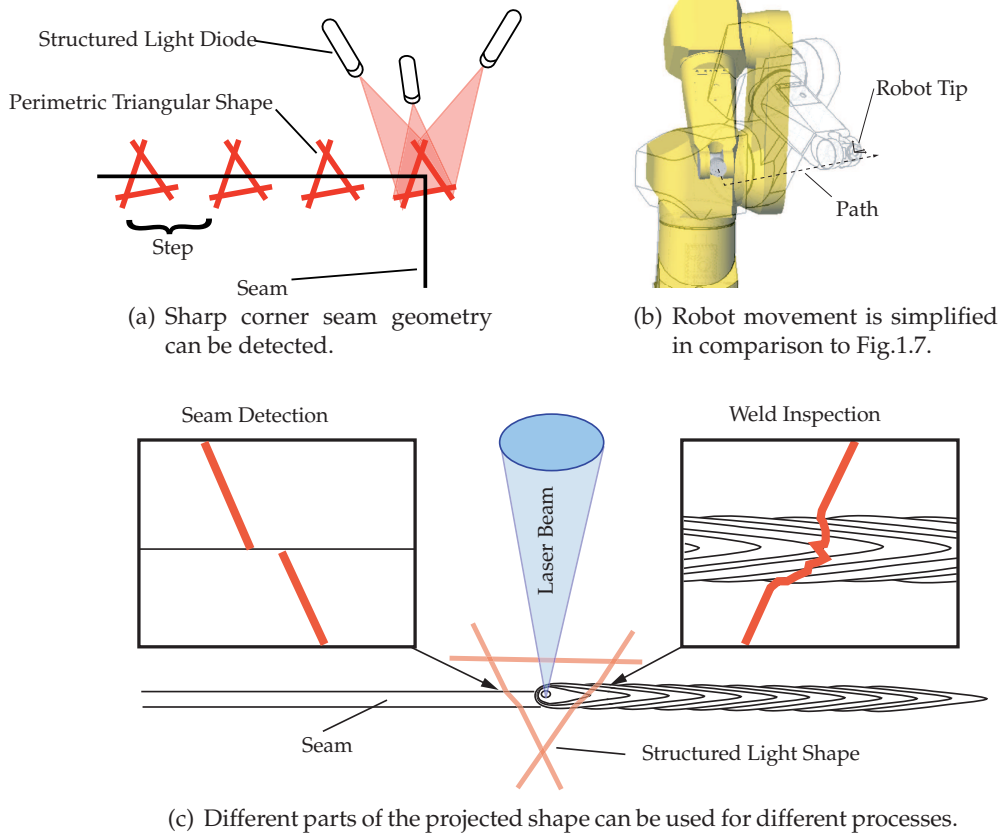
Structured Light Diode

Perimetric Triangular Shape

Step

Seam

(a) Sharp corner seam geometry can be detected.

Robot Tip

Path

(b) Robot movement is simplified in comparison to Fig.1.7.

Seam Detection

Weld Inspection

Laser Beam

Seam

Structured Light Shape

(c) Different parts of the projected shape can be used for different processes.

Figure 2.13: The perimetric sensor advantages.

Imaging Sensor

Laser Diode

Measuring Range

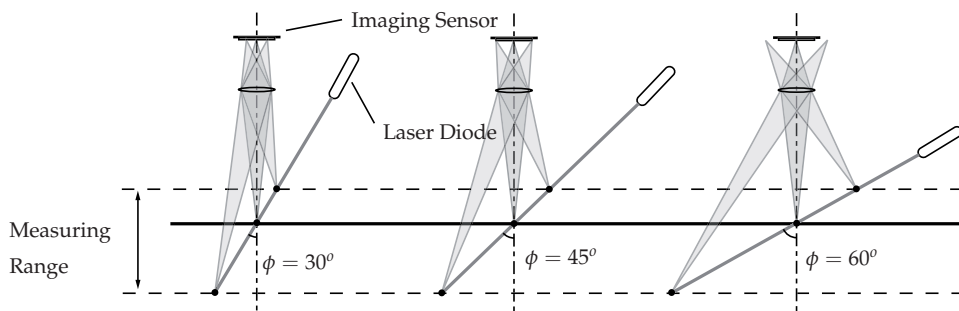$\phi = 30^o$ $\phi = 45^o$ $\phi = 60^o$

Figure 2.14: Triangulation setup for the same measuring range but different projection angles ϕ

diminishing the measuring resolution of the system. In general the angle ϕ defines the resolution ratio between the lateral and distance measurements. Still there are other parameters like the magnification factor of the optical components as well as the resolution of the imaging sensor, that also affect the measuring resolution of the system. These parameters are linked to the optical components of the system, rather than the setup configuration. When implementing such a system, the focal range of the imaging lens (the range at which the image is sharp enough), must also be considered. The optimum setup parameters depend on the measurement requirements of the sensor. The most commonly used values for the angle ϕ in practice vary between 30° and 45°.

The optical triangulation method is used for seam detection and weld inspection. In order to have the ability to measure all three positions and orientations, a 2D structured light shape is required. Furthermore, the detection of sharp corners requires the use of a perimetric 2D shape. It is preferred that the perimetric shape is not curved like an ellipse or a circle, as the detection of a height profile on such a shape requires too much computing power. Additionally the projection of such a curved perimetric shape for this type of measuring purposes can prove difficult. The triangular shape is therefore selected because it has the least number of sides compared to any other geometrical shape.

2.2.2   Laser process emission monitoring

Laser process emissions can be monitored with the use of photo-detectors and optical filters. Initially, a selection of the radiation wavelengths must be made from the spectrum that is emitted from the welding process. Optical filters are required to allows only the selected wavelengths to reach the photo-detector. The optical axis of the detector can be either coaxial or off-axis to the high power laser (Fig.2.15). As photo-detectors simple photo-sensitive components like photodiodes are used as well as imaging sensors. The choice of the configuration and the type of detector depends on the process that is monitored. When only the radiation intensity is required, any type of configuration can be used and simple photodiodes are adequate for the job. When mapping of the area around the melt pool is required (e.g. isothermal curves, size of keyhole) then coaxial view is preferred and the use of an imaging sensor is necessary.

There are several wavelengths that can be used for process control, see §2.1 (Optical Melt Pool Monitoring at page 20). The selection of the
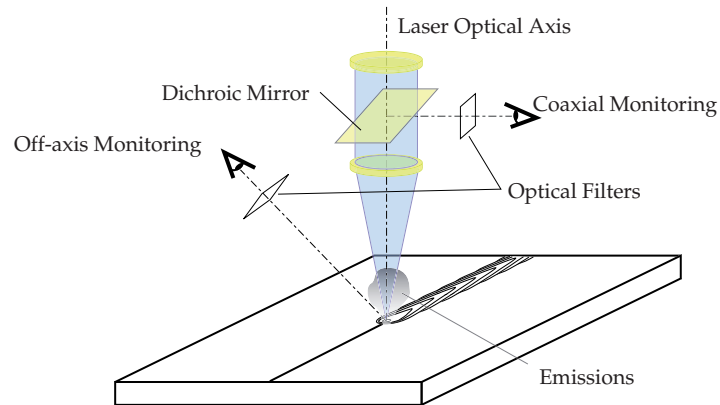
Figure 2.15: Process monitor coaxial and off-axis configurations.

wavelengths that are used depends on the workpiece material that is to be monitored. Materials like steel, aluminium, zinc coated still, etc have different emissions spectra. Therefore a suitable monitoring method must be applied accordingly.

Within this work the process monitor sensor that is developed performs best for steel welding. The sensor is based on sensing the plume radiation of the welding process. Nevertheless the design of the welding head allows the integration of other types of process control sensors.

36

Chapter 3

System Architecture and Sensor Integration

The development of an integrated system has to undergo several stages towards a prototype design. The first step is to determine the functions that will be realized (Chapter 2) and the design requirements for the current welding tool. Then the selection of the components necessary for the implementation of these functions must take place. Possible use of the same components for more than one function must be taken into consideration as it will lead to a more compact design. Finally, the integration of the sensors and the way that their measurement data is conveyed to the users must be defined and implemented.

In Chapter 2, two optical methods were chosen for the implementation of the sensing systems of the integrated laser welding head. It is therefore necessary to initially determine the required optical components (cameras, mirrors, lenses, etc) for these methods, as well as the optical path configurations that result from them. Further, the selection of the illumination sources and the optical sensors must take place. Additional electronics might be required for providing electrical power to the components (illumination sources, sensors, etc) or for interfacing the sensor's signals to the outside world. When the components of all the sensing processes have been developed, their mechanical integration into a prototype design takes place. Finally, a very important step is the development of communication interfaces of the prototype tool. This part is software which ensures that the information that the tool provides can properly be used by the machine that manipulates it.

3.1   Design Requirements

The developed welding head must meet several requirements that will ensure that it performs adequately when it is used. The requirements also influence the choice of components for the implementation of the sensors and the mechanical housing in general. A list of design requirements is presented in Table 3.1 and is explained further in the following paragraphs.

The first requirement is that the sensors provide the needed positioning accuracy. An offset in the lateral position of the focused high power laser spot over the seam, will lead to an unsatisfactory weld (Fig.3.1). This offset margin varies, depending on the type of material that is used for the welding process as well as the size of the focused laser spot. The size of the focused spot depends on the diameter of the laser fiber and the focal lengths of the collimator and laser focus lens. For the developed system a 0.6 mm laser fiber is used in combination with a 200 mm collimator lens.

Table 3.1: Design Requirements

Detection sensor resolution	50 μm for current lasers
	25 μm for future lasers (e.g. fiber lasers)
Process monitor sensor sensitivity	$4\text{x}10^{-7}$ W for 100 mm Laser focus lens
	$2\text{x}10^{-7}$ W for 150 mm Laser focus lens
	$1\text{x}10^{-7}$ W for 200 mm Laser focus lens
Inspection sensor resolution	10% of the material thickness
Structured light shape	Triangle
General requirements	Mountable to robots
	Primary optical components
	Lens cooling
	Cross jet protection
	Data exchange interfaces
Required percentage of back reflected illuminations	10% for imaging
	3% for process monitoring

The collimated beam is then focused by either a 200 mm, 150 mm, 100 mm focal length laser focus lens, which results to a spot of 0.6 mm, 0.45 mm and 0.3 mm respectively. For the spot size of 0.6 mm a tolerance of less than 0.2 mm is acceptable (Duley (1999)), whereas for the smallest spot size of 0.3 mm tolerances of about 0.1 mm are required (OldeBenneker and Gales (2007) and OldeBenneker (2000)). A general rule is that the allowed offsets are 1/3 of the laser spot size. In the meantime new laser concepts (disk laser, fiber laser) are coming on the market with spot sizes down to 0.1 mm which are used for thin components.
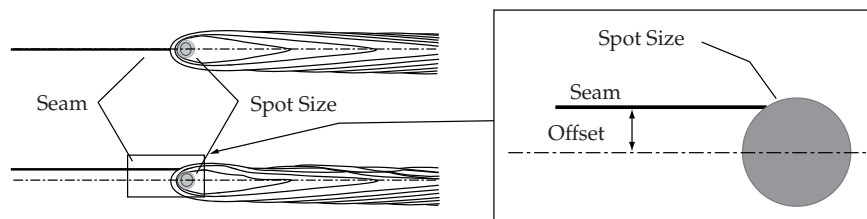

Figure 3.1: Two welds, one where the laser spot is accurately placed on the seam (top left) and one where there is an offset between them.

The requirements for the process control monitor sensor depend mainly on the laser process. As it is mentioned in §2.2.2 the process sensor that was selected for implementation in the welding head monitors the plume radiation from the welding process at the wavelength range between 400 nm and 600 nm. The first parameter that needs to be determined is the light sensitivity of the sensor. To determine this parameter, an estimation of the lowest illumination that reaches the sensor must be determined.

The emitting radiation form the workpiece during welding is described by Planck's law for black body radiation. This radiation is emitted from the melt pool. For the laser spot sizes that are mentioned in the previous paragraphs, it is safe to estimate the total melt pool area at about 1 mm^2, at anytime during the welding process. Using steel for an example the lower illumination value is determined as follows. Steel melts at the temperature of about 1800 K. Taking into consideration that the emission will be less compared to the Plank's black body radiation (emissivity of 0.5) and the wavelengths that are to be monitored (400 to 600 nm), the resulting black body illumination from the molten part of the steel is about 71 W/m^2. In the worse case the welding process will act as a point

source, emitting equal amounts of light in every direction. Only the part that reaches the sensor is important. This part depends on the optical path until the sensor. In Appendix B.4 an analysis of these calculations is given which results to a lower illumination values of 4.18×10^{-7} W, 1.86×10^{-7} W and 1.05×10^{-7} W for 100 mm, 150 mm and 200 mm focusing lenses.

The requirements for the weld inspection functionality of the system are defined by the quality criteria that are used. The quality criteria vary in accordance to the type of weld that is made and where the welded part will be used. For instance, in the cases where the part's durability is crucial, the weld quality is categorized according to the parameters that are related to durability (cracks, holes, big groves). On the other hand welds that are found sufficient for durability might fail at tests where overall smoothness of the weld texture is of importance.

Regarding geometric properties of the weld, like grooves, undercuts, etc, the ISO13919:-2:2001 (2001) norm provides typical guidelines from which the requirements for the resolution of the quality measurement can be deduced. In general the measuring system should be able to detect objects of at least 10% of the material's thickness. The inspection speed of the sensor is not critical when the inspection takes place after the welding process is finished. Nevertheless, in cases where the weld inspection is performed during welding, the sensor's speed must be such that it will allow the correct estimation of the weld quality. For example, a weld inspection sensor that moves over a workpiece of 1 mm thickness with a velocity of 100 mm/s, to be able to detect the smallest possible faults the sensor must be measuring with a frequency of at least 1000 Hz.

The structured light shape that is chosen is the triangle, which is implemented by the projection of three linear structured light diodes perimetric the laser tool center point (TCP_L) (Fig.3.2). The use of three linear structured light diodes ensures that the light intensity of each of the triangle's sides is the same. It also allows to adjust the projection angle of each of the triangle's sides. For each of the diodes to have the same triangulation properties, they must have the same projection angle towards the imaging sensor. For this to be possible, the imaging sensor is required to have a coaxial view to the high power laser spot. When the high power laser optical axis is perpendicular to a flat surface the equilateral triangle of Fig.3.2 will be viewed coaxially, where it can be seen that the positioning angle between the projector's axes must be 120°.

General requirements demand that the integrated head can be mounted on the end effector of industrial robots. It must also carry a
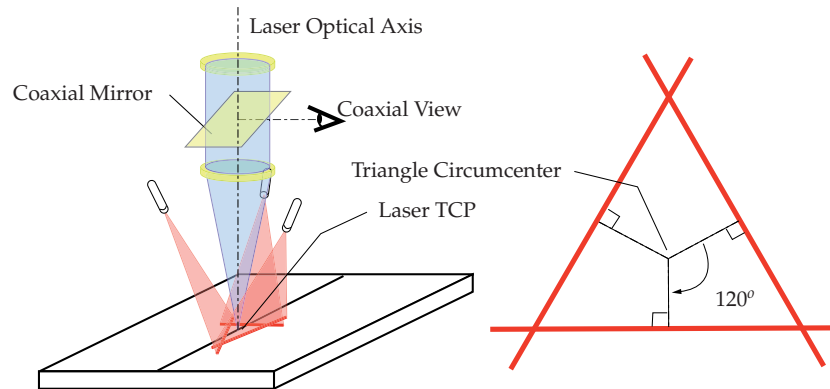
Figure 3.2: Projection of the triangular shape around the TCP and its coaxial view.

fiber mount for interfacing with the laser. To be able to perform welding a collimating lens after the fiber interface and focussing lens are also necessary. To provide a coaxial view to the high power laser, a coaxial mirror is required that transmits light of the high power laser wavelength and reflect all the rest illumination (or vice versa). The fiber mount, the collimator lens, the high power laser focus lens and the coaxial mirror define the primary optical components (Fig.3.3(a)).

To dissipate the heat from the laser beam on the optics, cooling should be integrated in the design. Further, cross jet nozzles and shielding glasses are needed for the protection of the laser optics from the welding process dirt and fumes.

It is important that enough illumination reaches both the imaging sensor for optical triangulation and the photodiode for process monitoring. By preliminary experiments it is known that about 10% of the reflected illumination around the melt pool is sufficient for imaging purposes. Only 3% of the process light is sufficient for laser process monitoring.

Finally, there are communication requirements that permit the sensor to correctly exchange data with any other system. This prescribes the need for communication interfaces that make this data transfer possible (§3.6).

3.2 Optics and optical paths

The main considerations of the optical design for this tool are: that it must be able to be used for laser welding, and that all sensors require to view the work piece coaxially to the high power laser beam. These two requirements immediately define at least the use of the primary optical components. The primary optical components consist of a laser collimator and a laser focus lens which are required for the laser welding and a coaxial mirror which provides a coaxial view to the high power laser optical axis (Fig.3.3(a)). Additional optical components will be necessary to accommodate the requirements of each sensing method. These optical components will be referred to as secondary optical components. The secondary optical components depend on the design preference and do not influence the main functionality of the tool, which is laser welding. Having the primary optical components as the basis, the rest of the optical path and its components can be selected.

3.2.1 Mirrors and beam splitters

There are two sensors that require access to the coaxial view of the laser tool center point. The first one is the optical sensor that is used for seam detection and weld inspection and the second one is the photodiode that is used for the process control sensor. For the accommodation of both sensors, two beam splitters/mirrors are required.

Since one of the mirrors exist in the primary optical components, a second mirror or beam splitter is required to provide access of the coaxial view to a second sensor. Depending on which component is used to provide the second coaxial view, the possible configurations are displayed in Fig.3.3.

In the configuration of Fig.3.3(b), a second coaxial mirror in used in series to the first one. According to the specifications of this mirror (Appendix A.1), it reflects about 12% for the radiation from the workpiece that is required for the sensory systems. This means that the lower mirror reflects 12% of the required radiation and transmits the remaining 88% towards the upper mirror. Similarly, 12% of the remaining radiation will also be reflected from the upper mirror. Therefore the first sensor receives about 12% of the original radiation whereas the second sensor receives about 11%. According to the stated requirements data (§3.1), 12% of the reflected radiation is more than enough for imaging purposes whereas the
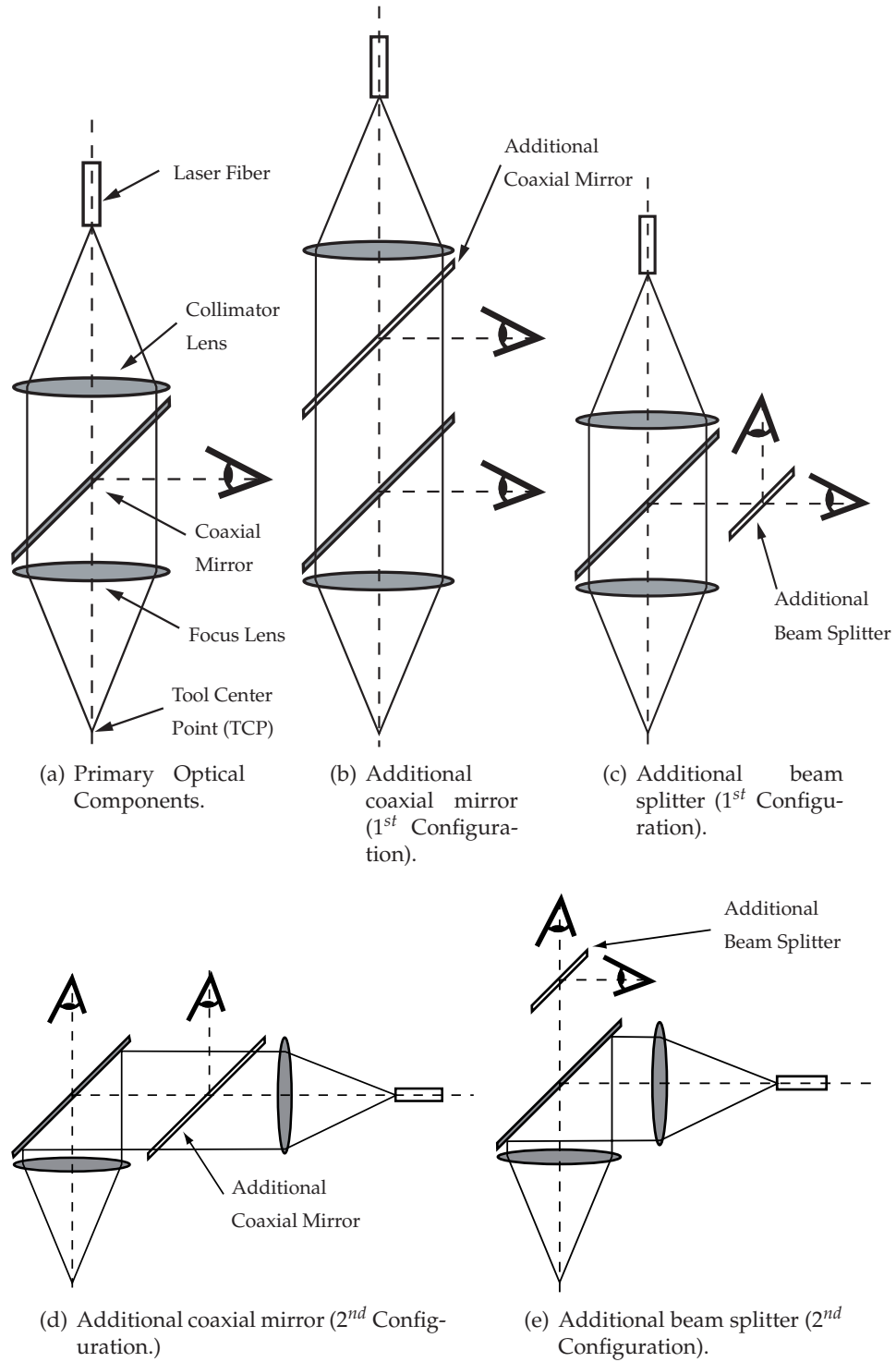
(a) Primary Optical Components.

(b) Additional coaxial mirror (1st Configuration).

(c) Additional beam splitter (1st Configuration).

(d) Additional coaxial mirror (2nd Configuration.)

(e) Additional beam splitter (2nd Configuration).

Figure 3.3: Possible configurations of the beam splitter position.

requirements for the process control sensors are about 3%. Even thought the selection of such an optical path allows enough radiation to reach the sensors, it almost doubles the length of the mechanical design. Furthermore, the coaxial mirror introduces a loss off a little more than 1% to the high power laser beam. The introduction of a second coaxial mirror will almost double that power loss.

In the configuration of Fig.3.3(c), a beam splitter is used. The beam splitter allows different percentages of all radiation to be reflected and transmitted. The beam splitter that is selected reflects 70% of all incoming radiations and transmits the remaining 30% (Appendix A.1). This means that the sensor on the reflecting side of the mirror receives about 8.4% of the original reflected radiation and the other sensor receives 3.6%. Such a configuration provides enough radiation for the process control sensor (3% was required) and almost enough illumination for the imaging sensor (10% was required). With this configuration the length of the mechanical construction is not increased whereas its width is slightly increased. Since the system is required to be compact, the solution with the use of a beam splitter is preferred.

Approximately the same conclusions about the size of the mechanical design are derived when a different type of mirror is used for the primary optical components. Such a mirror reflects the high power laser wavelength and transmits all the rest. As it is presented in Fig.3.3(d) and Fig.3.3(e) the design with the beam splitter is then also more compact than the one with the extra coaxial mirror. Between the two solutions of Fig.3.3(c) and Fig.3.3(e), the first one is selected as the position of the fiber mount allows the robot to perform rotations that do not endanger the fiber.

3.2.2 Lenses

In the integrated welding head (Fig.3.3) there are two additional lens systems which are necessary at the optical path of the secondary optical components. The first lens system is the one that is used for imaging purposes and the second is the one that is used by the process control photodiode. In combination with the laser focus lens, these additional lenses determine the magnification V of the object's image to the sensors.

In Fig.3.4, a ray trace of an object's image through the high power laser focus lens and an imaging lens is shown. The object exist at the focal plane of the high power laser lens, on which the welding process can be per-

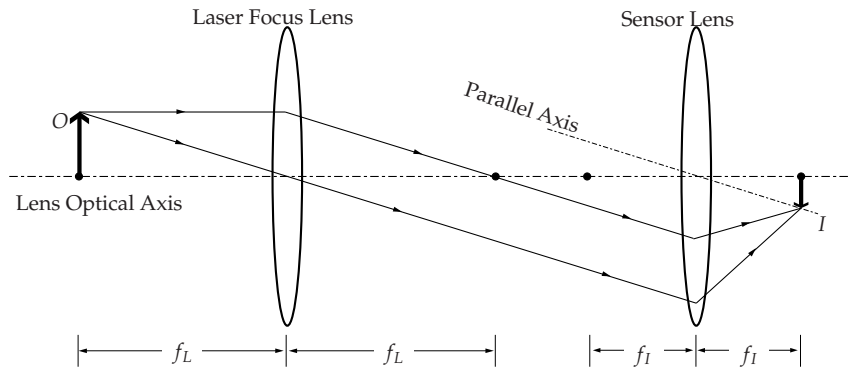formed. Similarly, the image exist on the focal plane of the sensor lens where the image is in focus.

Figure 3.4: Ray trace of an image with the use of two lenses, where the object exists on the focal plane of the first lens.

Since the object O is placed at f_L, the output of the laser focus lens will be a parallel beam. This parallel beam enters the sensor lens and is focused at distance f_I. The size of the image is derived with the help of a parallel axis to the collimated beam that passes through the center of the sensor lens. The size of the image I is the distance from the point where this axis crosses the sensor lens focal plane to the lens optical axis (Hecht (1998)).

The magnification V of the optical system is:

$$V = \frac{I}{O} = \frac{f_I}{f_L} \, , \tag{3.1}$$

The knowledge of the magnification and the object's and images's position is used to determine the lens focal length and vice versa.

If the object is a rectangle with width w_O and height h_O, then the image will also be a rectangle, where the width w_I and the height h_I are:

$$w_I = \frac{f_I}{f_L} w_O \, , \; h_I = \frac{f_I}{f_L} h_O \, . \tag{3.2}$$

The object rectangle is referred to as the field of view (FoV) of the sensor, whereas the image rectangle is the image field. The image field equals

the sensor size, which is determined by the physical dimensions of the photosensitive surface of an optical sensor.

For the integrated welding head, the size of the field of view depends on the size of the structured light shape of the triangulation setup (Fig.3.5). For the seam tracking functionality of the integrated welding head, it is important that the structured light diodes are visible to the imaging sensor during the welding process. From experiments it was determined that a FoV with a width w_O of 36 mm and h_O of 27 mm is sufficient.
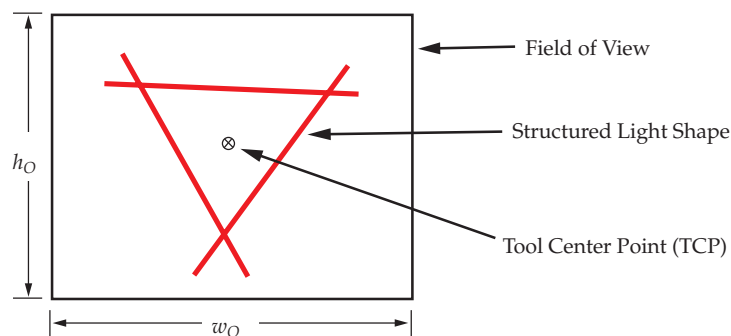
Figure 3.5: Field of view of the projected structured light perpendicularly at focal distance from work piece.

In Table 3.2, a list of required imaging lens focal lengths f_I are shown in relation to the laser focus lens (f_L) that is used, the selected field of view and several imaging sensor sizes (Hornberg (2007)). It is obvious that a change on the focal distance of the high power laser lens or of the projection angle of the structured light (related to w_O and h_O) or of the imaging sensor size might require a change of the imagining sensor lens in order for the system to perform adequately.

For practical reasons, we used off-the-shelf lenses. For example, a system that has a 100 mm laser focus lens and a 8.8x6.6 mm sensor size for the 36x27 mm FoV, should have a lens with focal length 24.4 according to Table 3.2. In this case a 25 mm imaging lens has been used, which results in a small decrease of the FoV towards 35.2x26.4 mm.

The next step involves the type of lens that needs to be used for the imaging sensor (singlets, multielement). The reflected illumination from the workpiece passes through the high power laser focus lens before it reaches the imaging lens. The laser focus lens is not optimized for wide

field of view imaging purposes and therefore it introduces distortions (radial, abberations, astigmatism, etc) to the original workpiece image.

The use of a single lens would aid to the compactness of the system, but it also adds to the distortions when used for imaging. When these distortions are added to the ones of the high power laser focus lens, the problem of their identification becomes very complex (§4.1). A multi-lens system on the other hand, which is already optimized for imaging purposes, might require more space but introduces minimal distortions to the image. This makes it possible for the initial distortions of the laser lens to be identified and corrected more easily. The optimum solution would be to design a lens system that will correct the disturbances that are introduced by the laser focus lens. Nevertheless, the use of a corrected multi-lens (as will be shown in §5.5.1 and §5.5.2) was proven sufficient for the measuring requirements of the welding head.

The lens that is required for the process control sensor has to satisfy only a few requirements. It needs to be compact and to be able to focus a parallel beam on the sensitive area of a photodiode. There are no explicit demands for magnification. The details of this lens are discussed in Chapter 6.

3.2.3 Optical Filters

Both sensing methods selected in Chapter 2 are optical, which means that they measure illumination intensities. For the triangulation method only

Table 3.2: Selected lenses in relation to sensor dimensions

w_O x h_O	f_L	w_I x h_I	f_I
36 x 27 mm	100 mm	4.3 x 3.9 mm	11.9 mm
		7.2 x 5.3 mm	20 mm
		8.8 x 6.6 mm	24.4 mm
36 x 27 mm	150 mm	4.3 x 3.9 mm	17.9 mm
		7.2 x 5.3 mm	30 mm
		8.8 x 6.6 mm	36.7 mm
36 x 27 mm	200 mm	4.3 x 3.9 mm	23.8 mm
		7.2 x 5.3 mm	40 mm
		8.8 x 6.6 mm	48.8 mm

the intensities of the structured light sources are important whereas for the process monitor only specific wavelengths are required. Without further precautions, the sensors will be illuminated by other light sources as well. For instance, the reflected light from the high power laser beam can significantly disturb the measured signals, thus reducing the signal-to-noise ratio, and making the task of selecting and processing the desired signals more elaborate. For this reason optical filters are introduced in the design, that allows only the selected wavelengths to reach each sensor.

The first filter that is used is the Nd:YAG filter which is placed between the primary and secondary optical components. This filter prevents any of the original or back-reflecting Nd:YAG radiation to reach the sensors.

The second filter placed before the imaging sensor optics to allow the detection of only the structured light radiation. It is a band-pass filter that allows only the radiation of the structured light diodes' wavelength to pass through. The selection of the specifications of this filter depends on the wavelength of the structured light that is used for triangulation. For the developed system in this work, the allowed wavelengths are near 660 nm due to the selected laser diodes (§3.3).

The third filter is also a band-pass filter that allows the radiation of wavelengths between 400 nm and 600 nm to reach the photodiode of the process control sensor.

The full optical path of the system with all the optical components is presented in Fig.3.6.

3.3   Optical sensors & Illumination sources

In Chapter 2 it is stated that an imaging sensor is required for the triangulation sensor, whereas a simple photodiode is sufficient for the process monitor. The two optical sensors that are used in the integrated welding head are described next.

As an imaging sensor the Philips Dica321 camera was selected (Appendix A.3). The camera contains a CMOS chip of 1280x1024 pixels which for a field of view of 36 mm provides a resolution of 35 μm/pixel which is enough for the seam detection and weld inspection requirements. Additionally, the chip performs image capturing with the optional use of a Region Of Interest (ROI) of customized size (Rhapsody (2006)). The ROI allows the reduction of the amount of data that is used for the sensing purposes which improves the response time of the sensor. The camera has
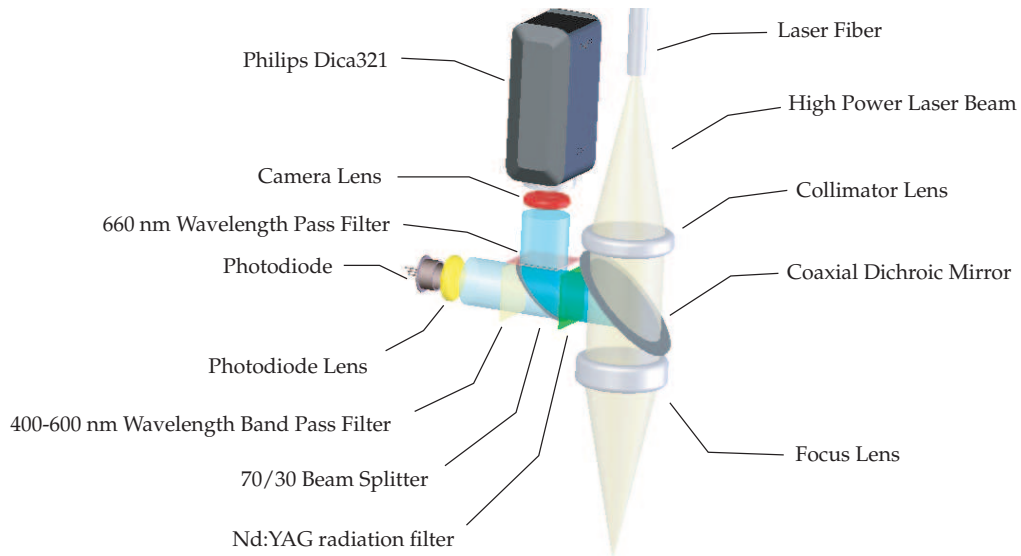
Figure 3.6: Complete optical components path of the integrated welding head.

two 1394 firewire ports that are used for connection with a host PC, two I/O ports and two RS232 ports which allow it to communicate and control external hardware, and an on board processor, which allows the camera to function in stand alone mode (without the use of an external PC).

The sensor must be functional even for the lowest light emission, which is according to Table 3.1 1.05×10^{-7} W. As a photodiode, a PIN-5DI Juraschek photodiode (Appendix A.4) was chosen. The photodiode is a silicon based photo receptor sensitive for radiations between 350 nm and 1100 nm. The photodiode has a maximum response frequency of about 66 MHz and a lowest detection signal of 3×10^{-11} W.

For the structured light illumination source the Lasiris SNF series laser diode has been selected (Appendix A.2). These diodes emit red light at the wavelength of 660 nm with a power of approximately 80 mW and a fan angle of 30°. The projected structured line has a uniform intensity profile throughout its length. The projected line's width varies from 35 μm to 70 μm for working distances of 100-200 mm. This allows sufficient sharp images of the lines. The On/Off state of each diode can be modulated with a TTL signal with a frequency up to 10 KHz. This enables them to be synchronized with the camera image capturing periods. For the inte-
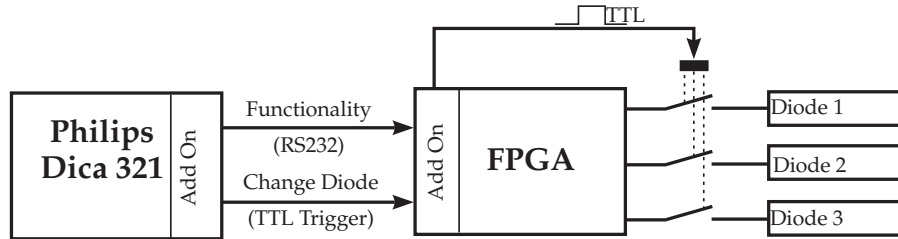
Figure 3.7: Diode synchronization scheme with camera and FPGA.

grated laser welding head three structured light diodes are used in order to project the triangular shape.

3.4   Electronic circuits design

There are several additional electronic circuits that are required for the correct functionality of the welding head. These electronics ensure the required power supply and the correct exchange of signals in an industrial environment where electromagnetic interference is usually present.

Several functions of the welding head require the synchronization of the camera image capture time with the projection time of the structured light laser diodes. As it is mentioned in § 3.3 the I/O and RS232 ports of the Philips camera can be used to send control signals to external hardware. Still the camera has only two out of the three required I/O ports to implement a direct synchronization scheme for the laser diodes. A Field Programmable Gate Array (FPGA) chip is used to perform the synchronization scheme (Appendix C.1). The general setup for the synchronization scheme is shown in Fig.3.7, where the 'Add On' layers are interfacing hardware from one system to the other.

As it is shown in Fig.3.7, there are two signals coming out of the camera that determine the camera-diode synchronization. The first one is the functionality signal which is delivered via the RS232, which selects which diodes are going to be lit and how they are going to be synchronized. The second one is a trigger signal (TTL) which informs the FPGA that the diode should be switched. In Table 3.3 the available functionalities are shown. Only two of the functionalities (4 and 5) make use of the trigger signal, that ensure that a different diode is switched on each time the camera cap-

Table 3.3: Diode status in relation to the camera signals

Functionality	Diode Mode
0	All diodes are Off. Trigger signal has no effect.
1	Only the first diode is On. Trigger signal has no effect.
2	Only the second diode is On. Trigger signal has no effect.
3	Only the third diode is On. Trigger signal has no effect.
4	First and second diode interchange their On/Off status in synchronization to the trigger signal. Only one diode can be On at anytime.
5	All diodes successively interchange their On/Off status in synchronization to the trigger signal. Only one diode can be On at anytime.
6	Only the first and second diodes are always On. Trigger signal has no effect.
7	All diodes are On. Trigger signal has no effect.

tures an image. This synchronization between the camera and the diodes is defined as the Switching Diode mode of the system.

The rest of the functionalities can be split into two additional modes. In the first one (None Mode) all diodes are switched off, and in the second one, Normal Mode, no synchronization between the diodes and the camera occurs. In the Normal Mode either one, two or three diodes are constantly on, forming a line, cross or triangle.

All of the electrical components of the integrated laser welding head are being supplied by a main power supply of 24V/2.5A. This supply is converted locally on the developed electronic boards regarding the local power needs. A description of the functionality of each of the developed electronic boards and their requirements is presented in the following paragraphs.
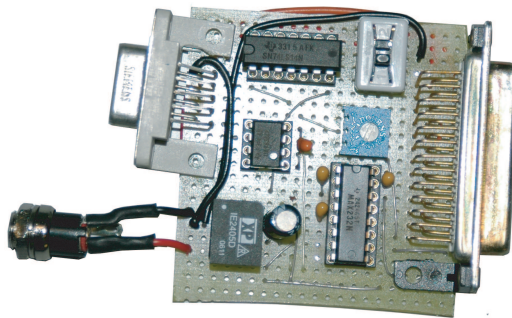
Dica321 Add On

The Dica321 Add On board converts the camera I/O and RS232 signals to differential signals. This conversion allows the elimination of any added interference on the signal lines. This board also is capable of supplying power to the camera through a switch in the cases where power is not provided by the firewire port. A general schematic of the functionality

of the board can be viewed in Fig.3.8(a). An image of the prototype electronic board is seen in Fig.3.8(b). The full electronic schematics and component description can be found in Appendix C.2. The inputs of the board is the 24 V power supply and the two signals from the camera. Part of the power supply is transformed to 5 V to be able to be used by the boards ICs, whereas the signals are converted to differential. The output of the board is a connection to the initial 24 V supply and the connections to the differential signals.
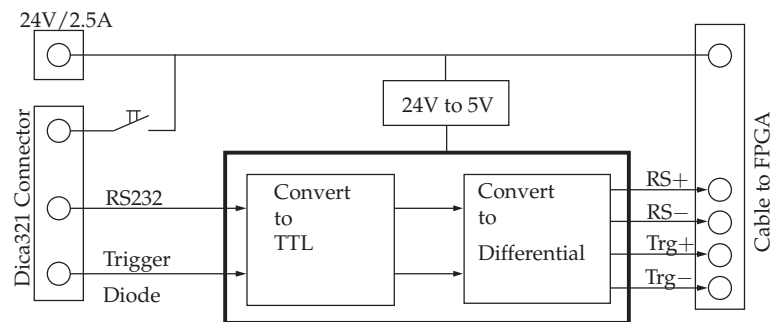
(a) General schematic of the Philips Dica321 add on board.

(b) Electronic board prototype of the Dica321 add-on.

Figure 3.8: General schematic and electronics prototype of the Philips Dica321 add on board.

FPGA Add On

The FPGA Add On board is the interface between the camera and the FPGA. This board combines the differential signals from the camera to

their original form while discarding any added interference during transmission. It also provides the necessary power supply for the FPGA board. A general schematic of the functionality of the board can be viewed in Fig.3.9(a). An image of the prototype electronic board is seen in Fig.3.9(b). The full electronic schematics and component description can be found in Appendix C.3. Its input is the the same as the output of the Dica321 Add on board. The output contains the recombined original signals of the camera as well a power supply of 5 V for the FPGA. In the schematic it is also shown that there is a cable that provides power to the Diode Power Supply board, as well as the TTL signals that are controlling the diodes.
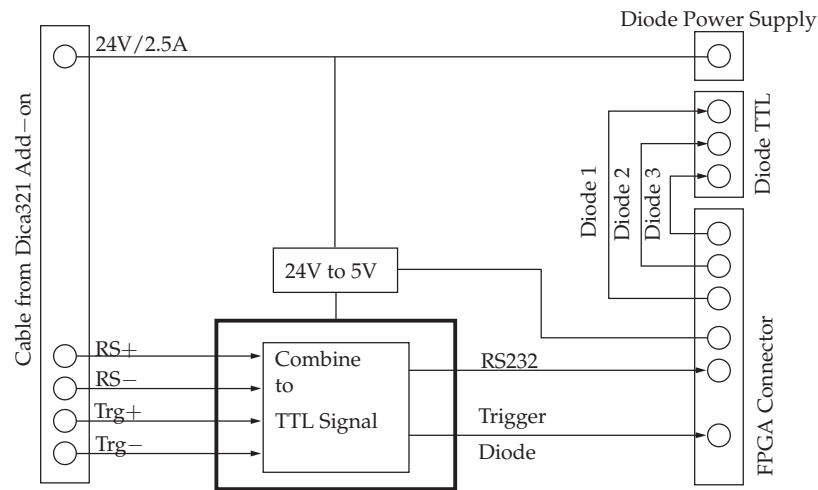
(a) General schematic of the FPGA add on board.
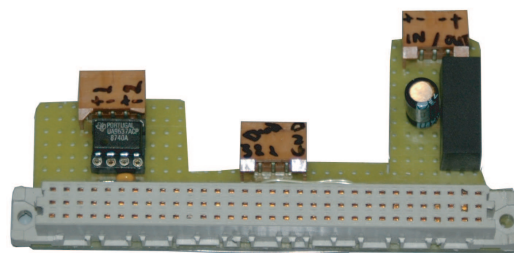
(b) Electronic board prototype of the FPGA add-on.

Figure 3.9: General schematic and electronics prototype of FPGA add on board.

Laser Diode Power Supply

The power requirements of each of the diodes is 5 V and 160 mA. Therefore it is necessary to convert the main power supply to one that can support the power requirements of the diodes. A voltage converter of 24 V to 5 V that can support up to 800 mA is used for this purpose. The three diodes are connected directly to the output of the power supply in parallel. Since each diode requires up to 160 mA, the voltage converter output can support the maximum required current for the three diodes of 480 mA. Details are presented at Appendix C.4.

3.5 Mechanical design and integration

The mechanical design is the stage where the housing of welding head is implemented. At this stage all components are positioned within the casing of the welding head. Therefore the mechanical design must take under consideration the accommodation of the following (in order of importance):

- Optical Path and Components

- Structured Light Laser Diodes

- Process Control Sensor System

- Electronic boards

- Additional parts (Cross Jet, Water Cooling, etc)

The first items that are to be accommodated into the welding head are the components that form the optical path as they were defined in § 3.2. In Fig.3.10, the implementation of the optical path inside the welding head is presented. It can be noted that the filter and the lens for the process monitor sensor are not placed in the main body. These components will be placed in the housing of the sensor itself that is attached to the Process Monitor Sensor Interface. This way optical process monitor sensors of different implementation or cameras can also be interfaced to the welding head.

The structured light laser diode holders are placed with an angle of 120° (Fig.3.11). The holders are designed to allow the projection angle of the structured light to be adjusted manually. Therefore it is possible for
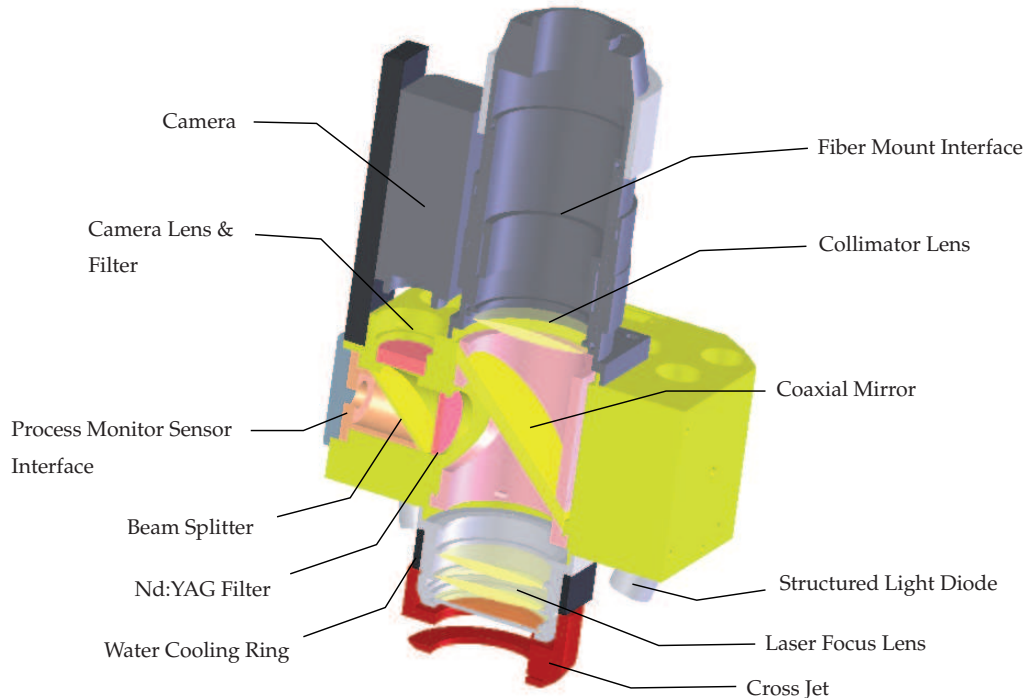
Figure 3.10: An section of the mechanical design of the welding head. The optical path of Fig.3.6 is clearly visible.

the same triangulation sensors to be adjusted and function for a variety of high power laser focus lenses with different focal distance.

The remaining body of the welding head is used for compartments for the electronic components of the system. The welding head body carries housing compartments for the FPGA board and its Add−on board, the power supply of the laser diodes, the laser diode electronics and the process control sensor electronics. The Dica321 Add−on board is housed with a separate casing that is mounted on the back side of the camera. In Fig.3.11 and Fig.3.12 the various compartments of the head are displayed. A detailed description of the connectors that were used is available at Appendix C.6.

Finally, the welding head body allows the integration of cooling water and Cross−Jet gas to it (Fig.3.11). They are necessary for the cooling of the high power laser focus lens and its protection from weld spatter.

Process Sensor
Interfacing

Diode Holders

FPGA Housing

120º

Cross Jet

Water Cooling
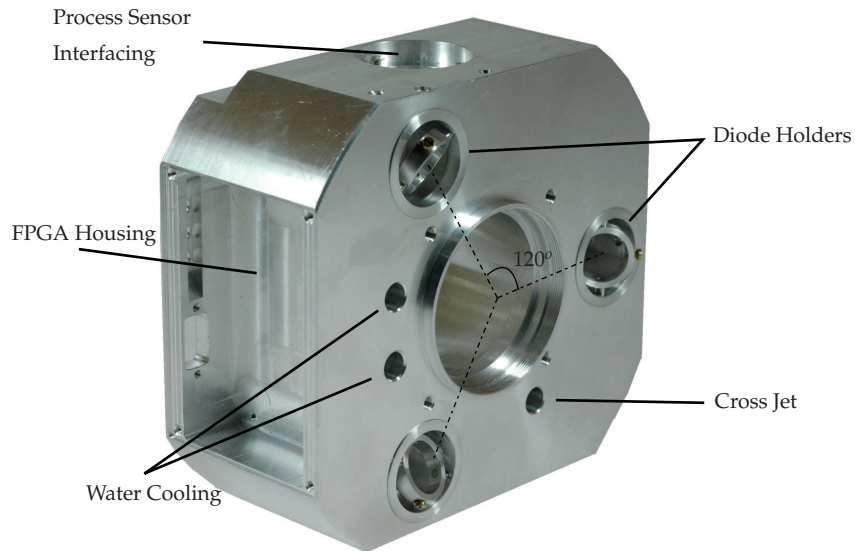
Figure 3.11: Integrated welding head main body bottom side.

170 mm

Laser Diode
Power Supply
Housing

Laser Diodes
Electronics
Housing

Process Sensor
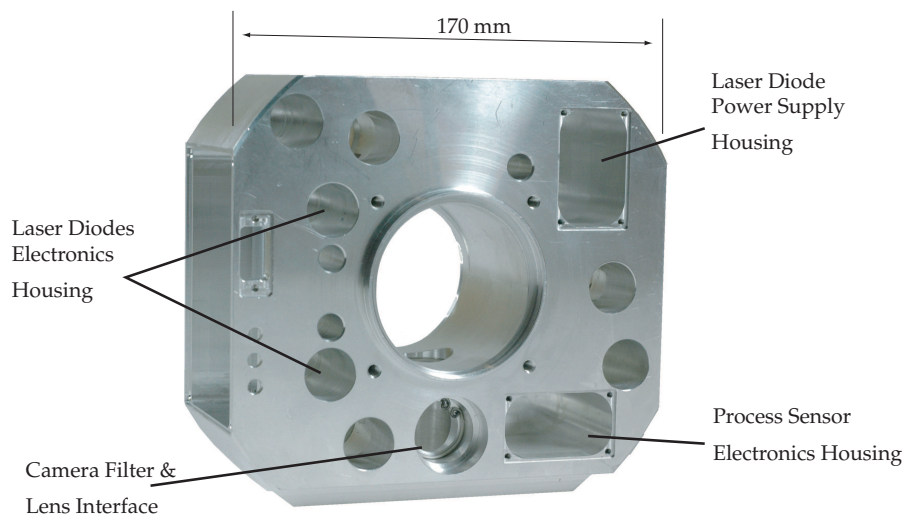Electronics Housing

Camera Filter &
Lens Interface

Figure 3.12: Integrated welding head main body top side.

3.6 Software Overview

The sensor data must be conveyed to other systems in the laser welding setup. The seam position must be provided to the positioning system (in this case an industrial robot), the laser process measurements to the process controller and the inspection data to the quality control system. This exchange of information is established through software which is developed for this purpose.

A description of the used software components and their interfaces will be presented in the following paragraphs.

INTEGLAS

INTEGLAS is the application that controls the parameters of the sensors of the integrated laser welding head (Appendix E.1). It has a graphical user's interface (GUI) that allows the system's user to:

- perform welding tool calibrations

- perform sensor calibrations

- select sensor functionality

- set the triangulation sensor resolution

- view the triangulation sensor parameters

- visualize sensors' outputs

- display measurement results/reports

- set camera operating parameters

- control structured light diode status

- convey data to other applications

INTEGLAS has been developed in Microsoft Visual C++ .NET environment (Microsoft (2002)) which in general is a C++ compiler, with the use of QT v4.0 (Trolltech (2006)) and Rhapsody (Rhapsody (2006)). The QT toolbox allows the easy development of GUIs, whereas Rhapsody is an image processing library from Philips which can be used with the Philips Dica321 camera.

3.6.1   24-LASER

One of the requirements of the integrated head is that it must be possible to be used by robots. 24-LASER is a software package that is specifically developed for sensor guided robotic laser welding (De Graaf (2006)). Therefore the sensor has to communicate with 24-LASER, which undertakes the task to control the robot. 24-LASER has a GUI interface and can perform various functionalities, a list of which is presented in Appendix E.2. The ones that are important for this work can be summed in the following:

- manipulate robot

- define trajectories and laser jobs

- connect to positioning sensors

- select the laser power output

- teach and track seams

- perform laser tool calibrations

- communication sockets (robot, sensor)

When the integrated laser welding head is used with 24-LASER, INTEGLAS is used to convey the sensor measurements. Other than the transfer of measurement data, the communication between the two applications also allows the calibration of tools and sensors, and the exchange of the tool and sensor definition parameters.

3.6.2   D-SPACE

D-SPACE offers a complete commercial set of hardware and software for real-time signal processing. It has a GUI, that allows the user to display and process the incoming signals and produce the required outputs. D-SPACE is used for translating the process monitor sensor's signals into laser power output levels. The output of the D-SPACE is a voltage signal between 0.1 and 10V that is connected to the laser controller.

3.6.3 Data and Data exchange

The majority of data flow takes place between the sensor and the robot control applications. A data exchange diagram between the applications is presented in Fig.3.13, whereas the description of the three main categories of data is given in the following paragraphs.
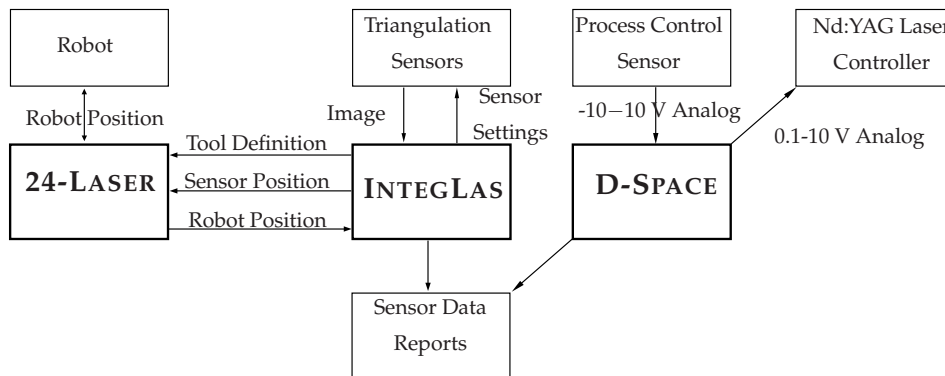

Figure 3.13: Data Exchange Diagram.

Seam Detection Data

The sensor measurements are meaningful only if they can be related to the coordinate system of the robot. For the same measurements to be used for laser welding a relation between the sensor tool coordinate system and the laser tool coordinate system must be established. These two coordinate systems and their relation can be identified by a number of calibrations performed by INTEGLAS and 24-LASER, which are explained in Chapter 4. Upon identification they are available for use to the 24-LASER application for the correct tracking of the measured path.

For the communication between the sensor and 24-LASER, ethernet communication is used. The sensor acts as a server where various clients can be connected to request sensor data. The server provides data about the tool and sensor identified coordinate systems, as well as sensor measurement data. Such a client is the 24-LASER application. Every time that 24-LASER requests new data from the server, the server (sensor) sends the latest measured values.

Process Control Data

The laser process sensor data interfaces to a signal processing platform. Any signal processing system can be used for monitoring the signals of the process monitor sensor. The one used in this work is a D-SPACE unit which was available in the laboratory. There is no interaction between the process monitor sensor system and either the 24-LASER or INTEGLAS applications. This system is autonomous, and when used for control purposes of laser welding process, it provides an analog signal for the control of the Nd:YAG laser power level.

Weld Inspection Data

The weld inspection process is a quality determination process. In the laser welding process there is no requirement to process the measurement data in realtime as long as at the end an overview of the quality of the weld is provided. The end result of weld inspection can be transferred to another machine for processing but in the most cases the end receiver of such a process is a human operator. It is therefore required that the output of the inspection process is in a form of a report that will enable the operator to access and assess the result fast.

For this reason, the output has the form of a report where all the values for the quality thresholds are displayed together with the positions along the inspected weld where these quality thresholds where crossed. Furthermore, an estimation is made about the overall quality of the weld. Finally, a three-dimensional representation of the weld (Fig.3.14), is available to the operator for observation purposes. The 3D representation carries colored arrows indicating the position along the weld where imperfections exceed the permitted values. Different colors represent different imperfections (e.g. Blue = Misalignment, Green = Convexity, Black = Undercuts, etc.).

The weld inspection process is performed by INTEGLAS application and communicates with 24-LASER only to acquire the position of the robot on each measurement. For the correct interpretation of the inspection data the coordinate system of the sensor must also be available.
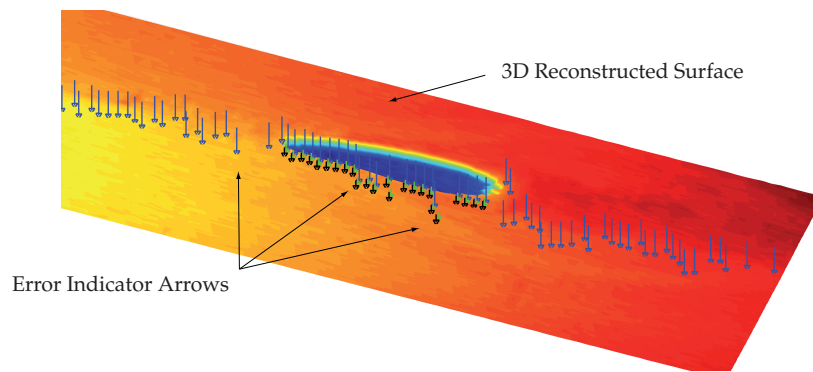
3D Reconstructed Surface

Error Indicator Arrows

Figure 3.14: 3D representation of the inspected weld with error indicating arrows.

62

Chapter 4

System Calibrations

For the fully integrated head three types of calibrations are necessary: the Optical calibrations, the Laser Tool point calibrations and the Sensor calibrations. The optical calibrations are performed to identify and correct for measurement errors like distortions, arising from image distortions caused by the optical components. The laser tool calibrations identify the position of the TCP_L and the laser tool coordinate system in relation to the robot end effector. The sensor calibrations are required to determine the sensor parameters (structured light projection angle, pixel-to-mm factor, etc.) and relative position of the sensor tool center point (TCP_S) and the sensor coordinate system to the robot end effector. Combining both tool calibrations, the sensor measurements can be related to the laser tool.

Although the calibrations are performed separately, there is a hierarchy that needs to be followed, namely:

1. Optical Calibration

2. Laser Tool Calibration

3. Sensor Calibration

Both the laser tool and the sensor calibration use the camera image for their measurements. Therefore the optical calibrations must be performed first. For the sensor calibration a number of movements need to be performed. These movements are related to the parameters of the laser head and therefore the laser tool calibration must be performed before the sensor tool calibration.

4.1   Optical Calibration

In §3.2, the optical path of the imaging sensor is defined. A number of optical components exist along the optical path, that influence the quality of the final sensor image. The biggest abberations come from the high power laser focus lens, because these lenses are optimized for focusing a collimated laser beam onto a small spot on their optical axis. These lenses are not optimized for imaging and therefore a number of distortions (radial, abberations, astigmatism, etc) will influence the camera images. Since the images will be used for seam detection and weld inspection, the optical system must be calibrated and the distortions in the images must be corrected for. This type of calibrations are known as camera calibrations. There are a variety of methods proposed for performing camera calibrations (e.g. Heikkila and Silven (1997), Tsai. (1987)). The method proposed by Zhang (1998) is selected to be applied in this case.

Merriam-Webster dictionary defines 'Distortion' as *a lack of proportionality in an image resulting from defects in the optical system*. It is important that a clear distinction is made between the deformations on captured image that fall under the category of 'Distortions'. The changes of the size of the objects in an image due to the point of view of the captured image can not be accounted as distortions because they do not originate from the optical system. Furthermore, lens errors like spherical aberrations and astigmatism should also be excluded, because they introduce a blurring effect and do not create a lack of proportionality in the image. Radial and tangential distortions on the other hand can not be excluded as they introduce changes in the proportionality of the image objects. In Fig.4.1 the effects of these distortions on an image are shown. The radial distortions introduce the barrel and pincushion effects on the image (Fig.4.1 b and c). The tangential distortions (also known as decentering distortions) derive from misalignments of the optical components and introduce a shifting of the principal optical axis of the lenses on the image. Thus the center of the radial distortions is also displaced (Fig.4.1 d and e).

The camera and lens calibration consists of two parts: the parameter identification of the distortions imposed by the lens and the camera, and the undistortion of the captured images according to the identified parameters. A description of the camera and lens calibration procedure is presented in the following paragraphs. Parts of the optical calibration section have been published in the Journal of Laser Applications (Entzinger et al. (2007)).
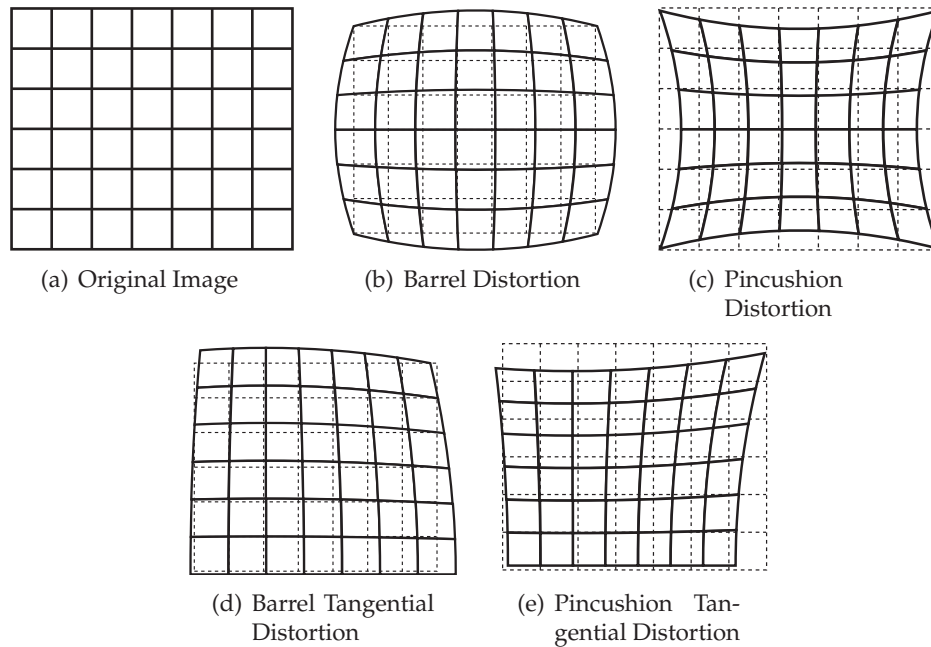
(a) Original Image

(b) Barrel Distortion

(c) Pincushion Distortion

(d) Barrel Tangential Distortion

(e) Pincushion Tangential Distortion

Figure 4.1: Examples of radial and tangential distortions on an image.

4.1.1 Distortion Parameter Identification

For the parameter identification a model of the camera-lens optical system is defined, and its performance is evaluated in relation to experimental data. The parameter identification consists of the following steps:

1. Definition of Camera Model

2. Definition of Lens Model

3. Acquisition of Calibration Data

4. Determination of Camera and Lens parameters

The camera model defines the way that the objects are formed on an image and is used for the identification of the camera parameters. The lens model defines the way the lens is affecting the image and is used in the identification of the lens parameters. The acquisition of calibration data is the measurement process where the input data for the model optimization

are gathered. Finally, the determination of the camera and lens parameters is the implementation of the optimization procedure.

Camera Model

A camera model is created to describe the way by which real world objects $[x, y, z]$ are formed on an image $[u, v]$ through a camera. The camera model is defined as a pinhole with coordinates $[x_c, y_c, z_c]$. Fig.4.2 shows a transformation according to a pinhole camera model Xu and Zhang (1996) where all light rays traveling through the pinhole form an image at the image plane.
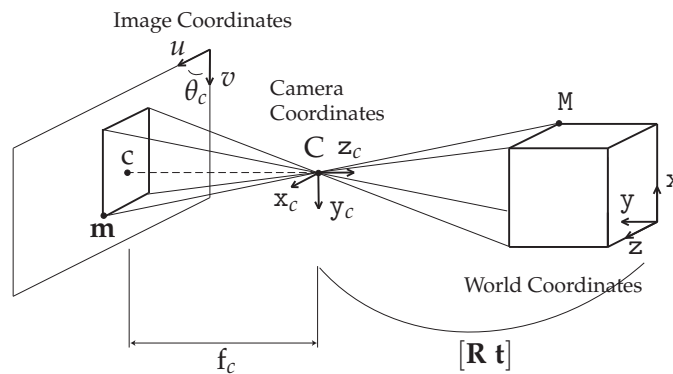
Figure 4.2: Coordinate Systems in Projective Geometry.

The camera position and orientation $[x_c, y_c, z_c]$ are expressed relative to the world coordinates $[x, y, z]$ using a rotation and translation transformation $[\mathbf{R} \, \mathbf{t}]$. The focal length f_c of the optical system is the distance from the pinhole C to the image plane. The principal point $c = [u_0, v_0]$ is the point where the optical axis crosses the image plane. The principal point is defined in the image coordinates u and v in image pixels. The axes u and v are not necessarily perpendicular, nor equally scaled.

The tilde ˜ when used on a vector, like in $\tilde{\mathbf{v}}$, is used to denote an augmented vector $[\mathbf{v}^T 1]^T$.

A point M in real world coordinates can be expressed in camera coordinates (M_c) using the rotation matrix $\mathbf{R}$ and translation $\mathbf{t}$ as following:

$$\mathrm{M_c} = \mathbf{R}\mathrm{M} + \mathbf{t} \Rightarrow$$

$$\begin{bmatrix} x_c \\ y_c \\ z_c \end{bmatrix} = \underbrace{\begin{bmatrix} r_{11} & r_{12} & r_{13} \\ r_{21} & r_{22} & r_{23} \\ r_{31} & r_{32} & r_{33} \end{bmatrix}}_{\mathbf{R}} \underbrace{\begin{bmatrix} \Delta x \\ \Delta y \\ \Delta z \end{bmatrix}}_{\mathbf{t}} \begin{bmatrix} x \\ y \\ z \\ 1 \end{bmatrix} \Rightarrow \tag{4.1}$$

$$\mathrm{M_c} = [\mathbf{R}\ \mathbf{t}]\tilde{\mathrm{M}}.$$

For a flat calibration object, the world coordinate z can be chosen to be z = 0 (i.e., the pattern is considered to exist in the xy-plane). Therefore, without loss of generality, we can use

$$\mathrm{M_c} = [\mathbf{R}\ \mathbf{t}]\tilde{\mathrm{M}} = \begin{bmatrix} r_{11} & r_{12} & \Delta x \\ r_{21} & r_{22} & \Delta y \\ r_{31} & r_{32} & \Delta z \end{bmatrix} \begin{bmatrix} x \\ y \\ 1 \end{bmatrix}. \tag{4.2}$$

The parameters $\mathbf{R}$ and $\mathbf{t}$ are the camera *extrinsic parameters*, as they specify a transformation outside the camera system.

A 3D point M is projected onto the 2D image plane resulting in point $\mathbf{m} = [u, v]$ by the projection

$$\frac{u}{x_c k_u} = \frac{v}{y_c k_v} = \frac{f_c}{z_c}, \tag{4.3}$$

or, in matrix-vector form (with s set equal to z_c by the lower row in the equation):

$$s \begin{bmatrix} u \\ v \\ 1 \end{bmatrix} = \begin{bmatrix} f_c k_u & f_c k_u / \tan\theta_c & u_0 \\ 0 & f_c k_v / \sin\theta_c & v_0 \\ 0 & 0 & 1 \end{bmatrix} \begin{bmatrix} x_c \\ y_c \\ z_c \end{bmatrix}, \tag{4.4}$$

Where the variables k_u and k_v in this equation specify the real world pixel sizes in u and v direction respectively. And the image parameters θ_c, u_0 and v_0 are included in this transformation to give the full camera transformation

The parameters in this transformation specify the internal behavior of the camera. These parameters are the camera *intrinsic parameters*. A change in the focal length f_c in Eq.4.4 cannot be distinguished from a

change in the pixel dimensions k_u and k_v. For this reason the f, which is the focal length in averaged pixel size, has been split off. The zooming part of the camera intrinsic matrix, consists of the upper-left 2×2 matrix, which is normalized to be non-magnifying:

$$s \begin{bmatrix} u \\ v \\ 1 \end{bmatrix} = \underbrace{\begin{bmatrix} \alpha & \gamma & u_0 \\ 0 & \beta & v_0 \\ 0 & 0 & 1 \end{bmatrix}}_{\mathbf{A}} \underbrace{\begin{bmatrix} f & 0 & 0 \\ 0 & f & 0 \\ 0 & 0 & 1 \end{bmatrix}}_{\mathbf{F}} \begin{bmatrix} x_c \\ y_c \\ z_c \end{bmatrix},$$

or

$$s\tilde{\mathbf{m}} = \mathbf{AF}M_c. \tag{4.5}$$

With:

$$\left\| \begin{matrix} \alpha & \gamma \\ 0 & \beta \end{matrix} \right\|_{\text{Fro}} = \sqrt{2}, \quad \text{thus:} \quad f = \frac{f_c \left\| \begin{matrix} k_u & k_u / \tan \theta_c \\ 0 & k_v / \sin \theta_c \end{matrix} \right\|_{\text{Fro}}}{\sqrt{2}}. \tag{4.6}$$

Here *Fro* denotes the Frobenius Norm.

A point expressed in the camera coordinate system can now be projected onto the image plane by Eq.4.5. The combination of Eq.4.1 and Eq.4.5 results to:

$$s\tilde{\mathbf{m}} = \mathbf{AF}[\mathbf{R}\ \mathbf{t}]\tilde{\mathbf{M}}, \tag{4.7}$$

which represents the translation from real world coordinates to image coordinates, for an ideal camera model.

Lens Model

In reality the image is formed by optics (mostly lenses) instead of a pinhole. These lenses introduce distortions (astigmatism, coma, radial etc.). As it was explained in §4.1 the most important distortions are the radial and tangential ones, because they introduce changes in the proportionality of the image objects. In literature often the first two radial distortions Zhang (1998); Jian et al. (2001); Ma et al. (2003) and sometimes also two tangential distortion components are taken into account Brown (1971). To

correct for these distortions we need to accurately estimate the distortion parameters.

In the following formulas, a breve (˘) denotes a distorted coordinate, with subscripts r and t to indicate radial and/or tangential distortion. For readability the subscript c for camera coordinates is left out.

The transformation from the real points x and y to the radially distorted points $\check{x}_r$ and $\check{y}_r$ is described by:

$$\check{x}_r = x + x \left[\kappa_1 \left(x^2 + y^2 \right) + \kappa_2 \left(x^2 + y^2 \right)^2 \right] \tag{4.8}$$

$$\check{y}_r = y + y \left[\kappa_1 \left(x^2 + y^2 \right) + \kappa_2 \left(x^2 + y^2 \right)^2 \right], \tag{4.9}$$

where κ_1 and κ_2 are the first and second order radial distortion parameters. The addition of two tangential distortion parameters τ_1 and τ_2 is given by

$$\check{x}_{rt} = \check{x}_r + \tau_1 \left(3x^2 + y^2 \right) + 2\tau_2 xy \tag{4.10}$$

$$\check{y}_{rt} = \check{y}_r + 2\tau_1 xy + \tau_2 \left(x^2 + 3y^2 \right). \tag{4.11}$$

The fact that the lens is fixed to the camera means that lens distortions should be added to the model after the real world to camera coordinates transformation (but before the perspective projection). The magnifying matrix $\mathbf{F}$ can be put on either side of the lens distortion transformation, as it is just a linear scaling. Here it was chosen to maintain $\mathbf{F}$ with the $[\mathbf{R} \ \mathbf{t}]$ matrix. To find the distorted image coordinates $\check{u}$ and $\check{v}$ in terms of the ideal coordinates the following equations are used:

$$\begin{aligned} \check{u} &= u_0 + \alpha \check{x} + \gamma \check{y} \\ \check{v} &= v_0 + \beta \check{y}. \end{aligned} \tag{4.12}$$

Substitution of Eq.4.8 and Eq.4.9 for the radial distortions, gives:

$$\begin{aligned} \check{u}_r &= u_0 + \alpha x + \alpha x \left[\ldots \right] + \gamma y + \gamma y \left[\ldots \right] \\ &= \underbrace{u_0 + \alpha x + \gamma y}_{=u} + \underbrace{\alpha x \left[\ldots \right] + \gamma y \left[\ldots \right]}_{=(u-u_0)[\ldots]} \\ &= u + (u - u_0) \left[\kappa_1 \left(x^2 + y^2 \right) + \kappa_2 \left(x^2 + y^2 \right)^2 \right], \end{aligned} \tag{4.13}$$

and

$$\begin{aligned}
\breve{v}_r &= v_0 + \beta y + \beta y \left[\ldots \right] \\
&= \underbrace{v_0 + \beta y}_{=v} + \underbrace{\beta y \left[\ldots \right]}_{=(v-v_0)[\ldots]} \\
&= v + (v - v_0) \left[\kappa_1 \left(x^2 + y^2 \right) + \kappa_2 \left(x^2 + y^2 \right)^2 \right].
\end{aligned} \tag{4.14}$$

The same substitution can be done for the tangential additions, which re-
sults in

$$\begin{aligned}
\breve{u}_{rt} &= \breve{u}_r + \alpha \tau_1 \left(3x^2 + y^2 \right) + \alpha 2 \tau_2 xy + \gamma 2 \tau_1 xy \\
&\quad + \gamma \tau_2 \left(x^2 + 3y^2 \right)
\end{aligned} \tag{4.15}$$

$$\breve{v}_{rt} = \breve{v}_r + \beta 2 \tau_1 xy + \beta \tau_2 \left(x^2 + 3y^2 \right). \tag{4.16}$$

4.1.2 Acquisition of Calibration Data

The calibration procedure relies on the comparison of (distorted) feature
points extracted from images taken using the optical system under investi-
gation on one side, with the ideal model feature points transformed using
the camera and lens models on the other. To be able to eliminate the cam-
era extrinsic parameters $[\mathbf{R}\ \mathbf{t}]$ several pictures of a calibration pattern (like
the one in Fig.4.3(a)) must be taken under different orientations. As the in-
trinsic parameters (i.e., camera and lens transformations) will be the same
for all images and the extrinsic parameters (i.e., rotation and translation)
will differ, it is possible to differentiate between these parameters.

Once images of the calibration pattern are available, the feature points
must be extracted. These feature points are either the four corners of the
individual squares of the pattern or the center of gravity of each of the
squares. Image processing algorithms take care for this identification of
the required object features. In Fig.4.3(b) examples of the detection of the
feature points are displayed.

The extracted feature point coordinates should be listed in the same
order as the coordinates in the ideal model. How they are ordered is
not important, as long as the model points and the extracted points can
be matched. An example of such an ordering of the extracted features is
shown in Fig.4.4, where the centers of gravity of the pattern in Fig.4.4(a)
are ordered from bottom to top and left to right (Fig.4.4(b)).

(a) Whole image

(b) Detail of one square
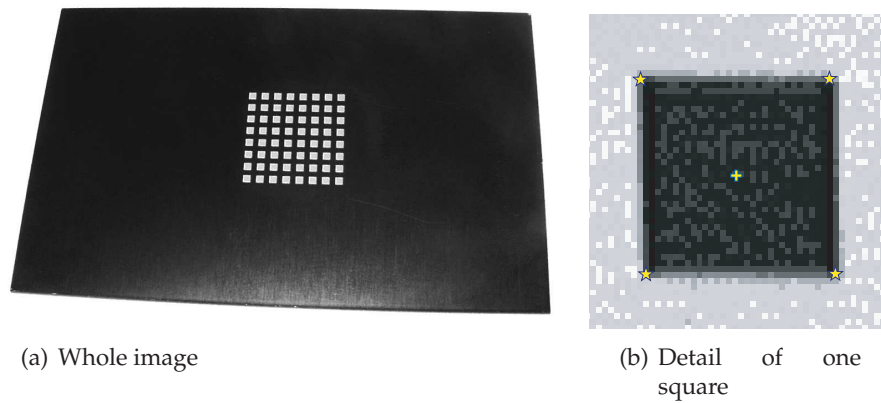
Figure 4.3: Calibration pattern laser engraved in anodized aluminium (a). Extracted feature points after image processing of one of the pattern's squares, depicted as stars for the corner points and cross for the center of gravity (b).
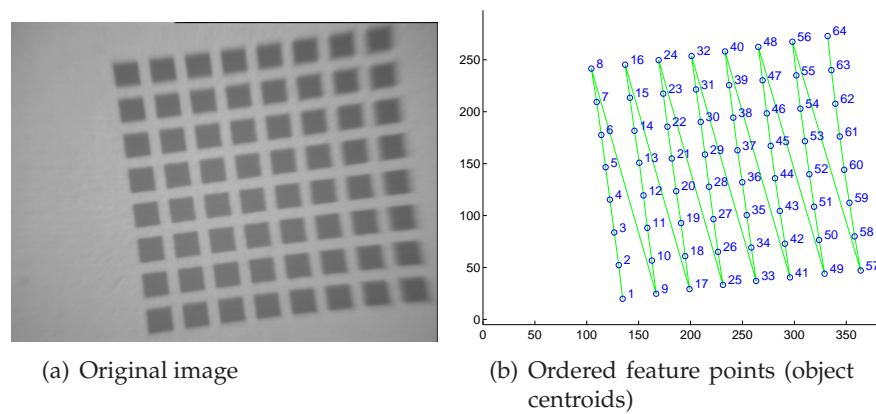

(a) Original image

(b) Ordered feature points (object centroids)

Figure 4.4: The extracted feature points are ordered in correspondence with the model points.

4.1.3   Camera & Lens Parameter Determination

To find the camera and lens parameters an implementation of the algorithm in Zhang (1998) was used, with the adaptation of keeping a constant zooming factor in the $\mathbf{A}$ matrix as pointed out in §4.1.1.

In this algorithm first a homography

$$\mathbf{H} = \mathbf{AF}[\mathbf{R}\ \mathbf{t}] \tag{4.17}$$

is calculated for every image. Actually $\mathbf{H}$ is the best fit between the model points and the actually extracted feature points according to

$$s\tilde{\mathbf{m}} = \mathbf{H}\tilde{\mathbf{M}}, \tag{4.18}$$

(similar to Eq.4.7).

As s in Eq.4.18 can be scaled arbitrarily, the 3×3 matrix $\mathbf{H}$ has 8 degrees of freedom. Rotation and translation can be fully described with 6 independent parameters, which means that two constraints should be formulated on $\mathbf{H}$. These constraints can be found in the orthonormality of $\mathbf{R}$. With these two constraints on each homography, it follows that at least 3 images are needed to solve for the 5 independent camera intrinsic parameters in $\mathbf{AF}$.

Once initial estimates are present for $\mathbf{AF}$ and the $[\mathbf{R}\ \mathbf{t}]$ matrices, an initial estimate for the lens distortions can be calculated. The radial distortion parameters κ_1 and κ_2 can be calculated by using the pseudoinverse to solve the matrix-vector form of Eq.4.13 and Eq.4.14:

$$\begin{bmatrix} (u-u_0)\left(x^2+y^2\right) & (u-u_0)\left(x^2+y^2\right)^2 \\ (v-v_0)\left(x^2+y^2\right) & (v-v_0)\left(x^2+y^2\right)^2 \end{bmatrix} \begin{bmatrix} \kappa_1 \\ \kappa_2 \end{bmatrix} = \begin{bmatrix} \breve{u}-u \\ \breve{v}-v \end{bmatrix}. \tag{4.19}$$

The radial plus tangential distortions from Eq.4.15 and Eq.4.16 can be solved in a similar way.

A non-linear least squares parameter optimization is performed to refine all estimates. All parameters are optimized simultaneously. To reduce the number of parameters, to optimize and to make sure an unconstrained optimization can be carried out, the rotation matrices are exchanged by their Rodrigues parameters (see Appendix B.3).

4.1.4 Image Undistortion

Once the parameters ($\mathbf{A}$, κ_1, κ_2, τ_1, τ_2) have been identified, the image can be corrected for the camera and lens distortions. Most procedures discussed in literature use the inverse of the distortion function to clear images from their distortions. For the non-linear distortion functions Eq.4.13 and Eq.4.14 used in this paper an iterative process is needed. Other researches have focussed on developing distortion functions that can easily be inverted (Ma et al. (2003)).

A faster approach uses look-up tables (LUT) for image undistortion. From the calibration procedure it is possible to calculate how each pixel of the image is distorted. A 2D LUT is distorted according to the identified distortion parameters Fig.4.5(a). Next, the undistortion of an image becomes a simple step of retrieving the intensity of the pixel in the distorted LUT (Fig.4.5(b)).
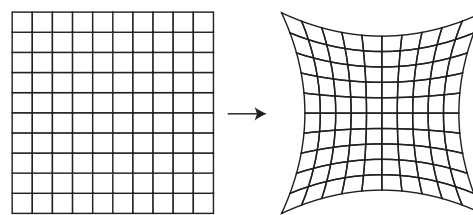
(a) Distortion of pixel coordinate values of an image coordinate LUT.
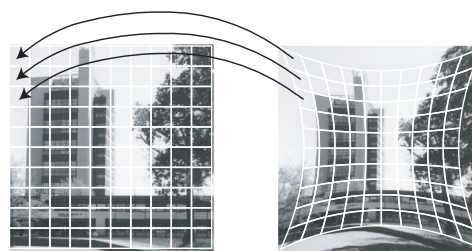
(b) Undistortion of captured image with the help of distorted LUT.

Figure 4.5: Use of look-up tables for image undistortion.

4.1.5   Calibration Experiments

A semi-professional digital photo camera has been calibrated as a test case. Because the lenses used for photo cameras are optimized for imaging, images are much clearer than those captured using the welding head. Moreover, the high resolution and large field-of-depth result in much better images and feature points are much easier to detect.

The thin line in Fig.4.6 shows the radial distortion for every point on the diagonal of the photo camera image. The distortions are negligible in a large central area, whereas the corners of the image moved nearly 1% (which would only be 0.75 mm when printed as a normal photo).As expected, from the quality of this camera and its lens, the radial distortions are very small.

When calibrating the integrated welding head optics the need for camera calibration for accurate position measurements becomes clear (thick line in Fig.4.6). Being almost 7.5%, the maximum distortion would be over 5 mm when printed as a photograph.

Estimations of the tangential distortions have been implemented as well. Their influence appears to be negligible compared to the radial distortions, which is in line with literature.

Calibration results based on full resolution images (768×576) or sub sampled images (384×288) did not show significant differences. In Fig.4.7(a), radial distortions are responsible for the deformation of the
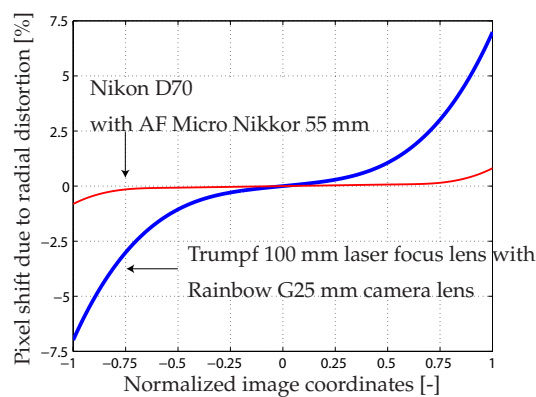
Figure 4.6: Shift of pixel data due to radial distortions. The shift percentage is plot against the distance from the image center. The thin line is for the photo camera, the thick line for the welding head.

(a) Original image   (b) Undistorted image
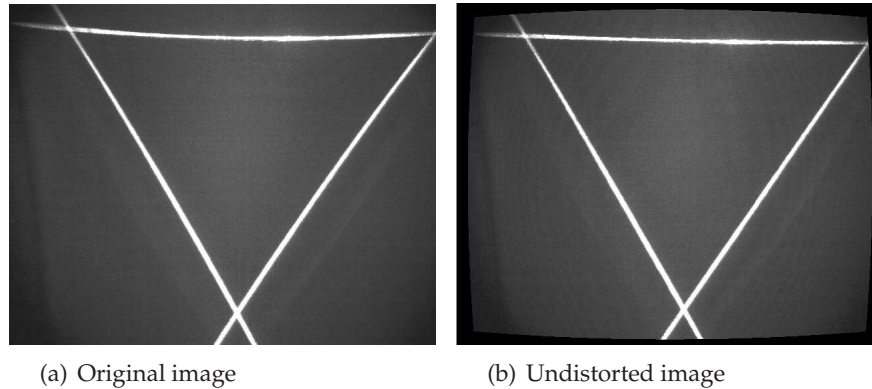
Figure 4.7: Radial distortions that are present in the original image (curved lines) are corrected with undistortion.

structured laser lines on the captured image. After undistortion the laser lines appear straight again in Fig.4.7(b).

Imaginary Calibration Results

To increase the speed of the calibration computations, the initial set of the calibration pattern images is divided to several overlapping subsets. Each of these subsets is then tested to obtain the camera calibration parameters.

In some tests imaginary calibration results showed up in the calculation of the camera intrinsic parameters. This is due to badly conditioned matrices, caused by highly correlated or contradicting input data. Imaginary data can also appear when one data set was used multiple times as input for a single calibration. In the current implementation, if imaginary results are detected, then calibration is terminated for the subset in question.

A remarkable improvement of the overall result can be obtained by leaving out images that cause imaginary results. An example of such an improvement is illustrated in Fig.4.8, where the RMS values resulting from the nonlinear LSQ optimization are presented. If the images that often occur in sets that provide imaginary results are allowed to participate in other image subsets, a frequency histogram like the one of Fig.4.8(a) is found. Whereas in the case where those images are excluded the result of Fig.4.8(b) is obtained. By comparing the two figures it is obvious that the omitted images do not contribute to the occurrence of small RMS values

(a) RMS values when all non-imaginary results are reviewed.

(b) RMS values of sets without images that often produce imaginary results.
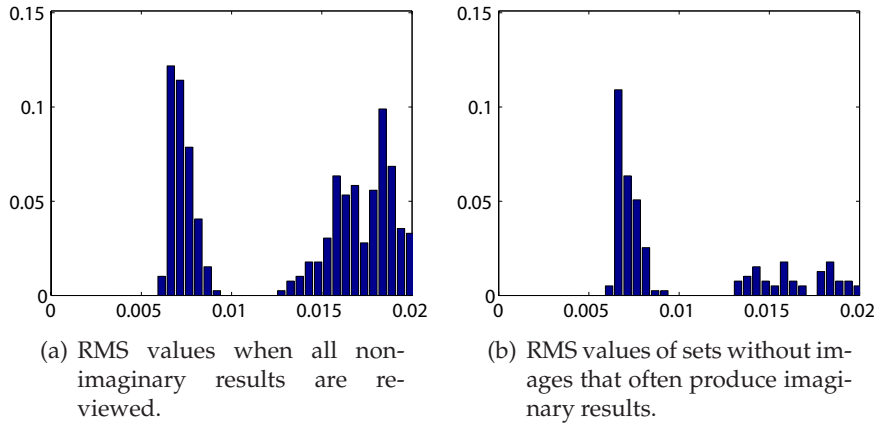
Figure 4.8: The plots are histograms, where in the horizontal axis are the RMS values of the image sets, and on the vertical is the number of the sets with approximately the same RMS value. The vertical axis is normalized according to the total amount of image sets that are used. The images that often occur in sets with imaginary results mainly contribute to the occurrence of high RMS values.

but on the contrary they mainly result to higher ones. The most important aspect is that these image sets do not only influence the RMS value, but also the first radial distortion parameter κ_1 and the factor f parameters. Therefore it is important to be able to discard bad data by reviewing the results and checking how often and when a certain image is linked to the presence of imaginary results.

Seam Detection Experiments

Several seam detection experiments have been carried out with and without image undistortion. As could be expected, image undistortion improves the measurement accuracy. The results of two of those experiments are presented further in this section. In these two experiments the sensor moves along a straight line. Every two millimeters the sensor performs measurements on the seam. The further a seam point exists from the sensor path, the less accurate its position measurement is due to distortions. For the current experiments a CCD camera of 384x288 pixels was used.

The first experiment involves the detection of a straight seam (Fig.4.9(a)). The seam is positioned in such a way under the sensor that its initial position will appear around the center of the sensor image

(therefore very little or no radial distortions exist) and gradually move towards the outer parts of the image where the correction of radial distortions is necessary. As displayed in Fig.4.10, there is a significant difference between the measurements of the distorted (thick line) and undistored (thin line) images. Even though the accuracy of the measurements has been improved with undistortion, there still exist errors of almost 100 μm. This is the limit of the accuracy necessary for laser welding. Further improvements can be possible with the use of higher resolution cameras.

(a) Straight line seam.

(b) Part of 182 mm radius circle curved seam.
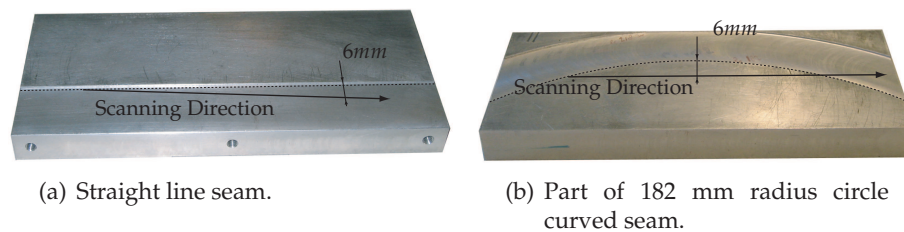
Figure 4.9: Pictures of the seam geometries that were used for the experiments. The arrowed line indicates the scanning direction whereas the dashed line indicates the seam.

In the second experiment the straight seam is replaced by a curve which is part of a circle with radius 182 mm (Fig.4.9(b)). The curved seam is placed under the sensor in such a way that it crosses the linear path of the sensor twice. This means that the beginning and the end of the curve exist on the same side of the linear path of the sensor, whereas the rest of the curve is located on the other side. In Fig.4.11 the measurement errors of the distorted (thick line) and undistorted (thin line) data are displayed. The shown errors are calculated distances of the measurements with a fitted circle through the undistorted data. Similar conclusions to the ones of the linear seam can be made in this case as well. The difference between the distorted and undistorted measurement errors is smaller. This is because the end point on the curve does not reach the outer parts of the sensor's image plane as was the case with the straight line seam.

4.2 Laser Tool calibration

For laser welding it is necessary to position the high power laser focal point (also known as TCP_L) on the seam. The TCP_L is a point fixed to the
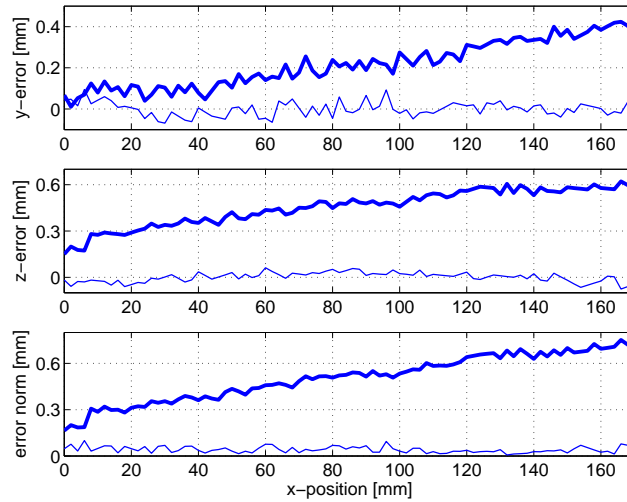
Figure 4.10: Distance between the points measured from distorted images (thick lines), with respect to a line fit through the undistorted measurements (thin lines), for the straight line seam of Fig.4.9(a).
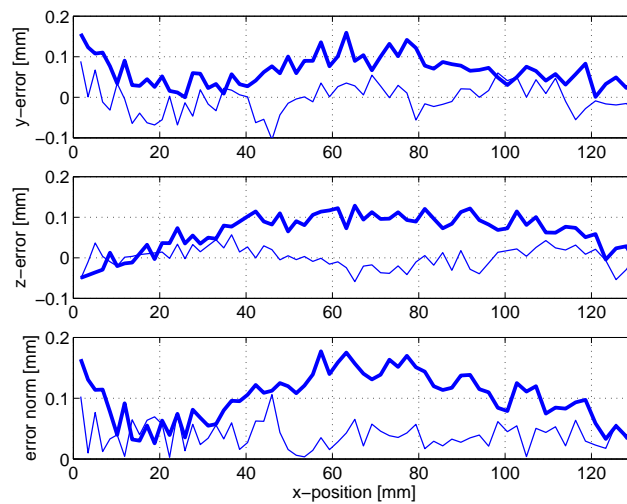
Figure 4.11: Accuracies from measurements on the curved seam test object, between the original situation (thick lines) and the image undistorted ones (thin lines).
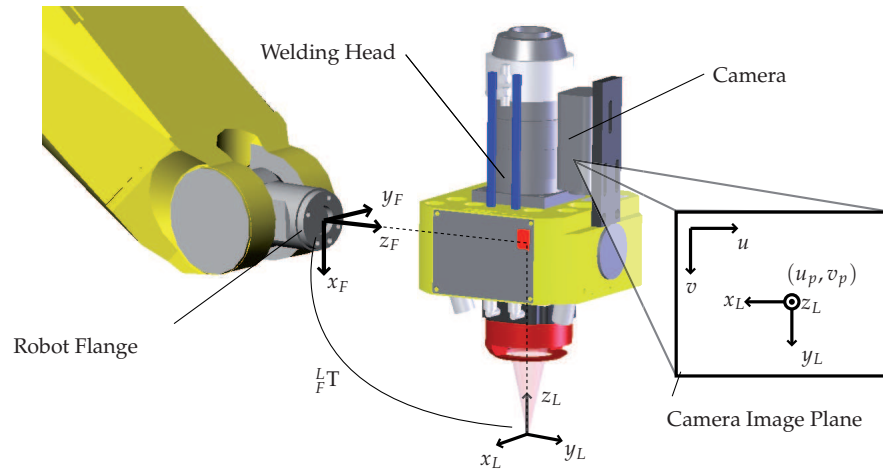
Figure 4.12: The laser tool coordinate systems of the laser welding head in relation to the robot end effector (flange). And the alignment of the image u, v and laser tool x_L, y_L axes when placed in an image plane.

welding head's laser focusing optics. For convenience, a coordinate system $[x_L, y_L, z_L]$ is also attached with its origin on the TCP$_L$. For robotic laser welding the transformation ${}_F^L T$ (Appendix B.2) between the laser tool L coordinate system $[x_L, y_L, z_L]$ and the robot's end effector flange F coordinate system $[x_F, y_F, z_F]$ should be known (Fig.4.12).

Laser tool calibration is the process which determines the transformation ${}_F^L T$. With this calibration the camera image coordinate system is also aligned to the laser tool's one. The relation between the three coordinate systems is shown in Fig.4.12. The completion of the laser tool calibration must ensure the following two statements come true:

- The x_L, y_L axes are aligned with respect to the camera

- The coordinate system of the welding head laser tool has its origin on the laser tool center point TCP$_L$, and the z_L axis coincides with the high power laser optical axis

The first statement ensures that any movements along the principal x_L and y_L axes correspond to equivalent movements along the image u and v axes. Since there is no physical restriction for the initial rotation around z_L, such an alignment provides easiness in the calculation of the displacements in the image.

The second statement ensures that the laser tool x_L, y_L and image u, v planes are parallel and therefore no additional calculations are required to compensate for angles around the principal x_L, y_L axes. Furthermore, since laser welding is performed within the depth of focus of the laser beam, it is common use to place the origin of the laser tool coordinate system on the laser focal point.

For the initiation of the laser tool calibration an initial estimation of the transformation $_F^L T$ is required. This transformation consists of three translations and three rotations that describe the transformation. The translations and rotations are performed on the base coordinate system's principal axes (in this case the flange).

$$_F^L T = [\underbrace{x_{FL},\ y_{FL},\ z_{FL},}_{Translations}\ \underbrace{\varphi_{FL},\ \psi_{FL},\ \omega_{FL}}_{Rotations}] \qquad (4.20)$$

The initial guess of the $_F^L T$ can be derived from the dimensions of the welding head's parts and their properties. For the example of Fig.4.12, the system of $[x_F,y_F,z_F]$ can be approximately translated to the one of $[x_L,y_L,z_L]$ if its origin is displaced along the positive z_F and x_F axes and rotated for 90° around the x_F and -90° around the y_F. The translation along the z_F can be calculated by the size of the welding head and the position of the laser optical axis, whereas the translation along the x_F can be calculated with the help of the position of the laser focus lens in the welding head, and the focus lens focal distance. This would result to:

$$_F^L T = [\ k,\ 0,\ m,\ \frac{\pi}{2},\ -\frac{\pi}{2},\ 0\ ] \qquad (4.21)$$

where k, m are the measured translations along the x_F and z_F. Indicative values of k and m for the three high power laser focal lengths (100 mm, 150 mm and 200 mm) are shown in Table 4.1

Table 4.1: Initial calibration values for k and m.

f [mm]	k [mm]	m [mm]
100	165	115
150	165	155
200	165	215

Further fine tuning of this initial estimation of the ^L_FT is performed by laser tool calibrations. If a conventional, non-automated, calibration procedure is used, all measurements has to be performed manually through a series of tests. To obtain the position of the TCP_L within the required accuracy, a sufficient amount of time must be invested.

The laser tool calibrations which will be described in the following paragraphs, are automated and less time consuming. The initial estimated ^L_FT is refined through an automated series of calibrations towards the exact one. For these calibrations the robot is used as a measuring tool. Work on laser tool calibration with the use of robots has been done by Tienhoven et al. (2005). These procedures are used for the requirements of the integrated laser welding head.

To carry out the calibrations the calibration tool of Fig.4.13 is used. The calibration tool consists of three parts: a mirror, a plate with a bright spot, and a black anodized aluminium plate. The top-side surfaces of these three parts belong to the same plane which will be referred to as *calibration plane*. The purpose of each of these parts will become clear in the following paragraphs.

All calibration calculations are performed according to image data, therefore an alignment of the image and laser tool coordinate systems as well as a relation between pixels in the image and the world dimensions
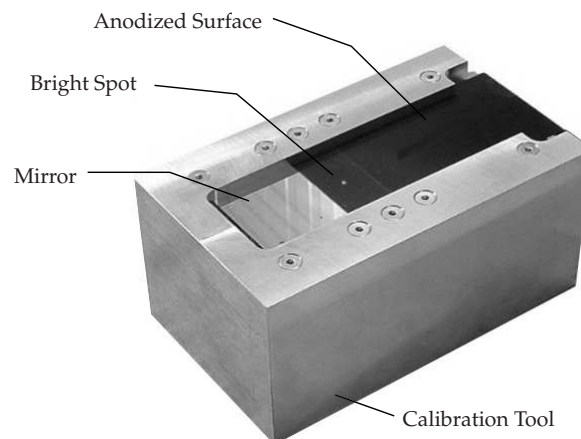
Figure 4.13: The object that is used for the welding head tool and sensor calibrations described in Tienhoven et al. (2005) and De Graaf (2007).

in millimeters must be established. Then the calibrations of the laser tool coordinate system are performed.

4.2.1 Perpendicularity and TCP_L Image Position

Firstly, the optical axis of the high power laser should be perpendicularly to the calibration plane. This process aligns the z_L axis of the laser tool with the normal vector of the calibration plane. After the calibration, any movement along the laser tool x_L and y_L axes will result to a movement parallel to the calibration plane, which is required for the following calibration steps.

The calibration is implemented with the procedure described in Tien-hoven et al. (2005). In short the welding head is placed above the mirror of the calibration object with the pilot laser switched on. Then the welding head performs a number of movements along its z_L axis, and the center of gravity of the reflected spot in the camera image is calculated. If the mirror plane is perpendicular to the z_L, then the center of gravity of the reflected spot will remain constant. If the mirror plane is at an angle, then the center of gravity of the reflected spot will move in the image. The direction and length of the reflected spot's movement are used to calculate and correct misalignment of the mirror's plane normal with respect to the z_L axis.

Once the z-axis is aligned, a new series of movements along the z_L is performed. This time, the size of the reflected spot is measured. Where the spot size is the smallest, the image coordinates $[u, v]$ of the spot center of gravity are defined as u_p and v_p which are laser pilot image focus position.

4.2.2 Image Alignment and Scaling Factor calibration

The purpose of this calibration is the alignment of the laser tool x_L and y_L axes with the camera image coordinates u and v, and to determine the scaling factor c_p of an image pixel size and real world dimensions. The alignment calibration identifies the relation between a movement in x_L, y_L plane and the image of the same movement in u, v plane (Fig.4.12). When both coordinate systems are aligned then $x_L \parallel u$ and $y_L \parallel v$. This alignment allows the direct translation of the image measurement data into measurements of the laser tool coordinate system.

For the alignment calibration, the bright spot of the pinhole of the object of Fig.4.13 is used. First, the welding head is displaced along its z_L axis, which is kept perpendicular to the top surface of the calibration tool,

until the bright spot is in focus. Then the welding head is moved over the light point, in predefined steps that define a rectangular matrix along its x_L and y_L plane. Images of the bright spot are taken at each spot of this matrix pattern in a sequence that is prescribed by the arrows in Fig.4.14(a). When all bright spot pictures are combined, Fig.4.14(a) is obtained, where all the spots are displayed.
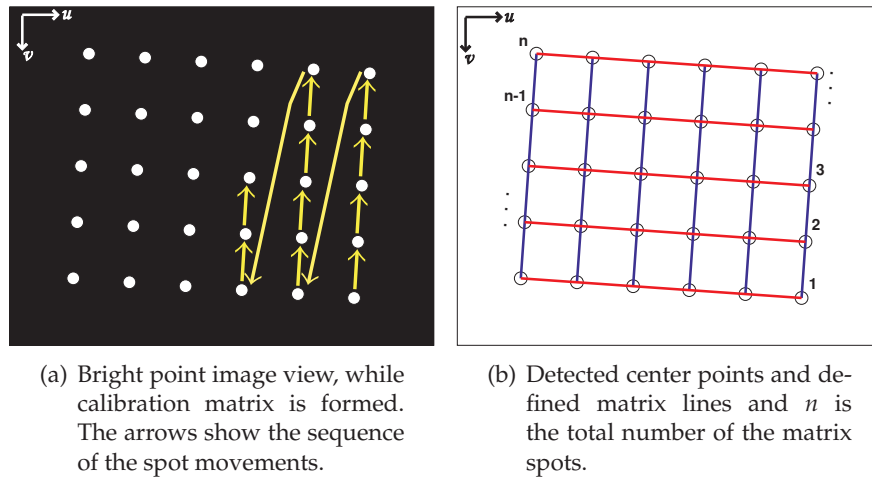

(a) Bright point image view, while calibration matrix is formed. The arrows show the sequence of the spot movements.

(b) Detected center points and defined matrix lines and n is the total number of the matrix spots.

Figure 4.14: The bright spot formed matrix (left), and the calibration results (right).

By detecting the center of gravity $[u_i, v_i]$ of the image matrix spots, lines can be fitted as shown in Fig.4.14(b) (where $i = 1 \ldots n$ is the acceding position of the bright spot in the matrix and n is the total number of the matrix spots). As it is mentioned, the movements of the welding head are performed in the laser tool coordinate system, whereas the positions of the bright spot are measured in the image coordinate system. When the systems are not aligned, an inclination is present at the identified matrix positions (Fig.4.14(b)). The slopes of the parallel lines indicate the existing misalignment.

The calculation of the alignment error can be derived by the slope of the identified matrix lines. Therefore all slopes of the parallel lines in the matrix are averaged, resulting two values a_h and a_v for the average horizontal and vertical matrix line slopes. Since the formed matrix is rectangular $a_h \simeq -1/a_v$. To align the camera coordinate system with the welding head's, the definition of the initial guess of the tool transformation $^L_F T$ has

to be corrected so that the resulting laser tool coordinate systems is rotated around its z_L axis with an angle of $\arctan(a_h)$, or $\arctan(-1/a_v)$.

The scaling factor c_p is calculated from the distances between neighboring image spots (both horizontally and vertically) divided by the accompanying laser tool movements. The c_p represents the number of pixels that is required to image 1 mm of an object. The difference between the scaling factors in the x_L and y_L directions should be minimal since the camera-lens calibration has compensated for possible non squareness of the camera pixels. The c_p and the average of all the scaling factors horizontally $c_{p,h}$ and vertically $c_{p,v}$ is calculated by:

$$c_{p,h} = \sum_{i=1}^{n-m} \frac{\sqrt{(u_{m+i} - u_i)^2 + (v_{m+i} - v_i)^2}}{\sqrt{(x_{L,m+i} - x_{L,i})^2 + (y_{L,m+i} - v_{L,i})^2}}, \tag{4.22}$$

$$c_{p,v} = \sum_{i=1}^{n-1} \frac{\sqrt{(u_{i+1} - u_i)^2 + (v_{i+1} - v_i)^2}}{\sqrt{(x_{L,i+1} - x_{L,i})^2 + (y_{L,i+1} - v_{L,i})^2}}, \tag{4.23}$$

$$c_p = \frac{c_{p,v} + c_{p,h}}{2} \ [pixels/mm], \tag{4.24}$$

where n is the total number of the matrix spots and m is the number of matrix rows, u_i and v_i are the center of gravity image coordinates of bright spot i, $x_{L,i}$ and $y_{L,i}$ are the robot measured real world coordinates of bright spot i.

4.2.3 Laser Tool z_L-axis calibration

After the alignment of the camera image and laser tool coordinate systems §4.2.2, it is important to move the z_L axis to coincide with the high power laser optical axis. Therefore the distance between the high power laser optical axis and the initially estimated z_L has to be identified and minimized.

The position of the high power laser optical axis can be derived by the position of the pilot laser axis which passes though the point $[u_p, v_p]$ in the camera image (Fig.4.12). Since the axis of the pilot laser is coaxial the high power laser z_L axis, it will also pass through the point $[u_p, v_p]$.

The next step is to identify where the position of the origin of the estimated laser z_L axis is in the image plane. For this step the bright spot of the calibration tool is used. With image processing, the center of gravity of the bright spot $[u_s, v_s]$ in the image plane is calculated and the laser tool is displaced along the x_L and y_L until the spot appears in the image plane

(a) Welding head side view.

(b) Camera view of the moving bright spot.
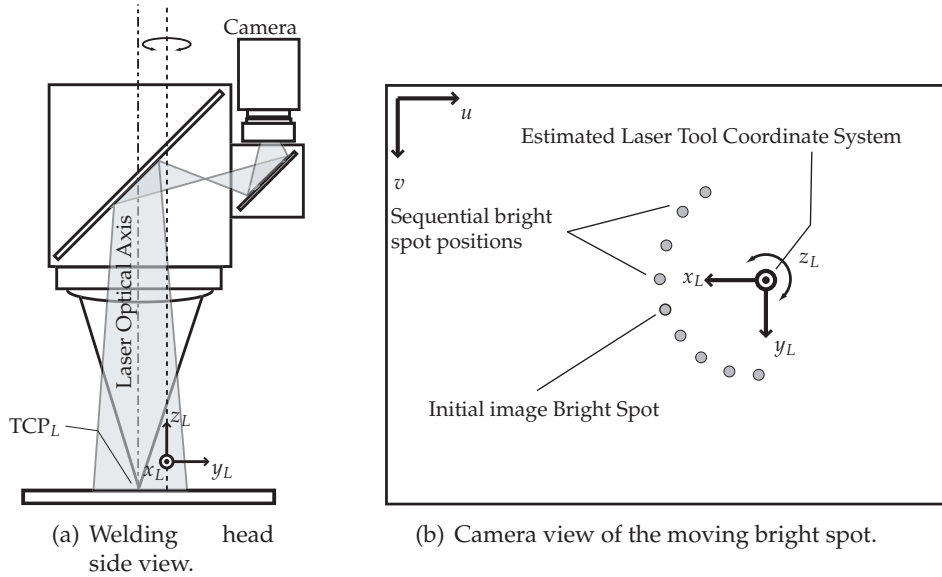
Figure 4.15: Calibration to identify the offset of the laser tool z_L axis towards the laser optical axis.

at the point where the laser optical axis exists. The displacements d_x, d_y along the x_L and y_L are calculated by:

$$d_x = -\frac{(u_s - u_p)}{c_p} \ , \quad d_y = \frac{(v_s - v_p)}{c_p} \tag{4.25}$$

At this point the tool will perform a number of rotations around the initially estimated z_L axis. If the z_L axis coincides with the pilot laser axis, then any rotations around the z_L would not result to any movements of the bright spot on the image plane. In the most common case where the initially estimated z_L axis does not coincide with the one of the pilot laser (Fig.4.15(a)), then any rotations around z_L would result to images like the one of Fig.4.15(b).

A number of rotations are performed around z_L axis and the positions of the pilot spots are recorded. Since the rotations are around the same axis, any present displacement of the spot should form a circle of which the center indicates the position of the laser tool z_L axis in the image. A linear circle fit is applied on the pilot spots for the calculation of the circle center $[u_c, v_c]$.

The calculated offsets $d_{L,x}$ $d_{L,y}$ of the laser tool origin in x_L and y_L origin are then calculated according to:

$$d_{L,x} = \frac{(u_c - u_p)}{c_p} , \quad d_{L,y} = \frac{(v_c - v_p)}{c_p} \tag{4.26}$$

These offset values are used to refine the definition of the $^L_F T$ so that the position of the origin of the laser tool coordinate system is corrected.

4.2.4   TCP$_L$ z_L offset calibration

The purpose of this calibration is to bring the origin of the estimated laser tool coordinate system on the focal point of the high power laser. This process consists of two parts:

1. Correct estimated laser tool origin towards the pilot laser focal point position

2. Identify high power and pilot laser focal point positions offset

z_L offset to pilot laser focus position

In the first part the offset between the estimated TCP$_L$ and the pilot laser focal position is determined. The pilot laser focal point is placed on the bright spot of the calibration tool. A number of rotations around the x_L or y_L are then performed. If the estimated TCP$_L$ coincides with the pilot laser focus position, then there will not be any displacements of the calibration tool bright spot in the camera image. In any other case a movement of the spot will be observed on the image as shown by Fig.4.16.

The rotations around the x_L or y_L axes and the positions of the pilot spots are recorded. Since the rotations are around the same axis, any present displacements of the spot is the result of an offset $d_{L,z}$ along the z_L axis. This offset can be calculated by:

$$d_{L,z} = \frac{d_i}{\sin \alpha} , \tag{4.27}$$

where α is the angle of rotation around x_L or y_L, and d_i is the distance between the initial v_0 and final v_n image positions of the bright spot in mm ($d_i = (v_n - v_0)/c_p$).

(a) Tool initial z coordinate

(b) Camera view of the moving pilot point
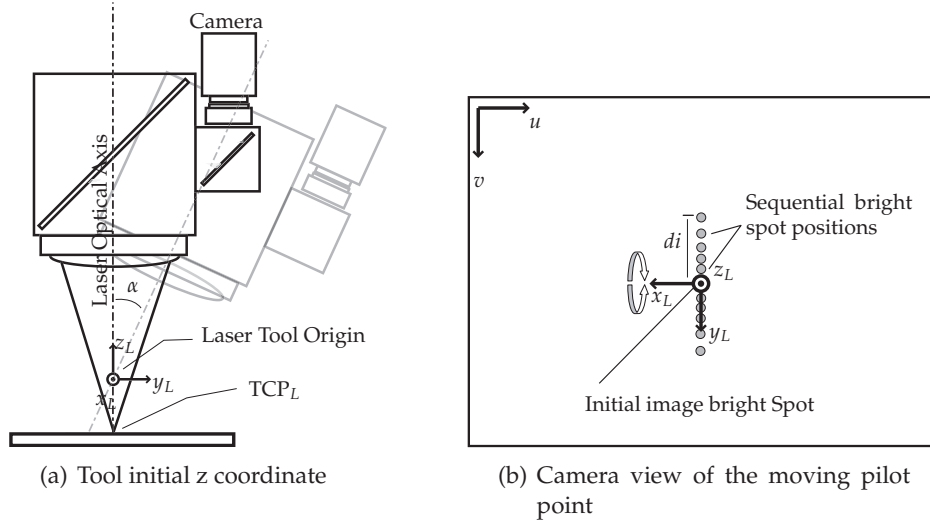
Figure 4.16: Calibration to determine the real z coordinate of the laser tool.

The calculated offset of then used to refine the ^S_LT so that the resulted laser tool origin will be corrected.

High power to pilot laser offset

The second part of the z_L offset calibration involves the accurate identification of the TCP_L position. For this calibration the high power laser is used to create spots on the anodized metal plate of the calibration tool. The TCP_L is placed slightly above the calibration plane and it is moved in constant steps along the z_L axis. At each step a laser pulse is released which created a spot on the anodized aluminium plate. A result of this process is displayed in Fig.4.17.
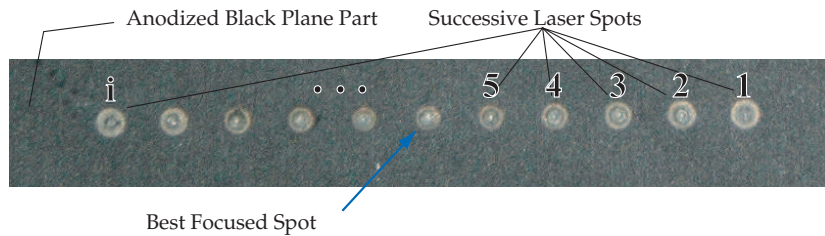
Figure 4.17: On the anodized surface the best focused spot can be determined.

It can be seen that in the beginning of the process the high power laser is out of focus and therefore bigger spots are being created. The spot size is becoming smaller when the high power laser is near its focal distance, and then the spots are getting wide again. After selecting the smallest spot, the final correction of the TCP_L can be calculated by:

$$d_{L,z} = i \cdot z_{L,Step} + z_i, \tag{4.28}$$

where i is the successive position of the spot as shown in Fig.4.17, $z_{L,Step}$ is the step size of the displacement of the TCP_L along the z_L, and z_i is the size of the initial displacement of the TCP_L above the calibration plane.

By correcting the ^L_FT for the high power laser to pilot laser offset, the laser tool calibration is complete. The resulting ^L_FT carries the exact transformation from the robot end effector (flange) to the high power laser focal point coordinate system.

4.2.5   Laser tool calibration experiments

Each of the automated parts of the laser tool calibration are tested to investigate the repeatability of the process. Initially for each of the calibrations steps is repeated several times to obtain the divergence of the process. Then the complete laser tool calibration procedure is performed several times and the resulting ^L_FT parameters are compared. The full camera frame of 1280x1024 pixels is used for the experiments.

Bright spot Center of Gravity

In the first experiment the center of gravity of the calibration tool bright spot's image is calculated. As it is shown in Fig.4.18, the spot's center of gravity position in the image is detected in the same position with subpixel accuracy (669 pixel in u and 546 pixel in v).

Image alignment and scaling factor

In the following experiment the scaling factor c_p as well as the matrix lines image angles for the alignment of the laser tool x_L and y_L with the image u and v is identified. As is shown in Fig.4.19, the angle has initially an offset of 0.25^o. After calibration the matrix maintains a slight orientation of about 0.04^o, which is significantly smaller than the capabilities of the
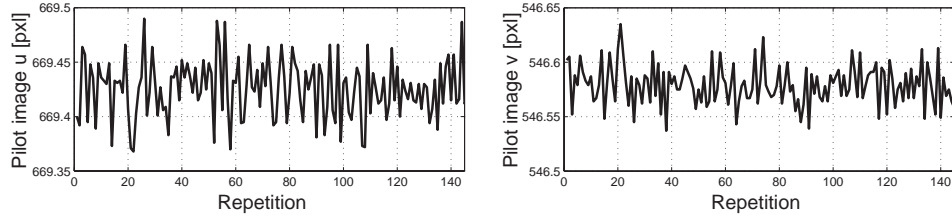
Figure 4.18: The image $[u_p, v_p]$ coordinates of the center of gravity of the bright spot.

handling robot. The scaling factor c_p is also stable at 39.4 pixels/mm (25 μm/pixel). For the calibration results that are illustrated in this paragraph a matrix of 8x7 (columns x rows) was used. The full frame of the camera imaging sensor (1280x1024 pixels) was also used.

Laser Tool z_L-axis calibration

For the laser tool z_L axis calibration, the tool is rotated around its z_L axis. The displacement of the bright spot of the calibration object in the image is used to calculate the offset of the current z_L origin to the real one. In Fig.4.20 is shown that the center of the detected circle stabilizes in the image with an radius accuracy of 4 pixels (approximately 0.1 mm). The total rotation that was implemented for the illustrated results is 32° and was performed in 10 steps.

TCP$_L$ z_L offset calibration

For the TCP$_L$ z_L offset calibration the tool is rotated around its x_L axis and the displacement of the bright spot of the calibration tool is used for the calculation of the z_L offset. For the plots of Fig.4.21 the welding head was rotated for a total of 14° and it was performed in 10 steps. As it is shown in Fig.4.21 the correction in z_L direction of the offset is stable within the margin of about 0.025mm.

Complete laser tool calibrations

For the complete laser tool calibration the calibration procedure was performed in two different locations and tool orientations. Since the robot is used as a measuring instrument for the calibrations it is necessary to
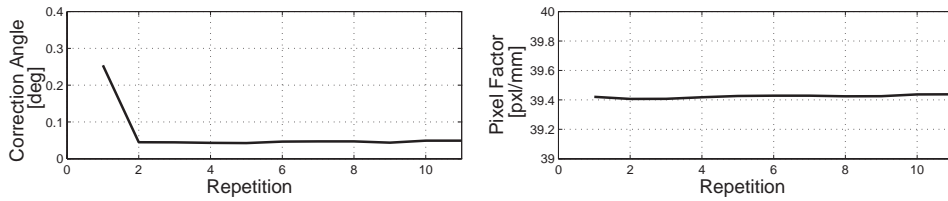
Figure 4.19: (Left) The fluctuation of the angle of the detected matrix lines. (Right) The values of the detected camera scaling factor c_p.
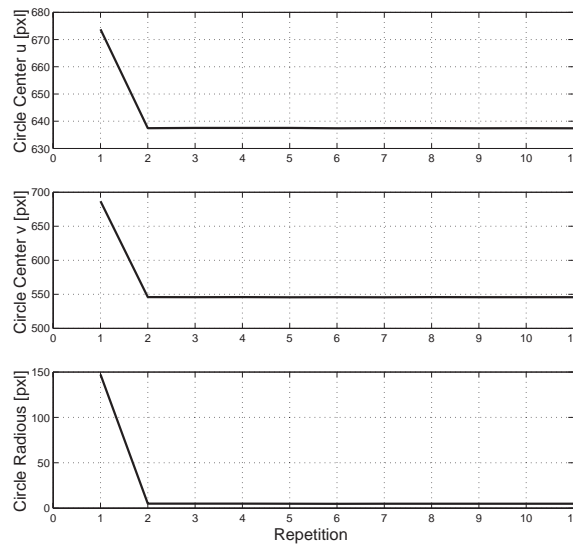
Figure 4.20: The position of the detected image circle center and its radius.
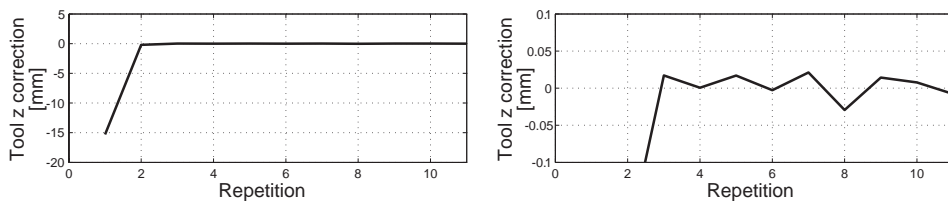
Figure 4.21: (Left)The correction of the laser tool origin along the z_L axis. (Right) A zoomed view of the right plot with y-axis between -0.1 and 0.1 mm.

investigate if different calibration positions/orientations would result to different laser tool transformations $_F^L$T.

At the first calibration position the calibration tool plane is parallel to the x, y plane of the robot base coordinate frame, whereas in the second one the calibration tool plane is rotated 30° in relation to robot base coordinate frame. At each position 10 laser tool calibrations are performed. At the end of each calibration the results of the $_F^L$T parameters are logged. These results are shown in Fig.4.22, where the thick lines are the calibration results where the calibration tool plane was under an angle of 30°.
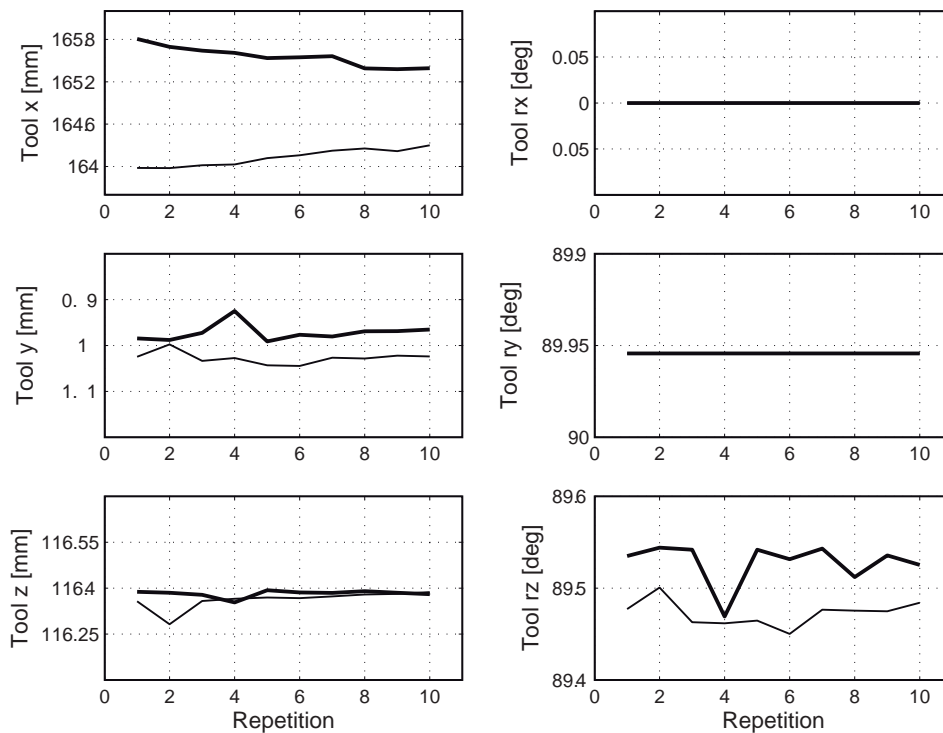
Figure 4.22: Complete laser tool calibrations where the calibration object is places under different angle (thin line for 0°, thick line for 30°). The results for the $_F^L$T transformation from the robot flange to the laser tool TCP$_L$.

As it is shown in Fig.4.22 for both sets of calibrations, the derived tool transformations $_F^L$T are quite constant. Nevertheless, a slight difference is found between calibrations at different positions. This difference depends on the robot positioning data as is shown also in the work of

De Graaf (2007). This is expected, as the kinematic model that the robot controller uses to calculate the tool positions and to move the robot can always slightly vary from the real one. In De Graaf (2007) is stated that: *"An accurate tool transformation can not be found due to the geometric errors that are present in the (Robot-Sensor) system. These errors are due to the fact that the robot geometric models do not correctly represent the actual robot geometry and thus influence the Laser Tool and Sensor calibration."*.

4.3 Sensor Tool Calibration

The sensor tool calibration is performed to determine the sensor setup parameters (structured light diodes projections angles, reference lines/planes, etc), and to establish the relation between the sensor tool center point TCP_S and the TCP_L.

The TCP_S is the reference point in relation to which seam position measurements are performed. The position of the TCP_S depends on the triangulation sensor's configuration (line, cross, triangle). Similarly to the laser tool calibration, the origin of the sensor tool coordinate system with axes $[x_S, y_S, z_S]$ is also placed on the TCP_S. This coordinate system has the same orientation as the laser tool coordinate system. If the TCP_S is not defined then it is placed initially on the TCP_L. The identification of the transformation between the sensor and the laser tool coordinate systems (e.g. Fig.4.25), enables the welding head to identify a seam point with the sensor and reach it accurately with the TCP_L .

The sensor tool calibrations consist of two steps:

1. Structured light diodes projection angles estimation

2. Sensor reference line/plane and TCP_S calibration

4.3.1 Structured light diodes projection angle estimation

This calibration leads to the calculation of the structured projection angle ϕ that is defined in §2.2.1. Initially, the welding head is placed over the anodized part of the calibration object. Since the laser tool calibration has been completed, the sensor z_S axis can be positioned perpendicularly to the anodized surface with the TCP_S on the calibration plane (§ 4.2). From this point, the calibration procedure for the projection angle of the structured light diode can take place. The process is repeated for each of the three structured light diodes.
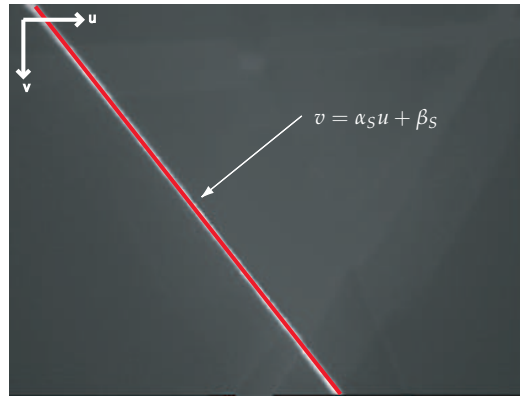
Figure 4.23: Fitted line on the structured light line projection in the camera image.
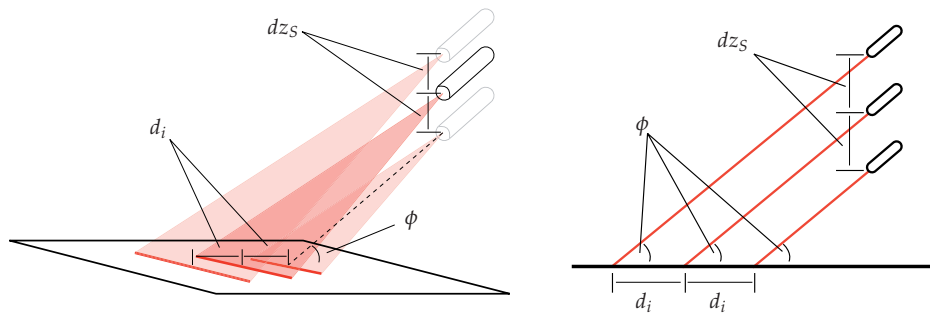
Figure 4.24: Displacement of projected line on the calibration plane, due to displacement steps of the sensor along its z_S axis.

When one of the diodes is switched on, a laser line is projected on the calibration plane. A least square line fitting is performed on the image pixels that belong to the projected line (Fig.4.23), and the equation of the fitted line in the image is derived as

$$v = \alpha_S u + \beta_S, \tag{4.29}$$

where α_S is the slope of the fitted line and β_S is its offset.

A series of displacements dz_S take place along the z_S axis of the sensor tool. This will result in a parallel displacement of the projected lines in the image (Fig.4.24). The line fitting process on the displaced line projection will result in the identification of lines that have the same slope α_S but different offset β_S changed by $d\beta_S$.

The distance d_i between two parallel lines is given by:

$$d_i = d\beta_S \cdot \sin(\frac{\pi}{2} - \arctan(\alpha_S)) \tag{4.30}$$

Then the resulting angle ϕ for the current displacement is given by:

$$\phi = \arctan(\frac{d_i}{dz_S}), \tag{4.31}$$

whereas the final value of the diode's projection angle is derived by averaging the various calculated angle values from each displacement.

4.3.2 Sensor reference line/plane and TCP$_S$ calibration

All optical triangulation sensor measurements for the workpiece orientations and positions are calculated as offsets from a reference. This reference can be a line or a plane. The type of reference (line or plane), which is used for the derivation of the sensor measurements, depends on the structured light shape of the optical triangulation sensor. The reference line is used for the single structured line sensor, whereas the reference plane is used for multiline structured line sensors (cross, triangle).

The TCP$_S$ and thus the sensor coordinate system exist on the reference line or plane. As is mentioned in the introduction of §4.3, the sensor coordinate system is aligned with the coordinate system of laser tool, and the estimated TCP$_S$ exists on the TCP$_L$. The TCP$_S$ is the reference point in relation to which the detected seam position offsets are calculated. The calibration and definition of each of the calibration lines and planes as well as the TCP$_S$ are presented in the following paragraphs.

Reference line

For the calibration of the reference line, the welding head is placed over the anodized part of the calibration object. The z_L axis of the laser tool is perpendicular to the calibration plane with the TCP$_L$ positioned on the calibration plane. At this position each of the structured light diodes is successively switched on and their image is captured by the camera. These lines are defined as the reference lines for each of the structured light diodes (Fig.4.25). The parameters α_S and β_S for each of the imaged lines are once more identified by a linear fit of the image line pixels. An index from 1 to 3 is appointed to each of the line parameters ($\alpha_{S,1}$ $\beta_{S,1}$, $\alpha_{S,2}$ $\beta_{S,2}$, $\alpha_{S,3}$ $\beta_{S,3}$)
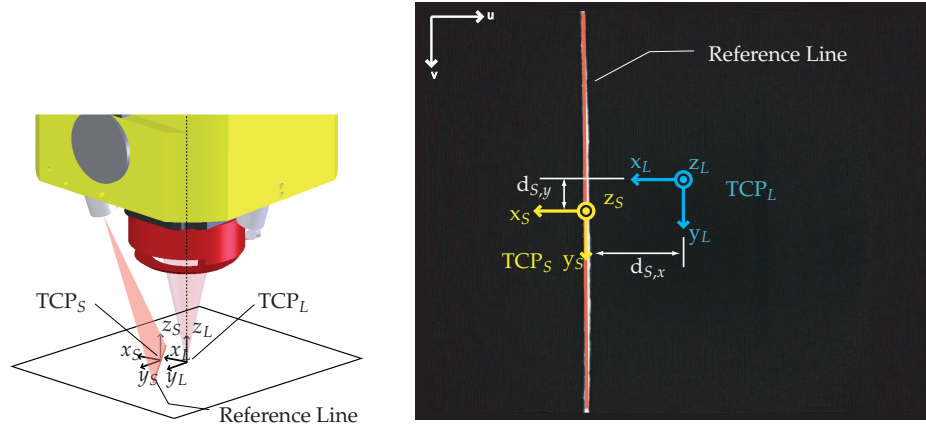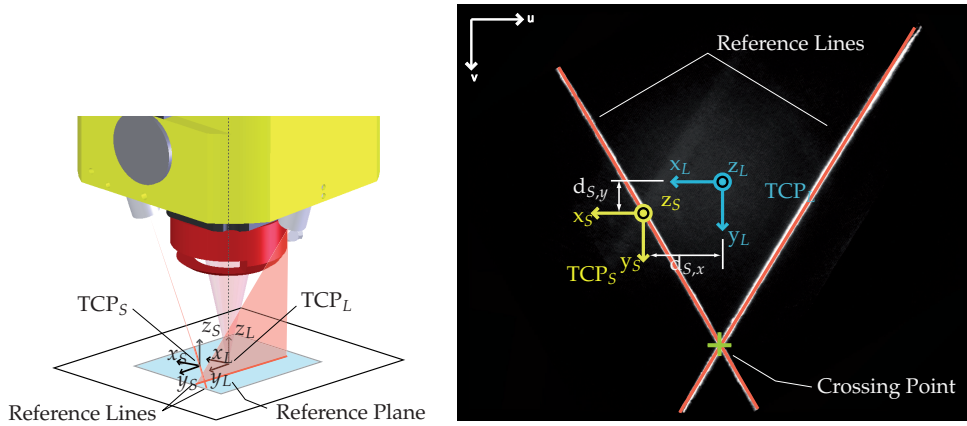
Figure 4.25: The single line sensor Reference Line, TCP_S, and sensor coordinate system in relation to the welding head and the camera image.

to distinguish between the three reference lines of the integrated welding head.

For a single structured line sensor the TCP_S is placed in the middle of the reference line in the image. This is convenient as the sensor will try to keep the detected seam within the central area of it field of view (Fig.4.25). By placing the TCP_S in the middle of the reference line the definition of the sensor tool can be completed.

Since the initial TCP_S was placed on the TCP_L and the sensor coordinate system is aligned to the one of the laser tool, it is possible to calculate the position of the final TCP_S by their offset on the camera image. The offsets $d_{S,x}$ and $d_{S,y}$ for the $[u, v]$ coordinates of the image is calculated by:

$$d_{S,x} = \frac{u_{x_L} - u_{x_S}}{c_p},$$

$$d_{S,y} = \frac{v_{y_L} - v_{y_S}}{c_p}. \tag{4.32}$$

Then the transformation $_L^S T$ from the laser tool coordinate system to the sensor tool one is defined as:

$$_L^S T = [d_{S,x}, d_{S,y}, 0, 0, 0, 0] \tag{4.33}$$

Reference plane

The reference plane for the cross or the triangular structured light shape is the plane that is defined by the reference lines that form the cross or the triangular shape. Three points A, B and C on the reference lines are sufficient to define a plane as was shown by Eq.2.7 (page 30):

$$D_{X,Ref}x + D_{Y,Ref}y + D_{Z,Ref}z - D_{Ref} = 0$$

where the determinants are defined as:

$$
D_{X,Ref} = \begin{vmatrix} 1 & y_A & z_A \\ 1 & y_B & z_B \\ 1 & y_C & z_C \end{vmatrix}, \quad
D_{Y,Ref} = \begin{vmatrix} x_A & 1 & z_A \\ x_B & 1 & z_B \\ x_C & 1 & z_C \end{vmatrix},
$$

$$
D_{Z,Ref} = \begin{vmatrix} x_A & y_A & 1 \\ x_B & y_B & 1 \\ x_C & y_C & 1 \end{vmatrix}, \quad
D_{Ref} = \begin{vmatrix} x_A & y_A & z_A \\ x_B & y_B & z_B \\ x_C & y_C & z_C \end{vmatrix}. \tag{4.34}
$$

The normal vector of the reference plane is defined as:

$$
\mathbf{n}_{Ref} = \begin{bmatrix} D_{X,Ref} \\ D_{Y,Ref} \\ D_{Z,Ref} \end{bmatrix}. \tag{4.35}
$$

In the case of the cross sensor these three points are the crossing points of the two reference structured lines and one point along each of the two lines. In the case of the triangular shape sensor, the three points are the corners of the structured light triangle.

As was shown in §2.2.1 the sensor reference plane is used for the calculation of the relative orientations of a measured plane. Any user defined plane can be set as a sensor reference plane.

The definition of the TCP_S for these two cases is different.

Cross shape

For the cross shape structured light sensor the TCP_S is placed in the middle of the reference line in the image that exists in the positive x_L direction of the laser tool coordinate system (Fig.4.26). The calculation of the offsets $d_{S,x}$ and $d_{S,y}$ of the TCP_S to the TCP_L, and the transformation ${}_L^S T$ are calculated with the use of Eq.4.32 and Eq.4.33.

Figure 4.26: The cross sensor Reference Plane, TCP_S, and sensor coordinate system in relation to the welding head and the camera image.

Triangle shape

For the triangular shape structured light sensor, the definition of the TCP_S is defined differently. The triangular sensor allows the detection of the seam with any side of the triangular shape. Therefore, the TCP_S of the sensor can not be fixed on one of the triangle's side.

As TCP_S of the triangular shape is selected the *incenter* of the triangular shape. The incenter is the point of concurrence of the triangle's angle bisectors (Fig.4.27(a)). The incenter of a triangle has the same distance from all of the triangle's sides.

Also for the triangle shape, the calculation of the offsets $d_{S,x}$ and $d_{S,y}$ of the TCP_S to the TCP_L, and the transformation $_L^S T$ are calculated with the use of Eq.4.32 and Eq.4.33.

4.3.3 Sensor tool calibration experiments

The sensor tool calibration experiments are performed to establish the repeatability of the sensor calibrations. Similar to the laser tool calibrations the position and the orientation of the tool during the calibration is expected to affect the final calibration results. Nevertheless, for a fixed position and orientation the calibration results should remain constant.

For this experiment the calibration tool plane was placed under three different orientations (0°, 15° and 30°) in relation to the x-axis of robot base
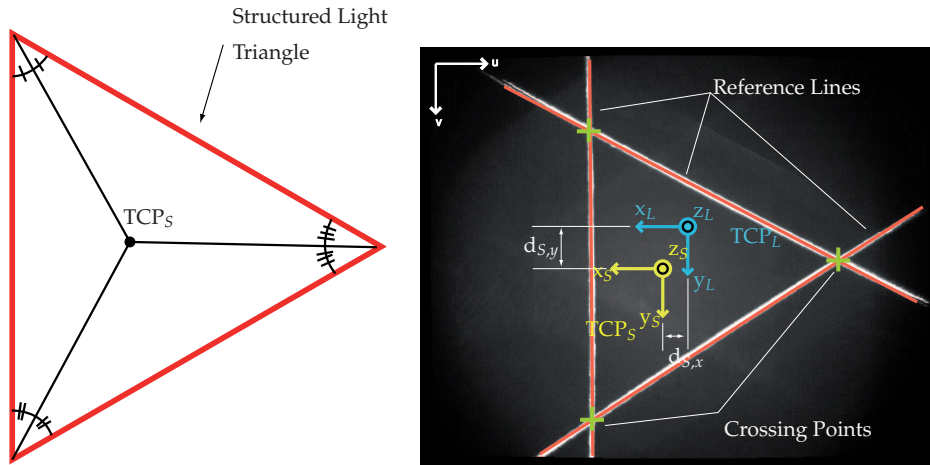
Figure 4.27: (Left) The structured light triangle and the position of the incenter *where the TCP$_S$ is placed. The triangle sensor coordinate system TCP$_S$ in relation to the TCP$_L$ in the camera image.*

coordinate frame. The integrated head was then placed perpendicular towards the calibration plane with the TCL$_L$ existing on its surface. At each orientation the sensor calibration procedure was repeated 10 times and parameters of each of the projected structured light diodes and lines were logged.

In Fig.4.28 the calculated projection angles of the structured light diodes as well as the line parameters of the projected image reference lines are shown. As it is expected, the position and orientation under which the calibration takes place influences the calibration result. Nevertheless, for each of the orientations separately the calibration results are constant.

The position of the calculated sensor TCP$_S$ for each of the diodes and the triangular shape are shown in Fig.4.29. From these plots it can be derived that the position of the sensor TCP$_S$ remains constant for the calibrations conducted under the same orientation. Therefore also the transformation $_L^S T$ from the sensor tool to the laser tool is also constant.

4.3.4   General conclusions

As shown in this chapter all optical and geometric parameters have been calibrated well within the specified accuracy. The full calibration of the integrated laser welding head is an elaborate job, and therefore GUI's were
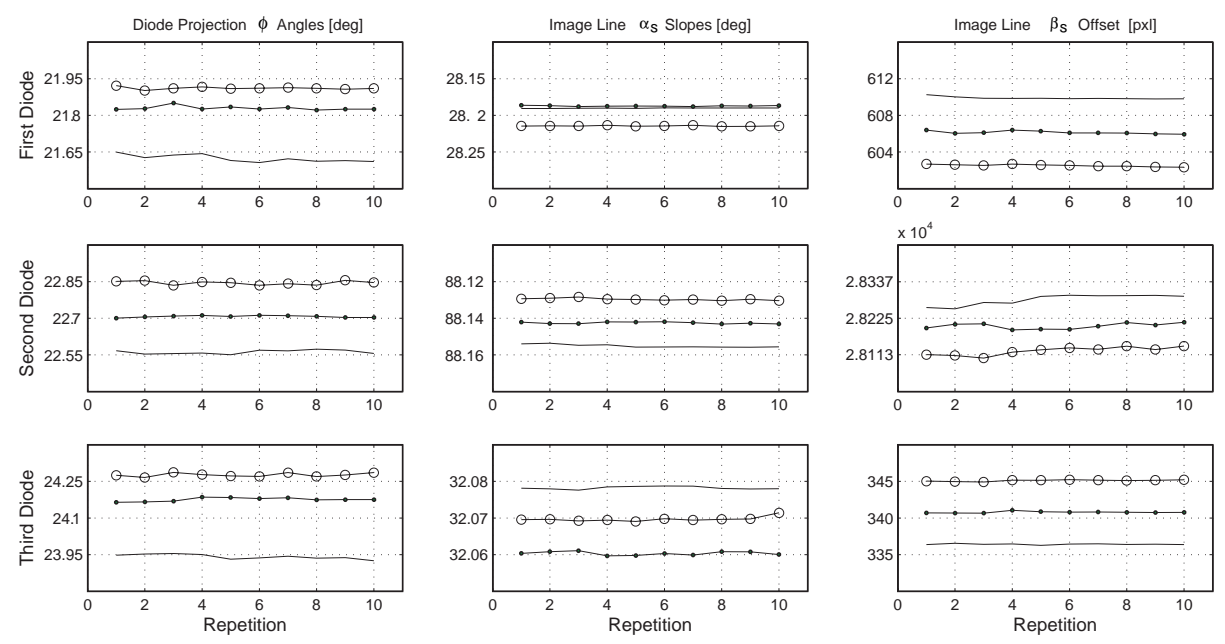
Figure 4.28: Sensor tool calibration results for different orientations. '-' for 0º, '.-' for 15º and 'o-' for 30º.

Figure 4.29: Sensor tool TCP$_S$ calibration results for different orientations. '-' for 0°, '.-' for 15° and 'o-' for 30°.

developed to automate and speed up the process. For the lens and camera calibration a toolbox is implemented in Matlab (see Appendix E.3), which performs all the necessary calculations. The result of the lens and camera calibration toolbox is a file containing the calibration parameters for the image undistortion. The toolbox allows the user to implement these calibrations in less than 20 min, depending on the number of calibration images that are used. The laser tool point and sensor calibrations are also automated. The calibration procedures are performed by IntegLas (see Appendix E.1). These calibrations require about 10 min to be completed, resulting in the positions and orientations of the TCP$_L$ and TCP$_S$.

Chapter 5

Seam Detection

By seam detection the position of a seam is identified in the sensor's coordinate frame. The integrated laser welding head is equipped with the three triangulation sensor configurations that are described in §2.2.1 (line, cross, triangle). Each of these three configurations provides a variety of information about the seam and the workpiece, and the selection of the one that is used depends on the required speed of the process and the type of seam trajectory.

In this chapter three topics will be addressed. The first topic handles the use of seam detection in robotic laser welding applications. The second topic elaborates on the manner by which the sensor's measurement data is derived from the camera images for each of the integrated laser welding head seam sensor configurations. The last topic contains experimental results to identify the measuring capabilities of the developed sensors.

5.1 Seam Detection Sensor and Robotized Laser Welding

Seam detection can be used in robotized laser welding as well for Seam Teaching as for Seam Tracking. In Seam Teaching the position of a known or unknown seam trajectory is measured and stored for further processing, whereas in Seam Tracking the current measured position is compared to a predefined seam path in real-time to correct any deviations from that path.

Seam teaching is performed by point-to-point measurements. Therefore the sensor takes a measurement of a seam point, then it is moved to another point over the seam, where a second measurement is taken and

so forth. This process is repeated until enough points are measured to identify the seam trajectory. In an automated Seam Teaching process the sensor moves from one point to the next in steps of equal distance along its x_S axis. To ensure that the seam is always in the field of view of the sensor, the measured points are extrapolated to adjust the movement direction and the sensor's orientation (Fig.5.1). This is implemented with the use of teaching algorithms like Tractrix (Nayak and Ray (1993)) and Polyfit (De Graaf (2007)). The sensor speed can be chosen arbitrary as Seam Teaching is done separately from the welding task which is performed at a prescribed welding speed. On the contrary, Seam Tracking is performed in real-time which sets the requirements for the minimum sensor measuring time. For instance, if the seam is welded and followed with a speed of 100 mm/s then the sensor must produce measurements with at least a frequency of 100 Hz to assure a maximum distance of 1 mm between successive measurements.
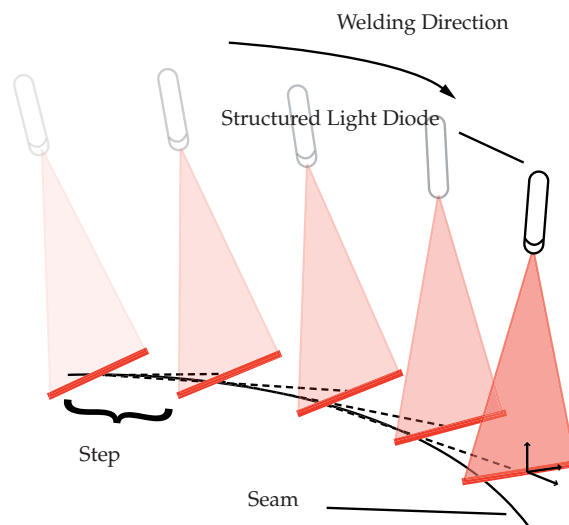
Figure 5.1: The Seam Teaching process when being performed with a Single Line sensor. Extrapolation of the measured points reveal the direction at which the next teaching step will be implemented as well as the required orientation of the sensor.

To detect a seam the optical triangulation sensor of the integrated welding makes use of the shape changes that occur on the intersection between the structured light and the workpiece planes (§2.2.1). It is easily

(a) Overlap Joint.   (b) Corner Joint.   (c) Rounded Corner.
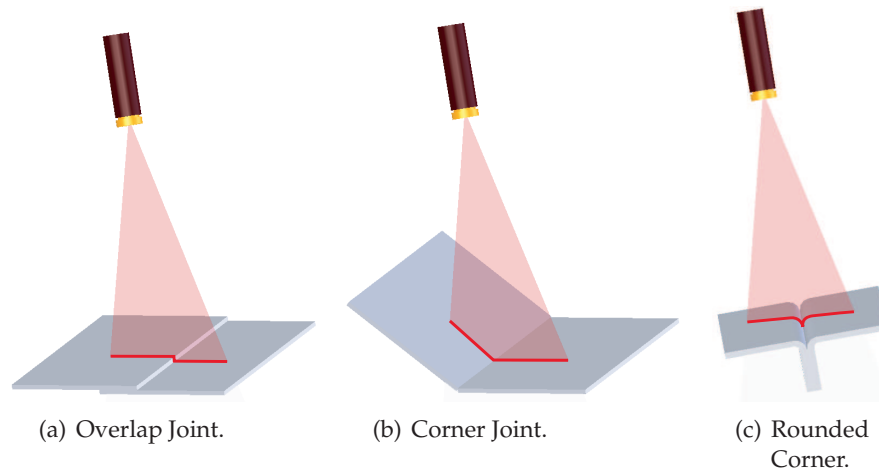
Figure 5.2: Different joint types result to a different changes along the intersection line between the structured light and workpiece planes. In the illustrated examples the intersection line shape changes to: (a) two parallel line pieces, (b) two line pieces forming a wide angle and (c) two linear pieces, each with a rounded corner.

understood that the shape of the intersection will vary according to the underlying joint configuration on the workpiece. As shown in Fig.5.2, where a single structured light line is used, the joint configurations influences significantly the shape of the intersection line.

The detection of the changes in the structured light intersection shape is performed with the use of a camera and image processing algorithms. For different types of intersection shapes (e.g. Fig.5.2), different seam detection image processing algorithms must be used to acquire the measurement data. As explained in §2.2.1 the ability of the sensor to measure some or all of the six parameters (3 positions and 3 orientations) of the position of the workpiece depends on the sensor's structured light shape.

The implementation of these seam detection sensor configurations is divided in two operating modes: Full Shape and Switching Lines. An overview of these two modes is shown in Table 5.1.

The Full Shape Mode contains three seam detection sensor configurations (Single Line, Crossing Lines, Triangular). For each of these sensor configurations, one, two or three structured light lines are projected constantly on the workpiece (forming a line, cross or triangle). The Switching Lines Mode contains only two configurations of sensors (Crossing Lines,

Triangular). Unlike the Full Shape Mode, the Switching Lines allows only one of the structured light lines to be projected at each camera image capture. This means that two (for Crossing Lines) or three (for Triangular) consecutive image captures are are necessary to obtain the sensor measurements.

The difference between the sensor configurations exist in the number of measurement data (3D position measurements and rotations) that they can deliver as well as their orientation dependency (Table 5.1). The orientation dependency refers to the sensor requirement to maintain a certain orientation relative to the seam trajectory in order to be able to take measurements. Perimetric sensors like the one of the Triangular configuration are not restricted by the orientation of the seam trajectory. For the Crossing Lines sensor, the ω_S rotation can only be obtained if the seam crosses both structured light lines. If the seam crosses only one line, then ω_S can be calculated by the seam teaching algorithm by combining consecutive measurements.

Throughout this chapter the overlap joint configuration will be used as an example.

Table 5.1: Seam Detection sensor operation Modes and configurations.

Operation Mode	Sensor Configuration	No$^\sharp$ Data	Orientation Dependent
Full Shape	Single Line	3pos 1rot	Yes
	Crossing Lines	3pos 3rot	Yes
	Triangular	3pos 3rot	No
Switching Lines	Crossing Lines	3pos 3rot	Yes
	Triangular	3pos 3rot	No

pos = Positions $[x_S\ y_S\ z_S]$,   **rot** = Rotations $[\varphi_S\ \psi_S\ \omega_S]$

5.2 Full Shape Mode

As mentioned in the previous paragraph, in the Full Shape Mode a structured light pattern is constantly projected on the workpiece. The shape of the pattern depends on the selected mode that the welding head sensor is operating in. When the sensor functions in Single Line sensor configura-

tion, only one of the diodes is constantly emitting light (Fig.5.3 (a), (b) and (c)). Whereas when the selected sensor configuration is either Crossing Lines or Triangular, two (Fig.5.3 (d), (e) and (f)) or three laser diodes are continuously emitting light to form a triangle (Fig.5.3 (g)). In this module there is no synchronization between the camera and the diodes.

5.2.1 Single Line Sensor

In the Single Line sensor configuration, only one line is projected on the seam. The single line sensor detects the position of the seam where it crosses the structured light line in the sensor's coordinate frame $[x_S\ y_S\ z_S]$ (as long as it exists within the sensor's field of view) and the rotation angle φ_S of the workpiece around the sensor's x_S axis (as shown in Fig.2.9 on page 27).

The detection example for the overlap joint is performed by the following steps which are also illustrated in Fig.5.4 (page 108).

The first step is to ensure that only the desired illumination wavelength reaches the camera imaging sensor, and minimize the influence of other illumination sources that might exist near the sensor. For this reason in the optical path of the camera filters (§3.2.3) allow only light with the wavelength of the laser diodes to reach the camera. Additionally, the radial distortions on the camera image by the high power laser focus lens are also corrected. The result of this step is shown in Fig.5.4(a).

The second step is to eliminate any noise that is present in the image, usually in the form of low intensity image areas. This noise can originate from the structured light diodes themselves or even from nearby light sources of the same wavelength. This filtering is performed by a threshold operation that allows only high intensity image areas to appear in the image. A threshold algorithm is applied on the image pixels p according to:

$$p_{u,v} = \begin{cases} 0, & p_{u,v} < T \\ 1, & p_{u,v} \geq T \end{cases}, \tag{5.1}$$

where u and v are the column and row coordinates of the pixel p in the image and T is the selected threshold value.

The pixels with higher intensity than the threshold value are set to 1 whereas everything else is set to 0. This way the grayscale camera image is also converted in to binary (Fig.5.4(b)). The threshold value can be selected

(a) 1st diode forms a line.

(b) 2nd diode forms a line.

(c) 3rd diode forms a line.

(d) 1st and 2nd diodes form the cross.

(e) 2nd and 3rd diodes form the cross.

(f) 3rd and 1st diodes form the cross.

(g) All three diodes form the triangle.
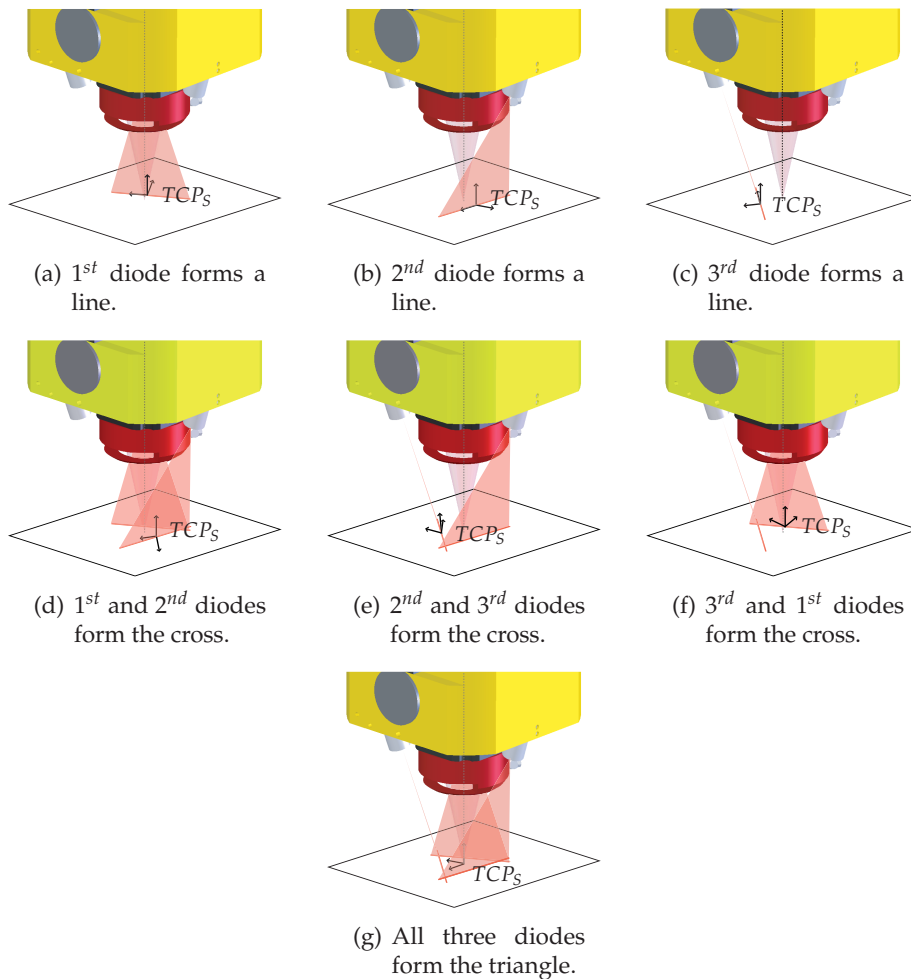
Figure 5.3: The structured light Full Shape Mode possibilities of the integrated laser welding head. (a), (b) and (c) are the single line sensor options . (d), (e) and (f) are the crossing lines sensor combinations. (g) is the triangular structured light projection. (Due to view angle of the illustration the third diode's projection plane is difficult to see).

manually between 0 and 255 by or with adaptive threshold techniques where the optimum value is calculated autonomously (Chan et al. (1998), Savakis (1998), Otsu (1979), Guo and Pandit (1998), etc.). The structured light diodes used for the welding head, have a well focussed beam profile and illumination power. Therefore a manual selection of the threshold level is adequate for the seam detection sensor.

The third step is to eliminate image noise that has high illumination intensity (set to 1 in the binary image). Such noise can originate from reflections on the dichroic minors and beam splitters in the cameras optical path. This noise appears as low intensity ghost images of the original structured light line and can easily be removed after being detected by their size and position in the image. This is performed with the use of object labeling algorithms. The labeling function identifies all separate objects that exist in the image (Fig.5.4(c)). For each of the labeled objects a number of parameters are returned that describe it (area size, bounding box, height, width, center of gravity, orientation, etc). Objects with small area size are excluded as noise. Such labeling functions are described in books like Russ (2002) and Van der Heijden (1994) as well as in papers like Suzuki et al. (2003). The two labels with the largest areas correspond to the two parts of the structured laser light.

The fourth step is to identify the line that corresponds to each labeled object. For each labeled object separately, a linear least square fit is performed on all of the object's pixels, to obtain the best straight line fit $u = \alpha v + \beta$. The fit is performed according to:

$$\alpha = \frac{\sum_{i=1}^{n} v_i \sum_{i=1}^{n} u_i^2 - \sum_{i=1}^{n} u_i \sum_{i=1}^{n} u_i v_i}{n \sum_{i=1}^{n} v_i^2 - (\sum_{i=1}^{n} v_i)^2} \quad , \tag{5.2}$$

$$\beta = \frac{n \sum_{i=1}^{n} u_i v_i - \sum_{i=1}^{n} u_i \sum_{i=1}^{n} v_i}{n \sum_{i=1}^{n} v_i^2 - (\sum_{i=1}^{n} v_i)^2} \quad , \tag{5.3}$$

where α and β are the identified line parameters, n is the total number of pixels belonging to the object, u_i and v_i are the column and row coordinates of an object's pixel.

Once the line parameters of the image objects have been identified, the seam points can also be determined. The seam points are the end points of the image objects. Their position in the image exists on the pixel on the edge of the labeled object whose image coordinates satisfy the identified object's line equation. For example in Fig.5.4(d), for the top image line

(a) First Step: Original camera image optically filtered.

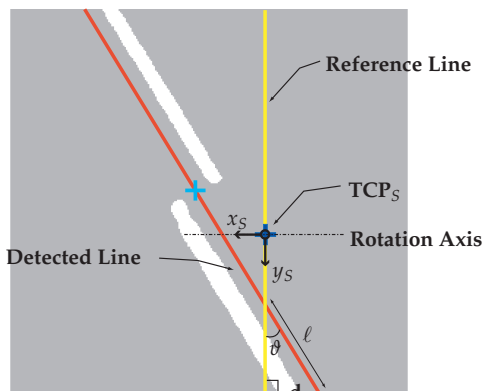(b) Second Step: Thresholded and filtered.
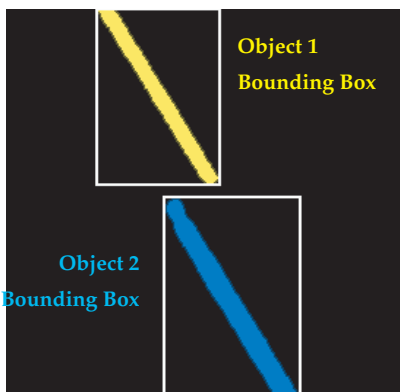
(c) Third Step: Labeled.
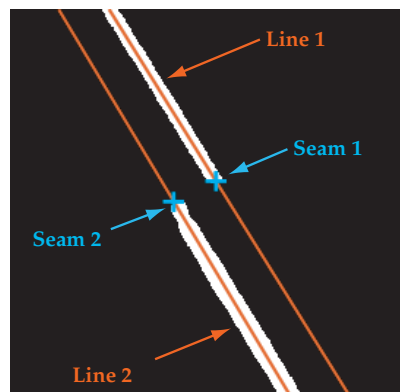
(d) Fourth Step: Identification of line parts and seam positions.
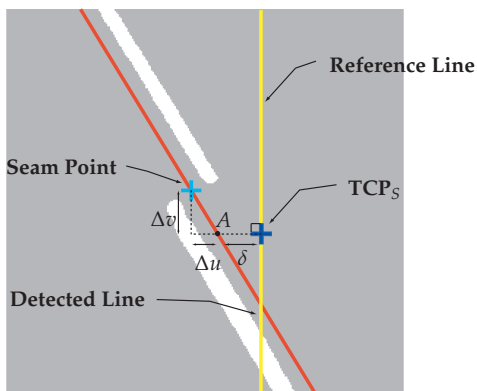
(e) Fifth Step: Calculation of seam position.

(f) Sixth Step: Calculation of workpiece rotation around x_S.

Figure 5.4: Steps followed for the identification of the line parts in the image for the derivation of the sensor's measurements.

object, Line 1 has been identified. Seam 1 is the point on the edge of the object that verifies the equation for Line 1. For the overlap joint, the seam is identified from the apparent breaking of the projected structured line image in two parts.

For the calculation of the seam point's position and the workpiece's orientation the average of Seam 1 and Seam 2 point positions as well as the average of the detected lines slope are used, as illustrated in Fig.5.4(e). By correlating the measured values of the line and the seam with the calibration data of the structured light line and the TCP_S the following calculations can be made for the seam point's position and workpiece orientation.

The position measurements deliver the required displacements in order for the supplied seam point's position to be translated to the TCP_S origin. From Fig.5.4(e) it can be derived that the required translation can be calculated from the following:

$$x_S = \frac{\Delta u}{c_p} \; , \;\; y_S = \frac{\Delta v}{c_p} \; , \;\; z_S = \frac{\delta * \tan(\phi)}{c_p} \; , \tag{5.4}$$

where $[x_S, y_S, z_S]$ are the measured translations in the sensor coordinate frame, c_p is the pixel-to-mm ratio as is defined in §4.2.2, Δv and Δu are the measured distances between the seam point and point A, in image pixels, along image row and columns, δ is the distance in pixels between the TCP_S and the point A (point where a perpendicular line to the reference line that passes from TCP_S crosses the detected line) and ϕ is the projection angle of structured light diode that is used.

The measured angle φ_S around the sensor's x_s-axis can be calculated according to Eq.2.3 in page 28. From Fig.5.4(f) it follows that:

$$d = \ell \tan \vartheta \; , \;\; z = \frac{d}{\tan \phi} \;\; \Rightarrow \;\; z = \ell \, \frac{\tan \vartheta}{\tan \phi} \tag{5.5}$$

$$\varphi_S = \arctan\left(\frac{z}{\ell}\right) = \arctan\left(\frac{\tan \vartheta}{\tan \phi}\right) \tag{5.6}$$
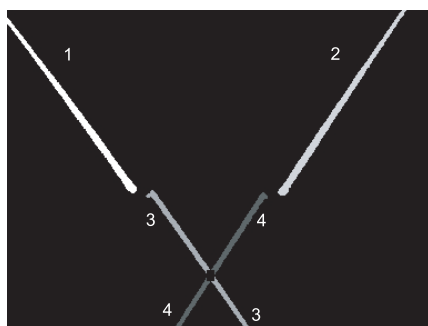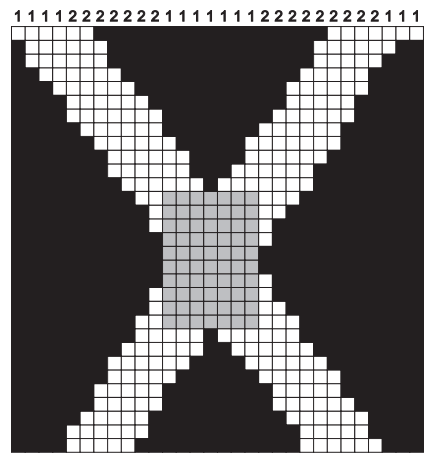
This process runs at a frequency of about 27 Hz. This is because the camera captures full frames and this is the maximum speed that it can reach. Selecting to capture regions of interest (ROIs) of the camera's imaging sensor significantly increases the process speed. ROIs are used to capture only the part of the image that contains useful data thus reducing

capturing time and amount of data. Careful selection of a ROI can increase the speed up to 12 times. Further process time optimizations can be achieved with optimizing the image processing algorithms.

5.2.2 Crossing Lines Sensor

In the case of the Crossing Lines sensor configuration additional steps are taken for the identification of the projected structured lines. Before any line fitting algorithms are applied on the image pixels, the separation of the lines that form the cross has to take place.

As in the Single Line sensor, also in the Crossing Lines one, the original image (Fig.5.5(a)) has to be filtered and converted into binary (Fig.5.5(b)). A labeling operation is then performed on the image to identify the existing image objects. The outcome of such an operation results in up to three identified objects, when the seam crosses both structured light lines Fig.5.5(c).

Each labeled object is then scanned twice, once along its rows and once along its columns. At each row and column the number of transitions from white areas to black are counted. For objects with only a line like the first and third ones of Fig.5.5(c) each row or column will contain only one transition from white areas to black. For the cross object there will be at least two such transitions in some part of the image. A zoomed in version of the cross object is given in Fig.5.5(d) as an example to illustrate the number of transitions along each of the rows and columns. At the regions where only one such transition exist at every row and column, it is concluded that only one line is present. At regions where the cross is present, there will be difference in the number of white-black transitions. As illustrated in Fig.5.5(d) the cross point exists at the place were both the rows and the columns score 1 transition after having scored 2 transitions.

By erasing the crossing point (gray area in Fig.5.5(d)) the cross is further separated into four linear pieces. These pieces are labeled, and grouped according to the original line that they belong. The final labeled result of the image after removing the cross point is illustrated in Fig.5.5(e). For each of the final labeled objects a linear fit is performed, similar to the one of the Single Line mode, as well as the detection of the seam points, which results to Fig.5.5(f). In addition to these operations the cross point in the image is also calculated, which is the junction of the identified line equations that form the cross.

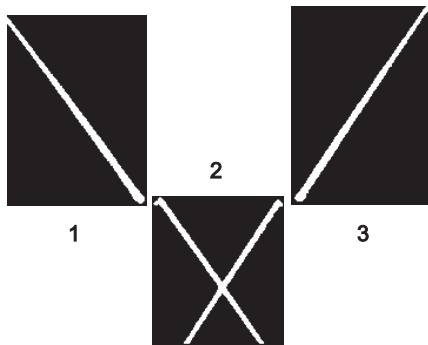For the calculation of the seam point's position $[x_S, y_S, z_S]$ a process

(a) Original camera image.

(b) Thresholded and filtered.

(c) Labeled objects of the binary image.

(d) Zoomed in cross object. The gray part is identified as cross junction.

(e) Separated linear parts after the elimination of the cross junction.
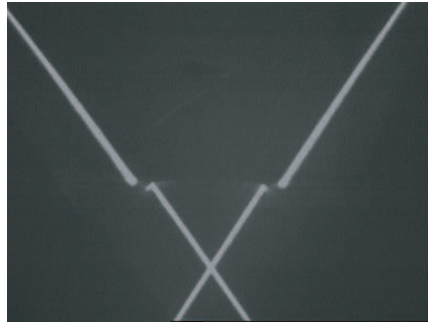

(f) Detected linear parts and seam points.
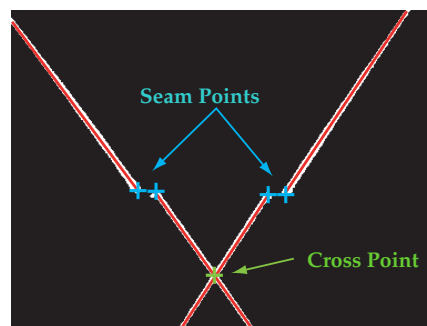
Figure 5.5: Steps followed for the identification of the line parts in the image for the derivation of the sensor's measurements.
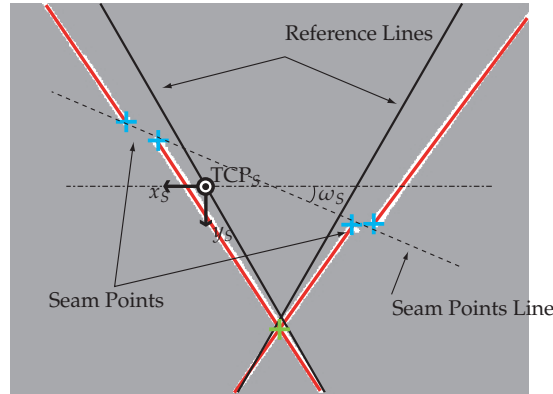
Figure 5.6: The reconstructed seam point line and the angle ω_S that it forms with the sensor x_S axis.

similar to the one of the single line is used. As is mentioned in §4.3.2, the TCP_S can be placed in either of the cross's reference lines. In the following example, the calculation of the $[x_S, y_S, z_S]$ values is carried out with the TCP_S placed on the leftmost reference line in the image as shown in Fig.5.6. Similar calculations are performed when the TCP_S is placed on the rightmost line. Choosing the TCP_S on the leftmost line means that the seam point on the leftmost line will be used for the position calculations.

The values $[x_S, y_S, z_S]$ can be calculated similarly to the single line sensor with the use of Eq.5.4. As it can be seen in the magnified part (Fig.5.7) of Fig.5.6, similarly to the Single Line sensor, the average Seam Point and point A (point where the perpendicular line to the reference line passing from TCP_S crosses the detected line) are used to determine the values of Δv and Δu and δ which are required for Eq.5.4.

The workpiece orientation is calculated with the use of the dihedral angle θ which is described in Fig.2.12 (page 31). For this reason the workpiece plane must be correlated to the calibration reference plane. For the identification of the workpiece plane three points on its surface are required, one of which is the cross junction and the other two can be selected randomly along each of the projected lines. Once the workpiece plane is identified, the dihedral angle θ can be calculated and split into rotations around the axes of TCP_S $[\varphi_S, \psi_S]$ (see Eq.2.12 and Eq.2.13 at page 2.12). The crossing lines sensor is also required to keep a certain orientation towards the seam
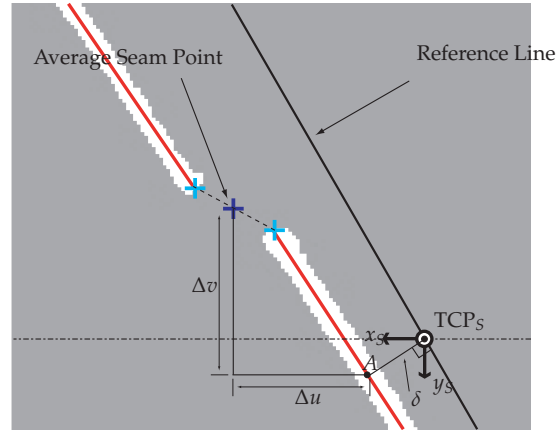
Figure 5.7: Zoomed part of Fig.5.6 for the explanation of the sensor displacement measurement calculations.

trajectory. For this reason the calculation of the rotation ω_S around the z_S axis is also required.

The ω_S calculation is only possible when the sensor is used to teach a seam. During teaching the seam intersects both structured light lines of the cross shape (Fig.5.6). The line that connects the detected seam points is used to calculate the rotation ω_S around z_S axis. The rotation ω_S is the angle formed by the sensor's x_S axis and the line that connects the detected seam points and it is equal to:

$$\omega_S = \arctan \alpha_\lambda - \arctan \alpha_{x_S} \tag{5.7}$$

where α_λ is the slope of the line that connects the two seam points in the image whereas α_{x_S} is the slope of the x_S axis of the sensor in the image. For the current cross sensor configuration $\alpha_{x_S} = 0$.

During the welding process the calculation of the ω_S is performed by the interpolation of measured points, similarly to the Single Line sensor.

The speed of this process is at 20 Hz. The cross shape extends to the full image and therefore ROIs can not be used to improve the speed. Nevertheless the speed of the system can be improved up to the maximum image capturing frequency of the camera (27 Hz), by optimization of the image processing algorithms.

5.2.3 Triangular Sensor

For the Triangular sensor configuration, the separation of the linear parts of the projected triangle in the image is becoming more complex. A solution similar to the one of the Crossing Lines sensor can also be used for the triangle though the correct identification of the triangle corners is not as simple. A more straight forward method is the use of Discrete Normal Radon Transform (Toft (1996), MathWorks (2003)) which for brevity will be referred to as Radon transform in the rest of this text.

The implementation of the Radon transform that is used for the detection of lines is based on the axiom that an infinite number of lines can pass through a single point. In a $x - y$ 2D coordinate system a line ℓ can be described as:

$$y = \alpha x + \beta, \tag{5.8}$$

where α and β the slope and offset of the line, and x and y the coordinates of any point along the line.

Another way to describe a line ℓ in an $x - y$ 2D coordinate system is by:

$$\rho_\ell = x \cos \theta_\ell + y \sin \theta_\ell \ , \tag{5.9}$$

where x and y the coordinates of any point along the line, ρ_ℓ is the distance of the line ℓ from the origin of the coordinate system and θ_ℓ is the angle that is formed from the projection of the origin of the coordinate system to the line ℓ and its x axis (Fig.5.8(a)).

In Fig.5.8(a), such a line ℓ that passes through the points A and B is presented. That line can be represented by a distance ρ_ℓ from the origin and an angle θ_ℓ. Any other line that passes through point A has its own unique angle θ and distance ρ. If the parameters of all the lines that pass through point A are plotted according their ρ and θ then a sinusoid shape of Fig.5.8(b) appears. This sinus curve is unique for that single point A.

If another point B is also plotted according its resulting ρ and θ values, then a second sinusoid curve will appear. The junction of the two sinusoid curves reveals the ρ_ℓ and θ_ℓ values of the line. Likewise, the sinusoid representations of all the points that belong to line ℓ will pass through point (θ_ℓ, ρ_ℓ) of the Radon plot. This property is used for the detection of lines in an image.

(a) A line ℓ passing through points A and B in an $x - y$ plane (2D space).

(b) Each point in the line is represented by a sinusoid curve on the Radon plot.
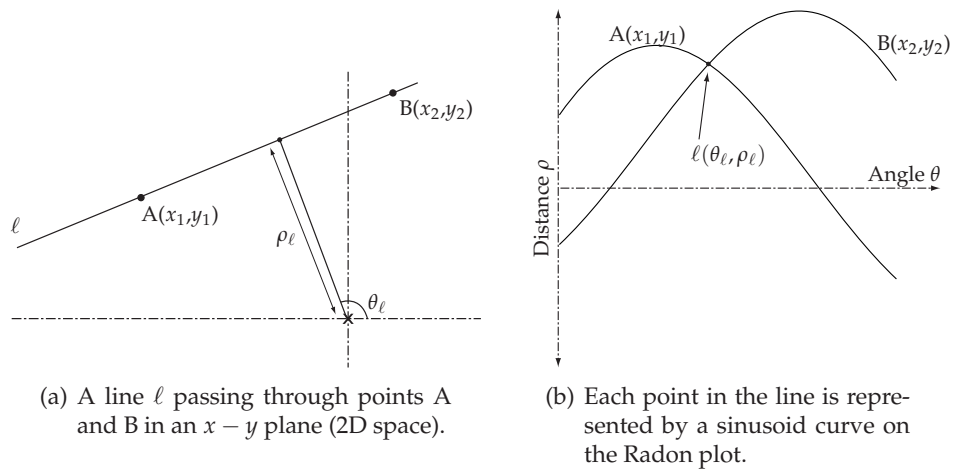
Figure 5.8: The representation of a line ℓ passing through points A and B in relation to the angle θ_ℓ and the distance ρ_ℓ in an image (left). The same line ℓ is represented by a single point in the Radon plot at the junction of the sinusoid curves of points A and B.

(a) Sample image.

(b) The Radon Map with the resulted values of the detected lines.
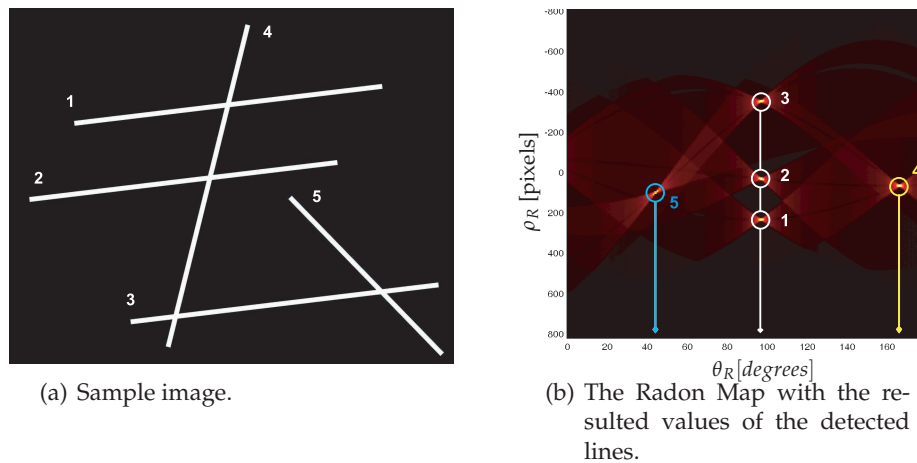
Figure 5.9: Steps followed for the identification of the line parts in the image for the derivation of the sensor's measurements.

In the image coordinate frame the coordinates change from $x - y$ to $u - v$, there are a discreet amount of points (pixels) that can belong to a line and a discreet number of angle values θ that are applied in Eq.5.9 for the calculation of the ρ. Furthermore, the more line points are used for the detection of the line, the bigger the number of sinusoid curves that will populate the Radon plot. Therefore each point of the Radon plot is assigned a value which counts the number of sinusoid curves that pass through it.

An example is illustrated in Fig.5.9. In Fig.5.9(a) five lines are present in the image plane three of which are parallel (lines 1, 2 and 3). The resulting radon map (Fig.5.9(b)) reveal the existence of five junction points, three of which (points 1, 2 and 3) indicate the existence of parallel lines in the image as they correspond to the same θ angle. The coordinates of these junction in the Radon plot are used in reverse to calculate the slope α and offset β of the existing lines ($v = \alpha u + \beta$) in the image according to:

$$\alpha = -\frac{1}{\tan \theta_i} \quad , \quad \beta = \frac{\rho_i}{\cos(\pi - \theta_i)}, \tag{5.10}$$

where ρ_i and θ_i the corresponding distance and angle at the junction point i.

Before the Radon Transform is applied on the original image (Fig.5.10(a)), it must be binarized, cleared of noise and labeled (Fig.5.10(b)). If the Radon transform is applied directly to the binarized image before the labeling function, a Radon map similar to the one of Fig.5.10(c) will result. In such a Radon map the pieces of the structured light lines appear close to each other and it is difficult to distinguish. The problem becomes worse when one of the broken parts is significantly smaller than the other. The smaller parts that score significantly less than their larger counterparts might not be detected as local maxima. For this reason, the labeling function of the binary image is important. Each of the labeled objects are projected on the radon map separately resulting at Fig.5.10(d) and Fig.5.10(e), for the top and bottom labeled objects.

When the lines have been identified (Eq.5.10), the seam points can be derived again by the overlapping of the identified line on the binary image, whereas the triangle corner points can be calculated by the junctions of the identified structured light lines (Fig.5.10(f)).

Similarly to the Crossing Lines sensor, the dihedral angle θ is calculated by correlating the detected workpiece plane with the calibration

(a) Original camera image.

(b) Labeled.

(c) Radon Transform of complete image.

(d) Radon Transform of top object.

(e) Radon Transform of botom object.

(f) Identification of linear parts and seam positions.
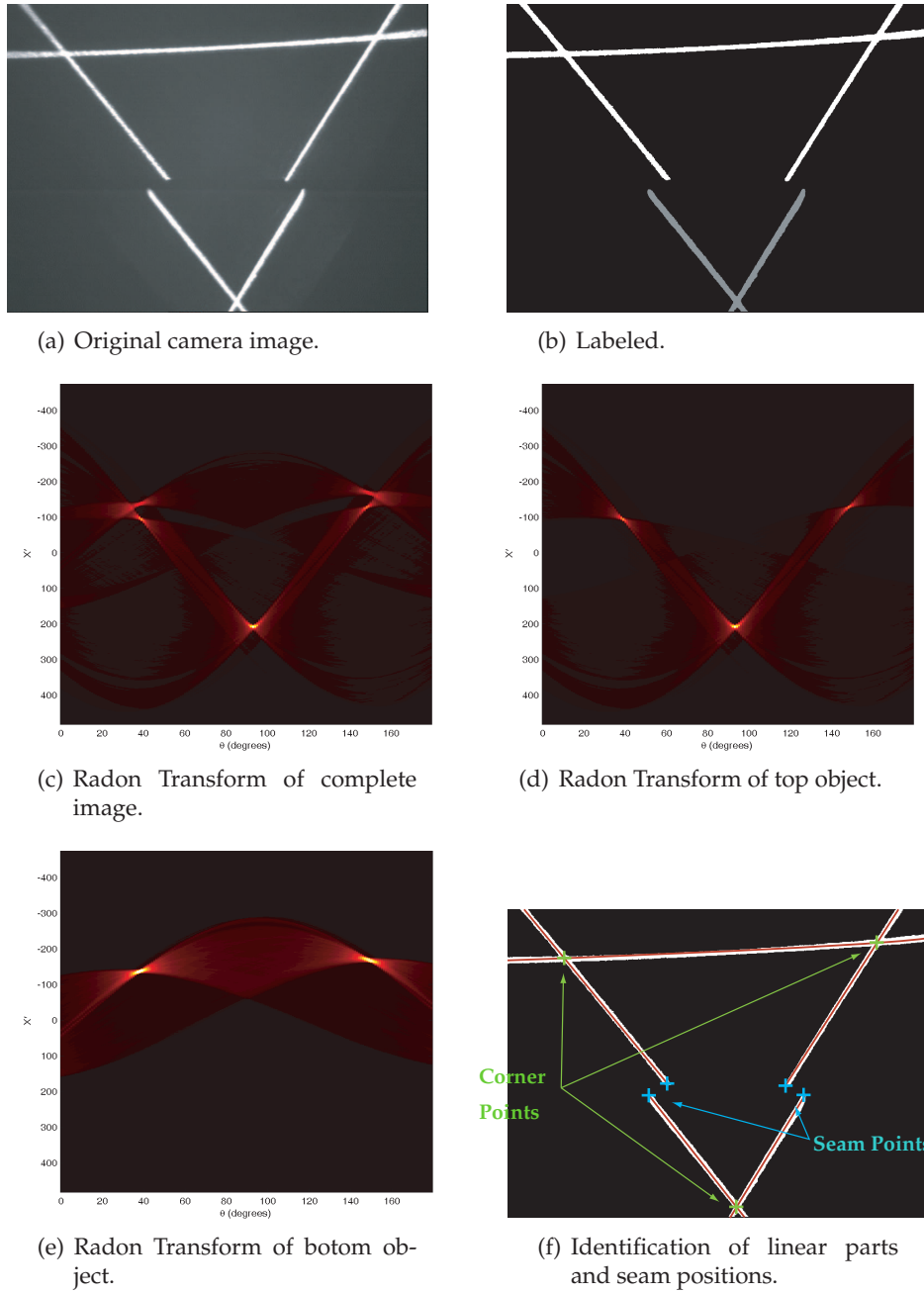
Figure 5.10: The use of radon transform for the identification of the linear parts of the image in the Triangular Shape mode for an overlap seam joint.
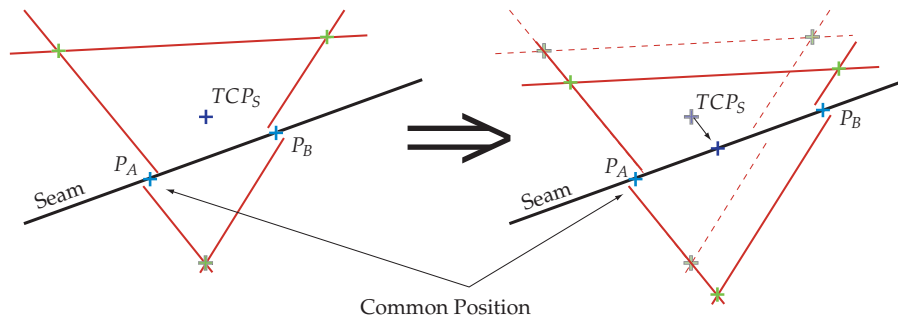
Figure 5.11: The desired position of the sensor towards a seam point P_A, during seam teaching requires that the TCP_S exists on the line that connects P_A and P_B, keeping the position of P_A constant after the move. On the right of the figure the dashed lines show the original position of the triangle and the solid lines show the new one.

plane. The values of the angles $[\phi_S, \psi_S]$ are calculated by splitting dihedral angle into components around the sensor's coordinate system with the use of Eq.2.12 and 2.13. The ω_S angle even though it can also be calculated, it is of no practical use since the triangular sensor does not need to maintain an orientation to the seam trajectory.

As is shown in §4.3.2 (page 97) the TCP_S origin exists on the incenter of the triangular shape. The resulted sensor measurement data depend on the function (Seam Teaching, Seam Tracking) that the sensor is used for.

During Seam Teaching, two seam points (P_A P_B) exist on the triangle sides (Fig.5.11). At the beginning of the seam teaching process one of the identified seam points (P_A P_B) is selected to be used for the detection. The same point is used until the completion of the seam teaching process. For this work P_A is selected for seam detection. The seam detection data are used to calculate the way that the TCP_S point should be moved on the line that connects P_A and P_B while keeping the position of P_A unchanged over the seam. The required process is visible on the right part of Fig.5.11 where the dashed lines are the original position and the solid lines are the new one. Note that the position of P_A remains unchanged.

By bringing the TCP_S on the seam line, the sensor ensures that the seam will always exist within the sensor's field of view regardless the seam orientation. In conclusion, two sets of measurement data must be provided for the sensor during seam teaching: for the displacement of the TCP_S and the position of the seam. The first is used to the calculation of the next
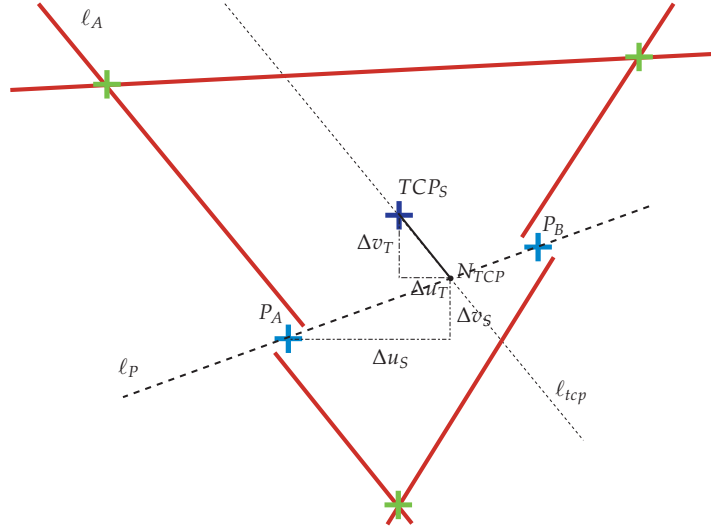
Figure 5.12: Components for the calculation of TCP_S displacement and seam position during seam teaching.

teaching step, and the second to replay or weld the seam. By providing two sets of data each new seam point can be taught in one step, without having to correct the robot position before a seam measurement is taken.

Fig.5.12 shows the necessary components for the computation of the TCP_S displacement. Initially, the direction of the TCP_S displacement must be determined. To keep the position of P_A unchanged, the TCP_S displacement direction must be parallel to the laser line that P_A belongs to. From the two laser line linear parts the top ℓ_A is used to define the direction as it is the one that belongs to the same triangular part as the TCP_S. Therefore, ℓ_{tcp} is introduced which is a line parallel to ℓ_A, and passes through TCP_S (Fig.5.12).

A second line present to Fig.5.12 is the line ℓ_P, which is the line that passes through P_A and P_B. The crossing of ℓ_P and ℓ_{tcp} is point N_{TCP} which is the new location of the TCP_S. Therefore the displacements dx_S and dy_S of the TCP_S in x_S and y_S directions is:

$$dx_S = \frac{\Delta u_T}{c_p} \, , \ dy_S = \frac{\Delta v_T}{c_p}, \qquad (5.11)$$

where Δu_T and Δv_T are the required displacements of the TCP_S along the image axes and c_p is the pixel-to-mm ratio.

The position of the seam is calculated as follows:

$$x_S = \frac{\Delta u_S}{c_p} \ , \ \ y_S = \frac{\Delta v_S}{c_p}, \tag{5.12}$$

where Δu_S and Δv_S are the measured values of the seam point P_A along the image axes and c_p is the pixel-to-mm coefficient.

The z_S measurement is calculated by the distance between the reference and the measured plane over the point P_A. For the reference plane z_S is zero as all measurements are performed relatively to that plane. It is therefore enough to calculate the z value of P_A on the measured plane, which is:

$$z_S = -\frac{u_P D_X + v_P D_Y - D}{D_Z c_p} \ , \tag{5.13}$$

where D, D_X, D_Y and D_Z the determinants of the measured plane as they are defined in Eq.2.4, u_P and v_P the image coordinates of the P_A and c_p the pixel-to-mm coefficient.

Each x_S, y_S, z_S measurement is logged together with the current position of the TCP_S in relation to the robot base frame. This is necessary for the calculation of position corrections during seam tracking.

At Seam Tracking the seam trajectory has been previously acquired either by seam teaching or other means. Therefore, a list of the x_S, y_S, z_S values is already available together with the TCP_S coordinates for each of the measurements.

During Seam Tracking the sensor tries to identify which of the logged measurement and TCP_S positions is closest to the current one, and use it to calculate the necessary corrections. First the current TCP_S position is passed to the sensor. The sensor then performs a search in the list with the logged measurement data and TCP_S coordinates to identify the logged seam position for the provided TCP_S coordinate. In the worse case the TCP_S coordinate will exist between two logged positions $TCP_S k$ and $TCP_S k + 1$ (Fig.5.13). In this case both logged seam positions will be combined as follows:
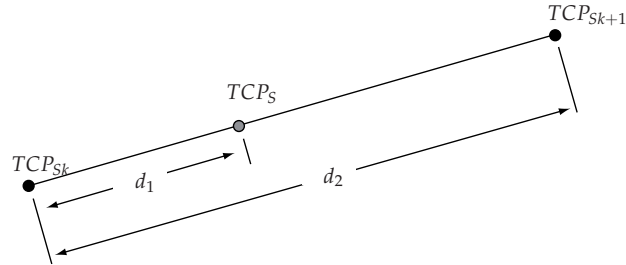
Figure 5.13: Use of the logged and current TCP_S values for the estimation of seam points.

$$x_{SN} = \frac{x_{S1}(1 - \xi) + x_{S2}\xi}{2}, \tag{5.14}$$

$$y_{SN} = \frac{y_{S1}(1 - \xi) + y_{S2}\xi}{2}, \tag{5.15}$$

$$z_{SN} = \frac{z_{S1}(1 - \xi) + z_{S2}\xi}{2}, \tag{5.16}$$

where $[x_{S1}\ y_{S1}\ z_{S1}]$ and $[x_{S2}\ y_{S2}\ z_{S2}]$ the $[x_S\ y_S\ z_S]$ values of the two logged measurements, $\xi = d_1/d_2$ is the ratio of the distance between the current TCP_S and the logged ones (Fig.5.13), and $[x_{SN}\ y_{SN}\ z_{SN}]$ are the estimated seam points for the current TCP_S.

If the tracking of the seam is performed accurately, then the current seam sensor measurements $[x_S\ y_S\ z_S]$ will be equal to the ones estimated by the logged ones $[x_{SN}\ y_{SN}\ z_{SN}]$. If not, then corrective actions need to be taken.

This situation is similar to the single line seam detection, where the detected seam position is corrected according to the TCP_S. The only difference in this case is that instead of the TCP_S the corrections are performed according to the $[x_{SN}\ y_{SN}\ z_{SN}]$ points. Therefore, Eq.5.4 are applicable for the position corrections. The angles $[\phi_S, \psi_S]$ are calculated from the dihedral angle as for the seam detection process.

The time performance of the sensor in the full shape mode is poor. The plotting of the radon map and the identification of the local maxima is a computation intensive process which become even more time consuming when the range of the detection angle becomes bigger. The process has a measurement frequency of about 4 Hz for an image of 366x288 pixels

which is not sufficient for the purposes of the integrated welding head. Prior knowledge can increase the measurement speed, by carefully selecting the detection angle range within the limits that the structured light lines are expected to be present. Nevertheless the systems performance is not sufficient. Regardless the slow measuring speed, the Triangular Shape mode provides in one measurement all the 6D data of the seam.

5.3 Switching Lines Mode

The Switching Line module is developed as a fast alternative for the Triangle of the Full Shape module. In the Switching Line module, only one of the three structured line diodes is switched on each time a camera image is captured. An example is shown in Fig.5.14, where three successive image captures are combined to reconstruct the triangular shape and detect the position of the seam and the orientation of the workpiece.
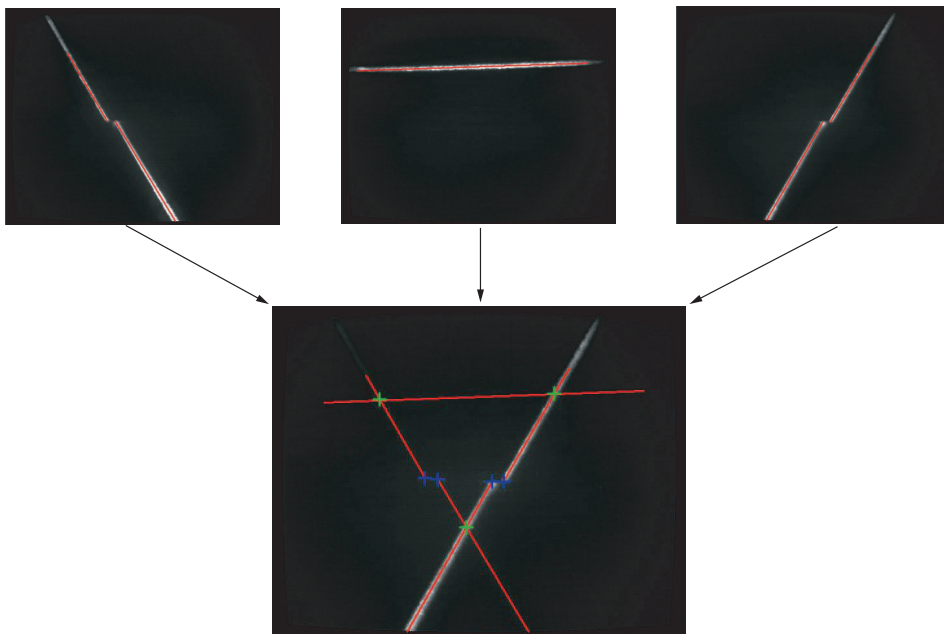
Figure 5.14: Three successive image captures are used to combine the final image.

The order in which the diodes are switched on/off depends on the mode that the triangulation sensor is operating at (Cross Shape, Triangle

Shape). At each of the captured images the Full Shape Single line algorithm is used to identify the sensor's line parameters in the image. Then, the information from all the successive images are combined to calculate all relevant data. Such a process is shown in Fig.5.15 groups of successive images are combined to reconstruct the triangular structured light shape.
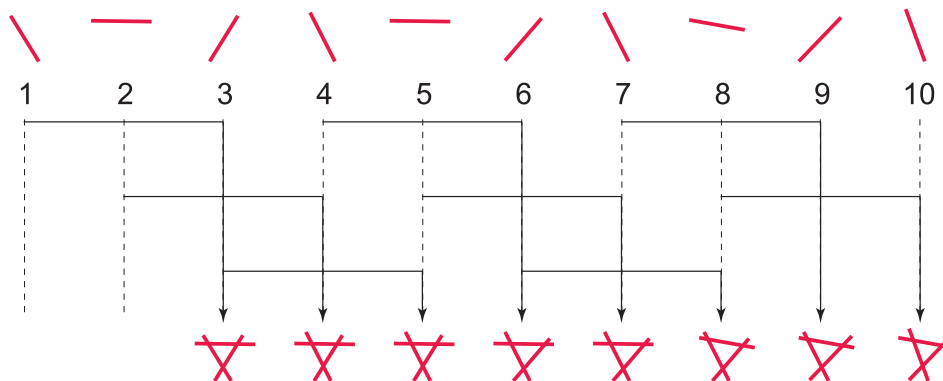
Figure 5.15: Reconstruction sequence of a Triangular sensor when functioning in a Switching Lines mode. On the top of the image the captured image lines and image number are illustrated. Three successive images are used to reconstruct the triangular structured light shape.

The implementation of the camera-diodes synchronization scheme and the cross and triangle shape sensor modes are described in the following paragraphs. Alternatives and extensions to the Switching Diode module are presented in §5.4.

5.3.1 Camera & Laser Diode Synchronization

The synchronization between the camera and the structured light diodes is achieved with the use of an FPGA chip as it is described in §3.4. The FPGA translates the signals from the camera to three TTL signals that signify which diode is switched on. The software that performs this translation is written in Verilog HDL (Palnitkar (1996)) and was compiled and programmed on the FPGA with the use of the Quartus II v5.1 (ALTERA CORP. (2005)) software from ALTERA®.

An Universal Asynchronous Reciever/Transmiter (UART) is programmed into the FPGA to enable the receiving of RS232 serial signals

from the camera. For the implementation of the UART a modification of the receiver that is found in chapter 12 of Ciletti (1999) is used.

Two signals can be transmitted from the camera towards the FPGA. The first is an RS232 signal containing the required module and mode that the sensor is to operate, and the second is a trigger signal which notifies the FPGA that the diodes should be switched. Upon initialization of the integrated welding head, the system is set to perform with the Triangle Shape mode of the Switching Line Module. Via the IntegLas application control panel the user can select the module and mode that the welding head sensors should perform.

The camera-diode synchronization is implemented with the generation of a trigger signal from the camera. Each time the captured image is processed the camera sends a trigger signal to the FPGA. The FPGA upon receiving the trigger signal, changes the status of the emitting diode in relation to the preselected working module and mode. The input/output signal configuration of the FPGA is illustrated in Fig.5.16, where *RS232* is the value of the Module and Mode signal, *Trigger* is the signal of the camera that the switching must take place and *Diode 1*, *Diode 2* and *Diode 3* are the TTL signals to the diodes (*high* signifying *ON*, *low* signifying *OFF*).

RS232	0	1	2	3	4	5	6	7
Trigger								
Diode 1								
Diode 2								
Diode 3								
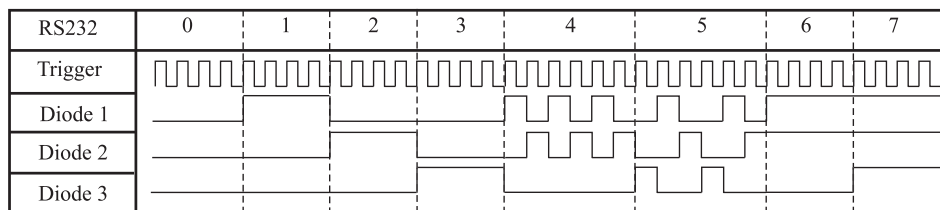
Figure 5.16: The I/O signals of the FPGA in relation to the operation Module and Mode of the sensor and the Trigger signal.

As is shown in Fig.5.16, for the Full Shape module (*RS232* values of 1, 2, 3, 6, 7) the trigger signal has no effect in the working state of the diodes. It is also shown that for the Switching Lines module (*RS232* values of 4 and 5), each trigger pulse switches the working state of the diodes allowing only one to be *ON* each time.

5.3.2   Cross Shape & Triangular Shape Configurations

These two modes differ from their Full Shape Module equivalents only on the manner in which the line data that form the cross or triangular shape

are acquired. When the shape's linear parts have been identified, the rest of the required calculations are the same as the ones that are defined in §5.2.2 and §5.2.3.

As was mentioned in the beginning of this section, in the switching lines module only one structured light line is switched on at each image capture. The reconstruction of the required shape (cross, triangle) is performed by the combination of the identified line data from successive image captures. Since only one line is present at each image the initial steps of the Single Line sensor of the Full Shape Module can be performed. This process will produce the position of the seam if it exist on the image and maximum two identified lines in the case that the line is broken. The use of these data depends on the mode that the sensor is performing under, which is described in the following paragraphs.

5.4 Alternative "Hybrid Modules"

Each of the two modules, "Full Shape Module" and "Switching Line Module", that were described in the previous sections, have unique advantages. The main advantage of the "Full Shape Module" is the image capturing time, whereas the strong point of the "Switching Line Module" is the simplicity and speed of the required image processing. The question that rises is whether it is possible to combine the advantages of both the above mentioned modules to one hybrid module.

There are two alternatives for a hybrid module that were not implemented and tested up to now.

5.4.1 RGB color module

To obtain a minimum capturing time and use simple and fast image processing algorithms, all image information has to be segmented and appear in the duration of one image capture. In the case of the triangulation scheme used in the integrated welding head, within one image capture three images containing only one of the structured lines is required.

This is possible with the use of a color imaging sensor and structured light diodes of the same wavelength as the sensitivity of the *Red*, *Green*, and *Blue* layer filters of the imaging chip. RGB color cameras capture three images simultaneously at the wavelengths of Red, Green and Red light and combine that data to produce the final color image. The use of laser

diodes that produce Red, Green and Blue structured light lines of the same wavelength as the camera filters will result to the appearance only one of the structured light lines in the relative color camera image layer. Such an example is illustrated in Fig.5.17 where the combined resulting image and the original captured layers are shown. Further, the use of simple and fast algorithms of the Switching Lines Module can be use in each of the RGB layers to provide the required seam data.

There are a number of considerations that have to be taken, for this alternative. Red and Green structured light emitting diodes are commercially available in a compact casing as required for the compact integrated welding head. The use of the blue diode creates a number of problems as, they are not commercially available in small sizes, and the quality of the structured light is not yet sufficient for these type of applications. Further more, the use of a color imaging sensor reduces the resolution of the image to one-third of the resolution of a monochrome sensor.

In the near future, all of the above problems might be overcome. There is ongoing research on the use of small fiber laser structured light projectors in a variety of colors with good quality. Additionally, the advancement of imaging sensor manufacturing provides faster and higher resolution color cameras. At this time though, the costs of such components is too high, or the components are too large in size to be considered for commercial use.

5.4.2 $R_1R_2R_3$ **monochrome module**

This module is similar to the *Color RGB Module*. This alternative overcomes the issue of unavailability of compact inexpensive blue structured light laser diodes. The solution is to use a similar architecture as the RGB imaging sensor, only instead of a Red, Green and Blue wavelength layers, three layers ($R_1R_2R_3$) for different wavelengths of the red spectrum will be used. For instance, R_1 at 635nm, R_2 at 650nm and R_3 at 680nm. These are commonly used wavelengths for the red structured light diodes.

An example of how this module performs is illustrated in Fig.5.18. In Fig.5.18(a) the projection of two structured laser diodes is shown, the horizontal line is projected by a red laser diode at 635nm whereas the vertical one my a laser diode at 650nm. In this image there is no filter applied. If a filter of 650nm$\pm$10nm is applied then Fig.5.18(b) is resulted where the vertical line (650nm) is more visible. In the proposed alternative of $R_1R_2R_3$, this would be the resulting image of one of the imaging chip's

(a) Combined Color Image

(b) Red Channel Layer.

(c) Green Channel Layer.

(d) Blue Channel Layer.
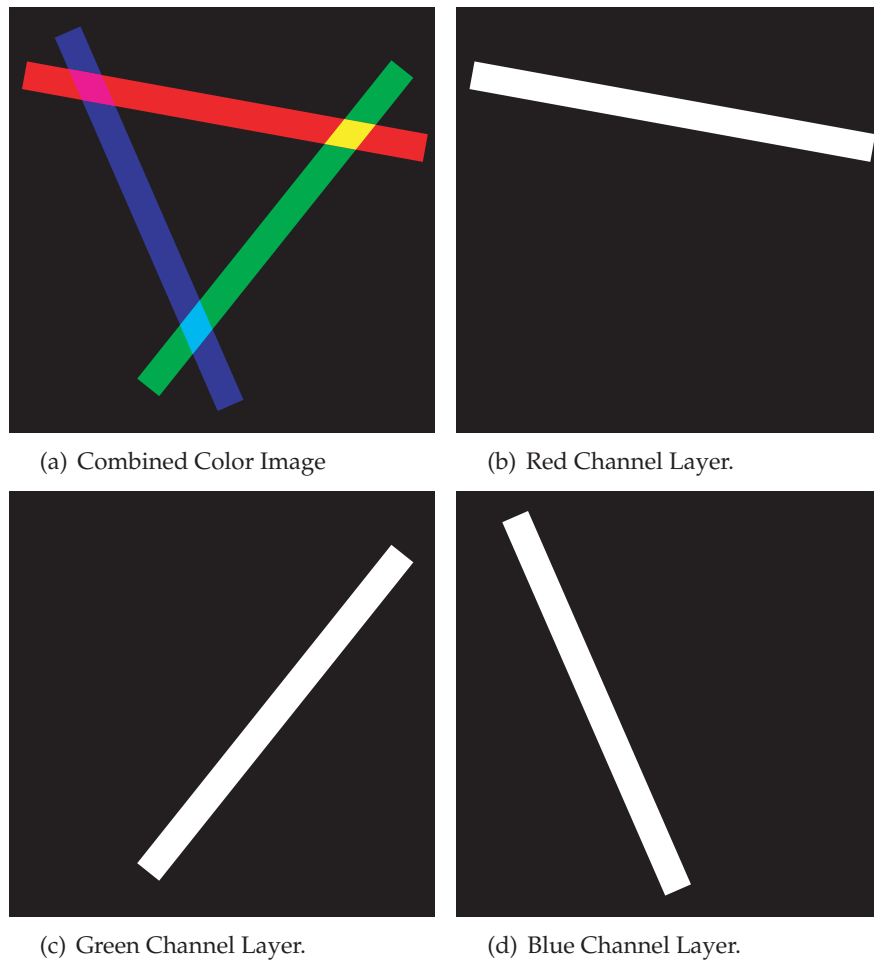
Figure 5.17: The resulting image of the combined Red, Green, Blue, layers of a color RGB camera.

(a) Original image without a filter.

(b) Original image with a Pass filter of 650 nm ±10 nm.

(c) Threshold result of the filtered image.
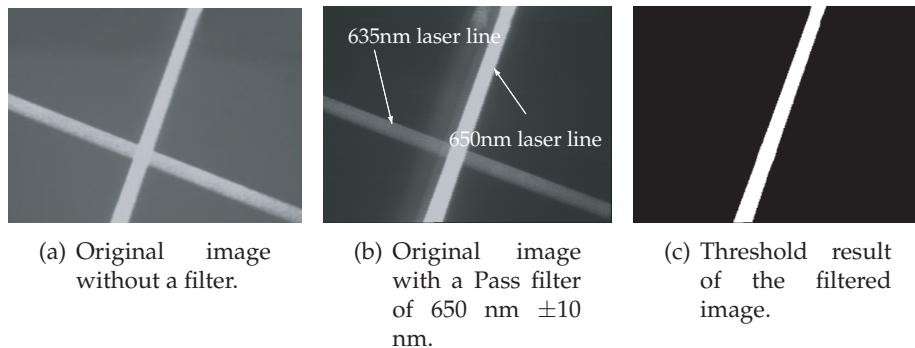
Figure 5.18: Sample images of 650 nm and 635 nm wave length laser lines with and without the use of interferometer filter.

layers. With a narrower band filter the horizontal line can be even eliminated completely. Nevertheless, even with the one used for this example the application of a threshold function on the filtered image (Fig.5.18(b)) is enough to to separate the line that is to be processed (Fig.5.18(c)).

This module makes use of three structured light diodes of the Red light spectrum, each with a different wavelength which is inexpensive and compact. The only draw back is that there is no commercial imaging sensor that captures the three different wavelengths of red instead the Red, Green, Blue. The development of a custom imaging sensor just for this purpose is not cost effective. In addition as in the case of the color camera, the resolution of the system will be reduced as again three layers need to be placed in one sensor.

A different approach would be to use three monochrome cameras that are supplied with the same view. Each camera has a filter that allows it to see only the light of one of the structured light laser diodes. The disadvantage of this method is that the use of three cameras will increase the volume and complexity of the integrated welding head.

5.5 Experimental results

The purpose of the seam detection sensor is to correctly detect a seam so that it can be used for the welding process. Additionally, the developed sensor should be capable of simplifying the required robot movements and since it does not depend on the seam trajectory orientation, it should

also be capable of detecting complete looped seem trajectories without the use of additional robotic axes.

A number of experiments were performed to investigate the capabilities of the seam detection sensor on the above mentioned issues. The experiments and their results are presented in the following paragraphs.

5.5.1 Detection Measurements

As a first step the measurement accuracy is investigated. In this experiment the robot is used as measuring device. The mode that is used is the switching diode triangular mode. The sensor is placed over a straight seam and the robot is moved in predefined positions and orientations.

The first experiment is the position measurement. The results are shown in Fig.5.19. Each row of plots in Fig.5.19 contains the measurement test results and the measurement residual errors. For each of the TCP_S axes individually the robot moves the welding head by steps of 0.2 mm, starting at -3.6 mm from the TCP_S origin and finishing at 3.6 mm after it. At each step a sensor measurement is taken. The first plot of each row slows the correlation between the robot displacements and the sensor measurements. The second plot of each row is the residual error defined as the difference between the robot displacement and sensor measurement. For the measurements along the x_S axis the maximum error is less than 0.1 mm with a standard deviation of 0.032 mm. For the measurements along the y_S axis the maximum error is also less than 0.1 mm with a standard deviation of 0.034 mm. The measurements along the z_S axis the maximum error is less than 0.05 mm with a standard deviation of 0.008 mm.

The second experiment is the angular measurement, the results of which are shown in Fig.5.20. Each row of plots in Fig.5.20 contains the angular measurement test results and the measurement residual errors. For each of the TCP_S axes individually the robot rotates the welding head by steps of 1° , starting at -10° and finishing at 10°. At each step a sensor measurement is taken. The first plot of each row is the correlation between the robot angular displacements and the sensor measurements. The second plot of each row is the residual error defined as the difference between the robot angular displacement and sensor measurement. For the measurements along the x_S axis the maximum error is less than 0.5^o with a standard deviation of 0.27^o. For the measurements along the y_S axis the maximum error is also less than 0.5^o with a standard deviation of 0.2^o. The
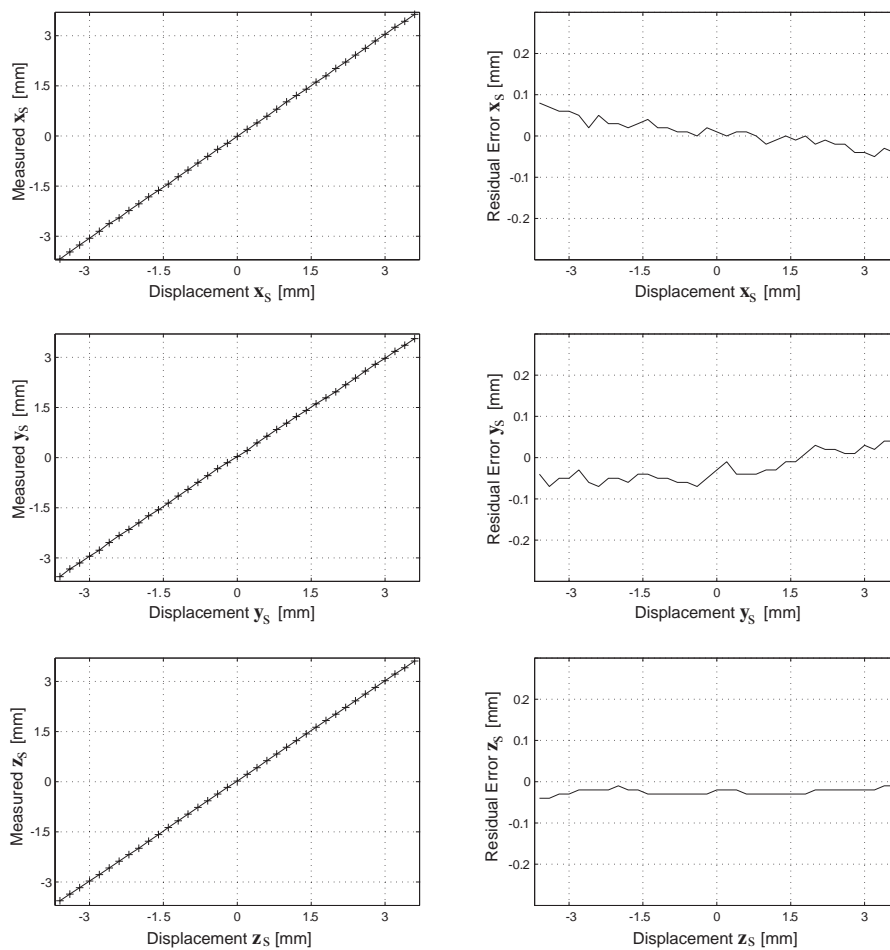
Figure 5.19: Seam detection triangular sensor position measurements. The robot performs predefined displacements which are correlated to actual sensor measured data [x_S y_S z_S] (Eq.5.12, Eq.5.13). The residual error between the performed displacement and relative sensor measurement are also plotted for each of the sensor's coordinates.
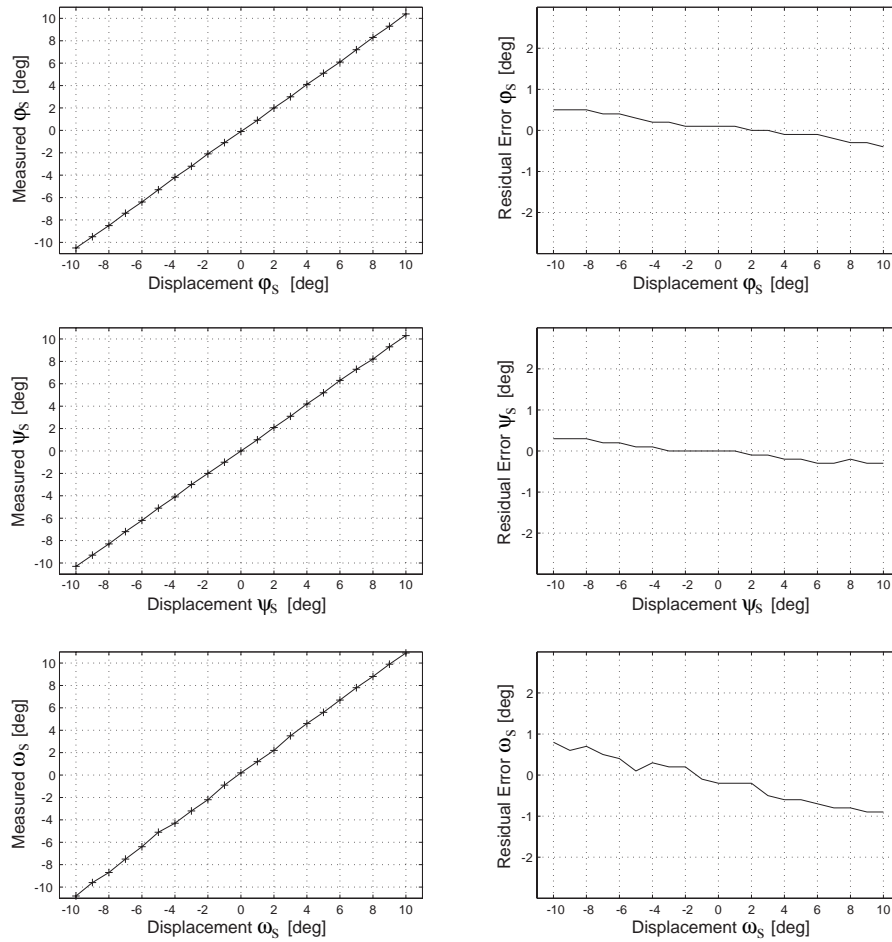
Figure 5.20: Seam detection triangular sensor rotation measurements. The robot performs predefined angular displacements which are correlated to actual sensor measured rotation data [φ_S ψ_S ω_S] (Eq.2.12, Eq.2.13, Eq.2.14). The residual error between the performed angular displacement and relative sensor measurement are also plotted for each of the sensor's coordinates.
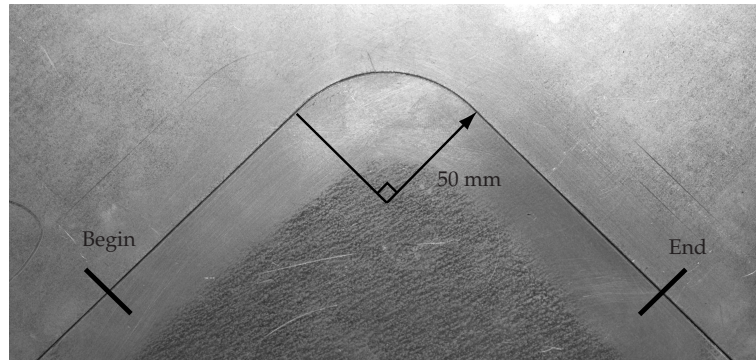
Figure 5.21: Round corner seam that was used for the TCP_S to TCP_L accuracy experiment. The radius of the corner is 50 mm, and the begin and end points of the detected path are also noted.

measurements along the z_S axis the maximum error is higher than 1° with a standard deviation of 0.54^o.

The measurements show that the sensor accuracy is sufficient for the required positioning tolerances (0.1 mm) of laser welding. The plots also show a reduction of the measurement accuracy of the seam position when the seam exists much further form the TCP_S. This measuring accuracy reduction appears due to shadowing effects on the structured light line of the sensor from the seam configuration. Further optimizations on the sensor detection algorithms will improve the sensor measuring accuracy for these cases. In general, such big offsets of the seam position from the TCP_S are not realistic for a seam teaching or tracking situations.

5.5.2 Sensor and Laser Tool Accuracy

Once a seam trajectory has been detected and taught it has to be welded. For this reason a seam trajectory is taught with the seam detection sensor and then is followed with the TCP_L. The seam trajectory that was used for this experiment is shown in Fig.5.21 (test parts are provided by Shiloh Industries, Ohio, USA). The seam trajectory consists of two linear parts and a round corner of 90° and 50 mm radius. The joint configuration is a butt-joint one part of which is 1 mm thicker. Two experiments were conducted, first with the use of the Single Line sensor, and then with the Triangular sensor.

In the first experiment, the seam trajectory is taught by the Singe Line

sensor with teaching steps of 2 mm and correcting the orientation of the sensor towards the seam on each step. Then the Single Line sensor TCP_S is adjusted that the reference line exists on the TCP_L. Thus when the taught path is revisited with the TCP_L, any positioning errors of the TCP_L can be measured with the help of the Single Line sensor.

The second experiment is similar to the first. This time the Triangular sensor is used without the use for correction of the sensor orientation on each teaching step. The teach steps are once more 2 mm. To measure the TCP_L positioning errors again the Single Line sensor's TCP_S is adjusted on the TCP_L, before revisiting the taught seam path points.

The results of both experiments are shown in Fig.5.22, where the measured errors in x_L, y_L and z_L for all of the taught seam trajectory points. For the Single Line sensor the largest errors appear on the round corner seam points (between points 40 and 70) at the y_L axis of the TCP_L. These errors occur during teaching, as the Single Line sensor deviates slightly from its preferred ω_S orientation for each of the teaching steps of the corner. These small orientation deviations introduce small errors from shadowing effects on the sensors structured light line. The measuring errors of the sensor can be reduced, by better image processing algorithms, the current result are sufficient however for laser welding.

For the Triangular sensor it is shown that there are small errors on the x_L and z_L components, and large errors along the y_L component. These errors arise from the use of an adjusted Single Line sensor to measure the positioning errors of the TCP_L. As mentioned before, the triangular sensor does not change its ω_S orientation in relation to the seam. Thus, when the path is replayed for the TCP_L accuracy measurement, the ω_S remains unchanged. Therefore the adjusted Single Line sensor does not have its optimum configuration for accurate results. From the plots of the Triangular sensor it can be seen that the most accurate measurements are around the measurement point 60, because it exists on the rounded corner, and for several steps the adjusted Single Line sensor happens to operate with its preferred ω_S. For the rest of the measurements the shadowing effects of the joint configuration on the sensor measurements introduce measurement inaccuracies. The measurement inaccuracies are not that evident on the x_L and z_L components, because the shadowing effect has a bigger influence on the v coordinate of the seam image point which is related to the y_S measurement of the sensor Eq.5.4). Even though the shadowing effect of the adjusted Single Line sensor is present and the sensor performs far from its preferred configuration, the measuring error does not exceed ± 0.4
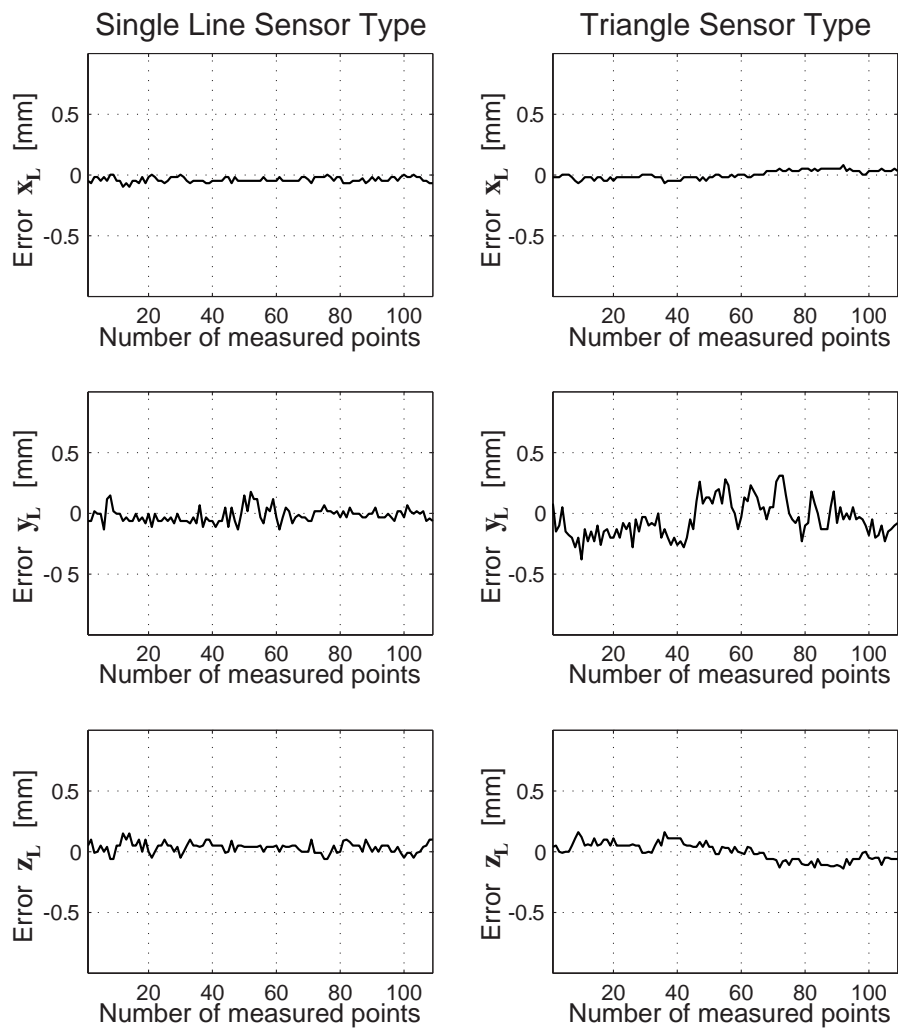
Figure 5.22: Comparison of the positioning errors of the TCP_L from the taught seam trajectory for the rounded corner seam. As seam detection sensors the Single Line and the Triangle configurations were used.
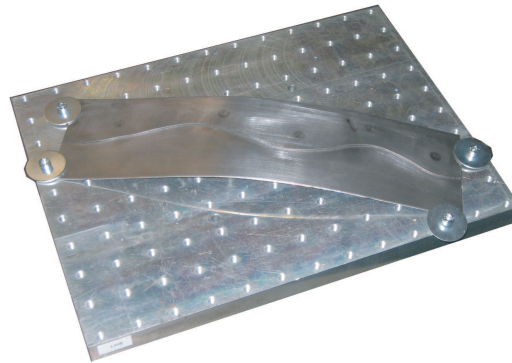
*Figure 5.23: 3D sinusoid seam.*
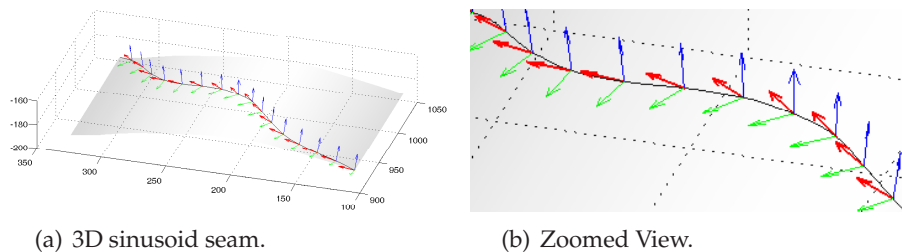
(a) 3D sinusoid seam.

(b) Zoomed View.

Figure 5.24: The reconstruction of the measured data of the Single Line sensor, for the sinus seam on a curved surface. The coordinate frames represent the position and orientation of the TCP_S at the measured points. Part of the image is magnified for better observation.

mm. It can be derived that the actual error of the TCP_L is much less than the one measured.

5.5.3 Robot Movement Simplification

This experiment demonstrates the influence of the seam detection sensor on the robot movement. For this set of experiments a 3D sinusoid seam trajectory as shown in Fig.5.23 is used. The 3D sinusoid seam trajectory was taught both with the Single Line and Triangular sensor. The resulted robot positions with the use of both sensors are shown in Fig.5.24 and 5.25.

In Fig.5.24 the measurements of the single line sensor are combined with the robot position to reconstruct the detected sinus seam. Along the reconstructed seam a number of the sensor's coordinate frame orientations

(a) 3D sinusoid seam.

(b) Zoomed View.
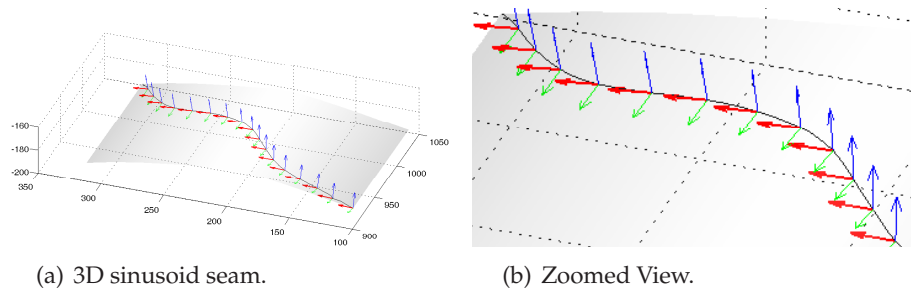
Figure 5.25: The reconstruction of the measured data of the perimetric Triangular sensor, for the sinus seam on a curved surface. The coordinate frames represent the position and orientation of the TCP$_S$ at the measured points. Part of the image is magnified for better observation.

are displayed. As is expected, the sensor orientation changes in order to satisfy the seam teaching procedure. The sensor orientation tries to follow the seam trajectory in order to keep it on the sensor's field of view.

When the triangular perimetric shape sensor is applied on the same seam the result of Fig.5.25 is produced. It can be seen, that the sensor in this case does not require additional changes to its orientation except the ones that allow it to follow the curvature of the surface. This simplifies the required robot movements for the following of such seam trajectories. This means that robots with fewer axes can also be used for welding such complicated seams.

To comprehend the impact of this functionality on the robot movement, the required robot movements for each of the trajectories must be examined. For this reason the taught seam paths from the Single Line and Triangular sensors were replayed by the robot, and the robot's six joint positions, angular velocities and torque were recorded. In Fig.5.26 the results of this recording are shown when the robot replayed the seam trajectory with the speed of 80 mm/s. It is evident that the required joint movements are significantly less when the Triangular sensor is used for the teaching of the 3D Sinusoid seam trajectory.

5.5.4 Looped Seam Trajectories

The rounded rectangle seam (Fig.5.27) is used to demonstrate the ability of the sensor to allow the use of robots in the detection and following closed loop seam trajectories without rotating the welding head. The Single Line
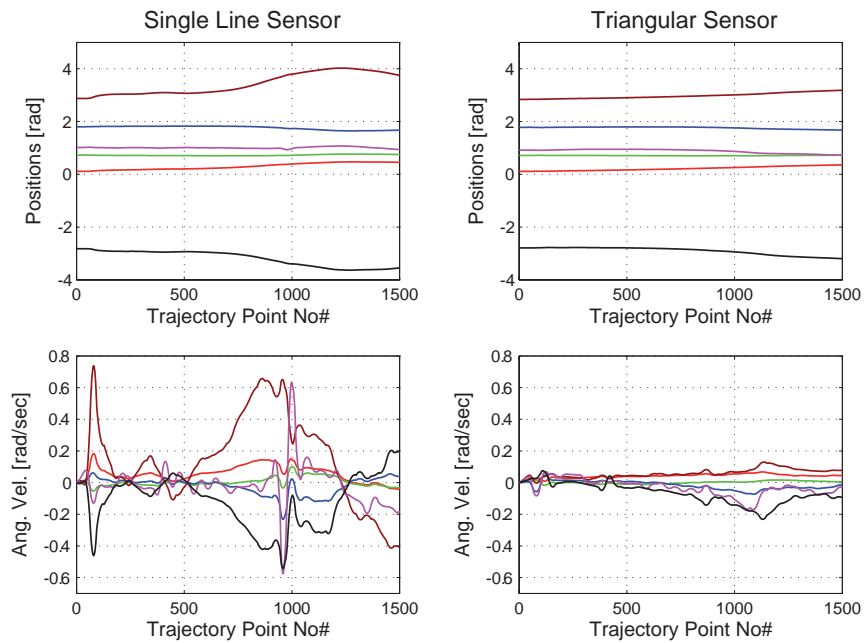
Figure 5.26: Plots of the six robot joint positions and angular velocities for the replay of the 3D Sinusoid seam trajectory, when taught by the Single Line and the Triangular Sensor. The seam trajectory is replayed with a speed of 80 mm/s.
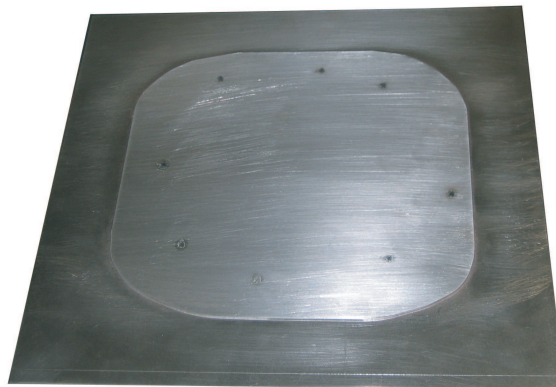
Figure 5.27: Rounded corner rectangular Seam.

(a) Rounded corner rectangular seam.

(b) Zoomed View.
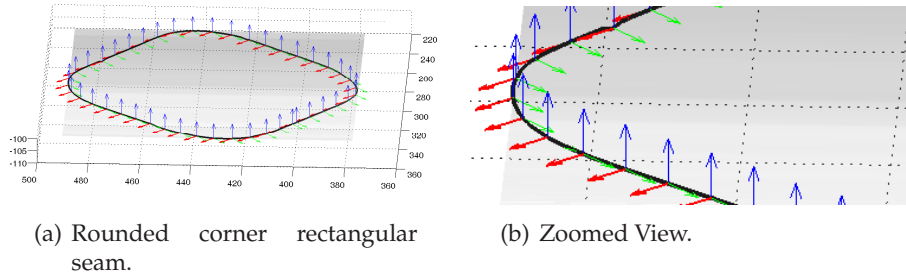
Figure 5.28: The reconstruction of the measured data of the perimetric triangular sensor, for the rounded rectangle seam.

sensor was not tested on this seam, because it is not possible for this type of sensors to follow a looped seam trajectory unless an additional external robotic axis is used.

Fig.5.28 shows the reconstructed data of the perimetric sensor measurements over the rounded corner rectangle seam. Clearly the sensor keeps the same orientation for the full length of the seam path. This means that at the corners the robot does not need to perform fast joint movements.

5.5.5 General conclusions

Three seam detections sensor configurations have been developed. The Triangular sensor is able to follow three dimensional and looped seam trajectories without having to rotate the welding head. This allows it to reduce the work load of the robots, and the necessity for additional external robotic axis. The sensors are within the required measuring accuracy for laser welding. A Switching Diodes module is implemented to increase the speed of the sensor up to 28 Hz. Finally, alternatives of the Switching Diode module, for the separation of lines of the perimetric shape in the image, are also proposed.

Chapter 6

Process Monitor

The Process Monitor sensor has to provide information about the laser welding process. This information is used to derive the laser welding state (conduction, partial or full penetration) and to control the laser power output accordingly. Within this work the Process Monitor sensor is developed for welding processes of steel, by monitoring the plume radiation.

6.1 Sensor Specifications

The plume radiation is detectable at the wavelength range of 400 - 600 nm (Postma (2003)). Therefore the selected photo-detector must be sensitive at these wavelengths. There are several ways in which the sensor signals can be used for monitoring the weld pool or real-time control of the laser power (Mori and Miyamoto (1997), Farson et al. (1997), Gu and Duley (1997)). Therefore, it is desirable for the sensor to be able to deliver measurements at a frequency of several kHz. Another consideration is the amplification gain of the sensor. Digital signal processing (DSPs) units require the sensor outputs to be in the range of ± 10 V or ± 15 V. To be able to make use of the full resolution of the DSPs, it is desirable to amplify the sensor signal as well within these range limits. It is also desirable to have a variable gain signal amplification, where high amplification gains can be selected for low radiation processes, and small amplification gains for high radiation. Further, it must be possible to identify the formation of a keyhole from the sensor data. Finally, the sensor electronics and signals must be protected from any type of interference (electrical, electromagnetic) within the work cell.

6.2 Definition of Welding Modes

The implementation of a controller for the laser power is based on the work of Postma (2003) and De Graaf et al. (2005). In that work, the laser power is gradually increased and the plume radiation is recorded (Fig.6.1).
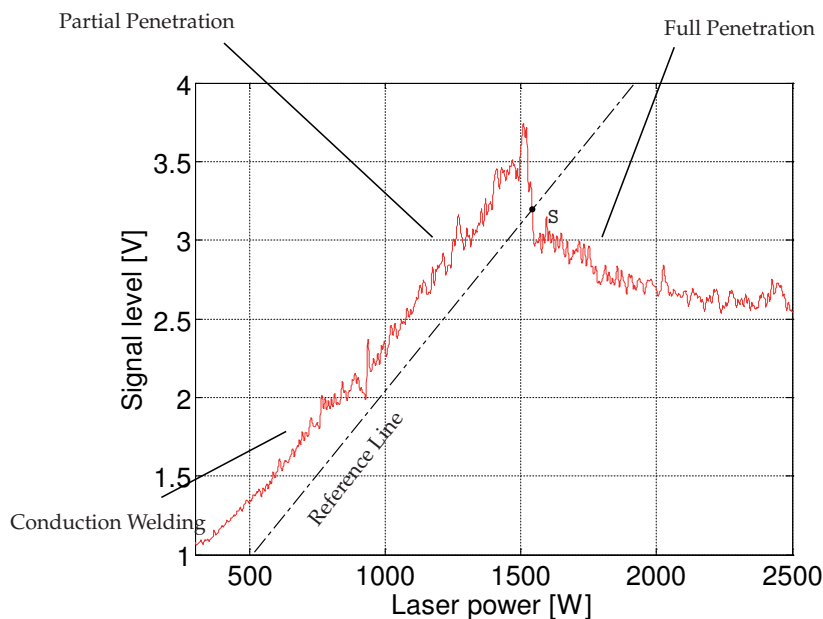
Figure 6.1: Sensor signal of emissions of the plume at 400-600 nm, the controller reference line and switching point S *as in De Graaf et al. (2005).*

It is seen that with increasing laser power the plume radiation emissions reach a peak and then it suddenly drops. For even more laser power the signal level generally decreases. The drop in the plot happens because of the formation of the through hole (Full Penetration), which allows the metal vapor to escape from the bottom side of the weld, resulting in a decrease of the emissions at the top surface. Before the peak Partial Penetration welding takes place while in the low emission values Conduction welding resides.

The control principle is as follows: A reference line is chosen in the emission graph (Fig.6.1). When the signal is above the line the laser power is increased, and when the signal is below the line the laser power is de-

creased. This adjusts the power towards the switching point S just in the full penetration area.

6.3 Sensor Design

The process monitor sensor consists of three parts: the electronics, the optics and the mechanical interface. The electronics include all the necessary components for the plume signal of the illumination and the generation of an electrical signal proportional to the detected emission level. The optics ensure that only the desired wavelengths are transmitted and are focused on the sensor's photodiode. The mechanical interface is the housing of the optics and the electronics and the manner in which they are integrated to the rest of the laser welding head.

6.3.1 Sensor Electronics

The first step of the design of the process monitor sensor is the selection of a suitable photodiode. The UDT Sensors PIN-5DI sensor was selected which is sensitive to the 400-600 nm radiation wavelength range and has a minimal response time of 15 ns (Appendix A.4). This response time is equal to a maximum response frequency of 67 MHz which is well above the requirement that the sensor detection speed is several kHz. Photodiodes generate an electrical current that is proportional to the amount of light that is projected onto the photodiode's photosensitive surface. The maximum current that is delivered depends on the type and size of the photodiode, and it is in the range 30-200 μA. Therefore small changes of light illumination result to small changes of the generated electrical current. To be able to sense these small currents, amplification of the photodiode output (generally known as pre-amplification) is necessary. An operational amplifier (Op-Amp) is used for this purpose.

According to Jung (2004) there are two ways to pre-amplify a photodiode with the use of an Op-Amp: the photovoltaic and the photoconductive (both being current-to-voltage converters). The main differences between the two pre-amplification types are listed in Table 6.1. The UDT Sensors catalog (UDT (2008)), mentions that the UDT photodiodes can be used in photovoltaic mode for applications that require responde frequencies of up to 350 kHz, whereas the photoconductive mode must be used to reach the photodiode's maximum response frequency. The designed

electronic board (Appendix C.5) allows the use of both pre-amplification designs, by changing the connection positions of the photodiode and pre-amplification resistors.

The photovoltaic pre-amplification design is the most suitable for this task, as it is accurate and within the required response specifications. Such sensors have been widely used in this type of processes and their results are known. Most of the experiments conducted in this work make use of the photoconductive pre-amplification design, to allow even higher measuring speeds and to evaluate how such a sensor would perform.

Table 6.1: Photodiode Pre-Amplification Types

Photovoltaic	Photoconductive

Photovoltaic	Photoconductive
No Bias Voltage	Reverse Bias Voltage
Linear	Nonlinear
Low Noise	Higher Noise
Precision Applications	High Speed Applications

Op-Amp = Operational Amplifier, **Ph**= Photodiode, **R** = Resistor, **Out**= Output Voltage, **GND**= Ground, **-V**$_{BIAS}$= Reverse Bias Voltage

The main task of the sensor is to identify the formation of a keyhole which is signified by the drop of the sensor's signal following an initial peak. Therefore the inaccurate measurement of the plume radiation value, and the nonlinearity of the signal do not introduce any problems as long as the signal drop is present and the three different welding states can be identified. The frequency response requirement of the sensor is also satisfied, since the photoconductive design yields higher sensor speeds. The remaining consideration is that of signal noise. The additional noise in the photoconductive design originates from biasing the photodiode, which introduces dark current and shot noise of about 10 nA and 5 nA respectively.

By using an ultra-low noise, precision high-speed operational amplifier like the LT1028 (Linear Technology) it is possible to make use of the full bandwidth of the photodiode. The photodiode electronic scheme is shown in Fig.6.2 and its implementation in Fig.6.3.
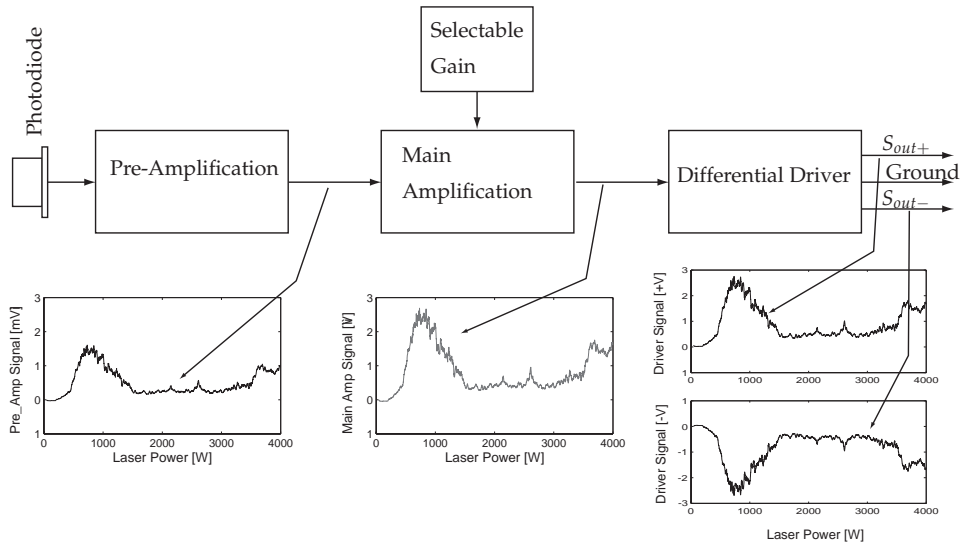
Figure 6.2: Schematic of the photodiode electronic board process. The first plot shows the pre-amplified photodiode signal [mV] as a function of the laser power. The second plot shows the amplified signal with selectable gain [V]. The third plot shows the amplified signal and its inverse [V] that are the outputs of the differential driver.
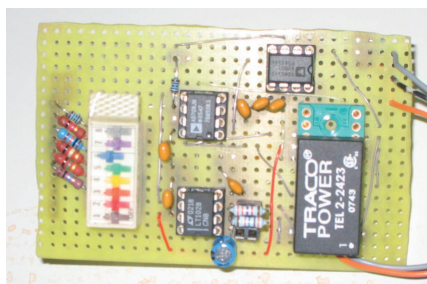
(a) Top Side - Electronics
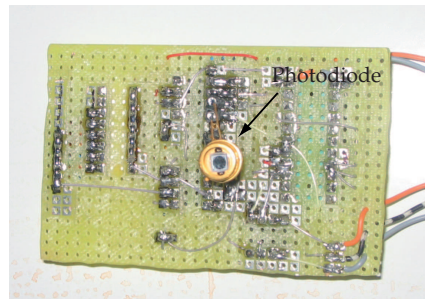
(b) Bottom Side - Photodiode

Figure 6.3: Both sides of the electronic prototype board.

As is shown in Fig.6.2, the input of the pre-amplification module is a the diode signal in μA. A non-linear amplified version of the photodiode signal, converted in [mV], is the output of the pre-amplification module.

The purpose of the main amplification module is to further amplify the pre-amplification output with a selectable gain. Again an operational amplifier is used in this case as an non-inverting amplifier and switches are used to select the different amplification values. The possible amplification values of the developed sensor are shown in Table 6.2.

Table 6.2: Sensor amplification values.

Switch Position	1	2	3	4	5	6
Gain	2	10	10^2	10^3	10^4	10^5

Only one switch at the time can be in state "ON"

Even though the selectable gain amplification increases the level of the sensor signal, it is still susceptible to noise from electromagnetic interference on the cable that connects the sensor to the DSP. For this reason a differential driver is used. The differential driver has two outputs: the original signal S_{out+} and the inverse of the original signal S_{out-}. When both signals are transmitted through the same cable they sustain the same noise, which can be identified and eliminated by the simple combination of the two signals (Eq.6.1).

$$S_{out} = \frac{S_{out+} - S_{out-}}{2} \qquad (6.1)$$

The main task is to identify the formation of a keyhole which is signified by the drop of the sensor's signal which follows an initial peak. Therefore the nonlinearity of the signal does not introduce any problems as long as the signal drop is present and the three different welding states can be identified. The higher noise level in the photoconductive pre-amplification is also disregarded as long as the three different welding states are clearly identifiable.

6.3.2   Sensor Optics

The sensor optical components ensure that only the desired radiation wavelengths are transmitted and are focused on the photodiode. To isolate the plume radiation a 400-600 nm band-pass optical filter is used. The

most cost effective design makes use of a *"of the shelf"* 400 nm high-pass optical filter (Fig.6.4(a)) and a 600 nm low-pass filter (Fig.6.4(b)).

As can be seen in Fig.6.4(b), the 600 nm low-pass optical filter also transmits almost all wavelengths over 790 nm. Therefore an additional optical component has to be used. A hot-mirror with 0° inclination and typical wavelength transmission of 410-700 nm (Fig.6.4(c)) is selected. The addition of the hot-mirror makes the 400 nm high-pass filter unnecessary. The resulting transmittance of the combined hot-mirror with the 600 nm low pass filter is shown in Fig.6.4(d).
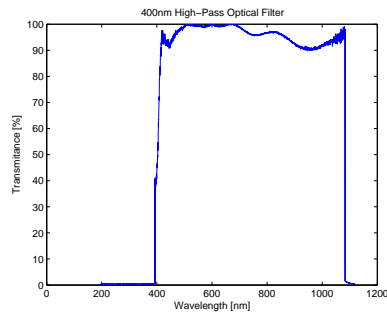
(a) 400nm High-Pass Filter.
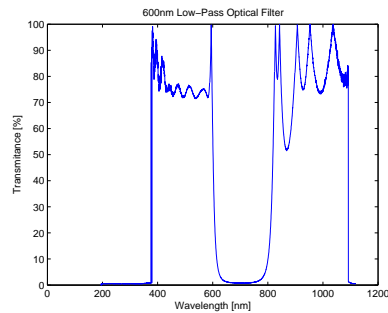
(b) 600nm Low-Pass Filter.
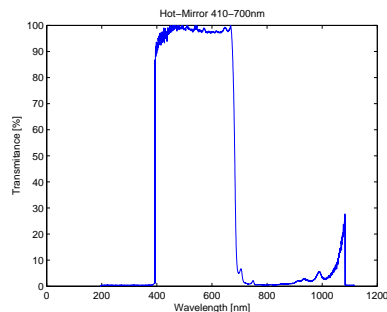
(c) Hot-Mirror 400-700nm.
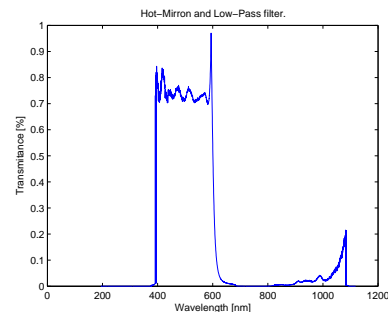
(d) Combination of Low-Pass Filter and Hot Mirror.

Figure 6.4: Spectrographic analysis of the optical components and their combination.

The last optic component is the focusing lens. The lens' focal length is determined by the size of the photodiode's photosensitive surface and the required field of view. From experience the plume emissions can be expected to exist in an area of 100 mm^2 around the TCL$_L$. The photosen-

sitive surface of the photodiode consists of a disk with diameter of 2.54 mm. Since the photodiode has coaxial view to the laser process, the high power laser focus lens will also contribute to the magnification factor from the field of view to the photodiode. The goal is to image a disc of 10 mm diameter on one of 2.54 mm diameter. This means that the desired magnification factor is about 0.25. Since the high power laser focus lens has a focal distance of 100 mm, the sensor lens must have a focal distance of 25 mm. The imaging qualities of the lens are not important as long as the lens transmits the necessary wavelengths. The change of the high power laser focus lens will result to different magnification values. For the 150 mm laser focus lens the sensor's field of view will have a diameter of 15 mm, and for a 200 mm laser focus lens the field of view's diameter will increase to 20 mm.

For compactness reasons, a sensor lens with a relative small size are preferable. The details of the optical components are listed in Appendix A.1.

6.3.3 Mechanical Interface

The whole system has been integrated in the designed welding head. Fig.6.5(a) shows the actual position where the interface is integrated in the laser welding head. As was shown in Fig.3.10 (page 55) the interface is placed in series with the 70-30 beam splitter, underneath the imaging sensor. The mechanical implementation of the sensor interface is shown in the picture of Fig.6.5(b), on which the beam splitter is placed. A number of guidance pins on the welding head ensure that the process monitor interface will always be placed with the correct orientation in the welding head.

A section view of the sensor components is seen in Fig.6.6. The first component of the interface holds a lens 25 mm that focusses the radiation on the photodiode surface. The second part of the interface holds the two selected optical filters. The last part houses the photodiode and the sensor electronics.

6.4 Experiments

A series of experiments were performed to calibrate the sensor and to investigate the applicability of the sensor for the identification of the keyhole

(a) Interfacing the sensor to the welding head.

(b) Implementation of the sensor design.
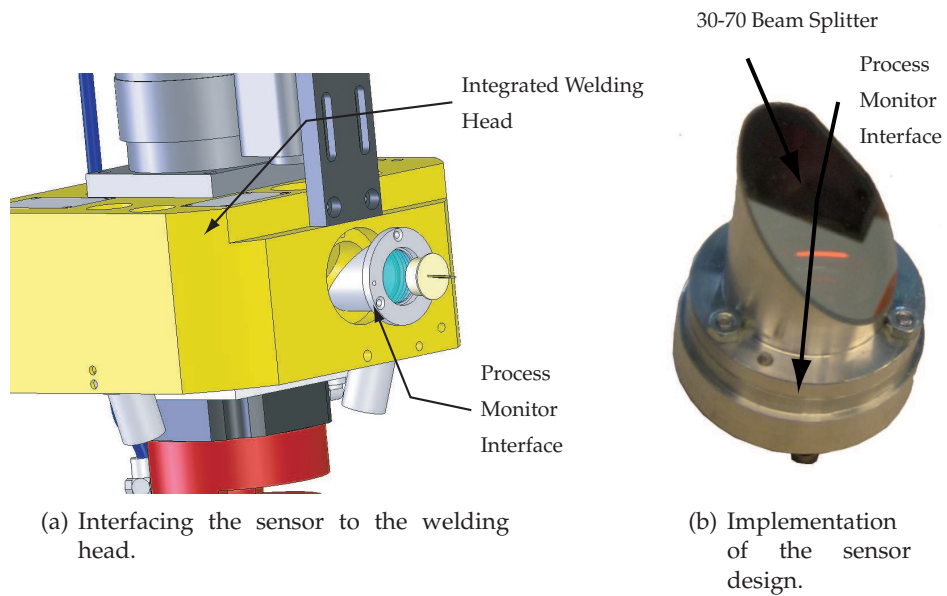
Figure 6.5: A section of the interfacing position of the process monitor sensor on the integrated laser welding head, and a picture of the implementation of the design.
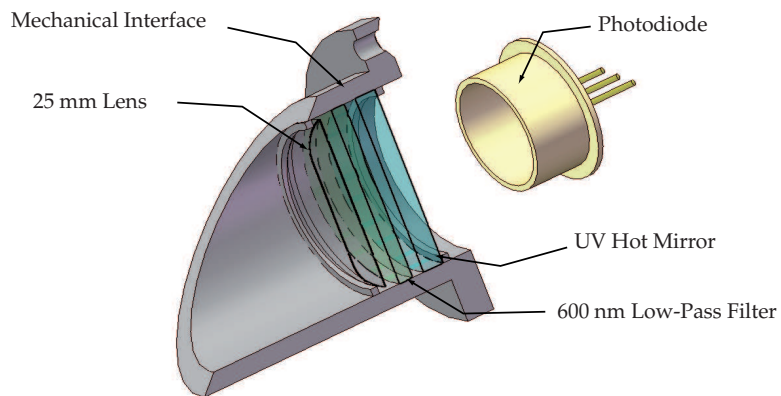
Figure 6.6: Mechanical interface of Process Monitor sensor for the integrated laser welding head.

formation during welding. The experiments involve collection of sensor data during the laser welding of steel plates. The laser welding is performed on steel plates of constant thickness of 1 mm with different welding speeds.

6.4.1 Experimental Setup

The experimental setup consists of the integrated laser welding head, a Stäubli RX130 robot, a dSPACE data acquisition system and a high power laser unit. The robot is programmed to move the integrated laser welding head with a linear trajectory over the seam while the welding process is performed with a ramping laser power from 40 W to 4000 W. The process monitor sensor data are collected and processed by the dSPACE system. The dSPACE system allows real time collection and processing of signals. A schematic of the experimental setup is shown in Fig.6.7.
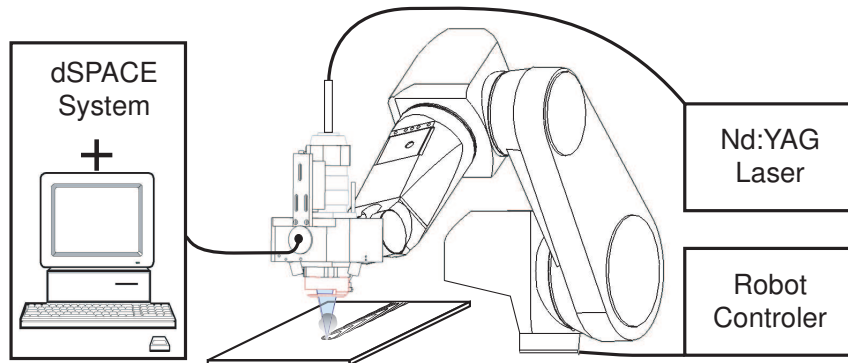
Figure 6.7: Experimental setup.

The process monitor sensor outputs a differential signal (S_{out+} and S_{out-}) to allow the elimination of noise that is accumulated by the cable between the sensor and the data acquisition system. To eliminate the signal noise the two signals are combined in dSPACE using Eq.6.1. The sampling rate of the dSPACE system was set at 2 kHz.

6.4.2 Sensor Gain Calibration

The gain calibration ensures that the right signal amplification is used for the laser welding process that is to be performed. In this calibration the the welding process is performed with a constant welding speed and a

ramping laser power. The initial gain of the signal is the smallest possible. The maximum value of the captured sensor output s_{out} is then used to identify the amount of gain G that can be applied for this welding process (Eq.6.2).

$$G = \frac{s_{max}}{s_{out}}, \qquad (6.2)$$

where s_{max} is the maximum allowable signal value, which depends on the signal processing unit that it is connected to (± 10 V or ± 15 V).

For example in Fig.6.8 the maximum sensor signal is $s_{out} = 0.75$ V and the allowable sensor output is ± 10 V. According to Eq.6.2 the optimum amplification gain is $G = 13.33$ times more than the one that is currently used. For the experiment of Fig.6.8 a gain of 100 was used, which means the the maximum allowable gain is $13.33x100 = 1333$. Since this actual value is not available by the developed sensor the closest value and below this gain must be selected. This means that a gain of 1000 is used.
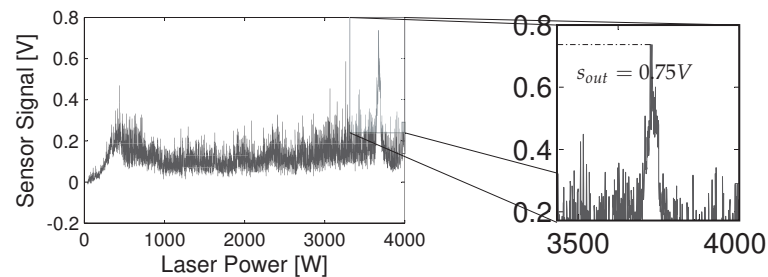
Figure 6.8: Example of a maximum value of an emission signal for the selection of the sensor's gain.

6.4.3   Experimental Results

For the experimental tests several welding jobs were performed with different welding speeds, varying from 60 to 160 mm/s. The combination of the sensor signals for processes with different welding speeds are shown in Fig.6.9. The results of the individual tests are shown in Fig.6.10. These tests were without low pass filter to examine the dynamics of the plasma emissions. For control purposes a 100 Hz low pas filter is used to distinguish the general signal trend (Postma (2003)).

In Fig.6.9 a number of the experimental results are combined in a single graph. It appears that higher welding speeds require higher laser power to achieve full penetration which also results to a higher signal level. From Fig.6.10, it is clear that the plume radiation shows a maximum which identifies the full penetration.
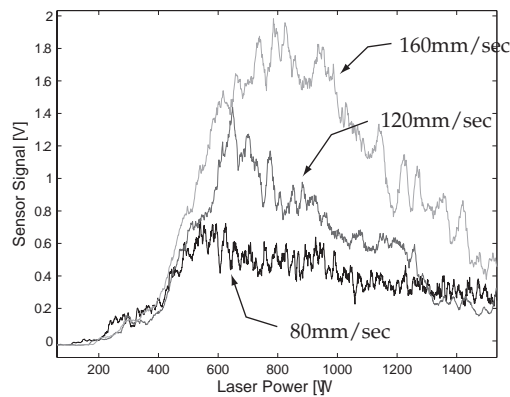
Figure 6.9: Sensor signals from different welding speeds.
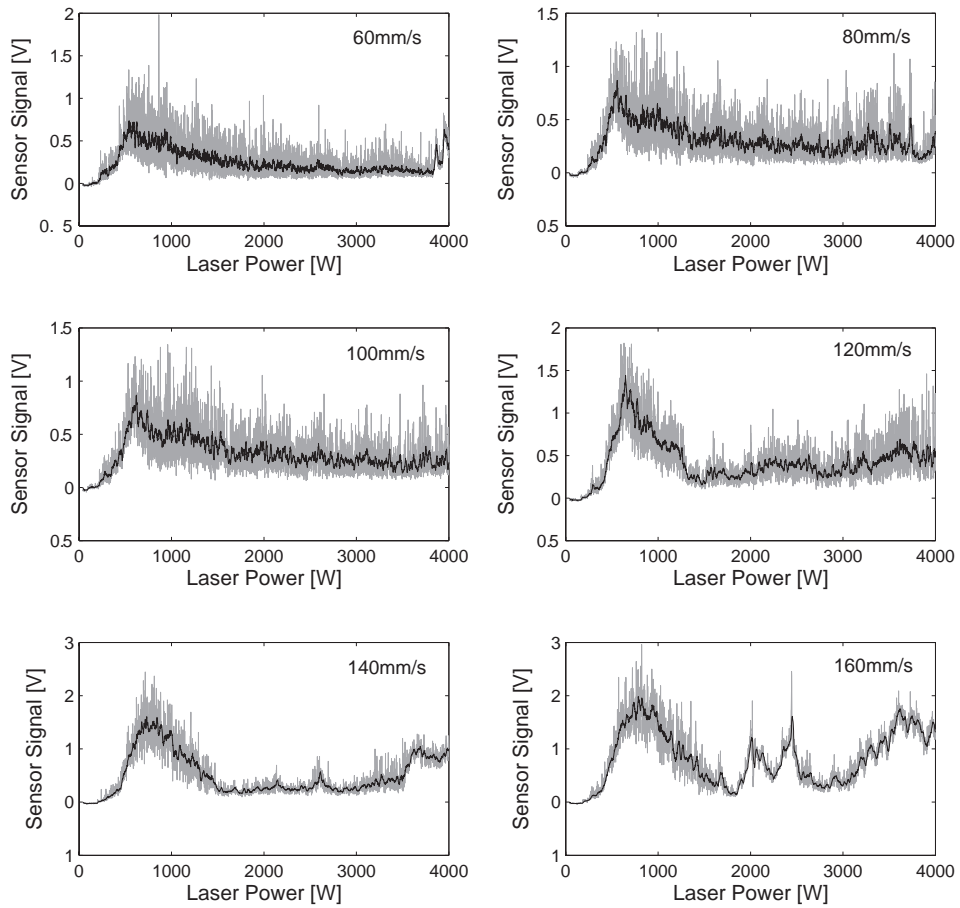
Figure 6.10: The output of the process monitor sensor for different welding speeds. The gray line is the original sensor signal, whereas the black line is observed with a low-pass filter.

152

Chapter 7

Weld Inspection

Weld inspection is the process that measures the quality of the welded seam. Within this work the weld inspection sensor uses the same triangulation principle that is used for **Seam Detection**. The triangulation setup allows the sensor to collect data about the surface topology of the welded seam. The collected data are further processed and a quality estimation is derived. Since this quality estimation is based on the surface properties of the weld, it cannot be used to derive accurate conclusions about the inner weld structure of the seam.

Due to the perimetric sensing ability of the integrated laser welding head, there is no need to maintain a relative orientation with the seam trajectory. This means that the welded part of the seam can exist on any of the sides of the triangular shape. Therefore it is important to be able to perform weld inspection on any part of the triangular perimetric shape. The diode switching functionality of the sensor system allows to perform the weld inspection on each of the triangular shape's lines individually. The process on how to collect data for weld inspection from such an image containing a single structured light line is discussed in the following paragraphs.

7.1 Definition of weld quality

Weld quality is a measure that is related to the properties and imperfections of the weld as well as the requirements for the weld job (e.g. in need of smooth weld surface or not, allow or not to have small cracks). To evaluate the weld quality, the weld properties and imperfections that are

important must be determined and measured. Furthermore, for each of the required weld properties and imperfections a set of boundaries must be provided which indicates whether the result is acceptable or not.
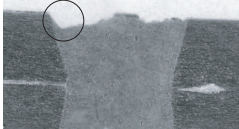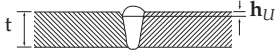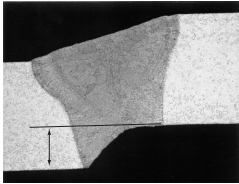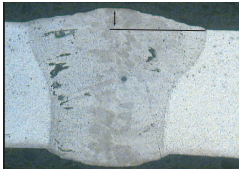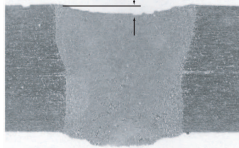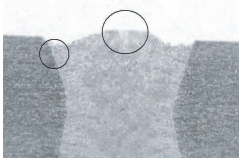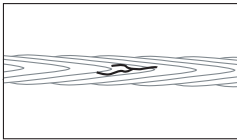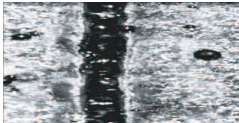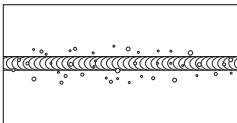
The evaluation of weld quality can be performed in a variety of ways. Two commonly used methods are the *Pass-Fail* and *Grading*. In both methods, initially, a set of weld properties has been measured. The *Pass-Fail* method simply investigates if all detected surface weld properties are within the allowable boundaries that the manufacturer has defined for the process. The *Grading* method makes use of a grading scheme. In this approach every weld property is assigned with a grade according to what extend they remain within the specified boundaries. The final welding quality is calculated by the average of all the property grades. Usually each property is accompanied by a weighting value that reflects the importance of each weld property.

7.1.1   The ISO 13919 Standard

The ISO 13919 standard (ISO13919:-2:2001 (2001) Part1 and Part2) offers guidelines for estimating the quality of a weld that was created with the use of electron or laser beam. This ISO standard is divided in two parts: the first part is for the welding of steel and the second part is for the welding of aluminium. The ISO 13919 contains a compilation of weld defects and imperfections that influence the quality of the weld. For each of the items of this compilation the acceptable limits are provided. These limits are divided in three groups, one for each level of quality that is required for the welding process's practical application. These three levels of quality are symbolized with **D** (Moderate), **C** (Intermediate) and **B** (Stringent).

The weld defects that are referred in the ISO 13919 and are related to the surface quality of the welded seam are listed in Table 7.1. The weld defects of Table 7.1 are an interpretation of the ISO standard as far as it is relevant to this work. For a more complete description of the possible weld defect the readers are advised to consult the original ISO 13919 norm (ISO13919:-2:2001 (2001) Part1 and Part2). The first column of the table shows cross sections of welded material with weld defects. The second column has drawings of the same weld defects with the measurement parameters that are necessary for the calculation of the quality. The third column has the ISO limit values for each of the defects depending on the required quality level (**D**, **C**, **B**).

Table 7.1: ISO 13919 surface weld quality property limit values.

Cross Section	ISO Sketch	Allowed Values
Undercut & Crater		**D**: $h_U \leq 0.15t \leq 2$ mm **C**: $h_U \leq 0.1t \leq 1.5$ mm **B**: $h_U \leq 0.05t \leq 1$ mm
Misalignment		**D**: $h_M \leq 0.25t \leq 3$ mm **C**: $h_M \leq 0.15t \leq 2$ mm **B**: $h_M \leq 0.1t \leq 1$ mm
Convexity		**D**: $h_C \leq 0.2 + 0.3t \leq 5$ mm **C**: $h_C \leq 0.2 + 0.2t \leq 5$ mm **B**: $h_C \leq 0.2 + 0.15t \leq 5$ mm
Sagging, Concavity		**D**: $h_S \leq 0.15t \leq 2$ mm **C**: $h_S \leq 0.1t \leq 1.5$ mm **B**: $h_S \leq 0.05t \leq 1$ mm
Crack		**D**: Not Permitted **C**: Not Permitted **B**: Not Permitted
Spatter		Depends on the application. Spatter is assumed to be of the same composition to the base and filler material.

t = Material thickness, h_U = Undercut Height, h_M = Misalignment Height, h_C = Convexity Height, h_S = Sagging Height, **D** = Moderate, **C** = Intermediate, **B** = Stringent.

7.1.2 Weld Defect Detection Methodology

The detection of a weld defect from the sensor measurement data requires several steps to be taken. The first step is to acquire the height information from the image data. This will result into a height profile, one for each of the measurements that are taken.

Further processing of the acquired height profile allows the calculation of the weld property values which are used to determine the weld quality. A distinction is made at this point between the weld defects that can be measured from each of the single height profiles, and the weld defects that require additional information. From Table 7.1 it is easy to conclude that the first four weld defects can be measured on each of the single height profile measurements, whereas additional information is required for the last two.

A series of successive height profiles obtained while the sensor moves along the welded seam, allow the three dimensional reconstruction of the surface topology. This reconstruction in used for the measurement of the last two defect of Table 7.1 (Cracks, Spatter).

Each of the measurement processes as well as the height profile acquisition will be discussed in the following paragraphs.

7.2 Sensor Requirements

For the weld inspection sensor there are two specifications: the sensor resolution and the sensor speed. The sensor resolution must be sufficient in order to detect the minimum size of the defects that are necessary for the quality estimation. From Table 7.1 it is derived that the smallest defect that is to be measured follows from the rule $\mathbf{h}_S, \mathbf{h}_U \leq 0.05t$ (Undercut, Sagging, Concavity), where t is the thickness of the material.

The sensor's resolution is about 35 μm per image pixel (x_S, y_S resolution) and about 60 μm z_S resolution. The required sensor speed depends on the speed at which the integrated laser welding head is moved over the welded seam. A measurement rate of 2-3 frames/mm is, from a practical point of view, sufficient for a weld inspection process. This means that for a robot speed of 100 mm/sec, the sensor speed must be between 200-300 frames/sec. Depending on the expected size of the weld defects, the required sensor speed can be slower or faster.
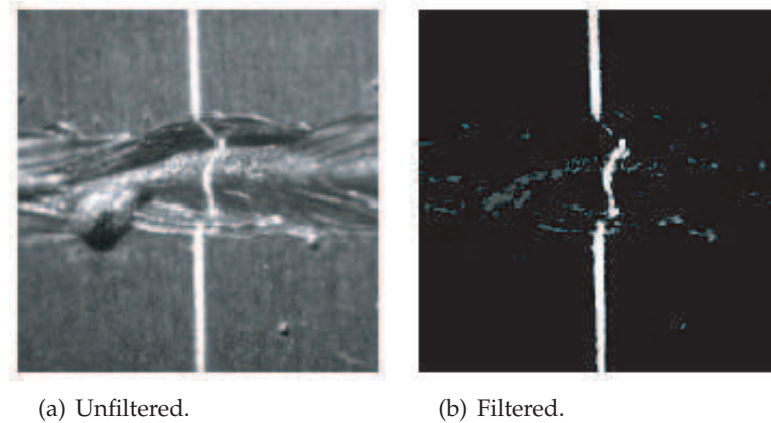
(a) Unfiltered.   (b) Filtered.

Figure 7.1: A structured light line being projected on a welded seam. Anomalies on the weld change the structured line image, which allows the acquisition of the height profile. The line can be easily distinguished from the rest of the illumination with the use of optical filters. Courtesy of Falldorf Sensors GmbH.

7.3 Height Profile Acquisition

Height profile acquisition is the process by which the height profile of a single weld measurement is obtained from the structured light line image data. Fig.7.1(a) shows a typical image from the camera in the optical triangulation setup when a structured light laser line is projected over a welded seam. With the use of the optical filters the contrast between the laser light and the background is enchained, and the selection of the necessary illumination on the image is achieved (Fig.7.1(b)). The extraction of the height profile of the weld from the captured image requires a number of steps.

Initially, a radiometric measurement on the image is performed. This means that the image is scanned along each row or column to detect the position of the pixel with the highest value at each row or column. The image scanning direction (row or column) depends on the orientation of the structured line in the image. For the image of Fig.7.2(a), the scanning direction is along the image columns. The pixel with the highest value is most likely to be a pixel that belongs to the projected structured light line (Fig.7.2(b)).

The next step is to normalize the grey level intensity of all pixels along their scanning direction according to their maximum value. This will result into an image where along the scanning direction the pixels with the

maximum intensity will be set to 1 and the remaining pixel intensities become:

$$\hat{p}_{u,v} = \frac{p_{u,v} - min_{sd}}{max_{sd} - min_{sd}}, \tag{7.1}$$

where $\hat{p}_{u,v}$ is the intensity of the normalized pixel at image coordinates u and v, $p_{u,v}$ is the original image pixel intensity at image coordinates u and v, min_{sd} is the minimum pixel intensity along the scanning direction sd and max_{sd} is the maximum pixel intensity along the scanning direction sd, the scanning direction sd can be either row or column wise.

The normalization operation can give rise to noise in an image, especially in cases were the maximum pixel value along the scanning direction is close to its minimum pixel value. Such normalization noise may appear when the sensor is out of focus. For these cases image enhancement operations (Grooth (2006)) can be applied to suppress the noise which has been amplified by the normalization process and to preserve the original projected structured light line in the image.

After the normalization operation has been performed (Fig.7.2(c)), a threshold operation is applied on the enhanced image to separate the background pixels from the structured light line. The threshold algorithm converts to background pixels (zero intensity) all pixels below the threshold value and leaves the rest of the pixel intensities unchanged. This is implemented by:

$$\check{p}_{u,v} = \begin{cases} \hat{p}_{u,v}, & \hat{p}_{u,v} \geq 0.7 \\ 0, & \hat{p}_{u,v} < 0.7 \end{cases} \tag{7.2}$$

The result of this operation is shown at Fig.7.2(d).

The final step is the actual identification of the position of the structured light line pixels in the image. For this purpose the center of gravity of the structured light line pixels in each row or column needs to be calculated. For this to be possible, the row or column pixels that might belong to the projected structured light line must first be identified. The structured light line pixels are most likely to exist near the pixel with the highest value (at each row or column). To determine the distance, from the pixel with the highest value, at which a pixel is still assumed to belong to the structured light line, the standard deviation σ_p of pixels along each row or column sd is calculated.

(a) Original Image.

(b) Radiographic Result.

(c) Normalized Image.

(d) Thresholded Image.

(e) Standard Deviation.
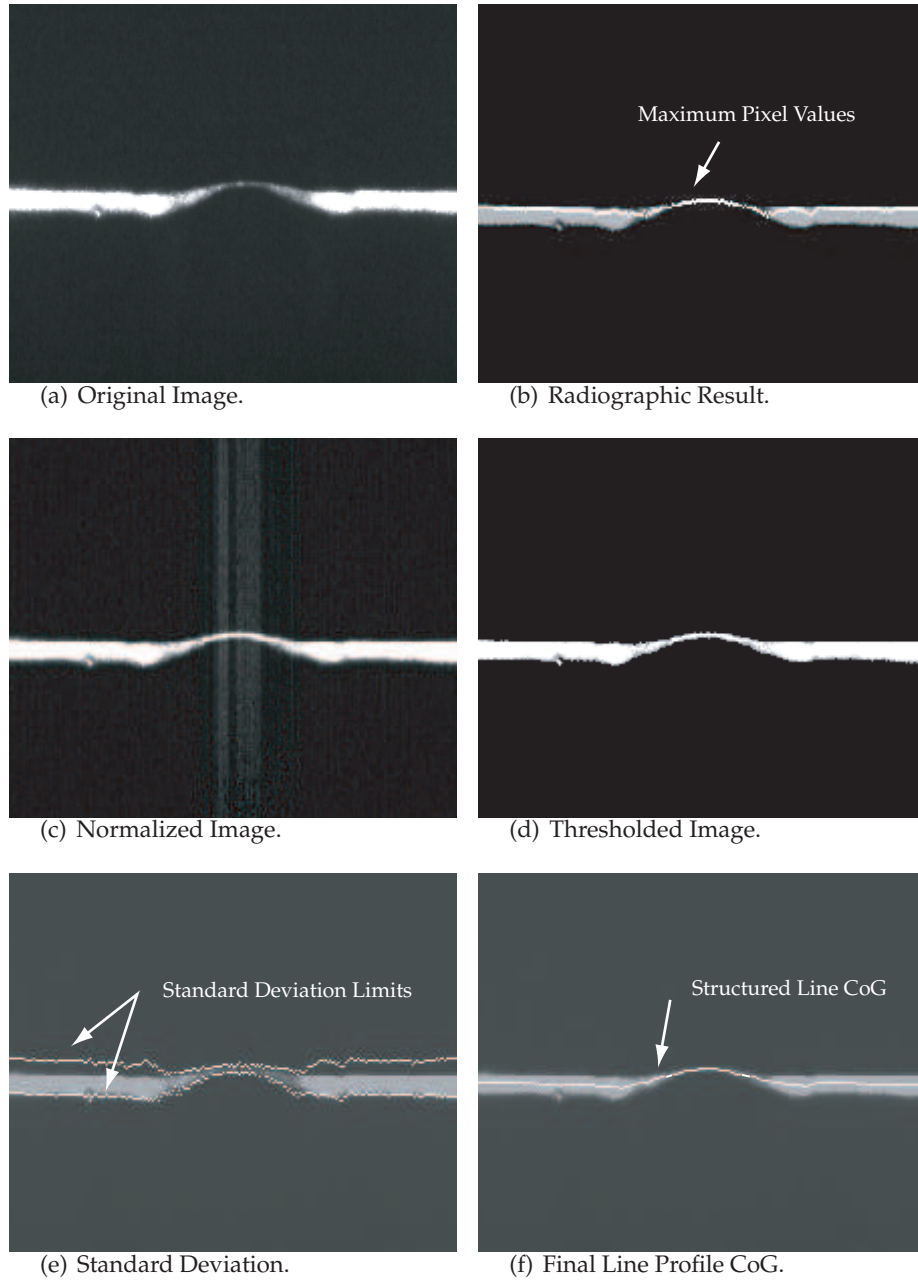
(f) Final Line Profile CoG.

Figure 7.2: The steps for the detection of the height profile points along the structured light line. The scanning direction for these images is along the rows.

$$\sigma_{p,sd} = \sqrt{\frac{\sum_{k=1}^{M}(\mu_{sd}-n_k)^2}{M}}, \tag{7.3}$$

$$\tag{7.4}$$

with

$$\mu_{sd} = \frac{\sum_{k=1}^{M}n_k}{M} \tag{7.5}$$

where $\sigma_{p,sd}$ is the standard deviation for row or column sd, M is the number of non-zero pixels in the scanning direction (row or column), n_k is the position of non-zero intensity pixels along scanning direction sd and μ_{sd} is the mean value of the non-zero pixel positions along scanning direction sd.

To ensure that all of the structured light line pixels are used in the calculation of the center of its gravity, an area of two times the value of the calculated standard deviation $\sigma_{p,sd}$ (Fig.7.2(e)) is used. Then the detected projected structured light line position on the image can be calculated by,

$$CoG_{sd} = \frac{\sum_{j=K}^{N}j\check{p}_{j,sd}}{\sum_{j=K}^{N}\check{p}_{j,sd}}, \tag{7.6}$$

with

$$K = m_{sd} - 2*\sigma_{p,sd} \ \ and \ \ N = m_{sd} + 2*\sigma_{p,sd}, \tag{7.7}$$

where CoG_{sd} is the position along the search direction sd which carries the structured light line pixel, $\check{p}_{j,sd}$ is the intensity of the thresholded pixel in position j and m_{sd} is the position of the pixel with the highest value in scanning direction sd.

The final result of the height profile process can be seen in Fig.7.2(f)as the CoG line. The position of the white pixels on each column is a direct measure of height of the underlying surface, as it will be outlined in the next section.
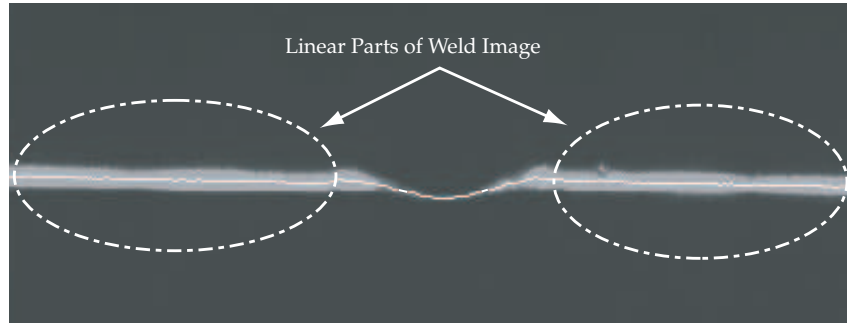
Figure 7.3: Linear parts of projected structured light line.

7.4 Single Height Profile Measurements

Once the height profile *CoG* is available the single height profile measurements are performed. Nevertheless, before the actual measurement take place it is important to identify which part of the height profile belongs to the weld and which to the non-welded surface. This distinction of the height profile parts assists in the further calculation of the weld defects. As is shown in Fig.7.3 the non-welded parts appear as lines at the structured light's image whereas the weld appears as an anomaly.

The initial step is to convert the height profile data from pixels to mm. This is implemented with the use of the reference line (§4.3.2) which will also link the height profile to the sensor's TCP_S. In Fig.7.4(a) the image height profile CoG and the corresponding sensor reference line are shown, both expressed in image pixels. For each pixel along the height profile, its distance to the reference line is calculated. Then the actual height position $z_{CoG,j}$ of the pixel j can be calculated according to Eq.7.8.

$$z_{CoG,j} = \frac{\delta_{p,j}}{c_p \tan \phi},$$

(7.8)

where $\delta_{p,j}$ is the distance between the pixel j of the height profile and the reference line in the image, ϕ is the projection angle of structured light diode and c_p is the mm to pixels ratio.

The result of this process is shown in Fig.7.4(b). The application of a first order difference function on the height profile is used to reveal the position of the weld anomaly in the height profile. This difference is computed as:

$$\delta z_{CoG,j} = \frac{z_{CoG,j+1} - z_{CoG,j}}{(j+1) - j} = z_{CoG,j+1} - z_{CoG,j} \ , \tag{7.9}$$

As seen in the result plotted at Fig.7.4(c), at the coordinates where the anomaly exists on the height data there is a concentration of either positive of negative spikes. In the linear part, if the spikes occur, they interchange between positive and negative. A 40-point moving average function is applied on the difference data. This means that the data are formed in groups of 40 consecutive points and their average slope k_j is computed.

$$k_j = \frac{z_{CoG,j+21} - z_{CoG,j-20}}{41}, \tag{7.10}$$

where j increases by steps of 20 ($j = 20, 40, 60,\ldots$), which means that each group has 50% overlap with its neighboring groups. The results of the moving average is plotted in Fig.7.4(d).

In the case where the height profile in not exactly parallel to the TCP_S x-y plane, the average slope k_{av} will be non-zero. For the cases where the welded parts form a corner joint configuration additional processing must be performed, which is not dealt with in this thesis.

The moving average result is used to identify the boundaries of the weld. The weld is most likely to exist where slopes differ from the average slope. Initially, the center of gravity (h_{CoG}) of the weld anomaly is identified with the use of Eq.7.11
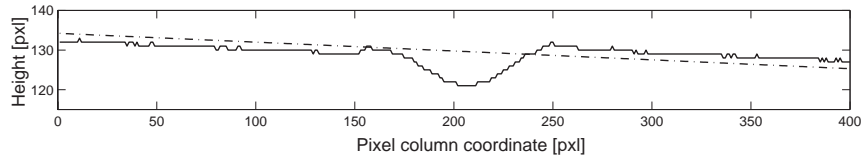
$$h_{CoG} = \frac{\sum_{j=1}^{L} K_j j}{\sum_{j=1}^{L} K_j}, \tag{7.11}$$
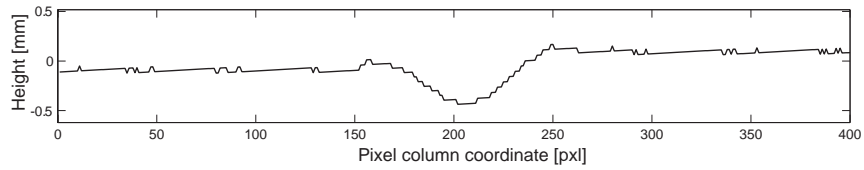
with,

$$K_j = \begin{cases} 1, & k_j - k_{av} \geq 0.002(k_{max} - k_{av}) \\ 1, & k_j - k_{av} \leq -0.002 \\ 0, & -0.002 < k_j - k_{av} < 0.002 \end{cases} \ , \tag{7.12}$$

where k_{av} is the average slope of the height profile, k_j is the value of the average slope at point j, K_j are the points that satisfy the condition of Eq.7.12 and L are the number of K_j points.
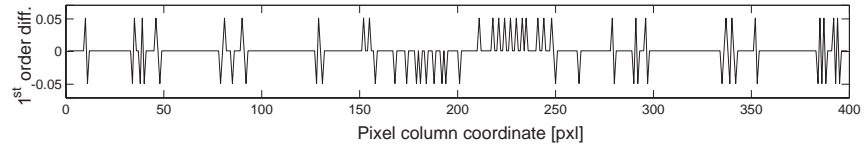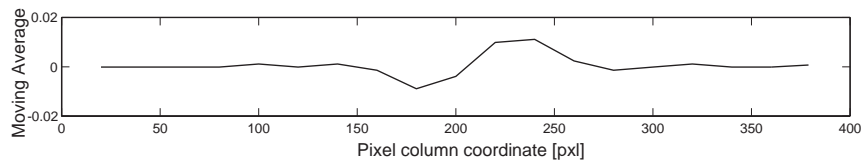
(a) The weld height profile in image pixels (-) and the structured light reference line (-.-).
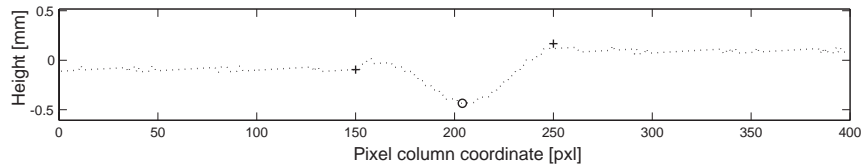

(b) The weld height profile in mm.

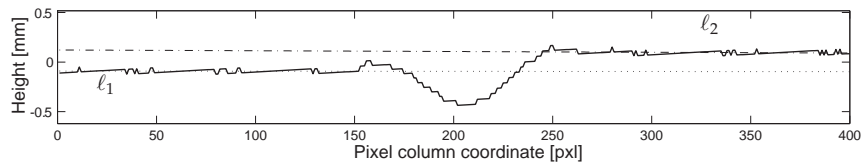(c) The 1st order difference of the height data.

(d) The moving average result k_j.

(e) The weld height profile in mm ($\cdots$), with the calculated h_{CoG} ($\circ$) and the two points at a distance of the standard deviation σ_{var} (+).

(f) The weld height profile in mm (-), with the calculated lines ℓ_1 ($\cdots$) and ℓ_2 (-.-) for the weld image linear parts.

Figure 7.4: The steps for the detection of the height profile points along the structured light line. The scanning direction for these images is along the columns.

Upon identification of the h_{CoG} point, the standard deviation σ_{var} of the moving average points is calculated (Eq.7.13). The σ_{var} is an estimate of the distance of the edges for the weld anomaly from the h_{CoG}. The height data that exist between the $h_{CoG} - \sigma_{var}$ and $h_{CoG} + \sigma_{var}$ coordinates are most likely to belong to the weld anomaly.

$$\sigma_{var} = \sqrt{\frac{\sum_{j=1}^{L}(K_j j - h_{CoG})^2}{L}}, \tag{7.13}$$

The calculated h_{CoG} and standard deviation values σ_{var} are shown in Fig.7.4(e).

Since the part of the height profile where the weld anomaly exists is identified, the linear parts of the height profile can also be extracted. This is implemented by fitting lines ℓ_1 and ℓ_2 to the height profile data.

$$
\begin{aligned}
\ell_1 : \quad & z_{CoG,j} = a_{\ell_1} j + b_{\ell_1} \\
\ell_2 : \quad & z_{CoG,j} = a_{\ell_2} j + b_{\ell_2}
\end{aligned}
, \tag{7.14}
$$

The height values $p_{h,j}$ that are used for the fitting of the lines are selected according to the condition:

$$
\begin{aligned}
for \ \ell_1 : \quad & 1 \leq j \leq h_{CoG} - \sigma_{var} \\
for \ \ell_2 : \quad & h_{CoG} + \sigma_{var} \leq j \leq E
\end{aligned}
, \tag{7.15}
$$

were j is the coordinate (of the scanning direction) of the height data that takes part in the line fitting, $z_{CoG,j}$ is the height value in mm and E is the total number of height values (in the case of the example of Fig.7.4 $E = 400$). The result of the line fitting is shown in Fig.7.4(f).

There are several cases where the process does not produce information for the identification of both lines ℓ_1 and ℓ_2. These are the cases where the weld is perfect or the weld exist near the edges of the height profile.

In the first case the values of the average slope k_j are between the -0.002 and 0.002 threshold values, which allow all the moving average data to participate in the calculation of the standard deviation σ_{var}. In this case only one line is fitted on all the height profile data.

In the latter cases, where the weld exists near the edge of the height profile, one of the two lines ℓ_1 and ℓ_2 is not identifiable. At these cases only one of lines is identified and used for the weld defect measurements.

With the identification of the linear parts, the calculation of the weld properties can start. The identification of the two linear parts ℓ_1 and ℓ_2 will assist in the calculation of the several weld imperfections as it is shown in the following paragraphs.

7.4.1 Weld Width h_W

The weld width is not a property that is directly connected with the quality of the weld. The surface quality of the weld is unaffected by it. Nevertheless, the weld width is related to the laser welding process. Fluctuations of the weld width are an indication of an unstable laser welding process.

The weld width is defined as the distance between the two edges of the weld (Fig.7.5(a)). The identification of the weld edges is performed with the use of the identified lines ℓ_1 and ℓ_2 and the height profile data. An example of the result of such a weld detection process is shown in Fig.7.5(b), in which case as weld width is either the distance between points A and E_R or the distance between points B and E_L.
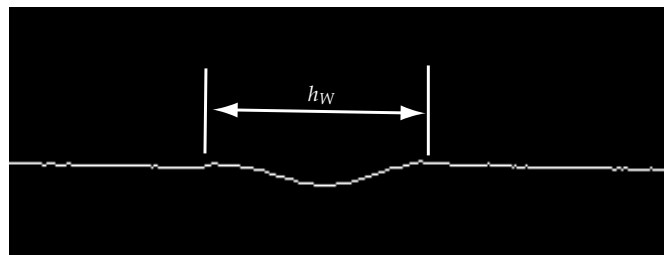
(a) Height profile of a weld in an image. The weld width and its limits are also noted.
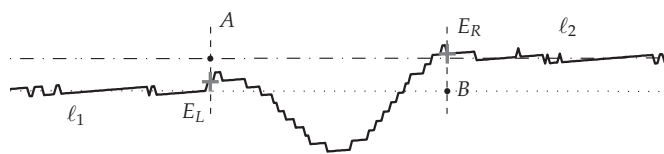
(b) Sketch of the height data of a weld, with the identified lines (ℓ_1, ℓ_2), the weld edges (E_L, E_R) and their projections on the lines (A, B).

Figure 7.5: Image of a height profile and definition of the points that are used for the calculation of the weld width.

The calculation of the weld width requires the identification of the

weld edges E_L and E_R. For E_L the distances of the pixels of the height profile, form left to right, are calculated. As E_L is selected the point after which the absolute value of the distance between the ℓ_1 and the height data is bigger than 0.06 mm (about 1 pixel). A similar approach is used for the E_R, with the only difference is that the distances used are between ℓ_2 and the height data, and the search for E_R is performed from right to left.

Upon identification of E_L and E_R, the calculation of the weld width h_W is performed in relation to the lines ℓ_1 and ℓ_2 from Eq.7.16.

$$
\begin{aligned}
for \ \ell_1 : \ & h_{W,\ell1} = d_{E_L,B} \\
for \ \ell_2 : \ & h_{W,\ell1} = d_{E_R,A}
\end{aligned} \ , \tag{7.16}
$$

where $d_{E_L,B}$ and $d_{E_R,A}$ are the distances between the points E_L, B and E_R, A, with the points A, B being the projections of E_R on line ℓ_1 and E_L on line ℓ_2 respectively (Fig.7.5(b)).

Depending on the slope of the lines ℓ_1 and ℓ_2, the values of $h_{W,\ell1}$ and $h_{W,\ell2}$ may be different. For reasons of consistency, the weld width value is calculated only in respect to one of the lines ℓ_1, ℓ_2 along the full weld length.
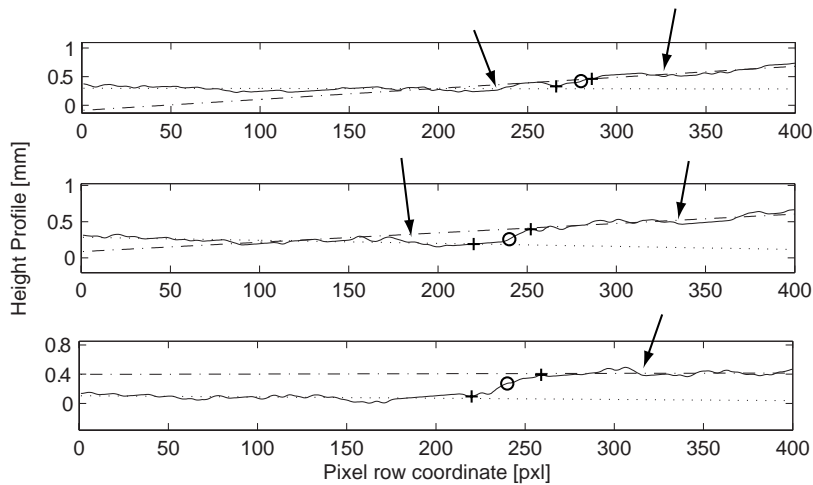

Figure 7.6: Several examples of height profile data with the detected edges E_L and E_R (+) and h_{CoG} (∘) as detected by the weld inspection sensor. The arrows indicate positions where the weld edges could also possibly exist.

Even though the task of identifying the weld edges might be trivial for the human eye, it can be quite an elaborate work for the weld inspection

sensor. This is because humans do not rely on just one type of measurement to arrive to a conclusion, which is the reality for the inspection sensor. For instance, the overall surface appearance and neighboring height profiles may provide valuable extra information. As it can be seen in the examples of Fig.7.6 the weld edge detection becomes more difficult even for humans when only one type of data is available. Within this work, the detection of the weld width is performed with the process previously described with the use of the measured height profile, without the combination of additional external measurement data.

7.4.2 Undercut & Crater h_U

As shown in Table 7.1, undercuts and craters appear as discontinuities along the weld surface. The difference between the undercut and the crater is that the undercut weld defect appears close to the weld edge.

(a) Image representation of Undercut/Crater height profile.
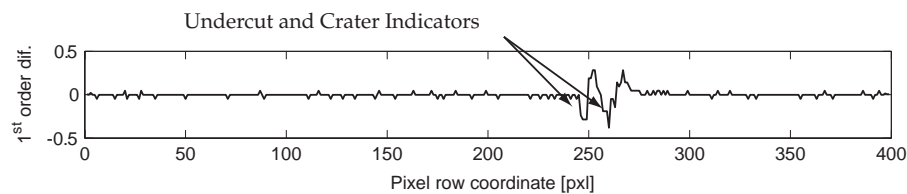
(b) 1st order difference of the height profile. The arrows indicate spikes that appear from the existence of the craters/undercuts.
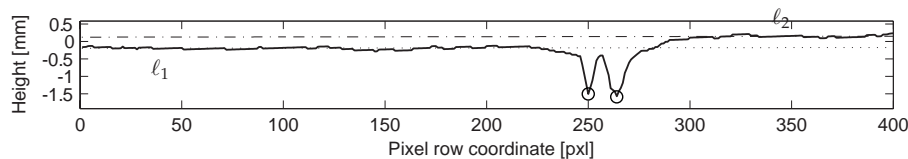
(c) Positions of the craters and undercuts ($\circ$) on the height profile.

Figure 7.7: Undercut image example and height profile measurement.

The existence of undercuts and craters is identified by the 1st order difference of the height data. In Fig.7.7(b) it is shown that there are two
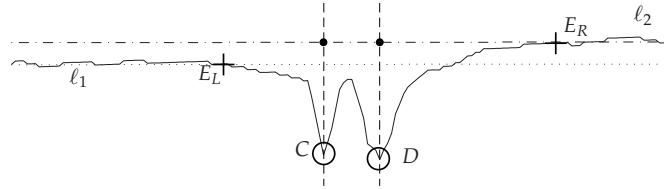
Figure 7.8: Two crater points (∘) detected on the height data. The E_L and E_R points (+) indicate the position of the weld edges.

spikes which are lower than the rest of the plot. This indicates that at these coordinates there is a sudden drop in the height profile. This drop might further continue with a smaller slope. The value for the undercut/crater depth h_U is the maximum depth in the height profile, or more precisely:

$$h_U = d_{\ell,z} \ ,\tag{7.17}$$

where $d_{\ell,z}$ is the maximum local distance between the identified lines (ℓ_1, ℓ_2) and the height data z_{CoG}, which exists after the detected sudden drop and before this distance remains unchanged or becomes smaller.

In the example of Fig.7.8, two such points C and D have been detected. It can be seen that both points C, D do not exist near the detected edge of the weld and therefore are classified as craters.

7.4.3   Misalignment h_M

The misalignment weld defect, is related to the wrong alignment of the material that is to be welded (Table 7.1). Accurate detection of misalignment defects requires that both linear parts (ℓ_1,ℓ_2) can be identified from the image (Fig.7.9(a)). In the case only one of the linear parts is identifiable (Fig.7.9(b)), an estimation of the misalignment can also be made, but the results may not be physically meaningful.

Fig.7.10 shows a generic misalignment case where both linear parts are identifiable but they are not parallel. When both linear parts ℓ_1, ℓ_2 are identifiable the misalignment value h_M is calculated by the distances $d_{E_L,A}$ and $d_{E_R,B}$ of the weld edge points E_L, E_R to the lines ℓ_1 and ℓ_2 respectively.

$$\begin{aligned}
for \ \ell_1 : \ \ h_{M,\ell 1} &= d_{E_L,A} \\
for \ \ell_2 : \ \ h_{M,\ell 2} &= d_{E_R,B}
\end{aligned} \ ,\tag{7.18}$$

(a) Image where both linear parts are present.
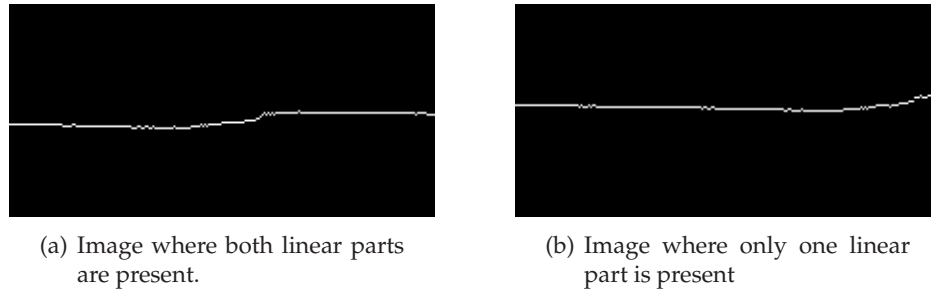
(b) Image where only one linear part is present

Figure 7.9: Image samples with detected the height profile line, for the two possible misalignment cases.
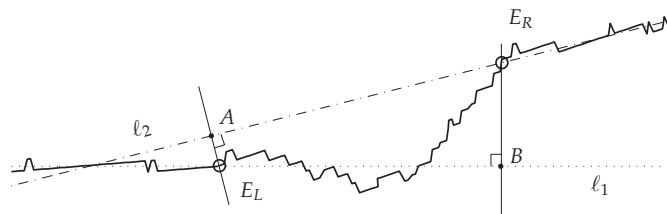

Figure 7.10: Sketch for the calculation of the misalignment height h_M when both linear parts ℓ_1 and ℓ_2 are identifiable.

There is no rule to decide which of the two values $h_{M,l1}$ and $h_{M,l2}$ is to be used for the measurement of the misalignment value, as the ISO standard does not cover the cases where the two linear parts ℓ_1 and ℓ_2 are not parallel. There are two solutions that are meaningful. The first one is to select one way of calculating the misalignment value (either $h_{M,l1}$ or $h_{M,l2}$) for the full inspection process. The other is to use the value that was calculated with the linear part that is closer to perpendicular with the high power laser's optical axis.

When only one linear part of the structured light line is visible then the misalignment can be estimated as the distance of the last point of the weld to the identified linear part (Fig.7.11)

$$h_M = d_{C,\ell 1} \ , \tag{7.19}$$

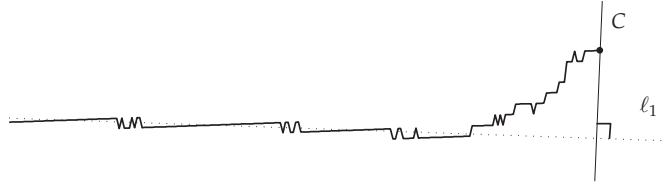where C is the last point of the weld height data.

Figure 7.11: Sketch for the calculation of the h_M when only one of the linear parts is identifiable.

7.4.4 Convexity h_C

Convexity is the excess of metal at the weld. This appears as a bump on the top or bottom side of the weld and is also visible in the sensor image (Fig.7.12(a)). The value for convexity can be calculated by the maximum positive distance between the height profile z_{CoG} and each of the identified lines ℓ_1 and ℓ_2. To acquire that value first the existence of a convex surface must be determined. A parabola of type $z = \alpha j^2 + \beta j + \gamma$ is initially fitted to the weld data (points between the weld edges E_L and E_R as shown in Fig.7.12(b)). For convexity the coefficient of the quadratic term must be negative. If the parabola vertex point is close (less than $0.2 x h_W$ mm) to the edges of the weld (E_L, E_R) then there is no convexity in the weld. Otherwise the height profile is scanned for its maximum value. As seen in Fig.7.12(c), point H of the height profile is the one that is furthest from lines ℓ_1 and ℓ_2.

The ISO 13919 standard offers guidelines for the detection of convexity only for the cases that the linear parts ℓ_1 and ℓ_2 are parallel. Nevertheless, in this work a set of rules has been defined that can provide meaningful results for the existence and value of convexity h_C, also for the cases that ℓ_1 and ℓ_2 are not parallel. These rules are:

- If the parabolic fit exists between the lines ℓ_1 and ℓ_2, then there is no convexity.

- If convexity exists, then $d_{H1,\ell1}$ and $d_{H2,\ell2}$ are calculated, which are the maximum distances of the lines ℓ_1 and ℓ_2 to the height profile.

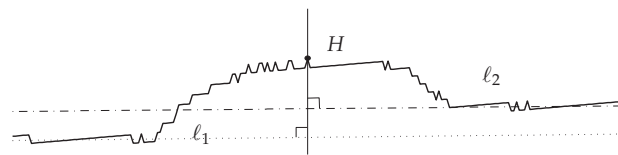- If there is no misalignment between ℓ_1 and ℓ_2 then $H_1 = H_2 = H$:

$$h_C = d_{H,\ell1} = d_{H,\ell2} \tag{7.20}$$

(a) Image representation of convexity height profile.
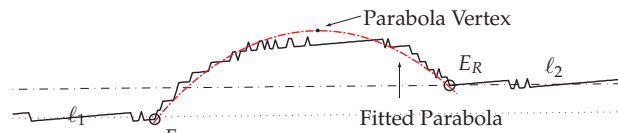
(b) Fitting parabola to points between the weld edges.

(c) Measurement of convexity h_C from a height profile.

Figure 7.12: Convexity image example and height profile measurement.

- If there is a misalignment between ℓ_1 and ℓ_2, and ℓ_1 is parallel to ℓ_2, then again $H_1 = H_2 = H$ (Fig.7.12(c)) and convexity h_C is calculated from

$$h_C = \min(d_{H,\ell 1}, d_{H,\ell 2}) \tag{7.21}$$

- If ℓ_1 is not parallel to ℓ_2, then the points H_1 and H_2 do not coincide. For this case there are two resulting values $h_{C,\ell 1}$ and $h_{C,\ell 2}$ for the convexity:

$$h_{C,\ell 1} = d_{H1,\ell 1} \ \text{ and } \ h_{C,\ell 2} = d_{H2,\ell 2} \tag{7.22}$$

In this case, for consistency reasons, one of the ways to calculate convexity must be selected and used along the rest of the seam inspection process. In this work the convexity value for this case is calculated with the use of $h_{C,\ell 1}$.

7.4.5 Sagging & Concavity h_S

Sagging and concavity are the weld defects that appear as a dent on the top side of the weld. When sagging occurs, the bottom side of the weld is pulled down by gravity and is convex (Table 7.1). Concavity on the other hand occurs from insufficient existence of material and there is no convexity on the bottom side of the weld.

The value for sagging and concavity is calculated in a similar manner as the one of convexity. A parabola of type $z = \alpha j^2 + \beta j + \gamma$ is fitted in the data between the weld edges to determine the possibility of the existence of a concavity. For concavity the coefficient of the quadratic term must be positive. The value h_S can be calculated by the maximum negative distance between the weld surface points and the identified linear parts. As seen in Fig.7.13(b), point A of the height profile is the one that is furthest from lines ℓ_1 and ℓ_2.

Similar to the convexity case also for the concavity the following rules are followed to determine its existence and value h_S.

- If the parabolic fit exists between the lines ℓ_1 and ℓ_2, then there is no concavity or sagging.

- If concavity exists, then $d_{H1,\ell 1}$ and $d_{H2,\ell 2}$ are calculated, which are the maximum distances of the lines ℓ_1 and ℓ_2 to the height profile.

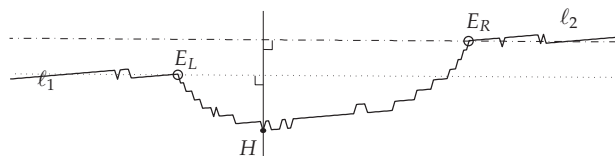- If there is no misalignment between ℓ_1 and ℓ_2 then $H_1 = H_2 = H$ then concavity is calculated by:

$$h_S = d_{H,\ell 1} = d_{H,\ell 2} \qquad (7.23)$$

- If there is a misalignment between ℓ_1 and ℓ_2, and ℓ_1 is parallel to ℓ_2, then again $H_1 = H_2 = H$ (Fig.7.12(c)) and concavity h_S is calculated from

$$h_S = \min(d_{H,\ell 1}, d_{H,\ell 2}) \qquad (7.24)$$

(a) Image representation of concavity height profile.

(b) Measurement of concavity h_S from a height profile.

Figure 7.13: Concavity/Sagging image example and height profile measurement.

- If ℓ_1 is not parallel to ℓ_2, then the points H_1 and H_2 do not coincide. For this case there are two resulting values $h_{S,\ell1}$ and $h_{S,\ell2}$ for the concavity or sagging:

$$h_{S,\ell1} = d_{H1,\ell1} \ \text{and} \ h_{S,\ell2} = d_{H2,\ell2} \tag{7.25}$$

  In this case, for consistency reasons, one of the ways to calculate concavity or sagging must be selected and used along the rest of the seam inspection process. In this work the concavity or sagging value for this case is calculated with the use of $h_{S,\ell1}$.

7.5 Surface 3D Reconstruction

The three dimensional reconstruction of the weld is performed by the concatenation of weld height profiles that are obtained from the individual seam inspection measurements. Attempting the 3D reconstruction of the raw image data without further processing will result to an image similar to the one of Fig.7.14(a), where the unprocessed concatenation of 80

height measurements is shown. Such 3D reconstruction has no clear physical meaning, because the changes of position and orientation of the sensor during measuring are not accounted in the reconstruction and the units of plot are not the same (x_n is the number of the measurement, y_{pxl} is the the number of rows or columns of the image scanning directions in Pixels, and z_{pxl} is the height profile in image Pixels). To achieve a true 3D reconstruction of the weld, the sensor parameters and sensor positions and orientations must be taken into account.

The sensor parameters (pixel to mm ratio, projection angle, etc) are used to transform all axes of the 3D plot in equal units. This is known as *Passive* reconstruction and the result is a ribbon-like surface like the one of Fig.7.14(b) ($x_{mm,s}$ is the travel distance in mm, $y_{mm,s}$ is the scanned width in mm, and $z_{mm,s}$ is the height profile in mm in the sensor's coordinate frame). *Active* reconstruction uses the sensor position and orientation data to compensate for position and speed changes of the sensor. This allows the actual reconstruction not only of the weld height profile but also of the seam trajectory as shown in Fig.7.14(c) ($x_{mm,w}$ is the actual traveled distance between measurements in mm, $y_{mm,w}$ is the scanned width in mm, and $z_{mm,w}$ is the height profile in mm in the world coordinate frame). Both methods (*Passive*, *Active*) are explained in the following paragraphs.

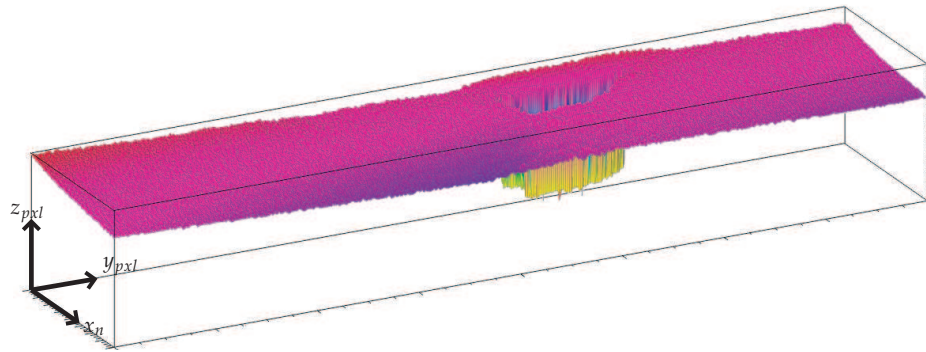### 7.5.1 Passive Reconstruction

In *Passive* reconstruction only the sensor parameters are used. This means that the y and z axis of Fig.7.14(a) are converted into mm according to:

$$y_{mm} = \frac{y_{pxl}}{c_p} \quad , \quad z_{mm} = \frac{z_{pxl}}{c_p \tan \phi} \quad , \tag{7.26}$$

where c_p is the pixel-to-mm ratio, ϕ is the projection angle of the structured line, y_{pxl} and z_{pxl} are the height profile values in pixels, and y_{mm}, z_{mm} are the resulting values of the height coordinates in mm.

The task that remains is to determine how the several height profile measurements are to be concatenated with each other. This means that two parameters have to be determined: the distance between two consecutive measurements d_{3D}, and their orientation a_T around the x axis.
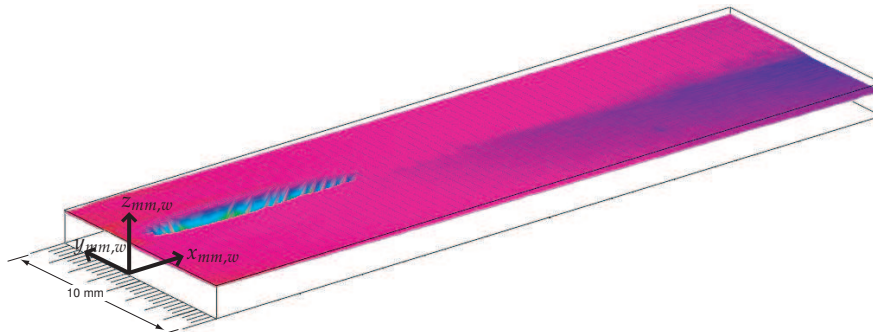
The d_{3D} can be approximated by the mean velocity of the robot $\bar{u}_R$ and the measuring speed of the sensor f_S:

(a) 3D reconstruction of raw image data.
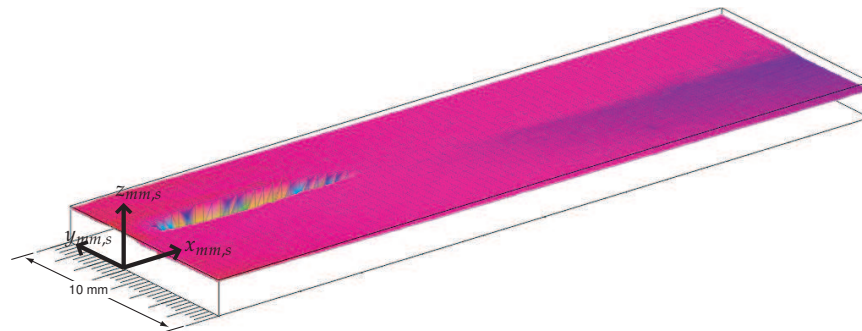
(b) *Passive* 3D reconstruction. The axes scales are equal.

(c) *Active* 3D reconstruction. The axes scales are equal.

Figure 7.14: The three different types of 3D Reconstruction. The differences are related to the consistency of the axes' units and the axes' scales. Variations in color between (b) and (c) indicate the differences between Passive *and* Active *reconstruction.*

$$d_{3D} = \frac{\bar{u}_R}{f_S} \; , \tag{7.27}$$

the result of which is expressed in mm/frame. For example, if the sensor measures at 100 frames/sec and the robot moves the sensor with a speed of 150 mm/sec, then the resulting d_{3D} is 1.5 mm/frame.

Since the robot positions and orientations are not available in the *Passive* reconstruction, a mechanism must be devised to reduce noise (positional or rotational) from vibrations. In *Passive* reconstruction it is assumed that at least part of each of the height profiles belong on the same plane. For this reason initially the lineal parts ℓ_1 or ℓ_2 are used to align the several height profiles. Furthermore, it is desirable to be able to reconstruct possible changes of the 3D surface's orientation. This can be implemented with the help a_T. The a_T is the orientation at which a new height profile is going to be aligned with the previous ones. To be able to disctinguish a real change of orientation from noise, the following smoothing filter is applied on the estimated a_ℓ of one of the identified linear parts of the height profile:

$$a_{T,x_n} = (1 - \gamma)a_{T,x_n-1} + \gamma a_{\ell,x_n} \; , \tag{7.28}$$

where, x_n is the number of the height profile measurement, $a_{\ell,j}$ is the identified slope of one of the linear parts (ℓ_1, ℓ_2) of the height profile for measurement x_n, a_{T,x_n} is the slope that will be applied to the current height profile, γ is the forgetting factor of the filter (in this work $\gamma = 0.1$) and a_{T,x_n-1} is the slope that was calculated for the previous measurement.

Once the individual measurements of the welded seam are combined topologically, the three dimensional reconstruction of the welded seam is resulted Fig.7.14(b).

7.5.2 Active Reconstruction

In *Active* reconstruction, the calculation of the distance d_{3D} between two consecutive measurements, and their orientation a_T around the x axis is calculated with the help of robot positioning data. All height measurements are expressed in a fixed world coordinate system (e.g. the base of the robot). For this purpose together with each weld surface measurement, the sensor TCP_S position and orientation in world coordinates is

also stored. Therefore the transformation $^S_B T$ from the robot base to the triangulation sensor is also known for each of the sensors measurements. Each of the height profile's pixel coordinates are converted in mm with the use of Eq.7.26 (same as *Passive* reconstruction).

The next step is to calculate the position of the structured line pixels in relation to the fixed robot base frame. This calculation is implemented by:

$$
\begin{bmatrix} x_{mm,w} \\ y_{mm,w} \\ z_{mm,w} \\ 1 \end{bmatrix} = {}^S_B T \begin{bmatrix} z_{mm,s} \ \tan\phi \\ y_{mm,s} \\ z_{mm,s} \\ 1 \end{bmatrix} , \qquad (7.29)
$$

where $[x_{mm,w}\ y_{mm,w}\ z_{mm,w}]$ are the world coordinates of a given point of the height profile, $[z_{mm,s}\ \tan\phi\ y_{mm,s}\ z_{mm,s}]$ are the coordinates of the same point in the sensor coordinate frame, ϕ is the projection angle of the structured light diode.

By plotting the processed results from each captured image, the reconstructed 3D height profile of Fig.7.14(c) is obtained. Even though the *Active* reconstruction converts the x axis in mm, in several plots it is convenient to use the measurement number instead of the mm scale. This allows an immediate identification of the height profile that the weld defect is identified in.

7.6 Reconstructed Surface Measurements

Surface measurement involve the identification of spatter and cracks in the weld. From these two only the detection of spatter will be further explained, as cracks are not accurately detected by triangulation. In addition the weld width can also be measured from the reconstructed surface and work that is conducted in that direction is also presented in the following paragraphs.

Weld Width

As was outlined in §7.4.1, additional information can assist in a more accurate detection of the weld edges. Such information can be acquired in various ways, one of which is by keeping a history of the already detected edges and search for the new ones only around the area where the previous ones where found. Another solution is to capture a complete image

of the weld and detect the edges using texture analysis. Work has been conducted towards the use of prior knowledge for the correct detection of the weld edges. More precisely, the application of plane fitting and *snake* algorithms has been investigated.

To determine the edges of a weld by plane fitting, a number of consecutive height profile measurements are used. First on each side of the weld linear parts of the height profiles are fitted as in §7.4.1. Next, a plane fit is applied to the linear parts on either side of the weld.

The edges of the weld are then identified from the junction points of the identified planes and the reconstructed surface. In Fig.7.15 such a plane fitting example is shown. The results of the plane fitting method in Fig.7.15(d), are comparable with the one of the single line fit and do not introduce any improvement.
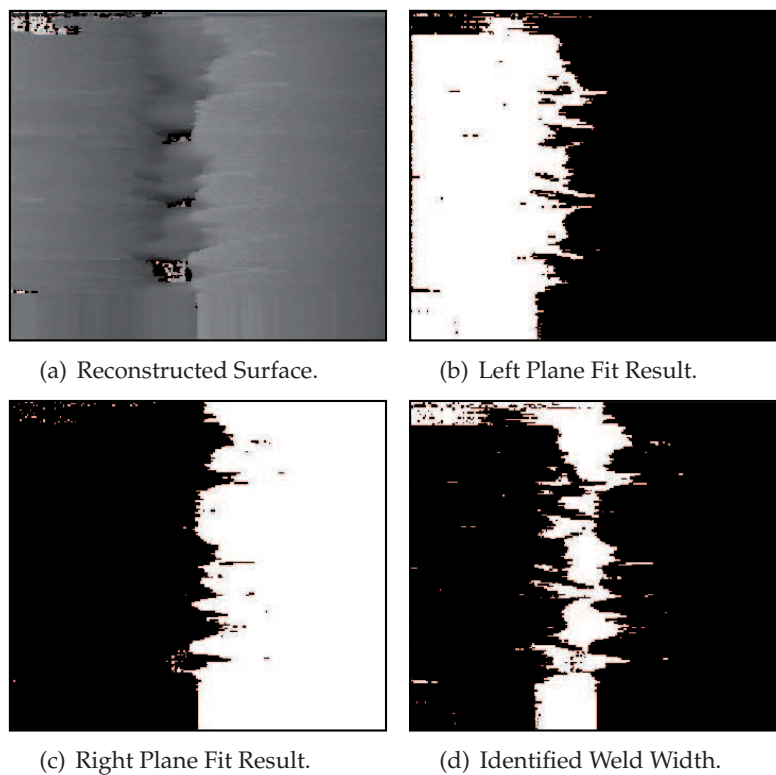

(a) Reconstructed Surface.　　　(b) Left Plane Fit Result.

(c) Right Plane Fit Result.　　　(d) Identified Weld Width.

Figure 7.15: Several parts of the plane fitting algorithm.

The *snake* algorithms (Grooth (2006)) are contour detection algorithms.

These algorithms require a starting point and a set of rules that govern their behavior. From this starting point they search for neighboring points that are strong candidates for weld edge points. Using statistics and the set of rules (e.g. how far the next candidate point can exist, what height value it is allowed to have) one of the candidate points is selected and a new search for weld edges is initiated. In this manner a snakelike edge contour results. This method requires that the initial edge points are accurately detected. Furthermore, if no edge point exists in the neighboring area of the snake, then the detection process fails. Some examples of snake edge detection is shown in Fig.7.16 also with combination of plane fitting.

The capturing of images of an complete area of the weld requires additional illumination sources and camera as not to interfere with the triangulation sensor. One possible for the illumination of the weld exploits light not containing wavelength components near the wavelength of the structured laser diodes. Alternatively, the illumination can be synchronized with the structured light projection in such way that it is "ON" only when the diodes are not projecting (Soudronic (2005)). Such an addition will increase the complexity and volume of the integrated welding head. It is therefore chosen not to pursue this direction.
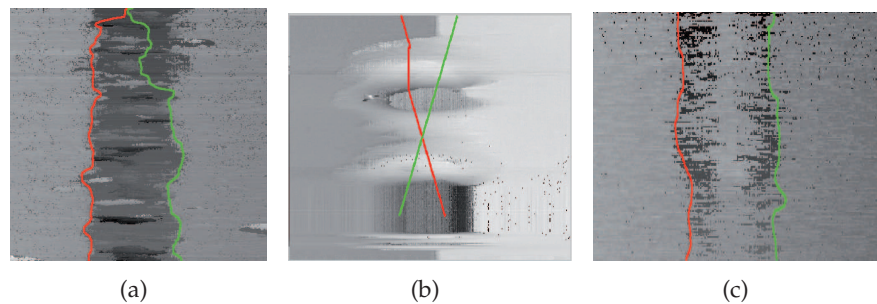

(a)   (b)   (c)

Figure 7.16: Several snake contour examples overlayed on 3D reconstructions of welds. (a) Detection of weld edge without prior knowledge of the starting weld edge points. (b) Failure of the edge detection due to unavailability of neighbouring edge points. (c) Detection of weld edge with assistance of plane fitting algorithms.

Spatter

Spatter consists of solidified droplets of metal coming from the melt pool. During welding, parts of the liquified metal are occasionally ejected from
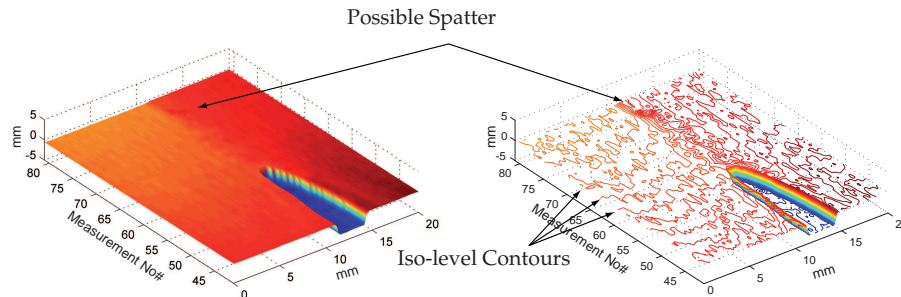
Figure 7.17: Left: Part of a surface 3D reconstruction. Right: The iso-level contour surface of the same 3D surface reconstruction.

the melt pool and solidify in the area around the weld. Spatter does not influence the structural quality of the weld, but it is often undesired in welded products.

Spatter is detected on the 3D reconstructed weld by performing a iso-level contour scan, which is the connection of points that have the same height in a contour. Such an example is shown in Fig.7.17, where the left side is a part of the *Active* 3D surface reconstruction and on the right side is its iso-level contour. Contours with the same color exist on the same height level and the height difference between two consecutive contours is 50 μm. The z and the y axes of the plot are in mm whereas the x axis scale is the measurement number of the height profile instead of its value in mm for easier identification of the measurements where the spatter appears.

The ISO 13919 standard doe not include guidelines on the expected minimum spatter sizes. Therefore the definition of the size to be detected as spatter is left to the operator. Within this work spatter is defined as an ellipsoid or circular object on the detected surface with at least 0.16 mm height. In the iso-level contour plot, such a definition of a spatter would be represented by at least by three closed contour lines of elipsoid/circular shape that exist in the same position (Fig.7.18). The size of the spatter drops depend on the material that is laser welded and therefore a minimum value for the spatter drop area must be defined by the operator. The spatter size is calculated by the size of the biggest closed contour. Its minimum size depends on the sensor resolution. Therefore for the current setup the spatter must be wider than 35 μm and higher than 60 μm.
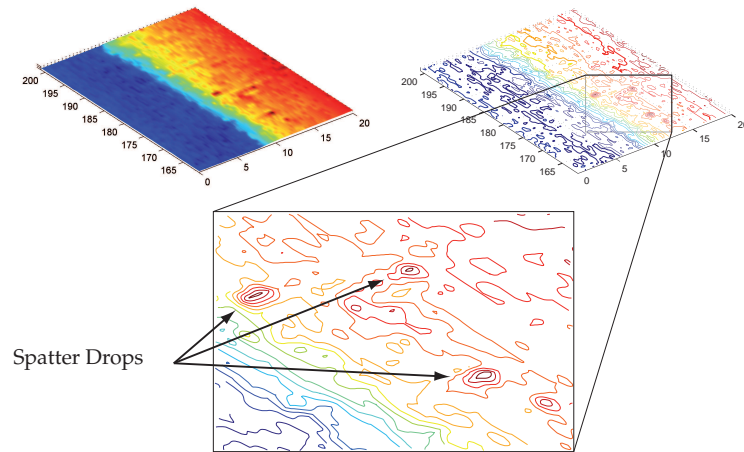
Figure 7.18: Top Left: Part of a surface 3D reconstruction. Top Right: The iso-level contour surface of the same 3D surface reconstruction. Bottom: Zoomed view of the contour plot containing spatter drops.

7.7 Experimental Results

The welded seam of Fig.7.19 was scanned and processed by the weld inspection sensor. *Active* 3D reconstruction was used for the weld height profile. The seam configuration of the weld is a butt joint, and the results for each of the weld defect measurements will be presented, where the quality of the weld is evaluated in accordance with the ISO 13919 standard.

The chosen welded seam shows a number of weld imperfections (weld excess, holes/undercut, convexity, misalignment). Therefore it allows the simultaneous testing of the algorithm for all the weld imperfections.

Weld Width

The weld width h_W is determined as is described in §7.4.1. The first step is the calculation of the weld center of gravity h_{CoG} and the standard deviation σ_{var}. In Fig.7.20(a) the detected h_{CoG} and σ_{var} are overlayed on the 3D reconstruction.

Once the h_{CoG} and σ_{var} values have been identified, then the linear parts ℓ_1 and ℓ_2 of the individual height profile data are calculated. This allows the detection of the weld edges E_L and E_R which are shown in
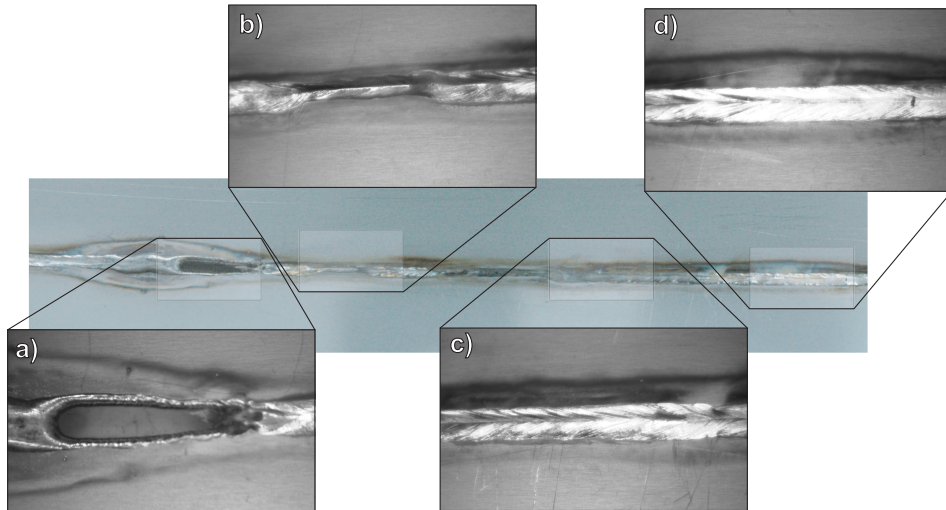
Figure 7.19: Photograph of the welded seam with weld imperfections. The weld was performed with a laser power of 1000 W, a welding speed of 15 mm/s and 0 mm offset of the laser focal point. a) Some weld excess and a hole. b) Evidence of misalignment resulting a thinner and badly formed weld. c) Slight convexity and the weld appearance reveals a small misalignment. d) Misalignment traces.

Fig7.20(b). Furthermore the identified weld edges E_L and E_R are also overlayed to the real image of the weld for comparison (Fig.7.20(c))

As it is seen in Fig.7.20(c), at several points, indicated by arrows, along the seam the weld edge detection has not performed perfectly well. As previously explained this is due to the way that the weld edge is defined to the sensor. As also mentioned more accurate edge detection require additional information.

Finally, the plot of Fig.7.21 shows the measured weld width along the welded seam. In general the weld width fluctuates mainly around the value of 1.2 mm. The fluctuations are an indication of an unstable laser welding process.

Misalignment

Following the detection of the weld edges E_L and E_R, the misalignment measurements also take place. The results of these measurements are shown in the plot of Fig.7.22. In Fig.7.22(a) a side view of the
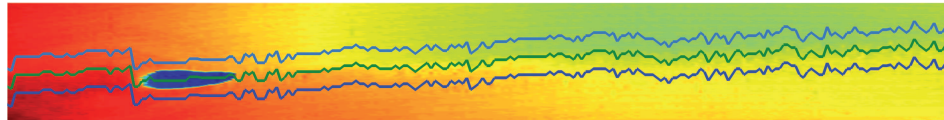
(a) Projection of the detected h_{CoG} (middle line) and σ_{var} (outer lines) points on the 3D reconstructed surface. The parts outside the σ_{var} points are used for the identification of the linear parts ℓ_1 and ℓ_2 of the individual height profiles.
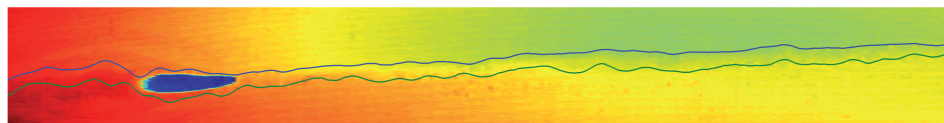
(b) The detected weld edge points E_L and E_R on the 3D reconstructed surface.
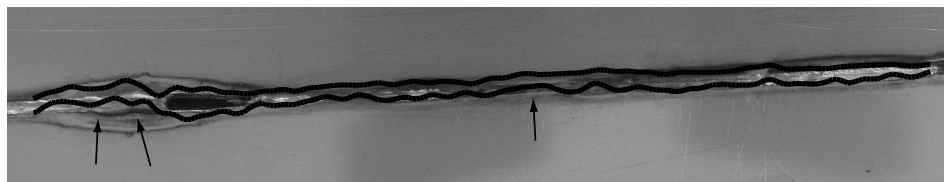
(c) The detected weld edge points E_L and E_R superimposed on the weld picture. The arrows indicate some of the points where the edge detection did not perform well.

Figure 7.20: Representation of the results of the intermediate steps towards the detection of the weld edges for complete welded seam.

real welded seam is seen. The misaligned parts of the weld appear as darker/shadowed parts along the center of the image. Three characteristics are visible in Fig.7.22(a). The first one is a small shadow caused by misalignment in the beginning of the image, next there is the hole which is also slightly misaligned, and then a more extended misalignment occurs that forms a wider shadow. The hole is visible in the side view because of the reflection of light on its misaligned side. Similar results are present in the plot of the sensor values in Fig.7.22(b). The detected misalignment values also form two parts: a small one in the beginning of the plot and a wider one that covers the rest of the plot.

Convexity and Concavity

Convexity and concavity are detected in a similar way and therefore are combined for the presentation of their results. Performing the convexity
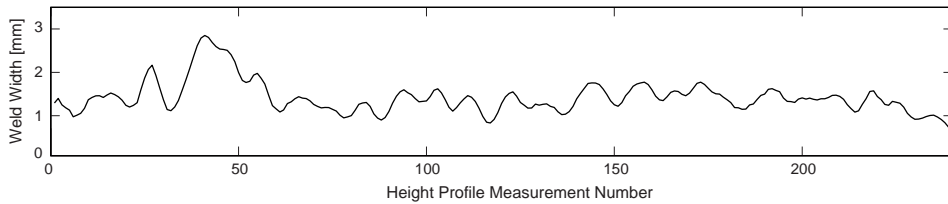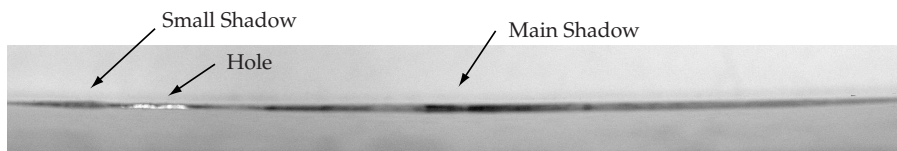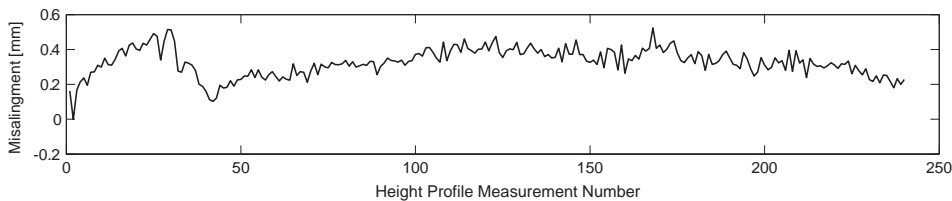
Figure 7.21: The weld width values along the measured welded seam.

(a) Side view of the welded seam where the profile of the misalignments between the two plates is visible.

(b) The misalignment values along the measured welded seam.

Figure 7.22: Image and plot for the comparison of the sensor misalignment measurement values with the misalignment profile visible in the side view of the measured weld.

and concavity measurements on the height profiles the plot of Fig.7.23 is obtained. The plot shows that there is a large convexity part of the weld between measurement 36 and 57, and there is no convexity. Nevertheless, from Fig.7.19 it can be seen that there is excess of metal of the part of the weld before the beginning of the hole. The reason for not detecting this convexity is due to the inaccurate detection of the weld edges. Furthermore this excess of metal appears in the misalignment plot of Fig.7.22(b) between measurement samples $0 - 35$.
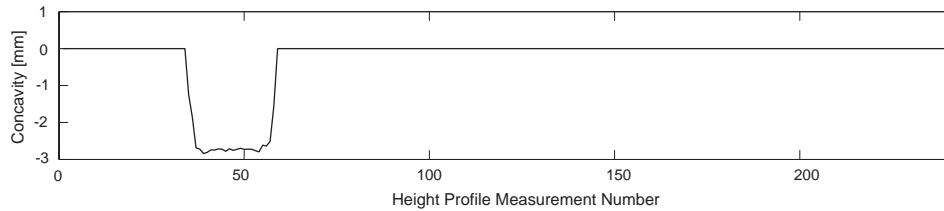
Figure 7.23: The concavity value along the measured welded seam.

Undercuts & Craters

The detected undercuts and craters are shown in Fig.7.24. The figure consists of four parts, the Right Undercut results, the Left Undercut results, the crater results and the combination of the three. By definition an undercut is a crater that exists very close to the weld edge. This means that the distinction between an undercut and a crater is connected to the accuracy that the weld edge is detected. Nevertheless, the restrictions for both the undercut and the crater are the same, and therefore the name under which they are classified is not important as long as they are detected.

As is also shown in Fig.7.24, the majority of the undercuts and craters exist in the area where the hole in the real welded seam. Nevertheless, the plot of the right undercut values appears to show that at several points there is no undercut, as if at that points the hole has no edges. That is because comparting to the edge detection image of Fig.7.20(b) the right edge is not detected accurately, and therefore the undercut is classified as a crater. By combining the plots it is shown that the detected craters are overlapping the missing right edge undercuts.

Weld Quality

To determine the weld quality, the sensor measurements are compared with the set of threshold values. If the imperfection that is measured by the sensor exceeds its corresponding value, then the weld does not pass the quality test for the current measurement. The required input variables for the quality test are, the thickness of the welded material, the level of the desired quality (Moderate, Intermediate, Stringent) and the type of imperfections for which the weld is to be tested. The thickness of the material and the quality level are used to calculate the quality threshold values according to the equations of Table 7.1. The selection of the imperfections
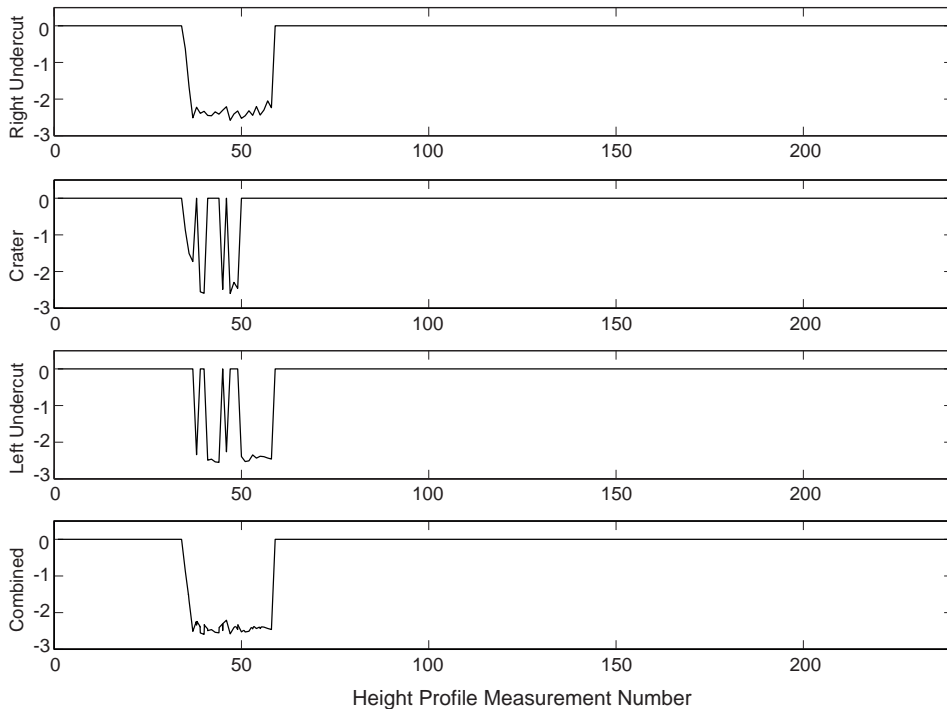
Figure 7.24: The undercut and crater measurements of the weld h_U. From top to bottom are to plots of undercut values along the left and right side of the weld, the crater values and the combined plot.

for testing is to allow several imperfections to exist without influencing the weld quality tests.

In Fig.7.25, the results for the combination of all the ISO 13919 quality levels (D = *Moderate*, C = *Intermediate*, B = *Stringent*) are plotted, where ∅ is used for the cases where none of the quality levels passes the weld quality tests. The thickness of the welded material is 1mm.

If a quality control fails the *Moderate* quality level, then it will also fail the more difficulty ones. Therefore, the y axis of the shows the quality test levels from the most difficult (*Stringent* B) towards the most easy (*Moderate* D). If the plotted line hits or passes a certain quality level, then for that measurement the weld has passed the test.

For the example of Fig.7.25, the weld passes the misalignment test at various points along the weld for the *Moderate* level but completely fails

for the *Intermediate* and *Stringent*. The weld passes all quality levels for the convexity test.
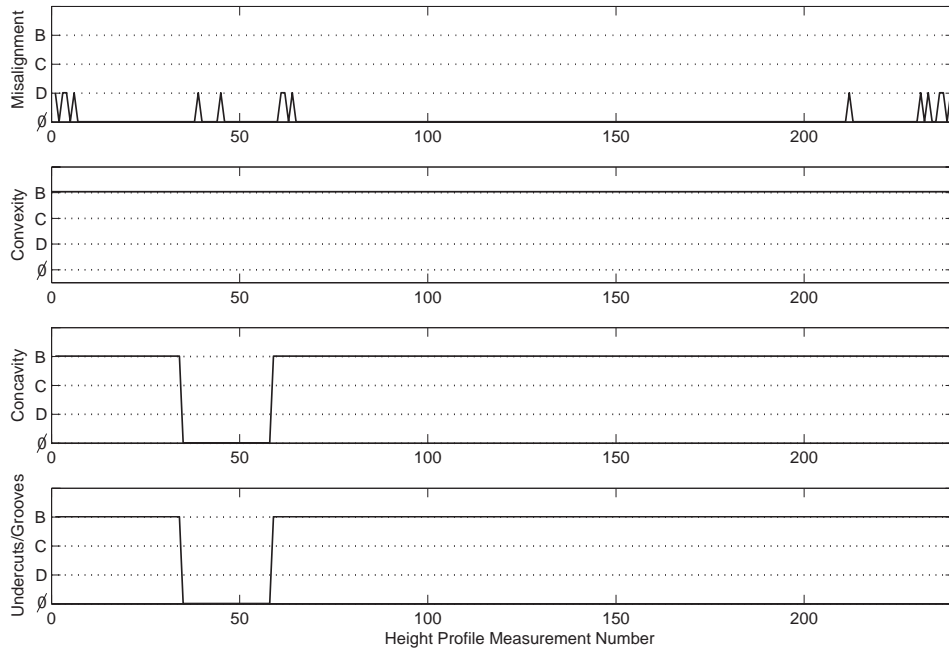

Figure 7.25: Quality test combination plot. Each weld defect has its own plot with all the quality levels as an y axes. The plot line indicates the level that the weld has passed the quality test.

The final mark of the weld is a failing one, since for all levels there are parts of the weld that fail. A final 3D representation is plotted for each of the quality levels with arrows that indicate the position of the detected weld imperfection. In Fig.7.26(a) and Fig.7.26(b) two such results are shown for the *Moderate* and *Intermediate* cases. Similar results are derived for the weld quality of the *Stringent* level.

7.8 General Conclusions

As shown in this chapter, a seam inspection system has been developed with the ability to measure the surface properties of the weld. A 3D reconstruction platform has also been developed. It allows the identification of weld imperfections such as spatter and provide the user with an 3D repre-
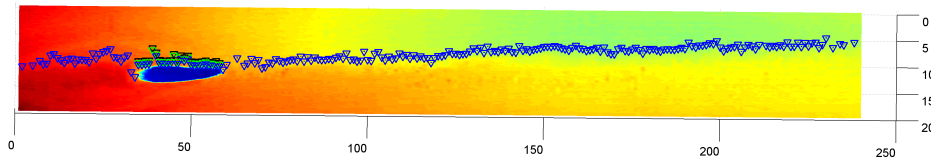
(a) *Moderate* weld defect results.
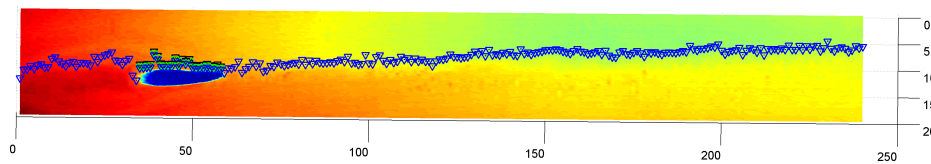
(b) *Intermediate* weld defect results.

Figure 7.26: The 3D weld reconstruction with the indicator arrows for the falling weld quality points. The colored arrows indicate different imperfections (blue = misalignment, red = convexity, green = concavity, black = undercuts/craters)

sentation of the sensor's measurements and the positions of the detected weld defects. Finally, a weld quality estimator was implemented according to the ISO 13919 standard.

All the required processes and calculations have been combined in the GUI application *Inspector* (see Appendix E.1.1). This is an interface provides user with all the seam inspection measurement results and quality estimation.

Chapter 8

Conclusions

To minimize the production time of laser welded parts while increasing the quality of the welded product, automation of laser welding process becomes necessary. Automation commands the use of sensors for the acquisition of the required data, in order to guide and control the involved mechanisms (robots, gantry tables, etc) but also to control and inspect the laser welding process and results. When the required sensor systems are not integrated with each other, they may interfere, which will result in noisy or faulty sensor data. In addition, the volume of the laser welding tool increases with the number of sensors used, resulting in a bulky systems which in turn limits the dynamic performance of the manipulator and the reach-ability of seams. Therefore it is necessary to integrate the required sensing functionalities in one compact tool. The design and the implementation of such a sensor integrated laser welding head is presented in this thesis.

The developed integrated laser welding head uses a single optical triangulation setup for both Seam Detection and Weld Inspection. The developed triangulation sensor projects a perimetric shape (in this work in the shape of a triangle) instead of a single line that is used by most commercially available systems. The perimetric sensor enables the system to follow complex seam trajectories with sharp corners without having to maintain the relative orientation to the seam trajectory. This reduces the work load of the handling robot, and enables the welding of closed loop seam trajectories without the use of external axes. The Process Monitor sensor is also integrated with the other two functionalities, as all sensors share the same coaxial view with the high power laser.

For accurate positioning of the laser spot over the seam, several cal-

ibrations are necessary both for the sensors as well as for the laser tool. Manual calibrations require a lot of time, and involve elaborate testing and measuring. For this reason automated calibration procedures are developed that use the robot as a measuring instrument. The developed calibration algorithms provide the required results faster and without the need for human intervention. The automated calibration procedures also increases the easiness by which the integrated welding head is integrated onto a robot. To further assist the robot integration process, communication interfaces have been implemented, to transfer the measurement data to robot control applications like 24-LASER. The Process Monitor sensor output has been designed to comply with use in industry.

The optical triangulation setup requires synchronization between the switching of the structured light lines and the camera. Special hardware has been developed to facilitate this synchronization with the use of an FPGA chip. Signal transmitting/receiving electronics for several electronic components as well as the amplification electronics of the process monitor sensor were also implemented.

For the display of the sensor results (Seam Detection, Weld Inspection) and control of the sensor parameters, a software application was developed. A Graphic User Interface was implemented to provide ease of use to the operator of the laser welding head. The GUI also includes software for the manipulation of the Stäubli robot, the required laser tool and sensor calibrations, as well as the communication with the robot control software 24-LASER. A toolbox with a GUI for the camera and lens calibration was also developed under the MatLab environment (Appendix E.3).

The implemented seam detection method has several advantages over the existing commercial ones. Therefore, a patent application was filed to further exploit this technology: *Perimetric Trajectory Detection Using Distinctive Structured Light Sources*. The patent application number is EP07112850.8 (see page 227).

The developed sensors should be further optimized for speed. Optimizations of the image processing algorithms will increase the measuring speed of the sensors. Additional improvements on the sensor speed can be achieved by using prior knowledge to reduce the amount of parameters that need to be measured for the calculation of the necessary sensor data. Furthermore, the welding head should be optimized for compactness. The implementation of the electronic boards on PCBs will allow the design of a more compact mechanical housing of the sensor components and decrease the size of the integrated welding head.

It is important also to mention alternative uses of the integrated welding head sensor's, other than simply teaching a seam and welding it. Such is the use of a prior knowledge about the seam trajectory (e.g. CAD data), and combine the seam detection sensor measurements to identify the seam trajectory on the product. Furthermore, at high welding velocities over sharp corners, even a sensor system like the Triangular sensor might not be able to avoid robot positioning errors. The use of the sensor in combination with control methodology such as the Iterative Learning Control (ILC) Hakvoort et al. (2006), or scanning mechanisms Hardeman et al. (2006) provide solutions to this problem.

192

Appendix A

Integrated Welding Head Components

A.1 Optical Components

In this section the optical components that were used for the implementation of the integrated welding head are presented. These optical components are:

Collimator Lens: Standard Trumpf f=200 mm collimation lens with defocusing (No#.22-24-80-00), and a fiber cable connector receptacle LLK-B coolable (No#.22-24-11-00).

High Power Laser Focus Lens: Standard Trumpf f=100 mm laser focusing lens D70 100A (No#.22-24-04-00) for welding applications. The Trumpf lenses of f=150 mm or f=200 mm can also be used.A Trumpf cooling ring (No#.22-24-25-00) and lens protection (No#.22-30-75-00) are also installed.

Coaxial Mirror: Standard Trumpf Würfel 0° coaxial mirror (No#.22-24-52-00, 12-18-08-26), Average reflectance of 12% between the wavelengths of 520-680 nm.

Beam Splitter: Schott Glass plate beam splitter, No#171243, type KG5, thickness 3 mm, with 70% reflection and 30% transmission at all wavelengths between 420 to 720 nm.

Camera Optical Filter: Melles Griot EDC 03FIV123 interferometer filter at 660 nm $\pm$10 nm.

Camera Lens: Tamron 25 mm C-Mount F/1.4 F/1.3 MP Camera manual lens with lock SKU# TA2514MPCL.

Process Monitor Sensor Lens: Melles Griot CVI 01LPX525 lens, type SF15, focal length of 25 mm, diameter 25 mm.

Process Monitor Sensor Filters: 600nm Low-pass filter from Melles Griot, Part No: 03SWP410 and typical transmission at 790nm. A Hot-Cold UV mirror with typical transmission at the range of 410-700nm from Melles Griot, Part No: 03MHG007.

A.2 Laser Diodes

The applied laser diodes are Lasiris^{TM} SNF Laser Diodes. The parameters of the selected diodes are listed below.

- Laser light wavelength at 660nm

- 80mW output power

- Line optics with 30° fan angle

- TTL modulated up to 20kHz

- Separated electronics

- 6V input voltage

- Over-temperature and ESD protection

A.3 Camera

The selected camera is the Philips Dica321 camera with an onboard processor for stand-alone functionality. The characteristics of the Dica321 camera are listed below.

- 1280x1040 pixels CMOS chip

- CMOS sensor physical size 2/3" (8.8x6.6 mm)

- Capture speed of up to 27 full frames per second

- Capable of one programmable Region of Interest (ROI)

- Integrated TriMedia processor

- Stand alone functionality

- IEEE 1349 Firewire connection with Host PC

- Two Flash Outputs

- One trigger Input

- Two general purpose outputs

- Two general purpose inputs

- VGA Output

- RS232 Serial Communication Interface

- Reset input

A.4   Photodiodes

The photodiode is from UTD Sensors, Inc. The characteristics of the photodiode are the following:

- The diode name is PIN-5DI and it is silicon based

- Photosensitive surface diameter of 2.54 mm

- Lowest signal detection level of $3\mathrm{x}10^{-11}$ W

- Spectral response 350-1100 nm

- Minimum responsivity 500 mA/W at 850 nm

- Max. response time of 15 ns

A.5 Laser

The laser system sets the requirements for the response time of the process monitor system. The process monitor must be at least as fast as the rate at which the laser can change its laser power output. In this work a Triumpf HL4006D 4000 W Nd:YAG laser is used that has a response time from 0.1 to 0.5 msec. The data acquisition system defines the resolution of the process monitor system. The laser pump changes the output laser power from 40-4000 W in relation to an input signal of 0.1-10 V. When an 8bit converter is used by the data acquisition system, then the resolution of the laser power change is approximately 15.5 W/bit.

Appendix B

Derivation of formulas and calculations

B.1 Optical Triangulation & Calibration Curve

A drawing of a simple optical triangulation setup is shown in Fig.B.1. In this figure a single spot is mapped through a lens on an photosensitive surface. The aim is to measure displacement z if all other parameters (a, x_p, ϕ, x, d_R, f_T) are known.
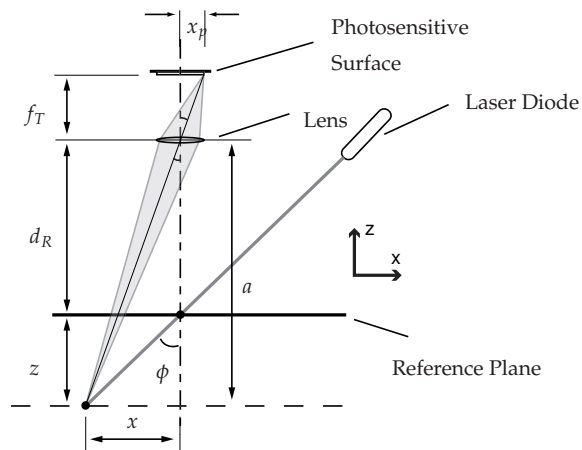

Figure B.1: Sketch of single light point mapped on a photosensitive surface.

From Fig.B.1 it is evident that:

$$z = d_R - a, \tag{B.1}$$

$$\frac{a}{x} = \frac{f_T}{x_p} \quad \Leftrightarrow \quad a = \frac{x \, f_T}{x_p}, \tag{B.2}$$

$$x = z \tan \phi \tag{B.3}$$

By substituting a and x,

$$z = d_R - \frac{f_T \, z \, \tan \phi}{x_p} \quad \Leftrightarrow \tag{B.4}$$

$$z \left(1 + \frac{f_T \, \tan \phi}{x_p} \right) = d_R \quad \Leftrightarrow \tag{B.5}$$

$$z = \frac{d_R \, x_p}{f_T \, \tan \phi + x_p} \tag{B.6}$$

In Fig.B.2, the same setup is shown, where the structured light beam hits a surface in three different height positions A, B and C. It is shown that equal distances on the photosensitive surface $A'B'$, $B'C'$ do not correspond to equal heights AB, BC due to zooming effects. Eq.B.6 is the mathematical expression of the calibration curve of Fig.B.2 which allows to correct for the zooming effects.
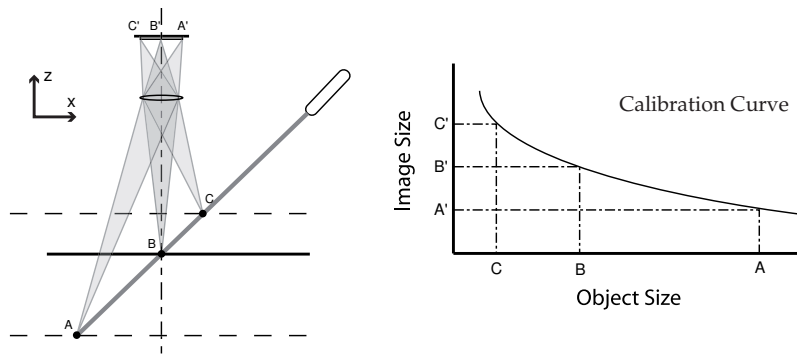

Figure B.2: Sketch of single light point position A, B and C mapped on a photosensitive surface at A', B' and C'. The corresponding calibration curve is also plotted.

B.2 Vectors & Matrices

Position Vector P

A position vector consists of three elements **x**, **y** and **z** one for each axis of the coordinate frame.

$$\mathbf{P} = [x\ y\ z]^T = \begin{bmatrix} x \\ y \\ z \end{bmatrix} \tag{B.7}$$

Rotation Matrix R

A rotation matrix consists of three orthonormal vectors $\mathbf{r}_x$, $\mathbf{r}_y$ and $\mathbf{r}_z$ that define the orientation of a coordinate system.

$$R = [\mathbf{r_x}\ \mathbf{r_y}\ \mathbf{r_z}] = \begin{bmatrix} r_{xx} & r_{yx} & r_{zx} \\ r_{xy} & r_{yy} & r_{zy} \\ r_{xz} & r_{yz} & r_{zz} \end{bmatrix} \tag{B.8}$$

Transformation Matrix T

A transformation matrix defines the position and orientation of a coordinate frame **B** in respect to a reference frame **A**. A transformation matrix $^A_B T$ consists of a rotation matrix and a position vector.

$$^A_B T = \begin{bmatrix} ^A_B R & ^A_B \mathbf{P} \\ 0 & 1 \end{bmatrix} = \begin{bmatrix} r_{xx} & r_{yx} & r_{zx} & x \\ r_{xy} & r_{yy} & r_{zy} & y \\ r_{xz} & r_{yz} & r_{zz} & z \\ 0 & 0 & 0 & 1 \end{bmatrix}, \tag{B.9}$$

where $^A_B R$ is the rotation matrix that defines the change of ordination between frames **A** and **B**, $^A_B \mathbf{P}$ is the position vector that defines the change of position between frames **A** and **B**.

Quaternion Vector Q

A quaternion Q is defined from the axis of rotation $\mathbf{v}_R$ and the angle θ according to

$$Q = \begin{bmatrix} q_0 \\ q_1 \\ q_2 \\ q_3 \end{bmatrix} = \begin{bmatrix} \cos(\frac{\theta}{2}) \\ \frac{v_{R_x}}{|\mathbf{v}_R|} \sin(\frac{\theta}{2}) \\ \frac{v_{R_y}}{|\mathbf{v}_R|} \sin(\frac{\theta}{2}) \\ \frac{v_{R_z}}{|\mathbf{v}_R|} \sin(\frac{\theta}{2}) \end{bmatrix}. \tag{B.10}$$

The homogeneous rotation matrix R is described by the quaternion elements according to

$$R = \begin{bmatrix} r_{xx} & r_{yx} & r_{zx} \\ r_{xy} & r_{yy} & r_{zy} \\ r_{xz} & r_{yz} & r_{zz} \end{bmatrix} = \begin{bmatrix} 2(q_0^2 + q_1^2) - 1 & 2(q_1 q_2 - q_0 q_3) & 2(q_1 q_3 + q_0 q_2) \\ 2(q_1 q_2 + q_0 q_3) & 2(q_0^2 + q_2^2) - 1 & 2(q_2 q_3 - q_0 q_1) \\ 2(q_1 q_3 - q_0 q_2) & 2(q_2 q_3 + q_0 q_1) & 2(q_0^2 + q_3^2) - 1 \end{bmatrix}. \tag{B.11}$$

Once the rotation matrix has been defined, the rotation angles around each of the sensor's coordinate system can be calculated by

$$\varphi = \arctan 2(r_{yz}, -r_{zz}) \tag{B.12}$$

$$\psi = \arctan 2(r_{xz}, r_{zz} \cos(\varphi) - r_{yz} \sin(\varphi)) \tag{B.13}$$

$$\omega = \arctan 2(r_{yx} \cos(\varphi) + r_{zx} \sin(\varphi), r_{yy} \cos(\varphi) + r_{zy} \sin(\varphi)) \tag{B.14}$$

Where φ is the rotation around **x** axis, ψ is the rotation around **y** axis and ω is the rotation around **z**.

B.3 Rodrigues' Rotation Formula

Rodrigues' rotation formula (Equation B.15) offers an efficient way to express a rotation matrix (Eq. B.16) as a rotation by an angle θ about a fixed axis specified by a unit vector $\boldsymbol{\omega} = \begin{bmatrix} \omega_x, \omega_y, \omega_z \end{bmatrix}$ Weisstein (2005). The Rodrigues' rotation formula is used for the camera calibration optimization process because it reduces the amount of parameters to be optimized.

$$\mathbf{R} = e^{\mathbf{\Omega}} = \mathbf{I} + \mathbf{\Omega} \sin\theta + \mathbf{\Omega}^2 \left(1 - \cos\theta\right), \tag{B.15}$$

$$= \begin{bmatrix} 1 + (1 - \cos\theta)\left(-\omega_z{}^2 - \omega_y{}^2\right) & -\sin\left(\theta\right)\omega_z + (1 - \cos\theta)\,\omega_y\omega_x \\ \sin\left(\theta\right)\omega_z + (1 - \cos\theta)\,\omega_y\omega_x & 1 + (1 - \cos\theta)\left(-\omega_z{}^2 - \omega_x{}^2\right) \\ -\sin\left(\theta\right)\omega_y + (1 - \cos\theta)\,\omega_z\omega_x & \sin\left(\theta\right)\omega_x + (1 - \cos\theta)\,\omega_z\omega_y \end{bmatrix}$$

$$\left. \begin{array}{c} \sin\left(\theta\right)\omega_y + (1 - \cos\theta)\,\omega_z\omega_x \\ -\sin\left(\theta\right)\omega_x + (1 - \cos\theta)\,\omega_z\omega_y \\ 1 + (1 - \cos\theta)\left(-\omega_y{}^2 - \omega_x{}^2\right) \end{array} \right], \tag{B.16}$$

with:

$$\mathbf{\Omega} = \begin{bmatrix} 0 & -\omega_z & \omega_y \\ \omega_z & 0 & -\omega_x \\ -\omega_y & \omega_x & 0 \end{bmatrix}. \tag{B.17}$$

The fact that $\boldsymbol{\omega}$ is unitary means that the fourth variable θ can be merged in. Without loss of information: $\mathbf{w} = \boldsymbol{\omega}\theta$. This shows that a regular 3D rotation matrix containing 9 parameters can be written in only 3 independent parameters using Rodrigues' representation. This is especially beneficial during rotation optimization, because there are less parameters and no mutual constraints.

The Rodrigues parameters $\boldsymbol{\omega}$ and θ can easily be calculated using Eq.B.18, because $\boldsymbol{\omega}$ must be unitary.

$$\mathbf{R} - \mathbf{R}^T = \begin{bmatrix} 0 & -2\omega_z \sin\theta & 2\omega_y \sin\theta \\ 2\omega_z \sin\theta & 0 & -2\omega_x \sin\theta \\ -2\omega_y \sin\theta & 2\omega_x \sin\theta & 0 \end{bmatrix}$$
$$= 2\mathbf{\Omega} \sin\theta, \tag{B.18}$$

A small problem may arise here when the arcsin function will return a value for θ between $-\pi/2$ and $\pi/2$, which it can also be $\pi - \theta$. This can be checked using one of the values from

$$\mathbf{R} + \mathbf{R}^T = \begin{bmatrix} 2 + 2\left(1 - \cos\theta\right)\left(-w_z{}^2 - w_y{}^2\right) & \cdots & \cdots \\ 2\left(1 - \cos\theta\right)w_y w_x & \cdots & \cdots \\ 2\left(1 - \cos\left(\theta\right)\right)w_z w_x & \cdots & \cdots \end{bmatrix}. \tag{B.19}$$

Once ω and θ are known they are multiplied to obtain three independent parameters in the form of **w**. Extracting ω and θ from **w** is easy because $\omega = \mathbf{w}/\|\mathbf{w}\|$ and $\theta = \|\mathbf{w}\|$, after which a full rotation matrix can be generated using Equation B.15.

B.4 Illumination calculations for lower illumination sensitivity of process monitor sensor

The lower illumination sensitivity that is calculated in this example is for steel and the investigated wavelengths are from 400 nm to 600 nm.

The radiation that is emitted by the molten steel can be described by Planck's law for black body radiation as:

$$E_{\lambda b} = \frac{2\pi h c^2}{\lambda^5 \exp\left(\frac{hc}{\lambda kT} - 1\right)}, \tag{B.20}$$

where $E_{\lambda b}$ is the spectral emissive power, λ is the wavelength, k the Boltzmann constant, h the Planck constant, c the speed of light and T the surface temperature.

The black body spectral radiance plot for the melting temperature of steel at 1800 K when the maximum amount of radiation is emitted (emissivity ϵ_n of 1) is shown in Fig.B.3. The emissivity is the ratio between the emitted radiation from the real surface compared to the ideal one calculated by the black body radiation equation.

The part that is interesting for the process monitor sensor is for the wavelengths between 400 nm and 600 nm. Also it is safe to assume that in real life the emissions are less, and therefore the emissivity ϵ_n should be reduced. For an ϵ_n of 0.5 the radiance plot of Fig.B.4 is resulted.

By integrating Eq.B.20 over the wavelength range 400-600 nm for the melting temperature of steel at 1800 K the resulting emissive power is 71 $W/m^2/sr$.

For the laser spot sizes that are mentioned in §3.1 it is safe to estimate the total molten material surface is about 1 mm^2, at anytime during the welding process. Therefore the illumination E_m from this surface is:

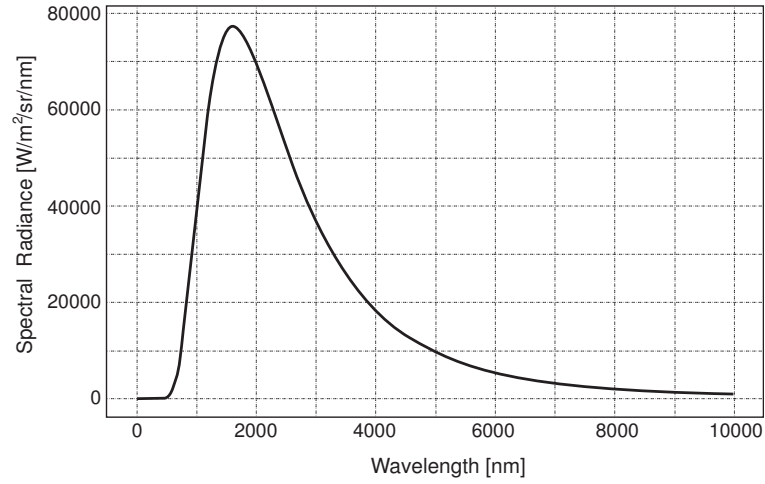$$E_m = 1x10^{-6}m^2 \cdot 71\frac{W}{m^2 sr} = 71x10^{-6}W/sr \tag{B.21}$$

Figure B.3: Spectral radiance plot for black body radiation at temperature of 1800 K, emissivity ϵ_n of 1 and for the wavelengths between 0-10 μm.

In the worse case the welding process will act as a homogeneous illumination point source. This can be represented as a hemisphere like the one shown in Fig.B.5. The solid angle of the illumination that will eventually reach the process monitor sensor initially depends on the focusing lens surface area and the focal distance f_L. Nevertheless, after the laser focus lens, the collimated illumination reaches the process monitor optics which in this case have smaller surface that the laser focus one. Therefore the solid angle depends on the surface of the process monitor sensor lens.

The solid angle of an object on a sphere is defined as:

$$\Omega = \frac{A}{r^2},$$ (B.22)

where A is the surface area of the projection of an object on a spherical surface in mm^2, and r is the radius of the sphere.

For the hemisphere of Fig.B.5 $r = f_L$.

The solid angle Ω_S of the process monitor lens surface is then:

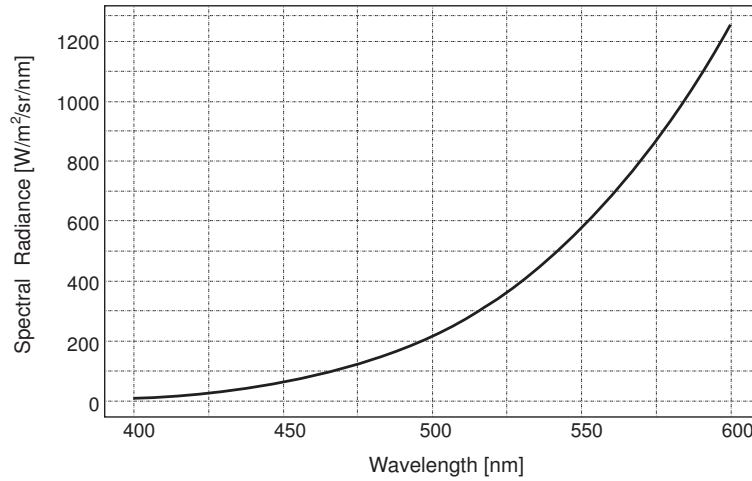$$\Omega_S = \frac{\pi R_S^2}{f_L^2},$$ (B.23)

Figure B.4: Spectral radiance plot for black body radiation at temperature of 1800 K, emissivity ϵ_n of 0.5 and for the wavelengths between 400-600 nm.

where R_S is the radius of the sensor focus lens.

If E_m is the radiance of the melt pool in *Watts* per unit of solid angle *sr*. Therefore the illumination E_L that passes through towards the process monitor sensor is:

$$E_L = \Omega_S \, E_m \; = \; \frac{\pi R_S^2 E_m}{f_L^2} \; . \tag{B.24}$$

According to the selected optical path, only 10% of the reflected radiation is split off by the dichroic mirror, and 30% of that radiation passes from the beam splitter to the process monitor sensor. In total 3% of the E_L will reach the photo diode, so:

$$E_S = 0.03 E_L = \frac{0.03 E_m \pi R_S^2}{f_L^2}, \tag{B.25}$$

where E_S is the illumination that reaches the sensor. For the developed system R_S=12.5 mm and the f_L can be either 100 mm, 150 mm and 200 mm. For these values the results for the lowest illumination is presented in Table B.1.
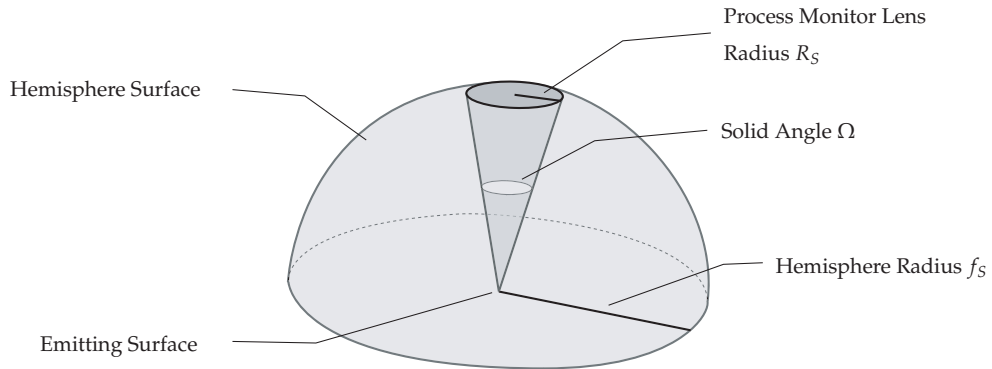
Figure B.5: Diffused emission of the melted area radiation forming a hemisphere.

Table B.1: Illumination the reaches the process monitor sensor in relation to the working distance

f_L	E_L	E_S
100 mm	1.39×10^{-5} W	4.18×10^{-7} W
150 mm	6.19×10^{-6} W	1.86×10^{-7} W
200 mm	3.49×10^{-6} W	1.05×10^{-7} W

As it was shown in Fig.B.3, the peak of the radiance is at about 1600 nm. It is therefore logical to expect to chose that range of wavelengths for the monitoring system. The major obstacle in this solution is that the available silicon based sensors are not capable to detect radiation at those wavelengths.

206

Appendix C

Electronic Component Boards

C.1   Field Programmable Gate Array - FPGA

The FPGA chip that is used is the ALTERA$_®$ *MAX*$^®$ EPM7128SLC84-15. The FPGA is programmed in Verilog HDL language with the use of the Quartus II v5.1 software of ALTERA$_®$.

The control circuit of the FPGA carries a reset button for the programmed process, a clock, a DIN96 interface to connect I/O signals and an LCD display. The board (Fig.C.1) is developed by the Signals & Systems group of the Electrical Engineering faculty of University of Twente.
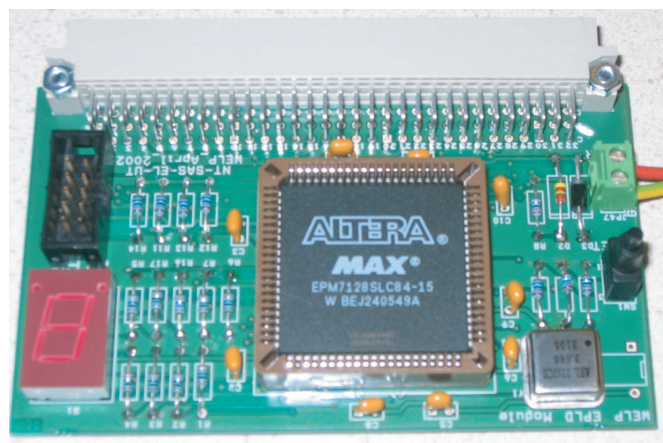

Figure C.1: The FPGA electronic board developed by the Signals & Systems group.

C.2 Philips Dica321 Add_On

This electronic board is designed to supply the camera with power, if necessary, and also to prepare the camera signals for transfer to the FPGA (Fig.C.2). Two signals are produced by the camera, an RS232 serial communication signal and a trigger signal. A Max232 chip is used to convert the serial signal's voltage levels to TTL, and a Schmitt Trigger circuit is used for the same reason with the camera trigger signal. Both signals are then passed though a differential driver before they can be connected to the FPGA cable.
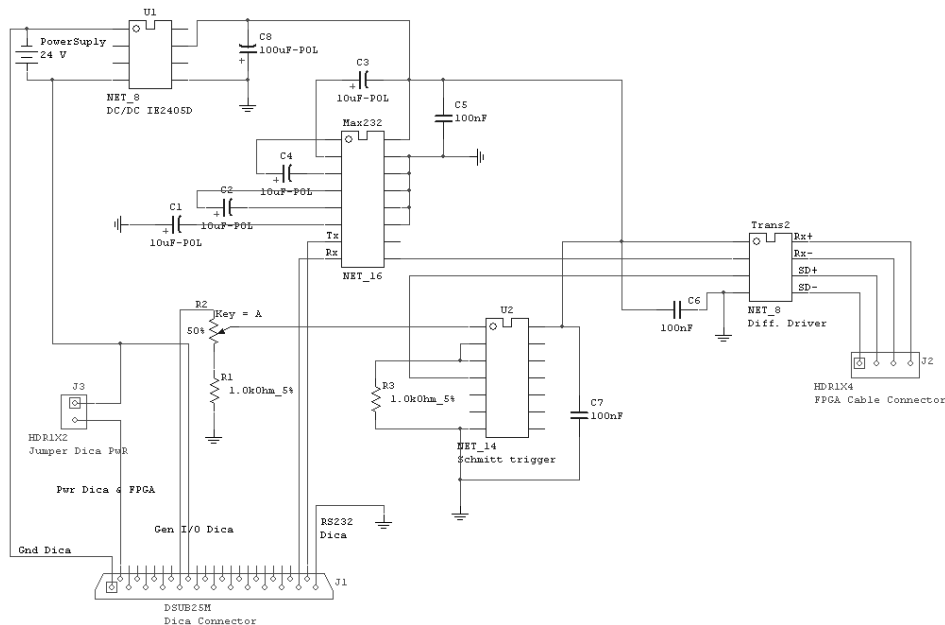

Figure C.2: The electronic schematic design of the Dica321 add_on board.

C.3 FPGA Add_On

This electronic board has been designed to combine the differential signals from the Dica add_on board to cancel out any additional noise, and forward the to the FPGA input pins. It also supplies the power for the FPGA board and forwards the FPGA TTL output control signals towards the structured light diode's TTL inputs (Fig.C.3).
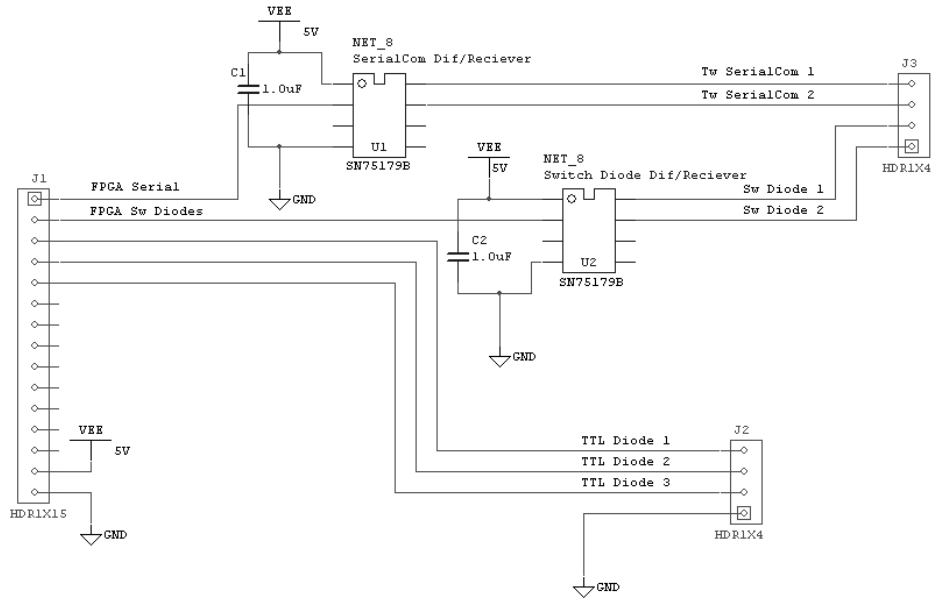
Figure C.3: The electronic schematic design of the FPGA add_on board.

C.4 Diode Power Supply

The diode power supply circuit consists of a single DC/DC converter from 24 V to 5 V with max current of 600 mA. The converter used is the C&D Technologies NDY2405C converter. Three parallel jacks are connected to its output to provide an interface for the structured light diode's power supply plugs.

C.5 Process Monitor Sensor

This electronic electronic board contains the complete monitor sensor. The design has a voltage converter that converts the 24 V input to the ±15 V that is required for the board components. The full schematic is shown in Fig.C.4.

The first component is the photodiode pre-amplification which is performed with the LT1028 amplifier. The pre-amplification is photoconductive, and can be changed to photovoltaic by simply connecting to GND the

end of the PIN 5DI photodiode that is biased with -15 V and removing the parallel 10 μF capacitor.

The pre-amplified signal is the imported in an amplifier AD708 where the gain can be selected by the switches next to the resistors.

Amplified signal is then inserted into a linear driver SSM2142 that has as outputs the original signal S_{out+} and its inverted one S_{out-}. Both signals together with the GND reference are the outputs of the sensor.
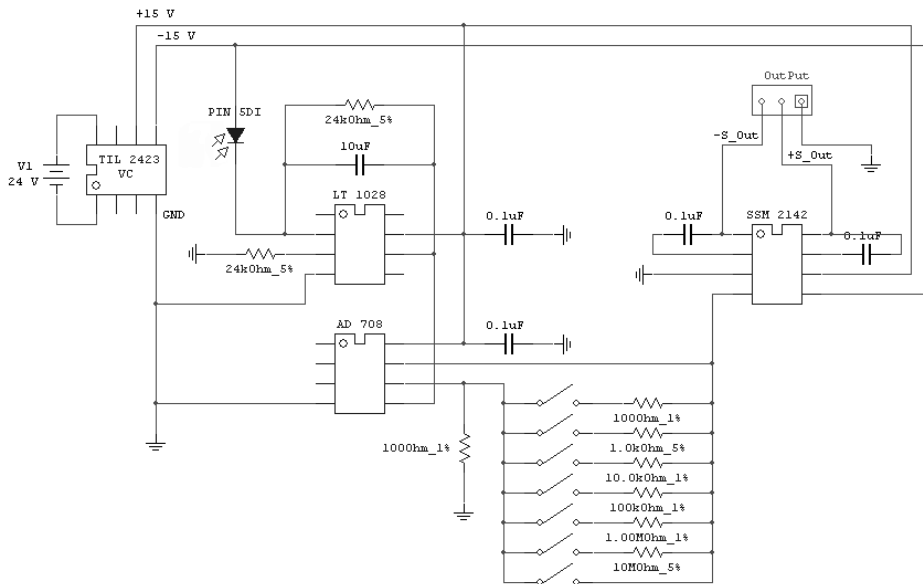

Figure C.4: The electronic schematic design of the Process Monitor sensor board.

C.6   Connectors

Sub D: Two pairs of 9-pin Sub D male and female connectors are used. The pairs are used for the cable that connects the Dica add_on board with the FPGA, and on the Dica add_on and FPGA add_on boards.

SMB: These connectors are used for the TTL signals from the FPGA to the diodes. Three SMB jacks (one for each of the diodes) come out of the mechanical housing of the welding head. Three SMB plugs with a corner are used on the structured light diodes part.

C.6. Connectors **211**

Micro D: For the connection with the Dica321 camera I/O interface a 25 Mirco D connector is required. The one that it is used in this design is delivered by **AirBorn**, part number MM-221-025-261-00WQ.

Power supply: Any type of power supply jacks and plugs can be used, so long as they can withstand up to 30 V and 300 mA.

212

Appendix D

Joint Configurations

D.1 Joint Configurations

Fig.D.1 and Table D.1, contain examples of the most commonly used joint configurations for laser welding without filler material and their tolerances as were published at FME-CWM (2002). The values in Table D.1 are indicative and can vary depending the laser spot diameter, the focal distance and the type of material.
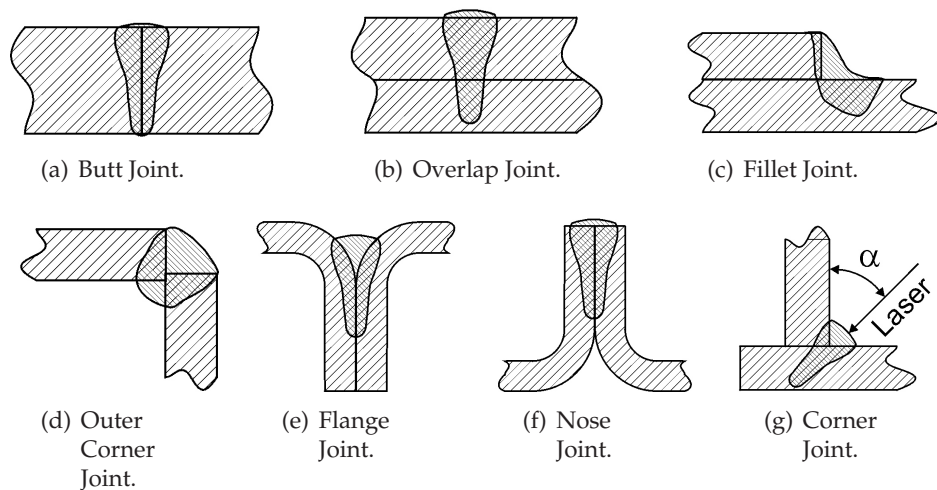

(a) Butt Joint.   (b) Overlap Joint.   (c) Fillet Joint.

(d) Outer Corner Joint.   (e) Flange Joint.   (f) Nose Joint.   (g) Corner Joint.

Figure D.1: Most commonly used joint configurations of seams.

Table D.1: Joint Configurations courtesy of FME-CWM

Seam Geometry	Geometrical Tolerances		Beam Position Tolerances	
	split distance [mm]	height misalignment [mm]	$\perp$ perpendicular to seam	$\parallel$ in focal direction [mm]
Butt Joint	0.1	0.2	±0.25	±0.05
Overlap Joint	0.1	N.A	±0.25	N.C
Fillet Joint	0.25	N.A	±0.25	±0.05
Outer Corner Joint	0.2	0.5	±0.25	±0.05
Flange Joint	0.125	±0.5	±0.25	±0.15
Nose Joint	0.125	±0.25	±0.25	±0.1
Corner Joint				
$40^o < \alpha < 60^o$	0.25	N.A	N.A	±0.125
$60^o < \alpha < 80^o$	0.25	N.A	N.A	±0.15

N.A = Not Applicable, **N.C** = Not Critical.

Appendix E

Software

E.1 INTEGLAS

INTEGLAS is the graphic user's interface with software that allows the user to set the working parameters of the sensor as well as overview the sensor performance and results. The two main windows of the INTEGLAS application are shown in Fig.E.1.
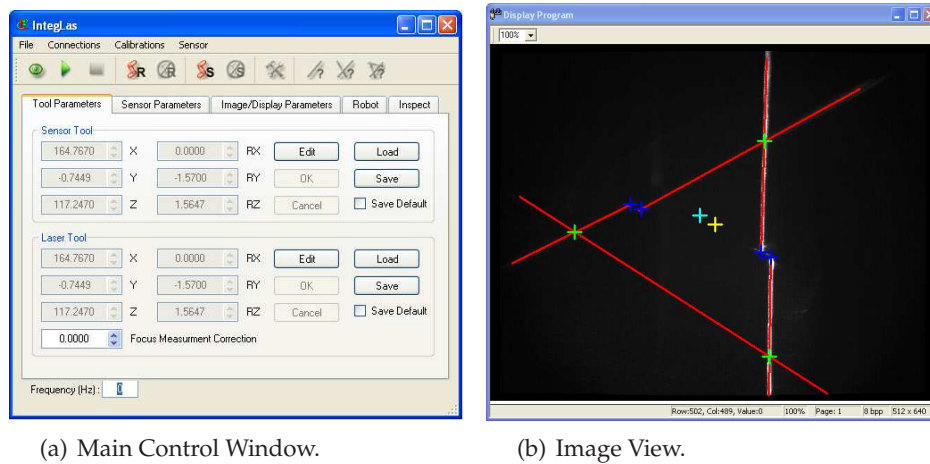

(a) Main Control Window.

(b) Image View.

Figure E.1: The two main windows of the INTEGLAS *application.*

Fig.E.1(b) shows the image window in which the results of the image capturing as well as the measured sensor data (seam points, structured light lines, TCP$_L$, etc) are being displayed. In Fig.E.1(a) the main control

window of INTEGLAS is shown. This window consists from various tabs menus and buttons that perform the following functions:

Tool Parameters *Tab* This tab displays the values for the TCP_L and the TCP_S. It allows the user to change the values, store them or load them from a previous stored file.

Sensor Parameters *Tab* This tab displays the sensor parameters that result from the calibrations like the projection angles ϕ of each of the structured light diodes, the c_p pixel-to-mm ratio, the virtual plane parameters, etc. The user can store the values or load previous stored ones.

Image/Display Parameters *Tab* This tab gives the user access to the camera parameters. The user can change the area size of the imaging sensor that will be captured and processed, as well as control the gain of the sensor. Furthermore the user is given control over the detected features that are desired to be displayed in the viewer of Fig:.E.1(b).

Robot *Tab* This tab gives the user access to the robot that is connected to the integrated welding head. The basic movement/rotation commands can be given to the robot in relation to the TCP_L.

Inspect *Tab* This tab allows the user to define the name of the file where the inspection data are stored and to start the inspector GUI application.

File *Menu* Menu where the loading of parameters and files accessible also from the tabs can take place.

Connections *Menu* This menu the connections with the robots and robot control applications can be requested and defined. The commands from this menu are responsible for initiating the treads for the communication with the robot, and for the delivering of the sensor measurement data to robot control applications like 24-LASER.

Calibrations *Menu* This menu contains the commands for the initiation of the laser tool calibration dialog and the sensor calibrations as well as updating the values of the **Tool Parameters** and **Sensor Parameters** *Tab*.

Sensor *Menu* This menu allows the user to select which type of sens-
ing is to be performed: Full Shape/Switching lines, Single
line/Cross/Triangle, Seam Detection/Weld Inspection.

Tool Bar *Buttons* These buttons are the ones that exist under the menu.
The first three control the camera function (Grab one image, Contin-
uous Capture, Stop). The next two are to connect and disconnect to
the default robot. The next two are to start or stop the transmission
of measurement data. The comes the laser tool calibration button,
and the sensor calibration buttons (last three).

E.1.1 INSPECTOR

INSPECTOR is a GUI application that performs all the inspection measure-
ments. The two windows of the application are shown in Fig.E.2.
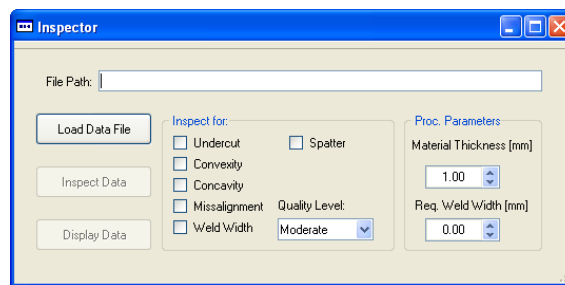
(a) Main Control Window.
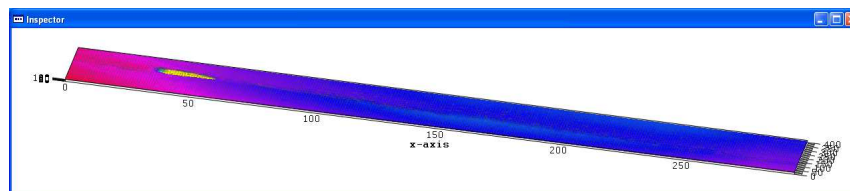
(b) Image View.

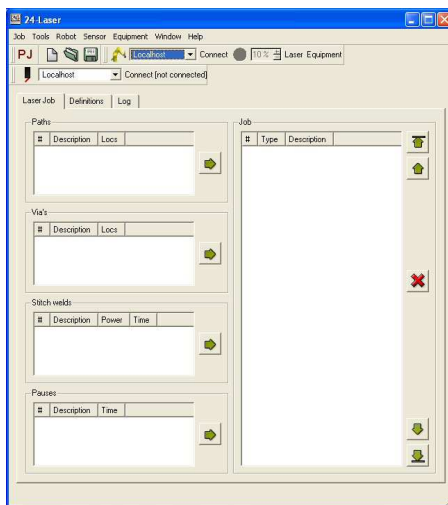*Figure E.2: The two main windows of the* INSPECTOR *application.*

When this application is launched, the window of Fig.E.2(a) appears
and the name of the file that contains the inspection data is requested.
The user can selects the weld defects that are to be measured as well as
the quality level by which the defects will be examined. The thickness of
the material must be provided. The user can view the three dimensional

reconstruction of the inspection data and the measurement results int he window of Fig.E.2(b).

E.2 24-LASER & Sockets

24-LASER is a graphical user's interface for preparing and performing laser welding jobs with or without the assistance of sensors. This software has been developed by (De Graaf (2007)). It has been used for the conduction of the seam teaching and welding experiments. Two of the most commonly used windows of the 24-LASER application are shown in Fig.E.3.

The window of Fig.E.3(a) is the main window where the user can have an overview of the defined weld path, the connected robot position and sensor data. The window of Fig.E.3(b) is the robot controller, through which the user can have complete control of the robot movement and external axes as well as an overview of the robot status.
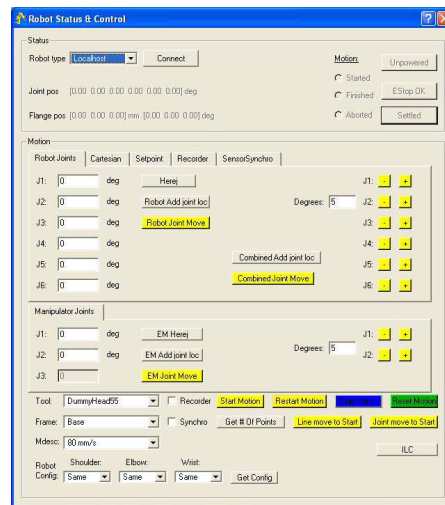
(a) Master Window. (b) Robot Control Window.

Figure E.3: The two main windows of the 24-LASER *application.*

The main functionalities of 24-LASER are listed below:

Robot Control This functionality is connected with the window of Fig.E.3(b). Robot control gives the user complete control over

the robot movements and rotations, speeds and accelerations. It also displays the status of the robot (Moving, Stopped, Enabled, Connected, etc).

Sensor Tool The sensor tool allows the acquisition of measurement data from a sensor. It also contains the required functionality in order to use the sensor data for teaching or following a seam.

Calibrations This part caries out the necessary calibrations for the derivation of the TCP_L and the transformation between the TCP_L and TCP_S for the cases that the sensor does not provide these procedures.

ILC Control This enables 24-LASER to use iterative learning control to improve the tracking accuracy of a seam with the use of sensor data.

Job Definition This is the functionality that allows the user to define the path that is to be welded. Several parameters can also be set and controlled, such as: welding velocity, accelerations, laser power, shielding gas, etc.

For 24-LASER two sockets for the Ethernet communication layer were implemented. These sockets are based on the Client-Server communication model and their implementation differs depending on their use. These sockets described in the following list.

Robot Socket This socket allows the robot to communicate with its environment. In its implementation the robot is the server and is constantly listening for the client's requests. Each request has a specific ID number, and the request can vary from asking the status of the robot to commanding it to perform a movement. This socket is also used from INTEGLAS to carry out the required calibrations.

Sensor Socket The sensor socket allows 24-LASER to receive data from connected sensors. In this case the sensor is the server, which accepts requests from the clients (in this case 24-LASER). Such a server is provided by INTEGLAS to be able to convey its measurement data to 24-LASER (client). Like the Robot Socket, every type of request has a specific ID number. The difference is that the client is limitedly only to acquiring data from the sensor.

E.3   Camera Lens Calibration Toolbox

Even though the steps of the camera and lens calibration are explicit, the
process itself is quite complex and multi-variable. Therefore there is a need
for a tool that allows a user to perform such a calibration without having
to know all the details of the process. For this reason an automated cali-
bration toolbox was developed (Entzinger (2005)) with a graphic user in-
terface that guides the inexperienced user through the calibration process,
but also provides the ability to the experienced user to interact during pro-
cess. This toolbox has been developed under MatLab. The main window
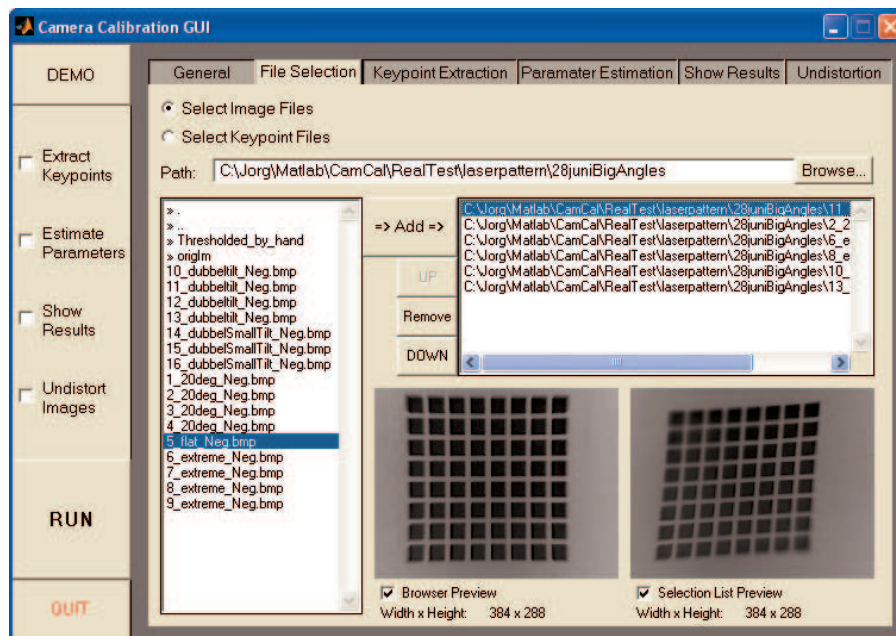of the toolbox is shown in Fig.E.4.

Figure E.4: (Left) Main window view of the camera and lens calibration toolbox.

The user can define the type of calibration pattern that is used and the
type of undistortions that is required to be detected. Furthermore, the de-
tection algorithm for the key point extraction can be selected as well as
the type of key points that are to be detected (centroid, corner). Addition-
ally to the toolbox's image selection mechanism the user is also allowed
to manually omit undesired images, as well as to view the process of the
parameter estimation and its intermediate results.

Finally, the user can view and undistort any image according to the estimated parameters, and repeat any part of the calibration process if any further optimization is required. The process also produces a calibration file that can be used from applications outside the GUI for undistortion.

Several of the steps and data that are produced from the toolbox for better overview of the calibration process and functionality are shown in Fig.E.5

(a) Original Image.

(b) Inverted Colors.

(c) Threshold and Labeled.

(d) Corner and center points.

(e) Sorted center points.

(f) Focal distance plot.

(g) Tangential parameter plot.
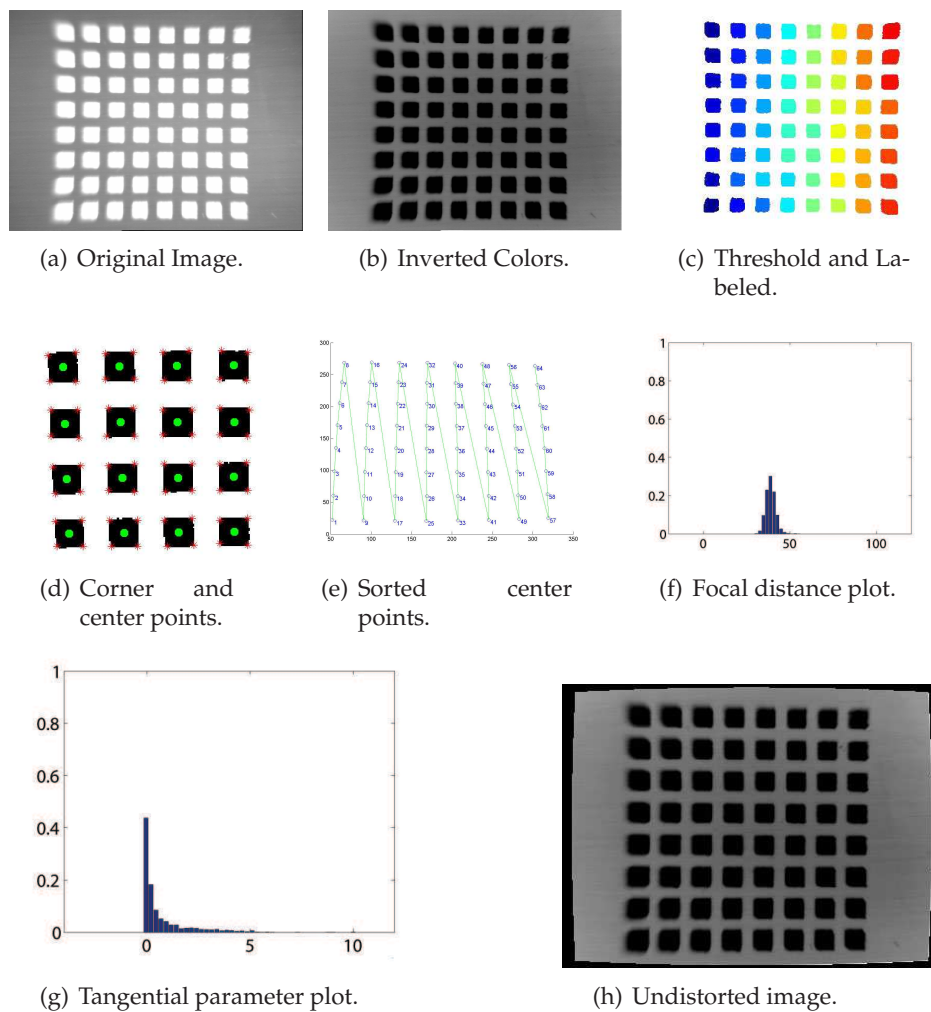
(h) Undistorted image.

Figure E.5: Several steps of the calibration procedure.

222

Appendix F

Mechanical Drawings

In this Appendix the mechanical drawing of all the custom made primary welding head parts are shown.
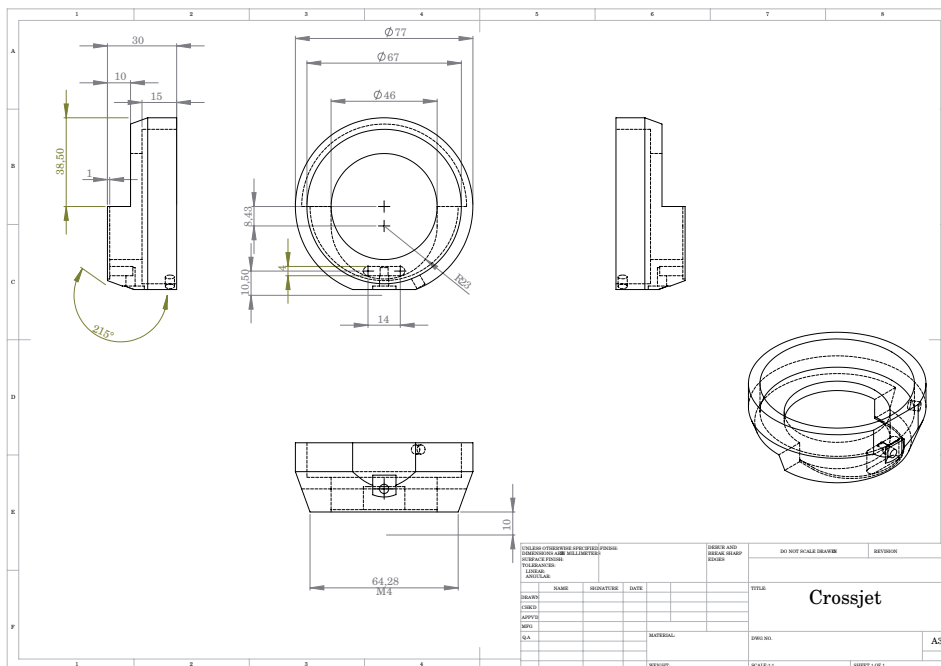
Figure F.1: Welding head Cross-Jet.
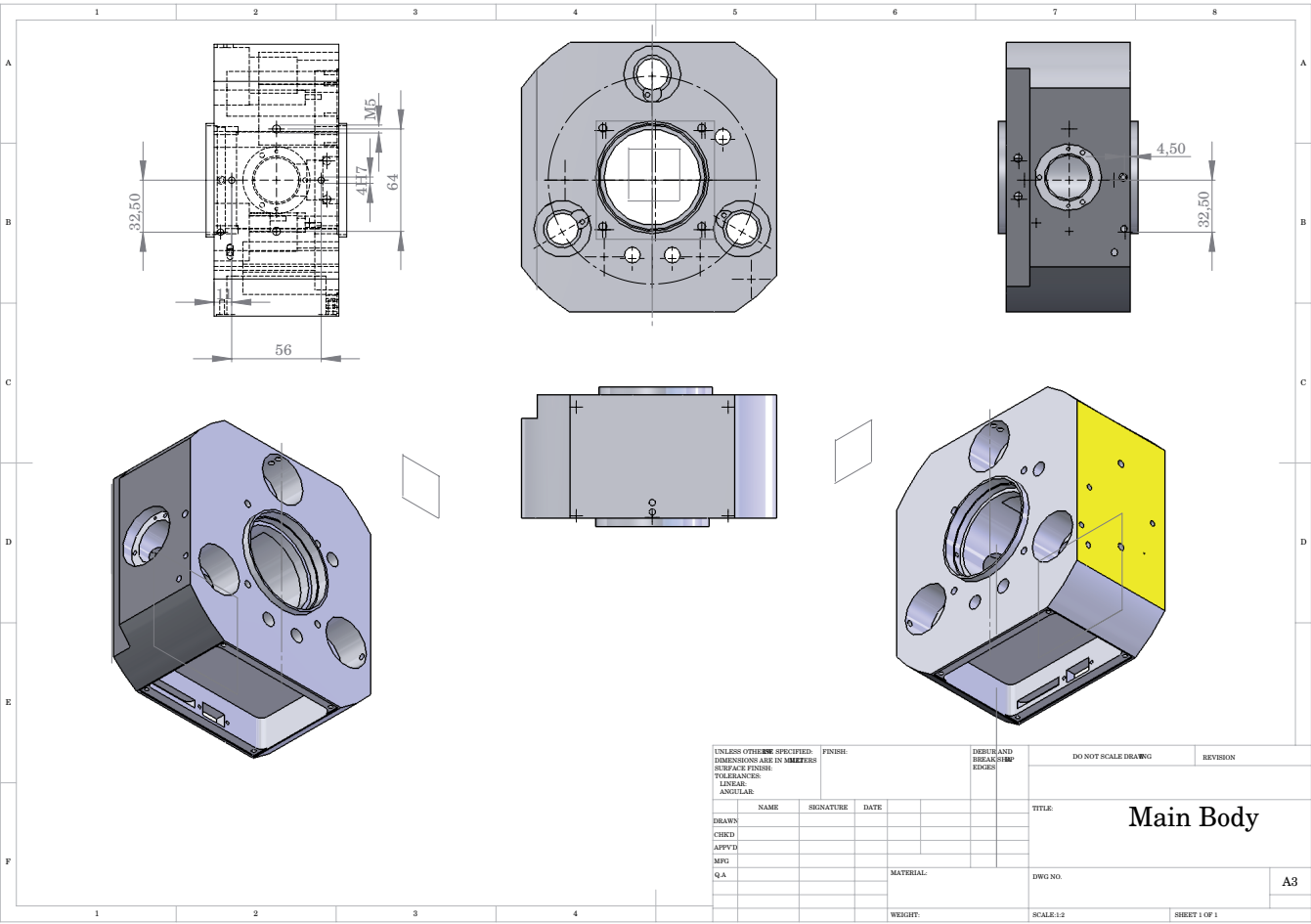
Figure F.2: Welding head main body.

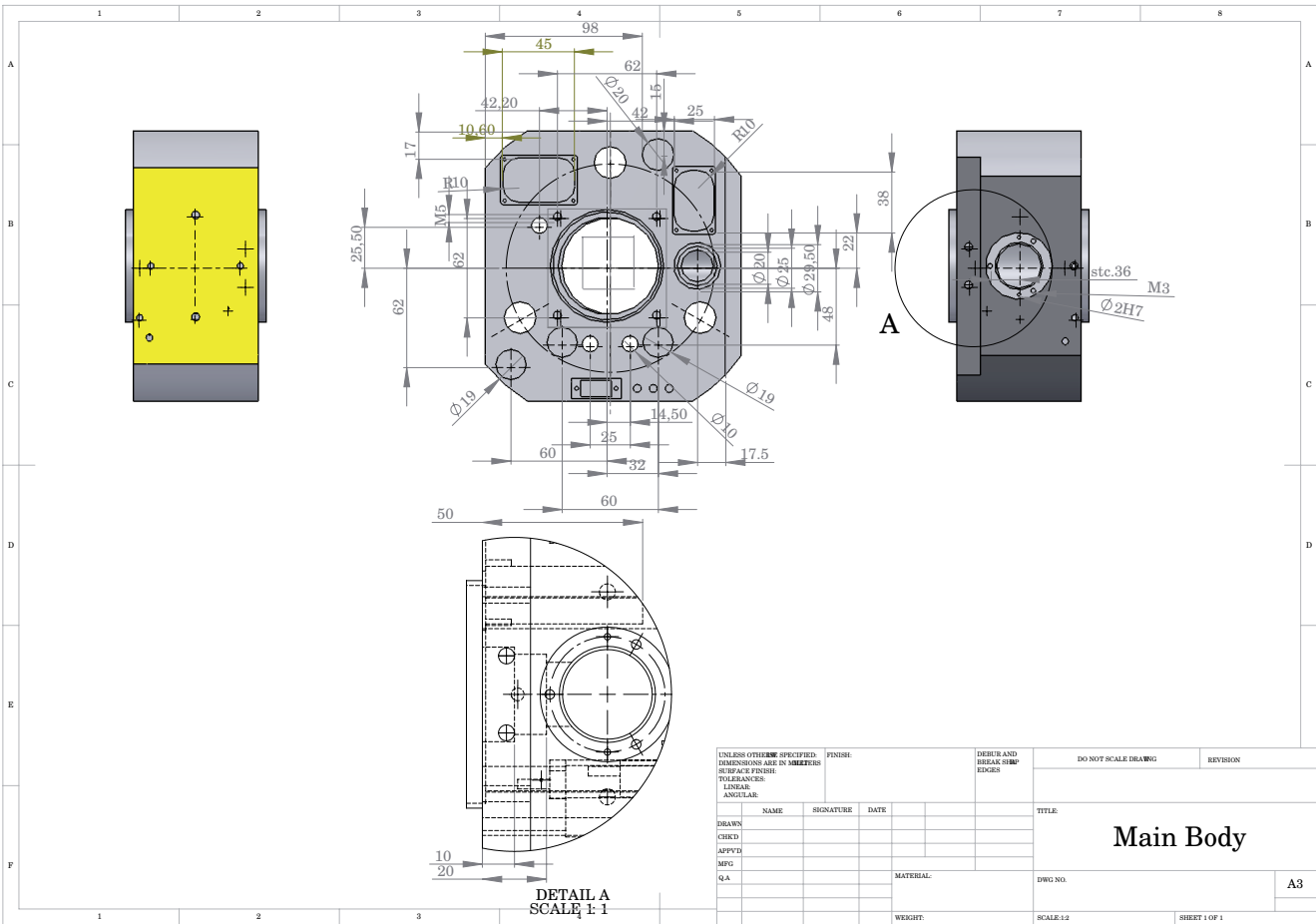|	NAME	SIGNATURE	DATE			TITLE:		
DRAWN							Main Body	
CHK'D								
APPV'D								
MFG								
Q.A				MATERIAL:		DWG NO.		A3
				WEIGHT:		SCALE:1:2	SHEET 1 OF 1	

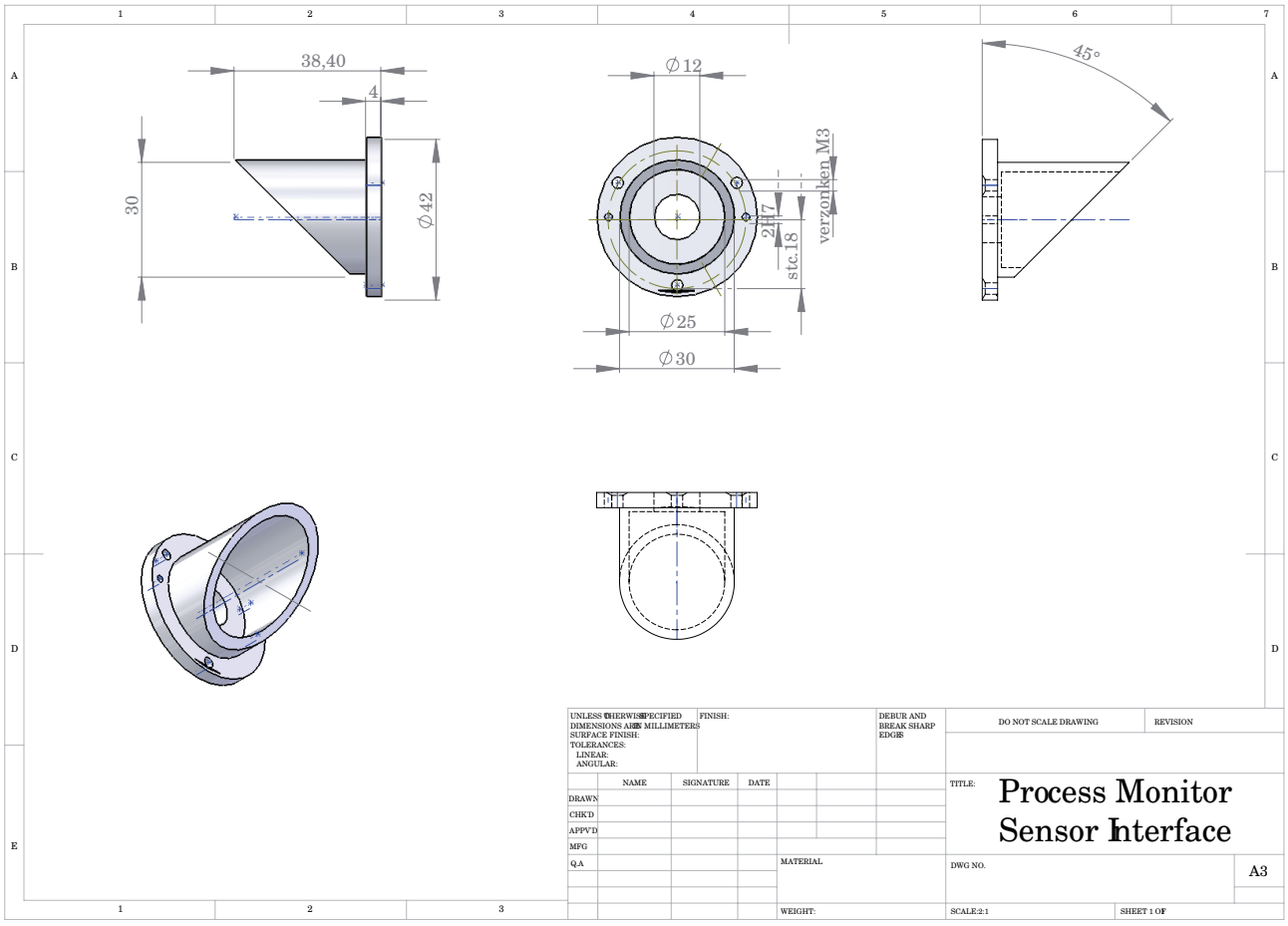*Figure F.3: Welding head main body.*

Figure F.4: Process monitor sensor mechanical interface.

Publications

Iakovou, D., Aarts, R.G.K.M., Meijer, J. (2005). "Integrated sensors for robotic laser welding." In "Proceedings of the Third International WLT-Conference on Lasers in Manufacturing", Munich, Germany, June 2005, Pages 121-126.

Iakovou, D., Aarts, R.G.K.M., Meijer, J. (2005). "Sensor Integrations for robotic laser welding processes." In "Proceedings ICALEO 2005", Miami, USA, October 2005, Paper No. 2301.

Entzinger, J.O., Iakovou, D., Aarts, R.G.K.M., Meijer, J. (2007). Improving coaxial measurements in laser welding by correcting distortions of a laser focus lens with a wide field of view." In "Journal of Laser Applications", August 2007, Vol.19, No.3, Pages 141-148, ISSN 1042-346X.

Iakovou, D., Aarts, R.G.K.M., Meijer, J. (2007). "Perimetric sensor for the detection and following of complex seam trajectories in robotic laser welding". In "Proceedings ICALEO 2007", Orlando, USA, November 2007, Paper No. 1901.

Iakovou, D., Aarts, R.G.K.M., Meijer, J. (2007). "Perimetric trajectory detection using distinctive structured light sources." Patent Application No. EP07112850.8, Submitted on July 20th, 2007.

228

Bibliography

Aalderink, B. , Aarts, R. , Jonker, J. , and Meijer, J. (2005). Experimental observations of the laser keyhole welding process of aa5182. In *Procedings ICALEO*, page 832 836. USA.

Altera Corp. (2005). *Introduction to Quartus® II*. Altera®, 101 Innovation Drive, San Jose, CA 95134, USA, v5.0 edition.

Bates, G. and Kelkar, G. (2002). Determination of a weld quality in pulsed Nd:YAG laser welds using IR and acoustic sensors. In *Procedings ICALEO*. USA.

Beersiek, J. (2001). A CMOS camera as a tool for process analysis not only for laser beam welding. In *Procedings ICALEO*, volume 92-93, pages 1185–1193. USA.

Bosner, G. and Parker, G. (1999). Robotic gas metal arc welding of small diameter saddle type joints using multistripe structured light. *Optical Engineering*, 38(11):1943–1949.

Brown, D. (1971). Close-range camera calibration. *Photogrammetric Engineering*, 37(8):855–866.

Camplin, K. (2001). Laser weld inspection with electromagnetic acoustic transducers (EMATs). In *Procedings ICALEO*. USA, Innerspec Technologies Inc.

Chan, F. , Lam, F. , and Zui, H. (1998). Adaptive thresholding by variational method. *IEEE Transactions on Image Processing*, 7(3):468–473.

Ciletti, M. (1999). *Modeling, synthesis, and rapid prototyping with the Verilog HDL*. Upper Saddler River, NJ : Prentice Hall.

Dilthey, U. (2005). Welding technology 1 - Welding and Cutting Technologies. ISF-Welding Institute, RWTH-Aachen University, Germany.

Duley, W. (1999). *Laser Welding*. Willey Interscience publications, University of Waterloo.

Entzinger, J. (2005). A flexible seam detection technique for robotic laser welding. Master's thesis, Mechanical Engineering (WA), University of Twente.

Entzinger, J. , Iakovou, D. , Aarts, R. , and Meijer, J. (2007). Improving coaxial measurements in laser welding by correcting distortions of a laser focus lens with a wide field of view. *Journal of Laser Applications*, 19(3):141–148.

Falldorf (2004). Specifications of near to focus sensor. Bremen, Germany.

Farson, D. , Sang, Y. , and Ali, A. (1997). Relationship between airborne acousic and optical emissions during laser welding. *Journal of Laser Applications*, 9:87–94.

FME-CWM (2002). Praktijkaanbeveling: Lassen van metalen met hoogvermogen lasers. Technical Report PA.02.12, FME-CWM, NIL, ITC, Bond voor Materialenkennis.

Graaf, M. de (2006). 24-Laser graphical user interface for sensor-guided laser welding. Netherlands.

Graaf, M. de (2007). *Sensor-guided robotic laser welding*. PhD thesis, University of Twente.

Graaf, M. de, Benneker, J. O. , Aarts, R. , Meijer, J. , and Jonker, J. (2005). Robust process-controller for Nd:YAG welding. In *International Conference on Applications of Lasers and Electro-optics*, Miami, USA. ICALEO'05.

Grooth, N. (2006). Development of a basic vision system for the surface analysis of laser welds. Master's thesis, Electrical Engineering (EEMCS, SAS), Mechanical Engineering (WA), University of Twente.

Gu, H. and Duley, W. (1996). A statistical approach to acoustic monitoring of laser welding. *Journal of Physics Applications*, 29(3):556–560.

Gu, H. and Duley, W. (1997). Discrete signal components in optical emission during keyhole welding. In *LIA proceedings ICALEO'97*, volume 83, pages 40–46.

Guo, R. and Pandit, S. (1998). Automatic threshold selection based on histogram modes and a discriminant criterion. *Machine Vision and Applications*, 10:331–338.

Hakvoort, W. , Aarts, R. , Dijk, J. V. , and Jonker, J. (2006). Iterative learning control for improved end-effector accuracy of an industrial robot. In *Proceedings of Symposium on Robot Control*. IFAC.

Halscha, M. , Schwarz, J. , Wildman, D. , and Wagner, F. (2003). Machine vision − the powerful tool for quality assurance of laser welding and brazing. In *Procedings ICALEO*. Florida, USA, Soudronic Automotive. No1302.

Hardeman, T. , Aarts, R. , Dijk, J. V. , and Jonker, J. (2006). A scanning mirror for robotic laser welding. In Jager, E. B. de and Meinsma, G. , editors, *Book of Abstracts 25th Benelux Meeting on Systems and Control*, page 143, Heeze, The Netherlands.

Hecht, E. (1998). *OPTICS*. Addison-Weslay, third edition.

Heijden, F. van der (1994). *Image Based Measurement Systems - Object recognition and parameter estimation*. John Wiley & Sons.

Heikkila, J. and Silven, O. (1997). A four-step camera calibration procedure with implicit image correction. In *CVPR '97: Proceedings of the 1997 Conference on Computer Vision and Pattern Recognition (CVPR '97)*, page 1106, Washington, DC, USA. IEEE Computer Society.

HIGHYAG (2005). Laser processing head PDT. Shahnsdorf, Germany.

Hornberg, A. (2007). *Handbook of Machine Vision*. Wiley-VCH.

INESS (2003). Integration optischer messmethoden zur prozesskontolle beim laserstahlschweißen. *Laser Magazin*, (1).

Innotec, S. (2004). Automatic contour recognitionin laser welding. Winterthur, Switzerland.

ISO13919:-2:2001 (2001). *Welding - Electron and laser beam welding - Guidance on quality levels and imperfections*. ISO©.

Jäckel, T. , Miesner, J. , Frischkorn, F. , Kreitlow, H. , Jackson, M. , and Parkin, R. (2003). Laser welding seam tracking. pages 593–598, London. ICOM, Professional Engineering Publishing.

Jian, X. , Malcolm, A. , and Zhongping, F. (2001). Camera calibration with micron level accuracy. Technical Report AT/01/037/PS, Singapore Institute of Manufacturing Technology.

Jones, B. E. (1987). Sensors in industrial metrology. *IOP invited paper*, pages 1113–1126.

Jung, W. (2004). *Analog Devices, Op Amp Amplications Handbook*. Newnes-Elsevier.

Jurca, G. (2001). LWM900, quality assurance in laser welding. Rodgau, Germany.

Klein, M. , Pouet, B. , Kercel, S. , and Kisner, R. (2002). In−process detection of weld defects using laser ultrasonics". In *Procedings ICALEO*. USA.

Lhospitalier, S. , Bourges, P. , Bert, A. , Quesada, J. , and Lambertin, M. (1999). Temperature measurement inside and near the weld pool during laser welding. *Journal of Laser Applications*, 11(1):32–37.

Lindskog, A. (2002). Seam tracking laser welding tool. In *Procedings of EALA*. Bad Nauheim, Germany, Permanova Lasersystem AB.

Luo, H. and Chen, X. (2004). Laser visual sensing for seam tracking in robotic arc welding of titanium alloys. *International Journal of Advanced Manufacturing Technology*, 26:1012–1017.

Ma, L. , Chen, Y. , and Moore, K. (2003). A new analytical radial distortion model for camera calibration. *CoRR: Computer Vision and Pattern Recognition*, (0307046v1).

MathWorks (2003). *Radon Transform*. Image Processing Toolbox.

Merklinger, H. (1992). The scheimpflug principle part i. *Shutterbug*.

MetaVision (2005). Laser vision applications in robot welding. United Kingdom.

Microsoft (2002). *Delivery Guide — Developing Microsoft® .NET Applications for Windows® (Visual C♯^{TM} .NET).* Microsoft Corporation.

Mori, K. and Miyamoto, I. (1997). Inprocess monitoring of laser welding by the analysis of riples in the plasma emmision. *Journal of Laser Applications*, 9:155–159.

Nayak, N. and Ray, A. (1993). Inteligent seam tracking for robotic welding. In *Advances in Industrial Control*. Springer-Verlag.

Noruk, J. and Boillot, J. (2006). Laser vision technology ensures six sigma-level quality is achieved in robotic welding. *Canadian Welding Association Journal*.

OldeBenneker, J. (2000). Toelaatbare toleranties bij het laserlassen van aluminiumlegeringen, *Technical Report* wa-683. University of Twente, Enschede, The Netherlands.

OldeBenneker, J. and Gales, A. (2007). Een vergelijking van het laserlassen met conventionele lastechnieken voor kleine series producten. *SKB FME-CWM*.

OST (2005). CSS - Circular Scanning Sensor. UK.

Otsu, N. (1979). A threshold selection method from gray-level histograms. *IEEE Transactions on Systems, Man, and Cybernetics*, 9(1):62–66.

Palnitkar, S. (1996). *Verilog Hdl: A Guide to Digital Design and Synthesis*. Upper Saddle River, NJ : SunSoft Press, a Prentice Hall title.

Plasmo® (2006). Plasmo® quality control and diagnosis systems. Stuttgart, Germany.

Postma, S. (2003). *Weld Pool Control in* N*d:*YAG *Laser Welding.* PhD thesis, University of Twente.

Precitec, K. (2005). Welding head YW50, high performance welding head for Nd:YAG and fiber laser. Germany.

Rhapsody (2006). *Rhapsody 3.0 for Dica-321*. Industrial Vision - Philips CFT, 3.0 edition.

Rimrock (2006). Smartac^{TM}, weld joint detection system. USA.

Russ, J. (2002). *The Image Processing Handbook*. CRC Press, 4 edition.

Sanders, P. , Keske, J. , Korneski, G. , and Leong, K. (1997). Capabilities of infrared weld monitor. In *Procedings ICALEO*, pages 1–10. USA.

Savakis, A. (1998). Adaptive document image thresholding using foreground and background clustering. In *International Conference on Image Processing*. ICIP.

ServoRobot (2005). Digi−las^{TM}, inteligent laser joining head with 3−d coaxial vision. USA.

Soudronic (2005). Souvis$^{®}$ 5000, weld inspection system. Neftenbach, Switzerland.

Suzuki, K. , Horiba, I. , and Sugie, N. (2003). Linear-time connected-component labeling baced on sequential local operations. *Computer Vision and Image Understanding*, 89(1):1–23.

Tienhoven, J. , Graaf, M. de, Aarts, R. , Jonker, J. , and Meijer, J. (2005). Combined sensor and laser tool calibration for laser welding robots.

Toft, P. (1996). *Radon Transform - Theory and Implementation*. PhD thesis, DTU.

Trolltech (2006). *Introducing QT$^{®}$,The Cross-Platform C++ Development Framework*. Trolltech, 4.0 edition.

Tsai., R. (IEEE 1987). A versatile camera calibration technique for high-accuracy 3d machine vision metrology using off-the-shelf tv cameras and lenses. *J. of Robotics and Automation*, RA-3(4):1165–1172.

UDT (2008). Udt photodiode catalog. Technical Report Revision 98.3, UDT Sensors Inc.

Vitronic (2005). Viro^{WSI} 3-d seam inspection technical information. Germany.

Vodanovic, B. (1996). Structured light tracks seam. *Sensor review*, 16(1):35–39.

Waiboer, R. (2007). *Dynamic modeling, identification and simulation of industrial robots*. PhD thesis, University of Twente.

Weisstein, E. (2005). Rodrigues' rotation formula. From MathWorld–A Wolfram Web Resource.

Xu, G. and Zhang, Z. (1996). *Epipolar Geometry in Stereo, Motion and Object Recognition - A Unified Approach*. Computational Imaging and Vision. Kluwer Academic Publishers, 6 edition.

Zhang, Z. (1998). A flexible new technique for camera calibration. Technical Report MSR-TR-98-71, Microsoft Research.